Viscous fingering instabilities and gravity currents

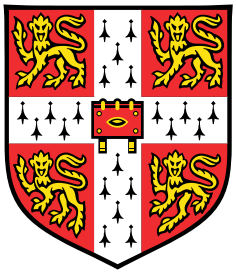

Tim-Frederik Dauck

Supervisor: Prof. J. R. Lister

Department of Applied Mathematics and Theoretical Physics
University of Cambridge

This dissertation is submitted for the degree of
Doctor of Philosophy

Trinity College December 2019

Declaration

I hereby declare that except where specific reference is made to the work of others, the contents of this dissertation are original and have not been submitted in whole or in part for consideration for any other degree or qualification in this, or any other university. This dissertation is my own work and contains nothing which is the outcome of work done in collaboration with others, except as specified in the text and acknowledgements.

Tim-Frederik Dauck
December 2019

Abstract

Viscous fingering instabilities and gravity currents

Tim-Frederik Dauck

This thesis examines the possible instability of radially spreading interfaces to the formation of fingers that break the axial symmetry. A well-known example of this occurs when a less viscous fluid displaces a more viscous immiscible fluid either in a porous medium or in a Hele-Shaw cell, which is commonly referred to as the Saffman–Taylor instability. There are three related problems studied in this thesis: a single-layer viscous gravity current spreading from a point source over a rigid surface, radial spreading of an intrusion displacing miscible fluid in a Hele-Shaw cell, and finally, a viscous gravity current spreading from a constant-flux point source over a uniform layer of ambient fluid with equal density but different viscosity.

For single-layer viscous gravity currents with constant volumes, an analytical solution is available, which is known to be stable. By means of a numerical linear stability analysis, it is shown here that more general currents, with volumes growing as power laws in time, are stable as well. For currents with constant influx, considering a small shift in temporal origin yields the least stable axisymmetric perturbation mode. This analytic solution is generalised, first to non-axisymmetric perturbations, and then to more general power-law influxes. The derived growth rate confirms theoretically the stability of this least stable mode. Further perturbation modes are found numerically, exploiting a scaling-invariance symmetry of the governing equations, and using a change of independent variable to mitigate the singular nature of the nose. Finally, the stability of a general moving front within the framework of lubrication theory is established by considering the asymptotic limit of large azimuthal wavenumber.

Miscible intrusions in a Hele-Shaw cell with negligible diffusion are known to form flat frontal shocks for a sufficiently viscous ambient fluid. Experiments and theoretical work suggest that these fronts become unstable, similar to the Saffman–Taylor instability. However, no formal stability analysis has been done thus far. This thesis caries out this

linear stability analysis, showing both that intrusions without a shock are stable and that intrusions with a shock are unstable. An asymptotic analysis of large azimuthal wavenumber shows that the model based on lubrication theory predicts rapidly growing perturbations in this limit. Therefore, the full three-dimensional Stokes equations would be required to predict a most unstable wavenumber. Analytic solutions for the general nonlinear evolution of the intrusion are found in the cases of axisymmetric perturbations and of equal-viscosity fluids.

Finally, a viscous gravity current spreading from a constant-flux point source over a uniform layer of ambient fluid is examined for the case of equal-density fluids. This case is identified as a singular limit in which the evolution equation for the interface becomes hyperbolic instead of parabolic. As a consequence, vertical shocks are predicted to form at the front of the intruding current for a sufficiently viscous ambient fluid layer, similar to the shocks found in Hele-Shaw flows. Reintroduction of a small density difference yields an Oleinik entropy condition, which predicts a unique shock height for the self-similar base state. The subsequent linear stability analysis reveals many similarities to Hele-Shaw flows, in particular the singular nature of large azimuthal wavenumbers. Experimental data obtained by others, compares very well overall to predictions of the theory. Finally, the cases of a single-layer current and of a Hele-Shaw intrusion are established as formal asymptotic limits of this two-layer current for large and small influxes, respectively.

Acknowledgements

First and foremost, I would like to thank my supervisor, Professor John Lister, for giving me the opportunity to work with him throughout my PhD. I am greatly appreciative of the time and support he has given so generously and for his perseverance and attention to detail. I am grateful for the many things I learned from him.

I gratefully acknowledge the Engineering and Physical Sciences Research Council for offering me a research grant to fund my studies, as well as Trinity College and the Department for Applied Mathematics and Theoretical Physics of the University of Cambridge. Without their support, this work would not have been possible.

I would very much like to thank my parents, Hartwig and Bernadette, and my siblings, Lars and Inga. They have always supported me in every way possible and have provided me with every opportunity throughout my life. I am very grateful for everything they have done for me.

A further, very special thank you to Rachel for her never-ending encouragement and reassurance, for enduring my ongoing rambling about spreading fluids and generally for the support I received from her and her parents, Diana and Nick.

Finally, I would like to thank Fujian White Crane Kung Fu and Tai Chi, and especially my instructor Karim Daoud and the chief instructor Dennis Ngo, for providing much-needed balance in the form of exercise and an attitude of perseverance and striving for success.

Table of contents

List of figures

List of tables

Chapter 1

Introduction

A key question often asked in fluid mechanics is whether a given flow is stable or unstable. By this, we mean whether small perturbations to the flow decay, or whether they grow to the point of changing the nature of the flow. Often a consequence is that a symmetry of the initial flow gets lost, and a more complex flow pattern develops. Such instabilities occur in many situations and are, for example, a key mechanism of how laminar flow becomes turbulent. However, not all instabilities are associated with the chaotic nature of turbulent flow, but instead occur in slow viscous flows leading to fascinating patterns. A simple everyday example is given by making pancakes: if the batter is simply poured into the pan and allowed to spread under its own weight, it forms a near perfect circular patch (figure 1.1a). If on the other hand the pan is swayed to spread the batter more quickly, it tends to finger and form streaks, possibly leading to gaps in the pancake (figure 1.1b). A similar instability can also be observed if too much oil is put in the pan, which causes the batter to finger even if the pan is

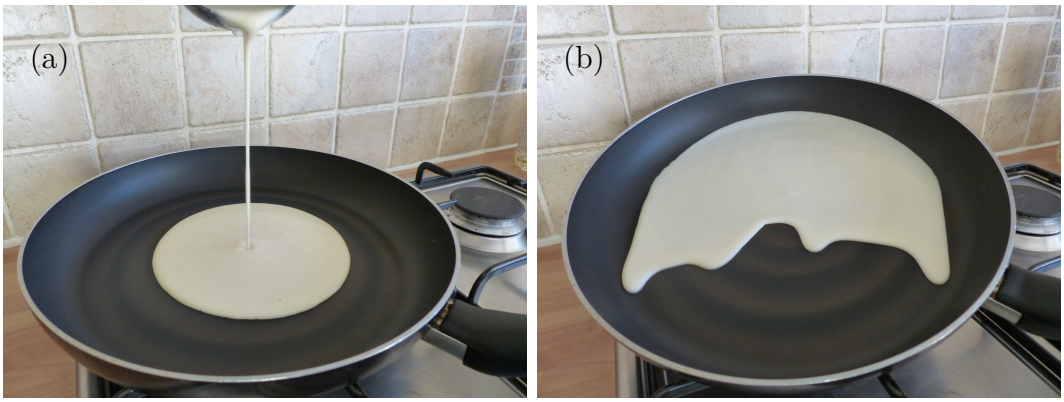

Fig. 1.1 (a) Making pancakes by passively spreading the batter leads to an axisymmetric pancake. (b) Making pancakes by actively tilting the pan leads to fingering.

horizontal, and which more closely relates to the problems studied in this thesis. Both of these examples combine the two aspects of fluid mechanics studied in this thesis: so-called gravity currents and fingering instabilities which will be discussed in more detail below.

1.1 Gravity currents

The general idea behind gravity currents is that fluid denser than the ambient spreads under its own weight along some form of boundary, displacing the lighter ambient fluid as a consequence. Equivalently, lighter fluids can displace a heavier ambient spreading underneath a boundary instead of on top of it. The presence of the boundary is crucial, and distinguishes a gravity current from a plume, which in some sense is much closer to fluid falling or rising vertically as opposed to spreading laterally. Plumes are described by different fluid mechanical principles (Turner, 1979), which we will not discuss in this thesis. Gravity currents, on the other hand, form a main part of this thesis, which is motivated in parts by the many different physical situations in nature and in industry, where they are applicable (Simpson, 1997).

For example, there are many violent geological processes which can be modelled as gravity currents. Avalanches consist of a heavy mixture of air and snow, which flows down along the solid boundary of the mountain slope, picking up snow and speed along the way (Hermann and Hutter, 1991; Naaim and Gurger, 1998). Similar currents, where the driving density difference is a result of heavy suspended particles in air, are given by pyroclastic flows made of hot gases, ash and other volcanic matter, released from an explosive eruption of a volcano (Saucedo et al., 2004; Stix, 2001; Valentine and Fisher, 1993). Subsequent mudflows called lahars, forming as a result of suspended pyroclastic material with a consistency similar to wet concrete (Naranjo et al., 1986; Worni et al., 2012), are an example where particles suspended in a liquid instead of a gas drive the gravity current. A second similar such example is given by so-called turbidity currents occurring underwater when heavy sediment-laden water flows down a slope in the seabed (Dengler and Wilde, 1987). A different source of density difference can be given by effects of temperature. For example, colder air tends to spread along the ground displacing the warmer air upwards, which can occur both in atmospheric weather fronts (Charba, 1974; Mayor, 2010), or in a cold draft from a doorway which is important in understanding ventilation in buildings (Wilson and Kiel, 1990).

However, not all gravity currents are fast-moving and turbulent in nature, but instead they can be much more viscous, spreading over longer time scales. A geological

example of this is given by viscous lava spreading over the rigid ground while gradually cooling and solidifying. If the lava is sufficiently viscous and the ground is flat the solidified current can form characteristic domes, which are observed not only on Earth (Griffiths, 2000) but also, for example, on Venus (McKenzie et al., 1992). In certain scenarios, even the evolution of solids can be described fluid mechanically as viscous gravity currents over sufficiently long time scales. For example, the slow creeping ice of glaciers and ice sheets, driven down slopes by their immense weight, can be modelled very successfully as shear-thinning gravity currents (Schoof and Hewitt, 2013). Understanding the impact of global climate change on the glaciers, especially of the Antarctic, plays a key role in predicting, for example, rise in sea levels, and hence is of great importance (Jacob et al., 2012). We also note that even solid rocks can sometimes be modelled as viscous or viscoelastic fluids, provided sufficiently long time scales. Two examples of such cases are given by the spreading of the lithosphere along the mid-mantle boundary (Kerr and Lister, 1987) and the gradual deformation of mountain ranges, such as, for example, the Tibetan plateau, which can be modelled as a gravity current flowing very slowly over the intruding Indian tectonic plate (Copley and McKenzie, 2007).

In industry, we find a wide variety of examples for gravity currents as well, such as the production of sheet glass using the Pilkington float process, where molten glass is allowed to float and spread over molten tin to achieve a very uniform thickness of the glass (Pilkington, 1969). A different application is the sequestration of carbon dioxide, which is one of many important mechanisms to reduce greenhouse gas emissions. This is done, for example, by injecting carbon dioxide into geological formations such as exhausted gas fields, where the reintroduced carbon dioxide spreads laterally as a gravity current underneath the impermeable caprock (Orr, 2009). It is crucial to monitor and understand this spreading process to prevent unwanted leakages and control the extent of carbon dioxide spreading. A similar example is given by the Deepwater Horizon oil spill in 2010, which resulted in nearly five million barrels of oil spreading out in the Gulf of Mexico, effectively forming gravity currents of the lighter oil floating on top of the heavier seawater. Again understanding the spreading of the contaminating oil in such a situation is key to minimising the resulting environmental damage.

The abundance of examples, ranging from natural physical processes through industrial applications to making pancakes, shows clearly that studying gravity currents is worthwhile and important. As a consequence, there are many investigations examining

gravity currents, both by using laboratory experiments or by developing theoretical models.

A key distinction between different types of gravity currents that needs to be made at this point, is related to the associated Reynolds number of the flow: on the one hand, high-Reynolds number currents occur when the flow velocities U and length scales L are large compared to the viscosity ν, i.e. $UL \gg \nu$. In these cases the high shear rates at the interface make the flow unstable through the Kelvin–Helmholtz instability and result in turbulence (Drazin, 2002). A theoretical model describing these turbulent gravity currents was first proposed by von Kármán (1940) and later corrected by Benjamin (1968), determining the rate of propagation in terms of a so-called Froude number at the front of the current. Hence, these currents can be thought of as predominantly governed by the nose. The turbulent nature of these currents also makes additional effects, such as entrainment of ambient fluid, relevant (Hallworth et al., 1996, 1993; Ungarish, 2009).

On the other hand, we will study low-Reynolds currents which are slow creeping flows where inertial forces can be neglected, and the buoyancy-induced pressure gradients are balanced by viscous forces only. Examples of these currents include glacial flow, the production of sheet glass, or honey spreading on toast. Often these currents become long and thin and hence vertical velocities become negligible (Oron et al., 1997), which allows them to be analysed by the approximation known as lubrication theory (Acheson, 1990; Reynolds, 1886). Models based on this approximation are usually singular at the nose, where technically the assumptions of a long and thin current break down. For some more complex cases, such as, for example, lava intrusions underneath elastic sheets of rock, these singularities at the nose would disallow any spreading within the model without introducing additional physics such as a pre-wetting film or a fracturing tip (Detournay and Garagash, 2003; Lister, 1990; Lister et al., 2013, 2019; Thorey and Michaut, 2016). Nonetheless, for simple currents without a cover, these models predict shapes and spreading rates which are in remarkable good agreement with experimental results (Huppert, 1982b; Longo et al., 2013).

As a consequence of the wide variety of applications and physical situations modelled as low-Reynolds-number viscous gravity currents, a wide variety of different flow geometries and fluid properties have been studied. For example, previous studies examine viscous gravity currents from a point or a line source on a rigid horizontal plane (Gratton and Minotti, 1990; Huppert, 1982a; Smith, 1969), within a channel (Longo et al., 2015; Takagi and Huppert, 2007), on an incline (Huppert, 1982b; Lister, 1992; Smith, 1973), towards a central hole (Diez et al., 1992; Zheng et al., 2014), at

an interface of two fluids (Hoult, 1972; Koch and Koch, 1995; Kowal and Worster, 2015; Lister and Kerr, 1989), or even with a permeable boundary (Acton et al., 2001; Neufeld et al., 2011; Pritchard and Hogg, 2002). Further investigations have included different physical ingredients, such as gravity currents in a saturated porous medium (Di Federico et al., 2012; Hesse et al., 2007; Huppert and Woods, 1995; Lyle et al., 2005; Vella and Huppert, 2006), gravity currents consisting of a density-stratified fluid (Pegler et al., 2016; Woods and Mason, 2000) or a non-Newtonian fluid such as, for example, ice (Balmforth et al., 2007; Fink and Griffiths, 1998; Gratton and Minotti, 1999; Griffiths and Fink, 1993; Hogg and Matson, 2009; Nye, 1952; Sayag and Worster, 2013), the effects of surface tension or an elastic cover on top (Hewitt et al., 2015; Lister et al., 2013), or the effects of cooling and solidification as applicable to lava flows or pancakes (Fink and Griffiths, 1990; Lyman and Kerr, 2006). Often the derived models allow the use of self-similar variables, thus reducing a time-dependent integration of partial differential equations to a simple spatial integration of ordinary differential equations (Gratton and Minotti, 1990). In general the diffusive nature of the governing equations tends to result in stable currents, and it has been shown, for example, that a single-layer gravity current of constant volume spreading over a rigid horizontal surface is stable (Grundy and McLaughlin, 1982; Mathunjwa and Hogg, 2006), corresponding in the introductory example to the pancake batter spreading passively in the pan (figure 1.1a). However, there are also known instabilities such as the fingering of a gravity current flowing down an inclined slope (Huppert, 1982a), corresponding to the active tilting of the pan to spread the batter (figure 1.1b). Theoretical results are obtained by stability analyses of perturbations to a base state, which itself is already time-dependent through the similarity variable. This is an important method used widely in this thesis.

1.2 Fingering instabilities

We now turn our attention to the second major aspect of this thesis: fingering instabilities. These describe fluid-mechanical processes where an evolving interface is prone to develop protrusions and thus loses some initial symmetry, such as a circular or linear interface. These instabilities classically occur, for example, when more viscous fluid gets displaced by less viscous fluid, usually either in a porous medium or in a Hele-Shaw cell, and in which case they are commonly known as Saffman–Taylor fingering after Saffman and Taylor (1958). A Hele-Shaw cell refers to a device consisting of two parallel rigid plates with a small separation, and was first introduced by Hele-Shaw (1897)

to visualise two-dimensional laminar potential flow past objects. The flow remains laminar, as opposed to turbulent, due to the small separation of the walls, and can be well described by a viscous Stokes flow. Developing the viscous theory reveals a striking resemblance between the governing equations for intrusions in a Hele-Shaw cell and those of two-dimensional viscous flow in porous media. Therefore, there have been a large number of studies investigating flows in Hele-Shaw cells as models for porous-media flows, as the plate separation of these cells is much easier to control than exact properties of actual porous media, and as the flow is much easier to visualise (Richardson, 1989).

Viscous fingering instabilities are of key interest in many natural and industrial settings, in particular where understanding and controlling the amount of mixing is important. Mixing ultimately always results from molecular diffusion along concentration gradients, and hence any instability which increases the surface area enhances the overall rate of mixing (Ottino, 1989). Due to this, and other reasons, examples of systems where the study and understanding of viscous fingering instabilities is important are plentiful: for example, in enhanced oil recovery, different fluids are injected into an oil reservoir after the yield from primary and secondary recovery methods has fallen away. This is to recover residual oil trapped in the porous rock, for example, by using carbon dioxide to mobilise the oil by reducing its viscosity, in which case mixing is desirable. On the other hand, when using so-called polymer floods it is desirable to avoid such instabilities to increase the volume of the reservoir flushed by the polymer solution (Lake, 1989). Another example, already mentioned when discussing gravity currents, is provided by the sequestration of carbon dioxide by injection into a suitable geologic formation. One mechanism for trapping the gas in its location is dissolution into the ambient fluid, which is greatly enhanced by any mixing induced by fingering instabilities (Huppert and Neufeld, 2014). Chromatography involves flow through a porous medium to separate a mixture into its constituents. If the flow becomes unstable this can lead to poor separation and hence it is desirable to avoid any fingering (Mayfield et al., 2005). Yet another example where viscous fingering plays a crucial role in porous media is given by the spreading through soil or sediment of contaminants, for example, from agriculture or industry. This could lead to pollution of groundwater aquifers, and therefore it is desirable to fully understand the combined effects of mixing and dispersion including any effects of fingering instabilities (Abriola, 1987). Controlling the mixing in microfluidic systems is of great interest in many applications in engineering and again influenced heavily by any potential fingering instability (Stone et al., 2004). Finally, we mention hydrothermal systems at midocean

ridges, where water in the porous ocean crust gets heated from below, resulting in rising plumes within the porous medium. As the water in the hot plumes is less viscous than the colder surrounding water, the plumes can split via a viscous fingering instability leading to irregular temperatures of the hydrothermal vents at the top of the the ocean crust (Coumou et al., 2006). There are many more examples one could give, showing the relevance of studies of the mechanisms and effects of fingering instabilities.

One work of particular interest to us is that of Yang and Yortsos (1997), who analysed the cross-sectional structure of intrusions into Hele-Shaw cells with negligible diffusion and surface tension. Their analysis revealed that the hyperbolic advection equations governing the self-similar evolution of the interface between the two fluids predict a frontal shock for the case of a sufficiently more viscous ambient fluid, where the critical viscosity ratio is $m_{\text{crit}} = 3/2$. Later, Lajeunesse et al. (1997, 1999, 2001) and also Bischofberger et al. (2014) experimentally observed a fingering instability very much like the classical Saffman–Taylor instability for immiscible fluids, however, with a different criterion for the onset of instability. Classically the Saffman–Taylor criterion is that the intruding fluid must simply be less viscous, i.e. a critical viscosity ratio of $m_{\text{crit}} = 1$. Instead, the experiments indicated a critical viscosity ratio for fingering close to $m_{\text{crit}} = 3/2$, strongly suggesting a relationship to the occurrence of shocks. A possible interpretation is that both a less viscous intruding fluid and a frontal shock are necessary to trigger the fingering instability for miscible fluids (Bischofberger et al., 2014; Lajeunesse et al., 1997, 1999, 2001). To the best of our knowledge, the actual linear stability analysis has so far not been attempted, and will form part of the work in this thesis. More widely, these results suggest that any flow where a frontal shock of a less viscous fluid intrudes into a more viscous fluid, can be subject to a fingering instability, in particular, if say a similar frontal shock were to develop in a two-layer viscous gravity current.

In fact, Kowal and Worster (2019a,b) recently discovered an example of a fingering instability in a system of a viscous gravity current spreading underneath a second viscous gravity current. They argued that the instability is driven by the dynamics at the front of the lower current, where they also found shocks for the case of equal-density fluids. However, the mechanism leading to the formation of shocks in this system is significantly different from the mechanism in Yang and Yortsos (1997), and derives from their implementation of the rigid lower boundary condition. They assume total displacement of upper-layer fluid, which results in no-slip at the bottom of the lower-layer current and therefore accumulation of lower-layer fluid at the front driven by the upper-layer fluid flux (Kowal and Worster, 2015).

and leads to accumulation of lower-layer fluid at the front

1.3 Thesis structure

This thesis investigates three distinct physical scenarios: the self-similar axisymmetric spreading of a two-layer equal-density viscous gravity current (Chapter 2) and its stability to general linear perturbations (Chapter 5), and also two related questions of the linear stability of a single-layer viscous gravity current (Chapter 3) and an intrusion into a Hele-Shaw cell with negligible diffusion and surface tension (Chapter 4). The structure of the thesis is as follows.

In Chapter 2, we examine a viscous gravity current spreading from a constant-flux point source over a initially uniform layer of ambient fluid with equal density and different viscosity. We use the standard approximation of lubrication theory to derive ordinary differential equations for the self-similar evolution of an axisymmetric current (§2.2). The limit of equal densities is singular, and therefore we consider local travelling-wave solutions near the front of the intruding fluid, based on a small but nonzero density difference, in order to regularise the problem and to derive conditions for any frontal shock that might form (§2.3). A simplified, fully time-dependent system, where the evolution of the top surface is prescribed or assumed known, is then used to illustrate the effects of the hyperbolic advection equation governing the evolution of the interface between the layers, and the subsequent approach to a frontal shock (§2.4). We numerically integrate the similarity equations (§2.5) and compare the solutions to experimental results obtained by others (Dauck et al., 2019). In Appendix 2.A, we derive equivalent results for the two-dimensional spreading from a line source as opposed to the axisymmetric spreading from a point-source.

In Chapter 3, we analyse the stability of a single-layer viscous gravity current spreading from a point source with a power-law flux. We first derive the naive perturbation equations based on a normal-mode analysis with small linear perturbations to an axisymmetric self-similar base state (§3.2), and then discuss several numerical shortcomings of the naive approach. We mitigate these by changing independent variable to deal with the singular nose, and by exploiting a scaling-invariance symmetry of the equations (§3.3), which is motivated by the phase-plane formalism of Gratton and Minotti (1990), but also applies to time-dependent and non-axisymmetric currents. The resulting equations are solved numerically to investigate the eigenspectrum of the normal modes (§3.4). For a constant-flux current, we compute an analytic solution by considering small shifts in the temporal origin, which we then extend to more

general influxes (§3.5). A further asymptotic analysis of large azimuthal wavenumber investigates the stability of a generic advancing front of a viscous gravity current within the framework of lubrication theory (Appendix 3.B). Additionally, we extend the model to a gravity current in a porous medium with power-law porosity and permeability in Appendix 3.A. Finally, in Appendix 3.C, we compare our results to those of Mathunjwa and Hogg (2006) regarding the stability of constant-volume gravity currents in porous media.

In Chapter 4, we consider an intrusion with negligible diffusion and surface tension into a Hele-Shaw cell. We derive nonlinear time-dependent analytic solutions for the cases of axisymmetric intrusions and equal viscosities (§4.3). By introducing a simplifying change of variables motivated by these analytic solutions, we derive the ordinary differential equations for non-axisymmetric linear perturbations to a self-similar axisymmetric base state (§4.4). We solve these equations numerically in order to find the normal-mode eigenspectrum (§4.5). An asymptotic analysis using the WKB method is used to examine the singular nature of large azimuthal wavenumber (§4.6). We confirm this asymptotic analysis by a separate method in Appendix 4.A using a local analysis as opposed to WKB expansion.

Finally, in Chapter 5, we turn to the main problem we set out to solve in this thesis: the linear stability analysis of equal-density two-layer viscous gravity currents spreading from a constant-flux point source over a rigid horizontal surface. We first derive the relevant equations of a linear normal-mode stability analysis, which are again based on scaling invariance and a change of independent variable, as in Chapter 3 (§5.2 with algebraic details in Appendix 5.A). We then solve the equations numerically (§5.3), and compare these both to the experimental data obtained by others and to the results for single-layer viscous gravity currents and Hele-Shaw flows. These two cases are derived as formal asymptotic limits in the case of small and large influxes, respectively (Appendix 5.B). Additionally, an analysis reveals two analytical solutions (Appendix 5.C), one by considering small shifts in the temporal origin as in Chapter 3, and a second for the case of fluids with equal viscosities.

In Appendix Z, we consider an illustrative toy model of a hyperbolic advection equation on $[0, 1]$ with zero velocity at the boundaries and the effect of diffusive regularisation on that. The equations are somewhat similar to Schrödinger's equation describing a particle trapped in a potential well, except that we consider advection instead of a simple potential forcing. We examine a top-hat advection velocity profile (§Z.2) followed by a triangular advection velocity profile (§Z.3), and we also include a linear diffusive term as regularisation. Both profiles allow for an analytic solution, in the

cases both with and without diffusion. Additionally, we consider asymptotic solutions for small diffusion, to better understand the relationship of a linear perturbation analysis of a fully hyperbolic equation to the zero-diffusivity limit. This analysis is to allow a better understanding of some of the features discovered in Chapter 5.

In the final chapter, we summarise our results and their implications, and discuss potential questions which future work might address.

Chapter 2

Shock-formation in two-layer equal-density viscous gravity currents

The content of this chapter forms part of the publication Dauck, T.-F., Box, F., Gell, L., Neufeld, J. A., and Lister, J. R. (2019). Shock formation in two-layer equal-density viscous gravity currents. *J. Fluid Mech.*, 863:730–756. The experimental work presented in this publication was done by Finn Box, Laura Gell and Jerome Neufeld, and the theoretical work was done by me.

2.1 Introduction

Viscous gravity currents result from density-driven flows in highly viscous materials, which have been the subject of many theoretical and experimental investigations. Various geometries have been considered, including simple single-layer flow over a rigid horizontal boundary (Gratton and Minotti, 1990; Huppert, 1982a; Smith, 1969), two-layer flows at a horizontal boundary or interface (Hoult, 1972; Koch and Koch, 1995; Kowal and Worster, 2015; Lister and Kerr, 1989), flows down slopes (Huppert, 1982b; Lister, 1992; Smith, 1973), non-Newtonian currents (Balmforth et al., 2007; Fink and Griffiths, 1998; Gratton and Minotti, 1999; Griffiths and Fink, 1993; Hogg and Matson, 2009; Nye, 1952; Sayag and Worster, 2013), currents with leakage (Acton et al., 2001; Neufeld et al., 2011; Pritchard and Hogg, 2002), flow underneath an elastic sheet (Hewitt et al., 2015; Lister et al., 2013) and flow towards a central hole (Diez et al., 1992; Zheng et al., 2014). These phenomena are of wide interest in many contexts, for

example, in industrial applications and geological systems (Huppert, 2006), such as lava flows (Griffiths, 2000) and ice-sheets (Schoof and Hewitt, 2013).

Theoretical analysis of the propagation of viscous gravity currents often makes use of lubrication theory, which is valid in the case of currents that are long and thin. Under these assumptions, many similarity solutions can be found, which describe the self-similar spreading of the fluids involved in many different geometries (see e.g. Gratton and Minotti, 1990). Beyond enabling prediction of the shapes and spreading rates of the currents, these base-state similarity solutions can also be used to perform linear stability analyses of possible symmetry breaking instabilities. Examples include the linear stability of a single-layer current over a horizontal surface in a porous medium (Mathunjwa and Hogg, 2006), the fingering instability that occurs when a fluid flows down a slope (Huppert, 1982a), the fingering instability of two nested viscous gravity currents (Kowal and Worster, 2019a,b), or the fingering instability of strain-rate-softening extensional flows of ice shelves (Sayag and Worster, 2019a,b).

Two-layer gravity currents with a free surface and with a nonzero density difference between the injected and ambient fluids were studied by Lister and Kerr (1989), motivated by application to the viscous spreading of the lithosphere along the mid-mantle boundary (Kerr and Lister, 1987). The authors identified different regimes for deep and shallow ambient layers compared to the radius of the spreading current. They considered the self-similar spreading of currents with volume of intruding fluid proportional to t^α, for both axisymmetric flows and two-dimensional flows. For spreading over a shallow ambient layer, they found critical values $\alpha = 1$ (constant influx) for axisymmetric spreading and $\alpha = 1/2$ for two-dimensional spreading; for smaller α the current thins and remains shallower than the ambient, while for larger α the current thickens and approaches the behaviour of a single-layer gravity current as in Huppert (1982b). The equations for the critical case, where the upper and lower layer thicknesses remain comparable (i.e. $\alpha = 1$ for axisymmetric and $\alpha = 1/2$ for two-dimensional spreading), were derived in an appendix and some numerical solutions were presented for the two-dimensional case. Lister and Kerr (1989) also conducted experiments in the deep and shallow regimes, measuring the extent of the current as a function of time and finding good agreement with the predicted scaling for the self-similar nose position. However, the actual profiles of the currents were not compared and, for the critical case of constant influx in the axisymmetric geometry, their model only applies at small influxes, where the spreading current is much thinner than the ambient layer.

In this chapter, we look at the critical case of an axisymmetric two-layer current with a fixed influx of one fluid into and over a pre-existing lubricating layer of a second fluid. In particular, we focus on the limit of equal densities, which we find is singular. The theoretical solutions are also compared with experimentally measured profiles.

Another type of a two-layer gravity current was studied by Kowal and Worster (2015) who analysed concurrent spreading of two injected fluids over a horizontal rigid surface with the upper, lighter fluid extending further due to being lubricated by the lower, less viscous fluid. While the authors also found shocks in the equal-density limit, the mechanism is quite different from that described in this chapter, and derives from their implementation of the rigid lower boundary condition. They assume total displacement of upper-layer fluid, which results in no-slip at the bottom of the lower-layer current and therefore accumulation of lower-layer fluid at the front driven by the upper-layer fluid flux.

The mathematical analysis of the limit of equal densities in our problem bears some resemblance to that for intrusion of a fluid into a Hele-Shaw cell filled with a fluid of equal density but different viscosity. A key distinction in the Hele-Shaw problem is the question of whether surface tension is significant or can be ignored. For miscible fluids or those with negligible surface tension, Wooding (1969) found and described a fingering instability comparable to the well-known Saffman–Taylor instability for flows with surface tension (Saffman, 1986; Saffman and Taylor, 1958). Further work by Paterson (1985) carried out a linear stability analysis for the limit of an inviscid intruding fluid with no surface tension in a Hele-Shaw cell, which predicted instability for all parameters and a most unstable wavelength that compared well to his experimental results. Yang and Yortsos (1997) extended this analysis to viscous intruding fluids, resolving the cross-sectional structure of the intruding flow using lubrication theory. They derived a kinematic evolution equation for the interfacial position, which we show bears some resemblance to the evolution equation of the interface in a two-layer gravity current. They found that, for sufficiently less viscous intrusions, vertical discontinuities, called shocks, are predicted by the kinematic equation to develop at the nose. The exact nature of these frontal shocks remains unclear as the shock height predicted by Yang and Yortsos (1997) disagreed with experimental measurements by Petitjeans and Maxworthy (1996) and with numerical simulations by Chen and Meiburg (1996) and Rakotomalala et al. (1996). Yang and Yortsos (1997) proposed that the shocks at the nose can plausibly be regularised by a local, fully two-dimensional Stokes flow around the nose, where lubrication theory breaks down, and that this would change the shock-fitting condition. To our knowledge, there has not been any work done confirming

this conjecture. More recently, other work has extended the basic ideas of Yang and Yortsos (1997). For example, Lajeunesse et al. (1997, 1999, 2001) analysed the flow in a vertical Hele-Shaw cell, including stabilising density differences in the analysis, and experimentally measured a critical viscosity ratio for the onset of a fingering instability. These authors also suggested a link between the instability and the formation of shocks by adapting the arguments of Saffman and Taylor (1958) to the vicinity of a shock. Bischofberger et al. (2014) found a different critical viscosity ratio for the onset of instability experimentally, but also suggested that the pressure drop associated with the steep interface is the key instability mechanism.

There are two significant differences between flows in a Hele-Shaw cell and the two-layer gravity currents analysed in this chapter. Firstly, the free top surface of a two-layer gravity current is evolving and hence the total thickness of the current varies in space and time. Secondly, the pressure gradients caused by nonzero but small density differences in a two-layer gravity current allow an explicit regularisation of any vertical shock discontinuities that may form.

The objective of this chapter is to develop the theory for the self-similar spreading of one fluid over a second fluid of differing viscosity but equal, or nearly equal, density. Surface tension and diffusion are assumed to be negligible.

The mathematical model for this spreading includes the evolution of the top surface, which adds complexity over the simpler model for a Hele-Shaw cell with fixed total height. However, we find that by including the regularising effect of small nonzero density differences, we obtain physically justified, so-called 'entropy' conditions for the evolution of any shock that develops. Therefore, modelling two-layer gravity currents provides a much better starting point for a linear stability analysis as the nature of the nose can be understood more easily with an exact condition for the frontal shock height in an axisymmetric similarity solution.

The set-up of the model and its assumptions are described in §2.2. The case of equal densities discussed in §2.3 is a singular limit of the model discussed in Lister and Kerr (1989) and it extends the Hele-Shaw model in Yang and Yortsos (1997) to include a free surface. The regularising mechanism given by small density differences is used to derive closed-form, consistent shock conditions. An illustrative calculation of a simplified time-dependent system in §2.4 is used to motivate the physically appropriate boundary conditions for a similarity solution. This leads to a closed system of ordinary differential equations, which is solved numerically in §2.5. These solutions are then compared to the results of laboratory experiments done by Box, Gell and Neufeld,

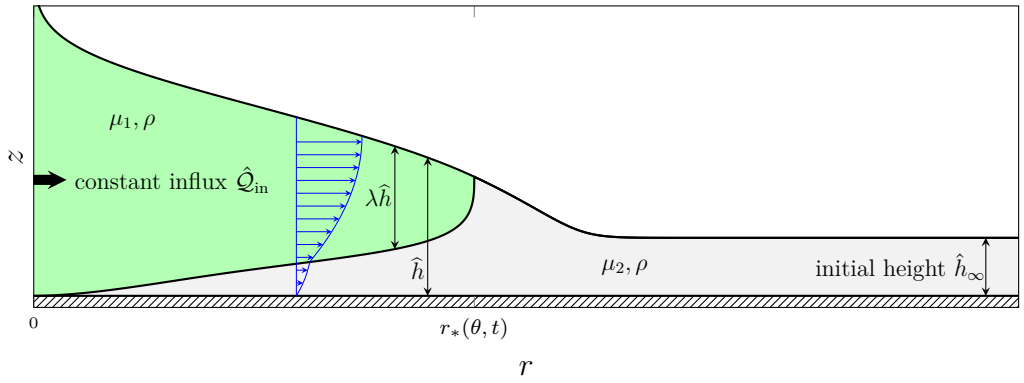

Fig. 2.1 A radial cross-section of an axisymmetric two-layer equal-density viscous gravity current with constant influx $\hat{\mathcal{Q}}_{\text{in}}$ of a fluid with viscosity μ_1 intruding over a layer of ambient fluid on top of a rigid horizontal surface with viscosity μ_2 and initial height $\hat{h}_\infty$. The dynamic variables defined are the total height of the current $\widehat{h}(r,t)$, the relative fluid fraction $\lambda(r,t)$ and the radial extent $r_*(t)$.

which measured the extent and the top-surface profiles of currents for various fluid properties and fluxes.

2.2 Model description

We consider a two-layer axisymmetric gravity current spreading over a rigid horizontal surface. The upper fluid is introduced at a constant volumetric rate $\hat{\mathcal{Q}}_{\text{in}}$ at the origin and spreads radially over a lower layer of fluid, which initially covers the entire horizontal plane with a constant thickness $\hat{h}_\infty$, as shown in figure 2.1. The fluids have viscosities μ_i and densities ρ_i, where $i = 1$ corresponds to the upper, intruding fluid and $i = 2$ to the lower, lubricating fluid. We define the horizontal extent of the current $r_*(t)$, the total height $\widehat{h}(r,t)$ and the upper-layer thickness $\widehat{d}(r,t)$. Surface tension and diffusion are assumed to be negligible. This can be expressed in terms of the Bond number $\text{Bo} = \rho g r_*^2/\gamma \gg 1$ and the Péclet number $\text{Pe} = U\hat{h}_\infty/\delta \gg 1$, respectively, where γ is surface tension, δ is the diffusion coefficient between the fluids and U is a characteristic velocity scale which can be estimated by the vertical outflow velocity $U = \hat{\mathcal{Q}}_{\text{in}}/A_{\text{in}}$ through a hole of area A_{in} at the origin.

After a short initial transient, the horizontal extent of the current is significantly greater than the vertical extent, $r_* \gg \widehat{h}$. In this limit, the vertical velocity is negligible and the pressure $\widehat{p}$ is therefore hydrostatic to leading order. Using these simplifying

assumptions and taking a constant pressure at the free surface we may write

$$\widehat{p} = \begin{cases} \rho_1 g \left(\widehat{h} - z\right), & \widehat{h} - \widehat{d} < z < \widehat{h}, \\ \rho_1 g \left(\widehat{h} - z\right) + (\rho_2 - \rho_1)\, g \left(\widehat{h} - \widehat{d} - z\right), & 0 < z < \widehat{h} - \widehat{d}, \end{cases} \tag{2.1}$$

where z is the height above the bottom surface and g the acceleration due to gravity.

The pressure gradient then drives a flow, whose horizontal velocity $\widehat{u}(r, z, t)$ is given by

$$\mu \frac{\partial^2 \widehat{u}}{\partial z^2} = \frac{\partial \widehat{p}}{\partial r}, \tag{2.2}$$

with boundary conditions

$$\widehat{u} = 0 \text{ at } z = 0, \qquad \frac{\partial \widehat{u}}{\partial z} = 0 \text{ at } z = \widehat{h}, \tag{2.3a,b}$$

$$[\widehat{u}]^+_- = 0 \text{ at } z = \widehat{h} - \widehat{d}, \qquad \left[\mu \frac{\partial \widehat{u}}{\partial z}\right]^+_- = 0 \text{ at } z = \widehat{h} - \widehat{d}. \tag{2.3c,d}$$

The boundary conditions impose no-slip at the bottom, no-stress at the top surface, and velocity and stress continuity at the interface between the fluids, respectively. Solving (2.2) with the boundary conditions (2.3) and driving pressure (2.1), we obtain the velocity profile

$$\widehat{u} = \begin{cases} \widehat{u}_1, & \widehat{h} - \widehat{d} < z < \widehat{h}, \\ \widehat{u}_2, & 0 < z < \widehat{h} - \widehat{d}, \end{cases} \tag{2.4}$$

with

$$\widehat{u}_1 = \frac{\rho_1 g}{2\mu_2} \left[\frac{\partial \widehat{h}}{\partial r} m z \left(z - 2\widehat{h}\right) + \frac{\partial \widehat{h}}{\partial r} (m-1) \left(\widehat{h}^2 - \widehat{d}^2\right) - \varepsilon \left(\frac{\partial \widehat{h}}{\partial r} - \frac{\partial \widehat{d}}{\partial r}\right) \left(\widehat{h} - \widehat{d}\right)^2 \right], \tag{2.5a}$$

$$\widehat{u}_2 = \frac{\rho_1 g}{2\mu_2} \left[\frac{\partial \widehat{h}}{\partial r} z \left(z - 2\widehat{h}\right) + \varepsilon \left(\frac{\partial \widehat{h}}{\partial r} - \frac{\partial \widehat{d}}{\partial r}\right) z \left(z - 2\widehat{h} + 2\widehat{d}\right) \right], \tag{2.5b}$$

where the flow is characterised in terms of two dimensionless parameters, the viscosity ratio $m = \mu_2/\mu_1$ and the relative density difference $\varepsilon = \rho_2/\rho_1 - 1$.

The various terms on the right-hand side of (2.5) can be interpreted as follows. The term proportional to the density difference ε results from the extra pressure gradient in the lower layer due to its greater density and to the slope of the interface between

the two fluids at $z = \widehat{h} - \widehat{d}$. The term proportional to the viscosity difference $m - 1$ results from the different velocity in the upper layer due to the different mobility $1/\mu_1$ of the upper layer. The remaining terms correspond to those for a one-layer gravity current of depth $\widehat{h}$.

Integrating the velocity (2.4) over the depth of the whole current and over the depth of the upper layer gives two local mass-conservation equations for $r < r_*$:

$$\frac{\partial \widehat{h}}{\partial t} = \frac{\rho_1 g}{3\mu_2}\frac{1}{r}\frac{\partial}{\partial r}\left[r\left\{\left(\widehat{h}^3 + (m-1)\widehat{d}^3\right)\frac{\partial \widehat{h}}{\partial r} + \tfrac{1}{6}\varepsilon\left(2\widehat{h} + \widehat{d}\right)\frac{\partial}{\partial r}\left(\widehat{h} - \widehat{d}\right)^3\right\}\right], \tag{2.6a}$$

$$\frac{\partial \widehat{d}}{\partial t} = \frac{\rho_1 g}{3\mu_2}\frac{1}{r}\frac{\partial}{\partial r}\left[r\left\{\tfrac{1}{2}\left(3\widehat{h}^2\widehat{d} + (2m-3)\widehat{d}^3\right)\frac{\partial \widehat{h}}{\partial r} + \tfrac{1}{2}\varepsilon\widehat{d}\frac{\partial}{\partial r}\left(\widehat{h} - \widehat{d}\right)^3\right\}\right]. \tag{2.6b}$$

Ahead of the nose of the current for $r > r_*$, there is only the lubricating fluid and we recover the classical single-layer gravity current equation

$$\frac{\partial \widehat{h}}{\partial t} = \frac{\rho_1 g}{3\mu_2}\frac{1+\varepsilon}{r}\frac{\partial}{\partial r}\left[r\left(\widehat{h}^3\frac{\partial \widehat{h}}{\partial r}\right)\right]. \tag{2.6c}$$

We impose a fixed initial height in the far-field, $\widehat{h} \to \widehat{h}_\infty$ as $r \to \infty$, and global mass-conservation for the upper and lower fluids, which can be written as

$$\widehat{\mathcal{Q}}_{\text{in}} t = 2\pi\int_0^{r_*} \widehat{d}(r,t)\, r\,\mathrm{d}r = 2\pi\int_0^{\infty}\left\{\widehat{h}(r,t) - \widehat{h}_\infty\right\} r\,\mathrm{d}r. \tag{2.7}$$

If $\varepsilon > 0$ it is appropriate to impose that the thickness of the upper-layer fluid satisfies $\widehat{d} = 0$ at the nose $r = r_*$; if $\varepsilon = 0$ it will turn out that we need to amend this condition to $\widehat{d} = \lambda_* \widehat{h}$, where λ_* is given by the shock conditions described by (2.33), in order to allow for the possibility of a frontal shock. Independently of the condition on $\widehat{d}$, there is zero upper-fluid flux through the nose in a co-moving frame, which gives the speed of the nose as

$$\frac{\mathrm{d}r_*}{\mathrm{d}t} = \frac{\rho_1 g}{6\mu_2}\left\{\left(3\widehat{h}^2 + (2m-3)\widehat{d}^2\right)\frac{\partial \widehat{h}}{\partial r} + \varepsilon\frac{\partial}{\partial r}\left(\widehat{h} - \widehat{d}\right)^3\right\}. \tag{2.8}$$

Together with continuity of total height and total flux at the nose given by

$$0 = \left[\widehat{h}\right]_-^+ \qquad \text{at} \qquad r = r_*, \tag{2.9a}$$

$$0 = \left[\left(\widehat{h}^3 + (m-1)\widehat{d}^3\right)\frac{\partial \widehat{h}}{\partial r} + \tfrac{1}{6}\varepsilon\left(2\widehat{h} + \widehat{d}\right)\frac{\partial}{\partial r}\left(\widehat{h} - \widehat{d}\right)^3\right]_-^+ \qquad \text{at} \qquad r = r_*, \tag{2.9b}$$

respectively, this gives a complete system of equations describing the two-layer viscous gravity current. A complete list of these boundary conditions in non-dimensional form is given below in (2.13).

2.2.1 Self-similar spreading

For an axisymmetric two-layer current, a constant influx rate corresponds to the critical case $\alpha = 1$ of Lister and Kerr (1989), for which there is a similarity solution in which the characteristic thickness of the spreading upper layer is constant (rather than growing or decaying in time). For such a solution it is natural to define a dimensionless total height by $H = \widehat{h}/\hat{h}_\infty$ and a dimensionless upper-layer thickness by $D = \widehat{d}/\hat{h}_\infty$. A scaling analysis of (2.6a), governing the evolution of the total height, suggests that the solution may be written as a function of the similarity variable

$$\xi = rt^{-1/2}\left(\frac{3\mu_2}{\rho_1 g\hat{h}_\infty^3}\right)^{1/2}. \tag{2.10}$$

We write $\xi_* = \xi(r_*, t)$ for the non-dimensional radial extent of the current. In order to describe the evolution towards self-similarity, we define a rescaled temporal variable $\tau = \log(t/\widehat{t})$, where $\widehat{t}$ is an arbitrary reference time scale. The local mass-conservation equations (2.6) then lead to a nonlinear dimensionless system of partial differential equations which consists of a fourth-order system up to the nose coupled to a second-order system beyond the nose, which is given by

$$\frac{\partial H}{\partial \tau} - \tfrac{1}{2}\xi\frac{\partial H}{\partial \xi} + \frac{1}{\xi}\frac{\partial(\xi q_H)}{\partial \xi} = 0, \qquad \frac{\partial D}{\partial \tau} - \tfrac{1}{2}\xi\frac{\partial D}{\partial \xi} + \frac{1}{\xi}\frac{\partial \xi q_D}{\partial \xi} = 0, \tag{2.11}$$

where $q_H(\xi,\tau)$ and $q_D(\xi,\tau)$ are the depth-integrated total fluid flux and upper-fluid flux respectively. For $\xi < \xi_*$ these are defined by

$$q_H = -\left[\left\{H^3 + (m-1)D^3\right\}\frac{\partial H}{\partial \xi} + \tfrac{1}{6}\varepsilon(2H+D)\frac{\partial}{\partial \xi}(H-D)^3\right], \tag{2.12a}$$

$$q_D = -\tfrac{1}{2}\left[\left\{3H^2 + (2m-3)D^2\right\}D\frac{\partial H}{\partial \xi} + \varepsilon D\frac{\partial}{\partial \xi}(H-D)^3\right], \tag{2.12b}$$

and for $\xi > \xi_*$ by

$$q_H = -(1+\varepsilon)H^3\frac{\partial H}{\partial \xi}. \tag{2.12c}$$

The boundary conditions on (2.11) and (2.12) for $\varepsilon > 0$ can be expressed in the dimensionless variables as

$$\text{prescribed influx of upper fluid:} \quad \xi q_D \to \mathcal{Q}_{\text{in}} \quad \text{as} \quad \xi \to 0, \tag{2.13a}$$

$$\text{zero influx of lower fluid:} \quad q_H - q_D \to 0 \quad \text{as} \quad \xi \to 0, \tag{2.13b}$$

$$\text{fixed initial height at infinity:} \quad H \to 1 \quad \text{as} \quad \xi \to \infty, \tag{2.13c}$$

$$\text{vanishing upper height at nose:} \quad D = 0 \quad \text{at} \quad \xi = \xi_*, \tag{2.13d}$$

$$\text{mass conservation through nose:} \quad \frac{\partial \xi_*}{\partial \tau} = \frac{q_D}{D} - \tfrac{1}{2}\xi \quad \text{at} \quad \xi = \xi_*, \tag{2.13e}$$

$$\text{continuity of total height:} \quad [H]^+_- = 0 \quad \text{at} \quad \xi = \xi_*, \tag{2.13f}$$

$$\text{continuity of total flux:} \quad [q_H]^+_- = 0 \quad \text{at} \quad \xi = \xi_*, \tag{2.13g}$$

where $\partial \xi_*/\partial \tau$ is the dimensionless speed of the nose in similarity space and

$$\mathcal{Q}_{\text{in}} = \frac{3\mu_2 \hat{\mathcal{Q}}_{\text{in}}}{2\pi \rho_1 g \hat{h}_\infty^4} \tag{2.14}$$

is the dimensionless volumetric influx.

The dimensionless influx $\mathcal{Q}_{\text{in}}$ can be related to the ratio of the height scale for a single-layer current $\hat{h}_{\text{sl}} = [\mu_1 \hat{\mathcal{Q}}_{\text{in}}/(\rho_1 g)]^{1/4}$ (Huppert, 1982b) and the far-field height $\hat{h}_\infty$ by noting that $\mathcal{Q}_{\text{in}} \propto m \left(\hat{h}_{\text{sl}}/\hat{h}_\infty\right)^4$.

At late times the evolution of the system becomes self-similar and independent of τ. In this limit (2.11) and (2.12) reduce to coupled ordinary differential equations, where the boundary conditions are the same as (2.13) only with a zero nose speed, $\partial \xi_*/\partial \tau = 0$.

2.3 The equal-density limit

For a nonzero density difference, $\varepsilon > 0$, a system of equations analogous to (2.11)–(2.13) has been studied and solved for the case of a two-dimensional, two-layer current with influx proportional to $t^{1/2}$ (see Appendix B of Lister and Kerr, 1989). However, the limit of vanishing density difference, $\varepsilon = 0$, is singular, which introduces several novelties that we discuss in this section.

Due to the equal densities of the two fluids, the slope $\partial(H - D)/\partial \xi$ of the interface between the fluids no longer contributes to the pressure gradient in the lower-layer fluid. Hence, the fluxes q_H and q_D become independent of $\partial(H - D)/\partial \xi$, which reduces (2.11) and (2.12) to a fifth-order system of nonlinear partial differential equations

(third-order before the nose coupled to second-order beyond the nose). This reduction in order causes (2.11b) and (2.12b), which govern the upper-layer thickness D, to change character from a parabolic equation to a hyperbolic equation.

To aid further analysis, we can derive an equation for the relative fraction $\lambda = D/H$ of upper to total fluid by considering (2.11b) $-\lambda$(2.11a) and using (2.12). After some algebra, we obtain

$$\frac{\partial \lambda}{\partial \tau} + \underbrace{\left(\frac{q_H}{H}\mathcal{F}' - \tfrac{1}{2}\xi\right)}_{U_c}\frac{\partial \lambda}{\partial \xi} + \underbrace{\frac{\mathcal{G}}{\xi H}\frac{\partial(\xi q_H)}{\partial \xi}}_{-W_c} = \frac{\varepsilon}{\xi H}\frac{\partial}{\partial \xi}\left(\xi H^4 \mathcal{D}\frac{\partial \lambda}{\partial \xi}\right), \tag{2.15}$$

where

$$\mathcal{F}(\lambda) = \frac{3\lambda + (2m-3)\lambda^3 + 3\varepsilon\lambda(1-\lambda)^3}{2 + 2(m-1)\lambda^3 + \varepsilon(2+\lambda)(1-\lambda)^3}, \tag{2.16a}$$

$$\mathcal{G}(\lambda) = \mathcal{F} - \lambda, \tag{2.16b}$$

$$\mathcal{D}(\lambda) = \frac{\lambda^2(1-\lambda)^3(3 + (4m-3)\lambda)}{4 + 4(m-1)\lambda^3 + 2\varepsilon(2+\lambda)(1-\lambda)^3}, \tag{2.16c}$$

will be referred to as the flux function, source function and diffusivity function, respectively, and the quantities shown as U_c and W_c are, we show later, the characteristic velocities in the hyperbolic limit $\varepsilon = 0$. (We have excluded the $-\xi/2$ term from the definition of the flux function for convenience, as this term only corresponds to the time-dependence of the similarity variable and does not play any role in the physical shock conditions.)

We observe that if we regard H and q_H as given, then (2.15) is a nonlinear advection–diffusion equation for λ. As $\varepsilon \to 0$ the diffusive term on the right-hand side vanishes and (2.15) becomes a purely hyperbolic advection equation. In the diffusive case, $\varepsilon > 0$, the solutions of (2.15) are smooth, but in the hyperbolic limit, $\varepsilon = 0$, smooth solutions are no longer guaranteed and discontinuities may form, which we will refer to as shocks. Where these shocks form, (2.15) is no longer valid locally with $\varepsilon = 0$ and we need additional conditions governing the evolution of the shock to ensure a well-defined solution.

For small but nonzero density differences $0 < \varepsilon \ll 1$ we may neglect the diffusive term, except where the interface becomes sufficiently steep that $\varepsilon\partial\lambda/\partial\xi = O(1)$. In particular, close to any shock formation in the hyperbolic system, the diffusive term becomes significant and acts as a local regularisation, as we discuss in more detail in §2.3.3. Motivated by this diffusive regularisation, we define an admissible solution for

$\varepsilon = 0$, as the unique solution to the hyperbolic equation that is the limit as $\varepsilon \to 0$ of the smooth solutions $\lambda^{\varepsilon}(\xi, \tau)$ to the diffusive system. The goal of this section is to derive shock conditions that determine which solutions are admissible and which are not.

The terms in (2.15) associated with the flux function $\mathcal{F}$ and source function $\mathcal{G}$ can be identified as horizontal and vertical characteristic velocities U_c and W_c of the hyperbolic system, respectively. It is the variation of the horizontal characteristic velocity U_c which is crucial in determining the existence of shocks. However, near any incipient shock the behaviour of U_c is locally determined by the behaviour of $\mathcal{F}'$, since the total height H and total flux q_H locally act only as a constant rescaling. Hence, we now analyse the properties of $\mathcal{F}$ to discuss in which cases shocks form.

2.3.1 The flux function $\mathcal{F}$

As we are interested in shock formation, we consider $\mathcal{F}$ in the hyperbolic limit $\varepsilon = 0$. For $\varepsilon = 0$ the flux function $\mathcal{F}$ is equal to the ratio of upper-layer fluid flux to total fluid flux and simplifies to

$$\mathcal{F} = \frac{3\lambda + (2m-3)\lambda^3}{2 + 2(m-1)\lambda^3} = \frac{q_D}{q_H}. \tag{2.17}$$

For the case $m \leq 3/2$ we find that the flux function is concave over the entire range $0 \leq \lambda \leq 1$ and hence $\mathcal{F}'$ decreases monotonically as λ increases, see figure 2.2. This implies that the thicker the upper layer as a proportion of the current, the slower its local horizontal characteristic velocity U_c and vice versa. Therefore, a current with upper-layer thickness decreasing towards the nose is self-spreading and no shocks form in this case.

However, for $m > 3/2$ there is a convex region near $\lambda = 0$ where $\mathcal{F}'$ increases with λ. This implies that a part of the current with a thicker upper layer will now have a faster horizontal characteristic velocity than a part of the current with a thinner upper layer nearer the front of the current. Therefore, in some region of the current, the horizontal characteristic velocity will decrease towards the nose, which leads to a convergence of characteristics and hence a steepening of the interface. Ultimately, this steepening mechanism leads to the formation of shocks.

To understand the physical origin of the convexity of the flux function $\mathcal{F}$ for $m > 3/2$, we consider the variation of $\mathcal{F}$ as $\lambda \to 1$ (near the origin) and as $\lambda \to 0$ (near the front of the current). First, near the origin as $\lambda \to 1$ in (2.17) we obtain the

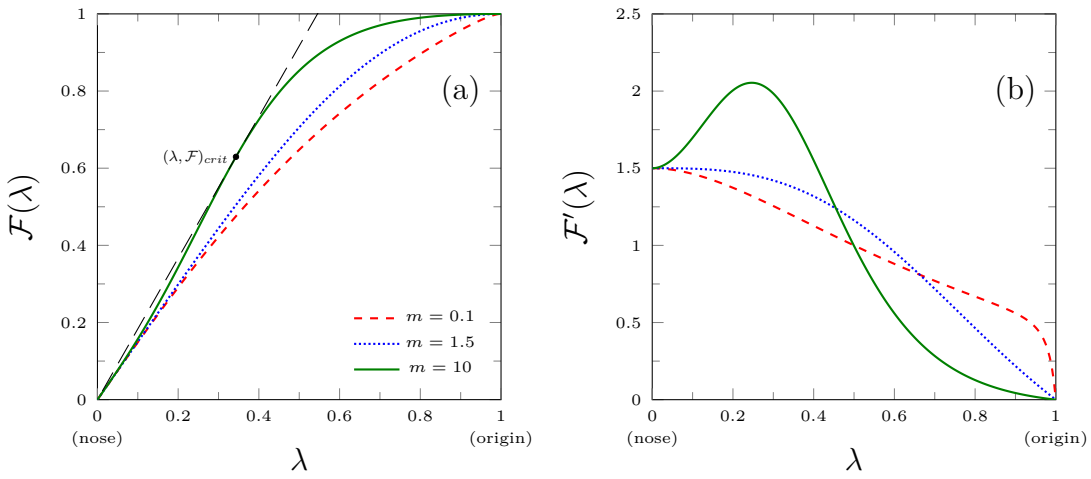

Fig. 2.2 (a) The flux function $\mathcal{F}(\lambda)$ for viscosity ratios $m = 0.1$, $m = 1.5$ and $m = 10$ (dashed, dotted and solid respectively); the long-dashed straight line is tangent to $\mathcal{F}$ for $m = 10$, and the point of tangency defines the critical value λ_{crit}. (b) The derivative $\mathcal{F}'$ of the flux function for the same viscosity ratios m.

expansion

$$\mathcal{F} \sim 1 - \frac{3}{2m}(1-\lambda)^2 + O(1-\lambda)^3. \tag{2.18}$$

The leading-order term, $\mathcal{F} \sim 1$, corresponds to the entire current consisting of upper-layer fluid and hence the total fluid flux q_H being equal to the upper-fluid flux q_D. The next-order correction is quadratic in $(1-\lambda)$ due to the no-slip condition at the rigid bottom boundary, and comes from integrating the leading-order linear velocity profile in the thin film of lower-layer fluid to obtain a quadratic expression for the lower-layer flux. This correction decreases as $m = \mu_2/\mu_1$ increases, since a more viscous lower-layer fluid reduces the velocity in the lower-layer fluid. The sign of the correction is such that the flux function is always concave near $\lambda = 1$.

In contrast, near the nose, expanding $\mathcal{F}$ as $\lambda \to 0$ gives

$$\mathcal{F} \sim \tfrac{3}{2}\lambda + \left(m - \tfrac{3}{2}\right)\lambda^3 + O\left(\lambda^4\right). \tag{2.19}$$

This expansion shows that if the upper layer is only a thin film, then, to leading order, it moves at a constant velocity of $3/2$, corresponding to the maximum velocity of the underlying parabolic velocity profile. The next-order correction to this is cubic due to the stress-free boundary condition on the velocity at the top surface. The sign of this correction reflects the occurrence of convexity in the flux function for $m > 3/2$. There

are two physical processes competing here: firstly, a larger λ corresponds to a thinner lower layer and hence a greater influence of the no-slip rigid bottom boundary, which results in a decrease in the average upper-layer velocity; but, secondly, if $m > 1$, the lower-viscosity upper-layer fluid can support a greater shear, which increases its flux in comparison to the lower-layer flux. These effects balance at $m = 3/2$.

In conclusion, we find that for $m \leq 3/2$, no shocks can form, whereas for $m > 3/2$, i.e. a sufficiently lower viscosity upper-layer fluid, there is a steepening mechanism that leads to the formation of shocks.

The critical viscosity ratio $m = 3/2$ can be compared to the known result for the onset of shock formation in miscible two-fluid flows in a Hele-Shaw cell as mentioned in Yang and Yortsos (1997) and Lajeunesse et al. (1997). When considering the Hele-Shaw flow, the same flux function $\mathcal{F}$ is found. This is due to the fact that the profile of the free-surface flow considered here can be thought of as half the profile of the flow between two rigid parallel plates, which has zero stress at the mid-plane between the two plates due to its symmetry. However, in contrast to the situation in a Hele-Shaw cell, the two-layer gravity current we are considering admits a simple diffusive regularisation via small nonzero density differences. This regularisation allows an analytical derivation of shock conditions, which is not available in the Hele-Shaw flow, for which the regularisation proposed by Yang and Yortsos (1997) relies on solutions to the full Stokes equations around the nose of the intruding finger. As we shall see, the diffusive regularisation has a significant effect on the location of the shock.

2.3.2 Shock conditions

We have established a steepening mechanism through which shocks can form for $m > 3/2$. It remains to discuss how these shocks evolve. The general theory of shocks in hyperbolic differential equations, see for example LeFloch (2002), characterises shocks according to the behaviour of the associated flux functions and derives conditions on the formation and evolution of these shocks from entropy considerations at the shock and the corresponding regularisations.

Applying this general theory to the equal-density limit of a two-layer viscous gravity current, we find two constraints for any shock: a condition giving the shock speed and a separate entropy condition governing which shocks are allowed according to the directions of the characteristics. Suppose, for example, we have a shock at position ξ_s extending from λ_r to λ_l, where λ_r is the limit of λ as $\xi \to \xi_s$ from the right and λ_l the same limit but from the left.

The first shock condition, often referred to as a Rankine–Hugoniot condition, is given by mass conservation across the shock. Equating the fluxes across the shock in the frame of the shock, gives the speed of the shock as

$$U_s\Big|_{\lambda_r,\lambda_l} = \frac{q_H}{H}\frac{\mathcal{F}_r - \mathcal{F}_l}{\lambda_r - \lambda_l} - \tfrac{1}{2}\xi, \tag{2.20}$$

where $\mathcal{F}_r = \mathcal{F}(\lambda_r)$ and $\mathcal{F}_l = \mathcal{F}(\lambda_l)$.

The second condition is an entropy condition which, in simple hyperbolic systems, is the Lax entropy condition

$$U_c\Big|_{\lambda_r} \leq U_s \leq U_c\Big|_{\lambda_l}. \tag{2.21}$$

Using (2.20) this can be simplified to

$$\mathcal{F}_r' \leq \frac{\mathcal{F}_r - \mathcal{F}_l}{\lambda_r - \lambda_l} \leq \mathcal{F}_l'. \tag{2.22}$$

This condition states that characteristics at the edge of the shock cannot move away from the shock. For a decreasing jump discontinuity, i.e. $\lambda_r < \lambda_l$, it implies that a strictly convex flux function leads to a shock, whilst a strictly concave flux function leads to a rarefaction wave, and vice versa for an increasing jump discontinuity $\lambda_r > \lambda_l$.

However, if the flux function has both regions of convexity and concavity then the Lax entropy condition no longer ensures a unique solution, as it only regards properties at the edge of the shock. A shock may split into multiple shocks connected by rarefaction waves depending on the local convexity or concavity of the flux function. Therefore, we instead consider the more general Oleinik entropy condition, which not only restricts the speed of the characteristics at the edge of the shock, but also ensures that the shock is internally consistent. Internal consistency here means that, if we were to consider the shock splitting into multiple smaller shocks, these would remain together, not allowing the formation of rarefaction waves in between them and hence remaining as a single shock. The Oleinik entropy condition can be written as

$$U_s\Big|_{\lambda_r,\lambda_i} \leq U_s\Big|_{\lambda_r,\lambda_l} \leq U_s\Big|_{\lambda_i,\lambda_l}, \qquad \text{for all } \lambda_i \text{ with } \lambda_r \leq \lambda_i \leq \lambda_l, \tag{2.23}$$

which again can be simplified to

$$\frac{\mathcal{F}_r - \mathcal{F}_i}{\lambda_r - \lambda_i} \leq \frac{\mathcal{F}_r - \mathcal{F}_l}{\lambda_r - \lambda_l} \leq \frac{\mathcal{F}_i - \mathcal{F}_l}{\lambda_i - \lambda_l}, \qquad \text{for all } \lambda_i \text{ with } \lambda_r \leq \lambda_i \leq \lambda_l. \tag{2.24}$$

Note that the Oleinik entropy condition (2.23) implies the Lax entropy condition (2.21) by taking the limits $\lambda_i \to \lambda_r$ and $\lambda_i \to \lambda_l$.

To understand the implication of the Oleinik entropy condition for the heights λ in which shocks can occur, we can think of a shock as a chord from $(\lambda_r, \mathcal{F}_r)$ to $(\lambda_l, \mathcal{F}_l)$ on the flux function curve, see figure 2.3a. This representation as a chord is warranted by the fact that the shock speed U_s is related to the slope of these chords in the same way that the speed of characteristics U_c is related to the tangent slope $\mathcal{F}'$ of the flux function. The Oleinik entropy condition implies that chords with $\lambda_r < \lambda_l$ must lie entirely above the flux function, whilst chords with $\lambda_r > \lambda_l$ must lie entirely below it.

We observe that the upper-layer fluid velocity (2.5a) increases monotonically from the bottom to the top of the upper layer at every position ξ and hence so must the distance travelled by the upper-layer fluid. This implies that the interface is monotonically sloped upwards and it follows that we must have $\lambda_r < \lambda_l$. (Note that this condition is for a current propagating to the right away from the source; it would need adaptation for a current propagating to the left.)

Hence, as we must have $\lambda_r < \lambda_l$, any chord corresponding to a shock must lie above the flux function and therefore the largest admissible shock is given by the chord that goes through the origin and is tangent to the flux function $\mathcal{F}$. This tangent construction defines a critical height $\lambda_{\text{crit}} > 0$ by

$$\mathcal{F}'(\lambda_{\text{crit}}) = \frac{\mathcal{F}(\lambda_{\text{crit}})}{\lambda_{\text{crit}}}, \tag{2.25}$$

which can be solved analytically to obtain

$$\lambda_{\text{crit}} = 2\left(\tfrac{2}{3}m - 1\right)^{-1/2} \sinh\left[\tfrac{1}{3}\sinh^{-1}\left\{(m-1)^{-1}\left(\tfrac{2}{3}m - 1\right)^{3/2}\right\}\right]. \tag{2.26}$$

Hence any admissible shock must satisfy $0 \leq \lambda_r < \lambda_l \leq \lambda_{\text{crit}}$.

Figure 2.3a shows three example chords on the flux function which all satisfy the Oleinik entropy condition (2.24), but only two of which correspond to admissible shocks with $\lambda_r < \lambda_l$. The two admissible shocks shown can be associated with distinct types: the chord **QR**, which has $0 < \lambda_r < \lambda_l < \lambda_{\text{crit}}$, corresponds to an internal shock; the chord **OP**, with $0 = \lambda_r < \lambda_l < \lambda_{\text{crit}}$, corresponds to a frontal shock at the top surface. The third chord **ST** does not correspond to an admissible shock, since to satisfy the Oleinik entropy condition (2.24) we must have $\lambda_r > \lambda_l$ for this chord, contradicting the requirement that the interface is monotonically sloped upwards.

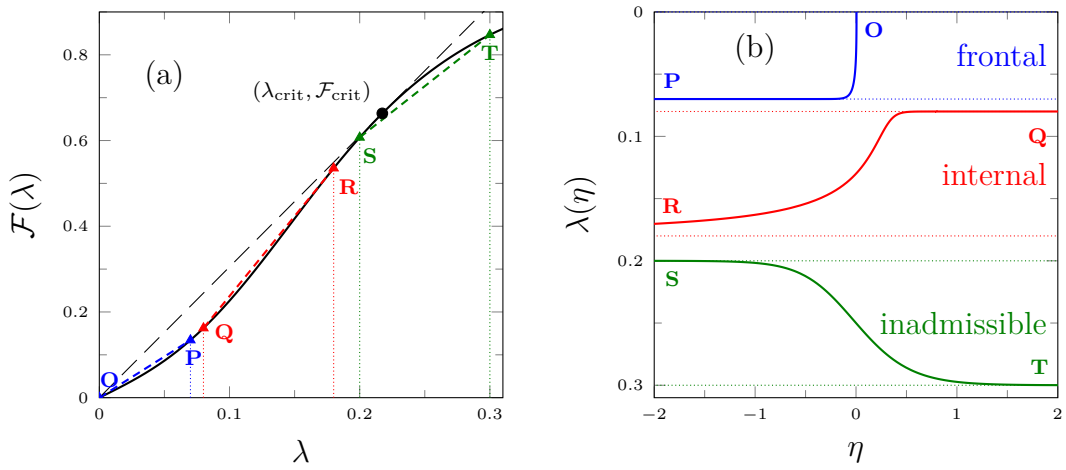

Fig. 2.3 (a) The flux function $\mathcal{F}$ for $m = 100$ with dashed chords representing hypothetical shocks: **OP** corresponds to a frontal shock with heights $(\lambda_r, \lambda_l) = (0, 0.08)$, **QR** to an internal shock with $(\lambda_r, \lambda_l) = (0.08, 0.18)$ and **ST** to a shock violating $\lambda_r < \lambda_l$ with $(\lambda_r, \lambda_l) = (0.3, 0.2)$. Again, the long-dashed straight line is tangent to $\mathcal{F}$, and defines $\lambda_{\rm crit}$. (b) The corresponding local travelling-wave solutions $\lambda(\eta)$ and their limits λ_r and λ_l. Note that we show λ increasing downwards to aid interpretation of the curves as the physical shapes of the interface relative to a top surface at $\lambda = 0$.

2.3.3 Regularised shock structures

To derive the Oleinik entropy condition from physical principles and to understand the local regularised structures of any shock that might occur, we recall that small density differences become significant near regions with a large slope of the interface, i.e. in particular near any shock. These regions can be analysed by defining a local coordinate η in a frame travelling with the shock by

$$\xi = \xi_s + \eta \left(\frac{\varepsilon H^4}{q_H} \right) \Bigg|_{\xi=\xi_s}, \tag{2.27}$$

where the factor $\varepsilon H^4/q_H|_{\xi=\xi_s}$ is the radial scale of the local travelling wave. We express (2.15) governing the relative fluid fraction λ in terms of this local coordinate, and expand in orders of ε. Noting that $\partial \xi_s/\partial \tau = U_s$, we obtain at leading order the equation

$$-U_s \frac{\mathrm{d}\lambda}{\mathrm{d}\eta} + U_c \frac{\mathrm{d}\lambda}{\mathrm{d}\eta} = \frac{q_H}{H}\Big|_{\xi=\xi_s} \frac{\mathrm{d}}{\mathrm{d}\eta} \left(\mathcal{D} \frac{\mathrm{d}\lambda}{\mathrm{d}\eta} \right). \tag{2.28}$$

The boundary conditions for this ordinary differential equation are $\lambda \to \lambda_{r,l}$ as $\eta \to \pm\infty$ respectively.

We note that the vertical characteristic velocity W_c does not influence the local dynamics near vertical shocks to leading order. This can be explained by noting that W_c arises from the divergence in the total flux q_H and is independent of the interfacial slope $\partial\lambda/\partial\xi$. Hence it remains $O(1)$ even close to a near-vertical interface.

We can simplify (2.28) and integrate once to obtain

$$\mathcal{D}\frac{\mathrm{d}\lambda}{\mathrm{d}\eta} = -\frac{\mathcal{F}_r - \mathcal{F}_l}{\lambda_r - \lambda_l}(\lambda - \lambda_r) + [\mathcal{F}(\lambda) - \mathcal{F}_r]\,. \tag{2.29}$$

This equation has fixed points where the right-hand side is zero. Hence, in particular, $\lambda = \lambda_r$ and $\lambda = \lambda_l$ are both fixed points. To ensure that a heteroclinic connection exists between these fixed points, there must not be any other fixed point λ_i with $\lambda_r < \lambda_i < \lambda_l$. This is equivalent to the Oleinik entropy condition (2.24), which means that the only admissible solutions under the diffusive regularisation $\varepsilon > 0$, are exactly those with shocks satisfying the Oleinik entropy condition.

Figure 2.3b shows the solutions to (2.29) corresponding to the shocks depicted as chords **OP**, **QR** and **ST** in figure 2.3a. Without loss of generality, the origin $\eta = 0$ was chosen to be at the average of λ_r and λ_l. In particular, the local travelling-wave solution to **ST** highlights the result that for this case $\lambda_r > \lambda_l$ and hence the interface slopes downwards rather than upwards.

We note at this point that the regularised shock structures corresponding to a frontal shock with $\lambda_r = 0$, for example the chord **OP**, have a square-root singularity at the front. This is consistent with the square-root frontal singularity obtained by Lister and Kerr (1989) for two-layer gravity currents with nonzero density differences and is the result corresponding to the cube-root frontal singularity for a single layer gravity current on a rigid surface as seen in Huppert (1982b).

2.4 Time-dependent fixed-lid solutions

2.4.1 A simplified model

To illustrate the evolution towards self-similarity and, in particular, the process of shock formation, we consider a simplified system, where we prescribe both the total height $H(\xi)$ and the total flux $q_H(\xi)$. This corresponds to a fixed evolution of the top surface. To ensure that the total fluid volume is still conserved, we choose H and q_H

such that they still satisfy

$$\tfrac{1}{2}\xi^2\frac{\partial H}{\partial \xi} = \frac{\partial(\xi q_H)}{\partial \xi}. \tag{2.30}$$

Prescribing H and q_H decouples (2.15) and has the further physical consequence that the pressure is no longer hydrostatic and given by H. Instead the pressure is given by the profile necessary to drive a mass-conserving flow in accordance with the prescribed evolution of H and q_H. This means we are effectively solving (2.15) with $\varepsilon = 0$ and under the simplifying assumption that both H and q_H are known, which we argue captures the essential behaviour of the advective evolution of the interface.

Suppose H and q_H are chosen to match the similarity solutions to the full coupled system, assuming that we have calculated these before. Then the interfacial position $\lambda(\xi,\tau)$ evolves under (2.15) from any initial condition to approach the similarity solution of the coupled system as $\tau \to \infty$. Furthermore, the pressure gradient approaches the hydrostatic pressure gradient in the same limit.

The time-dependent solution for λ can be found numerically via the method of characteristics for which we introduce characteristic curves $(\xi_c(\tau;\alpha), \lambda_c(\tau;\alpha))$, where α is a Lagrangian label for the characteristics. Any of these characteristic curves evolve from some initial condition according to

$$\frac{\mathrm{d}\xi_c}{\mathrm{d}\tau} = U_c\left(\xi_c, \lambda_c\right), \qquad \frac{\mathrm{d}\lambda_c}{\mathrm{d}\tau} = W_c\left(\xi_c, \lambda_c\right), \tag{2.31}$$

where U_c and W_c as functions of ξ and λ are given by (2.15) and (2.16).

As soon as shocks are encountered, as indicated by the intersection of characteristics, the evolution of the shock has to be treated separately to (2.15) taking into consideration the shock conditions (2.20) and (2.24), which determine the shock speed U_s and limit the maximal shock height by λ_{crit}.

2.4.2 An illustrative example calculation

A time-series of interfacial shapes $\lambda(\xi,\tau)$ for the viscosity ratio $m = 5$ is shown in figure 2.4. For illustration, the initial condition was chosen as $\lambda(\xi,0) = (1-3\xi/2)^2$. The interfacial shape clearly evolves towards a final steady state, which is the anticipated similarity solution. The corresponding characteristics are shown in figure 2.5, focussing on the region that forms a shock. In both figures, several points of interest have been marked, whose significance is explained below.

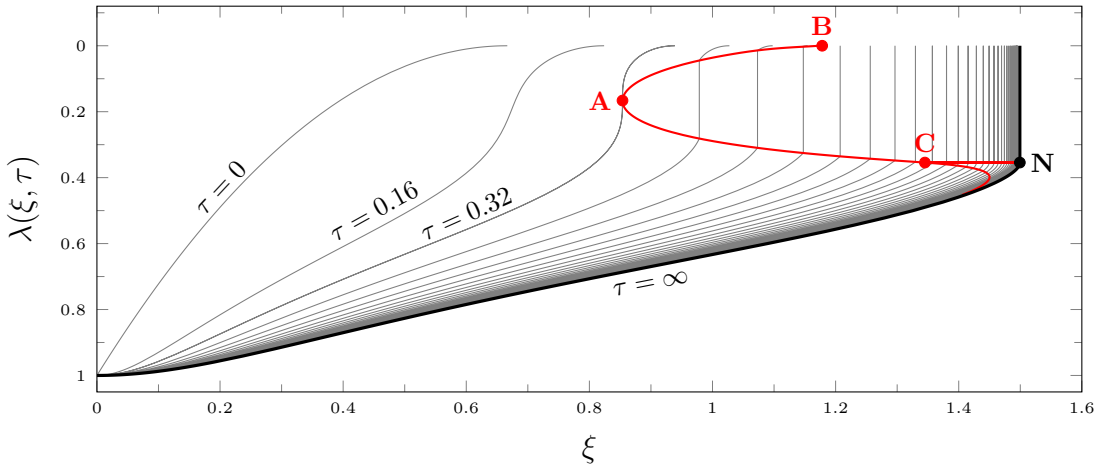

Fig. 2.4 A time-series of interfacial shapes $\lambda(\xi, \tau)$ for $m = 5$ in the simplified fixed-lid system, with points of interest **A**,**B**,**C** and **N** marked (see text). The shapes are shown at equal time intervals $\Delta\tau = 0.16$. The boundaries of the shock and the characteristic emanating from **C** are highlighted. Note that as in figure 2.3b we have reversed the λ-axis to aid physical interpretation.

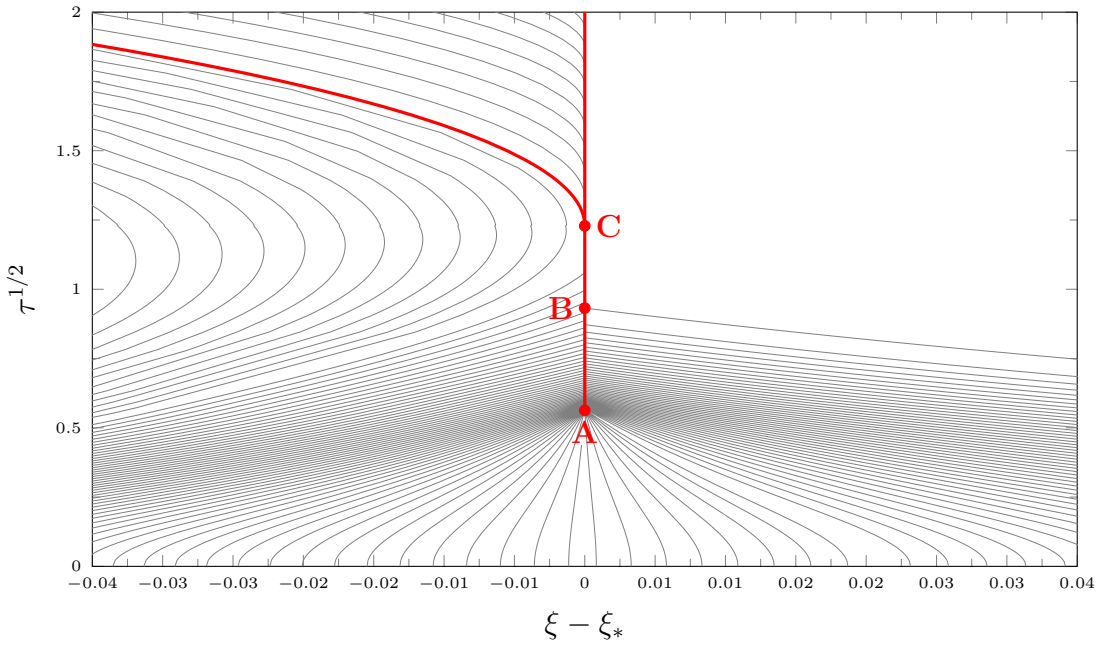

Fig. 2.5 The characteristics corresponding to the solution shapes in figure 2.4, focusing on the region near the shock by using coordinates $\left(\xi - \xi_*, \tau^{1/2}\right)$, where $\xi_*(\tau)$ is the shock position once it has formed and before that the radial position of the characteristic leading up to the shock. The same points of interest **A** to **C** are marked (see text).

Initially the profile is shock-free. However, since $m > 3/2$ the flux function $\mathcal{F}$ has a convex region where $\mathcal{F}'$ increases with λ. Therefore, U_c also increases with λ in this region and the steepening mechanism, associated with shock formation, applies in the upper part of the current (see figure 2.4). The interface steepens until the point **A**, where the interface becomes vertical, which constitutes the formation of a shock and corresponds to the first point where the characteristics intersect in figure 2.5. For the initial condition chosen for this illustration, the shock forms in the interior of the fluid, but other initial conditions can lead to a shock forming at the surface.

Once formed, the shock moves forward with velocity U_s. The parts just above and below the shock continue to steepen, eventually also becoming vertical and causing the height of the shock to grow. The edges of the shock $\lambda_{l,r}$ are given by the condition of a continuous interface, i.e. $\lambda(\xi) \to \lambda_{l,r}$ as $\xi \to \xi_s$ from below or above respectively. Hence, their evolution can be calculated from

$$\frac{\mathrm{d}\lambda_{l,r}}{\mathrm{d}\tau} = \left\{ (U_s - U_c) \frac{\partial \lambda}{\partial \xi} + W_c \right\} \Bigg|_{\xi=\xi_*, \lambda=\lambda_{l,r}} . \tag{2.32}$$

At point **B** (figures 2.4, 2.5) the growth of the shock reaches the top surface, i.e. $\lambda_r = 0$. This point corresponds to where the shock catches up with the characteristic on the top surface. From **B** onwards the upper boundary of the shock is fixed and can no longer grow. Correspondingly there are no more characteristics intersecting the shock from the right in figure 2.5.

Now only the lower boundary of the shock, λ_l continues to grow until it reaches the critical height λ_{crit} at point **C**. The shock has now reached maximal size, but the shock speed U_s at **C** is nonzero and the interface continues to evolve.

The evolution from **C** onwards contains a new feature, absent from classical shocks: a region associated with a one-sided characteristic shock. The characteristic going through the point **C** moves away from the shock and leaves a region between itself and the shock, which needs to be computed differently. This region is filled by characteristics emanating from the shock itself. These initially have the same horizontal speed U_c as the shock speed U_s, but a nonzero vertical speed W_c, which carries them into the region that needs filling. The characteristics emanating from the shock carry away the information $\lambda_l = \lambda_{crit}$, i.e. that the shock cannot grow beyond λ_{crit}. Ultimately, the entire shape of the interface is affected by this information that the shock height is limited. We note that if the shock were initially bigger than this critical height λ_{crit}, then the vertical part below the critical height would fall behind the shock as its

characteristic speed is less than the shock speed. In this situation, the interface would thus flatten and again establish the critical shock height.

We recall that the shock speed U_s also depends on the position ξ and hence the shock speed continues to change after point **C**, even though the shock height is fixed. The speed slows down as $\tau \to \infty$, allowing an approach to a final steady-state similarity solution at point **N**.

2.4.3 Altered boundary conditions for coupled steady similarity solutions in the limit of equal densities

The illustrative example described above shows that for $m > 3/2$ the steady-state similarity solution has a frontal shock of height λ_{crit}. This changes the boundary condition (2.13d) of zero upper-layer height at the nose. Mathematically, we note that the horizontal velocity of the characteristics at a shock in steady state must be equal to the speed of the shock, since otherwise there would be steepening or flattening of the interface resulting in an unsteady profile. Furthermore, in steady state these velocities have to be zero in the similarity frame and hence $U_s = U_c = 0$ at any shock. The only shock that satisfies this is a frontal shock with height λ_{crit}. Therefore, we relax the boundary condition (2.13d) that $\lambda = 0$ at $\xi = \xi_*$ and instead replace it by

$$\lambda = \begin{cases} \lambda_{\text{crit}}(m), & m > 3/2 \\ 0, & m \leq 3/2 \end{cases} \qquad \text{at} \qquad \xi = \xi_*. \tag{2.33}$$

We also note that the point $(\xi, \lambda) = (0, 1)$ is the only stable fixed point of the hyperbolic equation (2.15) with $\varepsilon = 0$ and hence all characteristics will tend to that point. This implies that the boundary condition (2.13b), requiring $\lambda = 1$ at $\xi = 0$, is satisfied automatically and can therefore be ignored when solving the equations numerically. Having one fewer boundary condition matches the reduction in order of the differential equations in the limit $\varepsilon = 0$. We note that the redundancy of the boundary condition (2.13b) in the limit of zero density difference is not apparent in the steady similarity equations, but only becomes apparent in the time-dependent system.

2.5 Numerical similarity solutions

Having established the appropriate boundary conditions in the previous section, we are now in a position to integrate the fully coupled steady versions of (2.11) and (2.12) with

$\varepsilon = 0$ using boundary conditions (2.13a,c,e-g) and (2.33). The numerical integration was carried out using AUTO, which is a continuation and bifurcation software package for ordinary differential equations (Doedel et al., 2007). We regularised the square-root singularity of the nose by inverting the variables and considering ξ, H and q_H as functions of λ as the independent variable. The numerical accuracy of the solutions was verified through changing the number of grid points, the continuation step-size and the precision goal. For some sample cases, we also calculated solutions using a variable-step-size shooting algorithm which showed agreement with the AUTO solutions.

Figure 2.6 shows a tableau of solutions for a variety of values for $\mathcal{Q}_{\text{in}}$ and m. We see that for $m < 3/2$ there are no shocks in the similarity solutions, whilst for $m > 3/2$ there is a frontal shock. Associated with this discontinuity in the upper-layer thickness, there is also a discontinuity in the gradient of the top surface, and hence the pressure gradient, as this is necessary for a continuous total flux. We note that there is a square-root singularity at the nose for all m, which for $m > 3/2$ joins smoothly onto the vertical shock. Furthermore, we note that for all m there is a logarithmic singularity at the origin, which arises from applying lubrication theory at a region where the current is not long and thin and the full two-dimensional Stoke's equation should be used. However, this does not affect the shape and spreading of the current beyond a small region near the origin of extent comparable to the thickness. Finally, we observe that for all parameters there is a region of lower-layer fluid extending all the way to the origin, which is a direct consequence of the no-slip boundary condition on the rigid bottom. This is a key distinction from the way Kowal and Worster (2015) implemented the bottom boundary condition in their model.

We observe that, as might be expected, larger influx rates $\mathcal{Q}_{\text{in}}$ lead to larger radial extents ξ_* and overall a larger total height H of the current. Somewhat surprisingly, large changes in m have significantly less impact, with the extent ξ_* increasing slightly and the total height H decreasing slightly as m increases, which is in accordance with global mass conservation.

In the case of a much more viscous upper-layer fluid, i.e. small m, we observe a region near the origin, where nearly all the less viscous lower-layer fluid is expelled. At the point where this region ends and the lower layer ceases to be as thin we observe a smooth kink in the top surface.

We observe two further trends: firstly, as the influx $\mathcal{Q}_{\text{in}}$ decreases, the top surface flattens except close to the source at the origin; and secondly, as both the influx and viscosity ratio increase, the upper-layer fluid seems to start flowing on top of

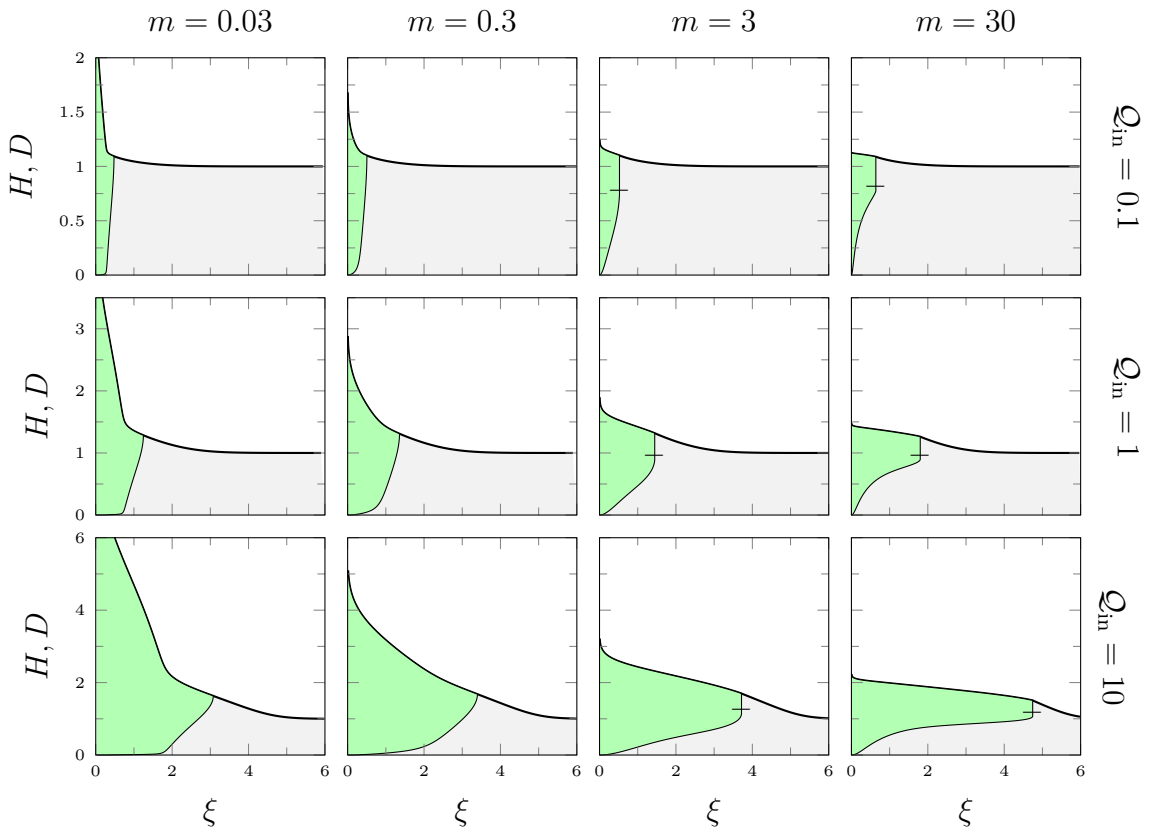

Fig. 2.6 Profiles of numerically calculated similarity solutions as functions of the similarity variable ξ for influx rates $\mathcal{Q}_{\mathrm{in}} \in \{0.1, 1, 10\}$ and viscosity ratios $m \in \{0.03, 0.3, 3, 30\}$, showing the presence of a frontal shock for $m > 1.5$. The horizontal tick shows the height of the shock.

the lower-layer fluid. In the corresponding limits, these currents are analogous to the flow in a Hele-Shaw cell, where the 'flat top' in the gravity current corresponds to the midplane between the two rigid boundaries of the Hele-Shaw cell, and to a single layer-gravity current flowing over an approximately rigid lower layer, respectively. These physically motivated limits can be analysed analytically, from which it may be shown that the nose position scales as $\xi_* \sim 1.424\mathcal{Q}_{\mathrm{in}}^{3/8} m^{1/8}$ in the case of a single-layer current as long as $\mathcal{Q}_{\mathrm{in}}^{-1} m^{-3} \ll 1 \ll \mathcal{Q}_{\mathrm{in}}^{3} m$, and $\xi_* \sim (2\mathcal{Q}_{\mathrm{in}}\mathcal{F}'_{\mathrm{crit}})^{1/2}$ in the case of a 'flat top' current as long as $\mathcal{Q}_{\mathrm{in}} \ll m \ll \mathcal{Q}_{\mathrm{in}}^{-3}$. For a detailed derivation of these asymptotic limits, we refer to Chapter 5.

2.5.1 Comparison of theory and experiments

Box, Gell and Neufeld carried out their experiments in a rectangular 48.5 cm × 48.5 cm tank, using glycerol–water solutions with salt added to make density-matched fluids of

#	$\hat{h}_\infty$ [mm]	$\hat{\mathcal{Q}}_{\text{in}}$ [$\text{cm}^3\,\text{s}^{-1}$]	μ_2 [Pa s]	μ_1 [Pa s]	ρ [$\text{g}\,\text{cm}^{-3}$]	m	$\mathcal{Q}_{\text{in}}$	ξ_*^{exp}	ξ_*^{num}	$\Delta\xi_*$
1	1	2.4	1.7	1.7	1.26	1.0	160	9.4	10.3	9.2%
2	2	3.3	2.0	2.0	1.26	1.0	16	3.7	4.3	11.8%
3	3	1.7	2.2	2.2	1.26	1.0	1.8	1.7	1.8	5.3%
4	5	1.7	2.1	2.1	1.26	1.0	0.22	0.73	0.73	0.2%
5	1	2.6	0.70	1.8	1.26	0.40	72	7.0	7.3	5.0%
6	1	1.6	0.70	2.0	1.26	0.40	43	5.3	6.0	11.0%
7	3	1.6	0.70	1.9	1.26	0.40	0.51	0.95	1.03	8.0%
8	5	1.6	0.70	1.9	1.26	0.40	0.068	0.44	0.43	3.5%
9	1	2.6	0.19	1.6	1.26	0.12	19	3.9	4.2	8.6%
10	1	1.6	0.20	1.7	1.26	0.12	12	2.9	3.6	18.4%
11	3	1.6	0.20	1.7	1.26	0.12	0.15	0.50	0.59	16.1%
12	5	1.5	0.20	1.6	1.26	0.12	0.018	0.20	0.23	11.3%

Table 2.1 The values in each experiment by Box, Gell and Neufeld of the initial height $\hat{h}_\infty$, influx $\hat{\mathcal{Q}}_{\text{in}}$, viscosities μ_i and densities $\rho_1 = \rho_2$ together with derived quantities such as the viscosity ratio m, the non-dimensional influx $\mathcal{Q}_{\text{in}}$, and the experimentally measured and numerically computed nose positions, ξ_*^{exp} and ξ_*^{num} respectively, and their relative deviation $\Delta\xi_*$.

different viscosities. The initial height $\hat{h}_\infty$ ranged from 1 mm to 5 mm and the intruding fluid was introduced at a steady rate through a 1 cm wide hole. Modified Reynolds numbers based on the vertical outflow velocity and $\hat{h}_\infty$ as height scale ranged from 0.003 to 0.02, and Péclet numbers based on the diffusivity of water in glycerol ranged from 5×10^3 to 3×10^4, indicating that a viscous model neglecting diffusion is a valid approximation. The exact set-up and details of these experiments are given in Dauck et al. (2019) and the experimental parameters are given in table 2.1.

While experiments were carried out for a wide range of influxes and viscosity ratios, we only consider those with a more viscous intruding fluid in this chapter, as less viscous intrusions tended to become unstable and no longer to remain axisymmetric. See Chapter 5 for further discussion of this instability.

Firstly, the experimental measurements show that, with the similarity variable given by (2.10), the profiles of the top surface collapse well onto a self-similar shape, thus supporting the application of the theory developed above. A representative example of this collapse is shown in figure 2.7.

Figure 2.8 compares the self-similar total-height profiles $H(\xi)$ obtained from the numerical calculations with the measurements from the experiments. The theory

captures the trend of the top-surface profiles very well over a wide range of influxes $\mathcal{Q}_{\text{in}}$ and viscosity ratios $m < 1$ and reproduces most features of the flow. In particular, the experiments demonstrate the same trend as observed in the numerical calculations: with increasing influx, $\mathcal{Q}_{\text{in}}$, the pre-existing fluid layer plays an smaller role such that the injected fluid forms a more compact current, with a sharp, distinct nose. As also predicted by the model, the viscosity ratio m has a significantly smaller effect on the shape of the current than the effect of changes in the influx $\mathcal{Q}_{\text{in}}$. For several values of $\mathcal{Q}_{\text{in}}$ and m, a small bump is observed between the nose and origin in the experiments, but is absent from the numerical calculations. The cause of the bump is not clear, but it seems to have little effect on the overall profile.

In figure 2.9 we compare the nose positions ξ_* as measured in the experiments with the values calculated using the model above, which reveals a fairly good fit with relative deviations in the range of 5 % to 20 %. The trend is again captured very well, especially considering the simplifying assumptions made, the difficulty resolving the exact nose position from the colour change, and the uncertainties in the physical parameters. Again, both the experimental data and the numerical model show that the nose position depends mainly on the influx $\mathcal{Q}_{\text{in}}$ with only a comparatively small variation with the viscosity ratio m. In particular, both the numerical calculations and the experimental data seem to be approaching the correct asymptotics $\xi_* \sim \mathcal{Q}_{\text{in}}^{1/2}$ as $\mathcal{Q}_{\text{in}} \to 0$ and $\xi_* \sim \mathcal{Q}_{\text{in}}^{3/8}$ as $\mathcal{Q}_{\text{in}} \to \infty$.

Overall, the agreement of the numerical and the experimental results suggests that the theory captures the relevant physical processes involved and gives a good description of the experimental results.

2.6 Discussion and conclusions

The axisymmetric spread of a viscous gravity current over a uniform layer of a second fluid of equal density has been analysed theoretically and compared to laboratory experiments. Through the application of lubrication theory, we derived evolution equations for the top surface and the fluid–fluid interface. In this framework a self-similar rescaling was found that is a function of three non-dimensional parameters: the ratio of fluid viscosities, m; the relative density difference, ε; and a non-dimensional influx, $\mathcal{Q}_{\text{in}}$, defined in (2.14) from the dimensional influx rate, the pre-wetting film thickness and the fluid properties.

In the limit of equal densities, $\varepsilon \to 0$, the interfacial slope no longer contributes to the hydrostatic pressure gradient in the lower-layer fluid and therefore the nature

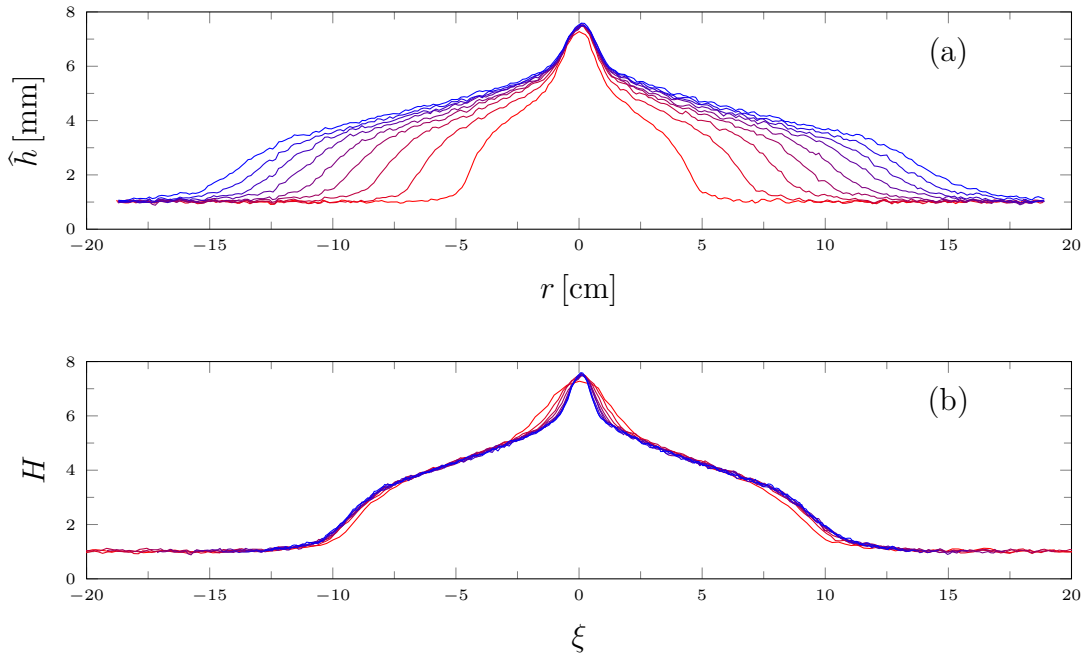

Fig. 2.7 (a) The measured profiles plotted every 10 s for experiment #1. (b) The same profiles as functions of the similarity variable ξ. A similar collapse is observed in the other experiments.

.

of the flow and the interfacial evolution changes. Mathematically, $\varepsilon \to 0$ is a singular limit of the governing equations in which the equation for the depth ratio, λ, changes from a parabolic advection–diffusion equation (Lister and Kerr, 1989) to a hyperbolic pure-advection equation.

As a consequence of the hyperbolic feature of the governing equations for equal densities, the solutions are no longer intrinsically smooth and, instead, vertical discontinuities, or shocks, can form on the interface. We find that these form for a sufficiently more viscous lower-layer fluid and that the critical viscosity ratio for this transition is $m_{\text{crit}} = 3/2$. This transition can be understood by noting that, for a given pressure gradient, the average upper-layer fluid velocity increases with the relative upper-layer thickness, since, although more of the upper-layer fluid is closer to the no-slip bottom, more of the whole flow is the less viscous fluid.

Reintroducing a small density difference between the fluids, $0 < \varepsilon \ll 1$, regularises the equations near the nose and, by analytically solving for local travelling-wave solutions, we obtain a shock condition commonly known as the Oleinik entropy condition. This regularisation justifies the assumptions of a long thin current. Further analysis reveals that for $m > 3/2$ the self-similar solution has a frontal shock with relative

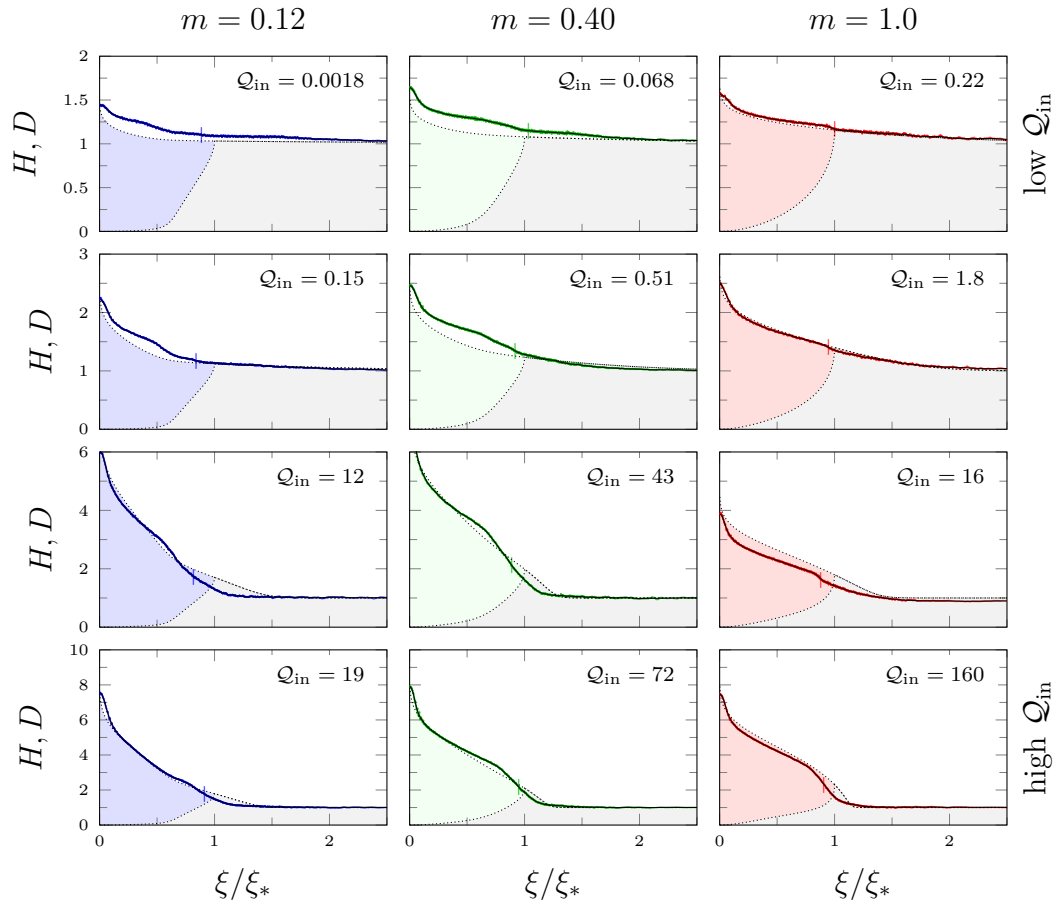

Fig. 2.8 Measured (solid) and computed (dotted) heights H and D as functions of $\xi/\xi_*^{\rm num}$, so the similarity variable is rescaled by the numerical nose position, for a range of values of $\mathcal{Q}_{\rm in}$ and m.

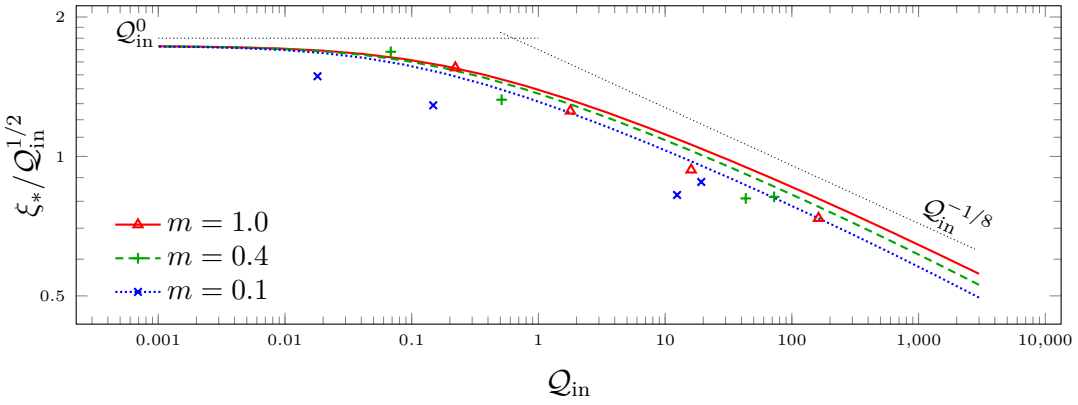

Fig. 2.9 Log-log plot of the measured (symbols) and computed (curved lines) nose positions, $\xi_*^{\rm exp}$ and $\xi_*^{\rm num}$, respectively, as functions of $\mathcal{Q}_{\rm in}$ and rescaled by $\mathcal{Q}_{\rm in}^{1/2}$ with m fixed. The predicted asymptotic dependence on $\mathcal{Q}_{\rm in}$ for large and small $\mathcal{Q}_{\rm in}$ is $\xi_* \sim \mathcal{Q}_{\rm in}^{3/8}$ and $\xi_* \sim \mathcal{Q}_{\rm in}^{1/2}$ respectively (thin straight lines).

height $\lambda_{\text{crit}}(m)$, which is the maximal shock height allowed under the Oleinik entropy condition.

We note that, whilst large variations of $\mathcal{Q}_{\text{in}}$ have a proportionately large effect on the shape and spreading rate of the current, variations of the viscosity ratio, somewhat surprisingly have a significantly smaller impact.

The numerical solutions also provide a connection both to single-layer gravity currents (e.g. Huppert, 1982b) in either the limit of large influx rates ($\mathcal{Q}_{\text{in}} \to \infty$) or of very viscous lower layers ($m \to \infty$), and to the flow in a constant-width Hele-Shaw cell (e.g. Yang and Yortsos, 1997) in the limit of small influx rates ($\mathcal{Q}_{\text{in}} \to 0$). For a detailed asymptotic analysis we refer to Chapter 5.

To test these theoretical predictions, we compared the results to experimental data presented in Dauck et al. (2019) confirming that the evolution of the current is self-similar. Furthermore, we found good agreement between the experiments and theoretical predictions for the top-surface shape and the nose position as a function of $\mathcal{Q}_{\text{in}}$ and m, suggesting that the essential physics is captured by the theoretical model.

The shocks which we found in equal-density two-layer viscous gravity currents can be contrasted to some more-familiar shocks found in other hyperbolic systems, such as those in gas dynamics and in hydraulic jumps (e.g. Billingham and King, 2001). In these cases the shocks are known as classical shocks and their evolution is constrained by an entropy condition which allows characteristics only to enter the shock and not to leave it; thus initial conditions with characteristics diverging from an initial discontinuity yield an expansion fan rather than a shock. On the other hand, in nonclassical shocks characteristics can leave the shock and hence the shock conditions must be determined by locally resolving some regularising mechanism near any shock discontinuity (see, for example, Jacobs et al., 1995).

The shocks found in equal-density gravity currents and in Hele-Shaw cells, are both examples of nonclassical shocks which are, in these cases, related to a nonconvex relationship between the relative thickness of the intruding fluid and the corresponding relative flux of intruding fluid, i.e. the flux function $\mathcal{F}(\lambda)$. In fact, the systems are governed by the same flux function and hence the critical viscosity ratio $m_{\text{crit}} = 3/2$ is the same in two-layer viscous gravity currents and in equal-density miscible two-fluid flow in a Hele-Shaw (Lajeunesse et al., 1997, 1999, 2001; Yang and Yortsos, 1997).

However, for the shocks occurring in equal-density gravity currents, there is a simple regularisation given small density differences as described above, making them one-sided characteristic shocks. In comparison, the shocks in flows in a Hele-Shaw cell are thought to be regularised by the much more complicated two-dimensional Stokes equations

(Yang and Yortsos, 1997). In fact, laboratory experiments (Petitjeans and Maxworthy, 1996) and numerical simulations (Chen and Meiburg, 1996; Rakotomalala et al., 1996) suggest that, in a Hele-Shaw cell, the shock heights exceed the maximal shock height permitted by the Oleinik entropy condition, making them undercompressive shocks.

The existence of a solvable regularisation and therefore of simple shock conditions significantly facilitates any analysis in the case of two-layer gravity currents, such as, for example, a linear stability analysis along the lines of Mathunjwa and Hogg (2006). This investigation of the stability of the interface for a two-layer viscous gravity current is presented in Chapter 5. The comparable problem of a miscible intrusion in a Hele-Shaw cell is known experimentally to be unstable (Wooding, 1969) and a theoretical model is discussed in Chapter 4. Indeed, in some further exploratory experiments conducted by Box, Gell and Neufeld, for $m > 3/2$ there is the suggestion of a new and complex fingering pattern arising from the instability of the interface. We anticipate that the vertical shocks and the associated jumps in pressure gradient play a crucial role in the instability mechanism, as has been suggested for the flow in a Hele-Shaw cell by Lajeunesse et al. (1997, 1999, 2001) or Bischofberger et al. (2014).

Appendix 2.A Two-dimensional geometry

A two-dimensional two-layer current with upper-layer volume $V_{\mathrm{2D}} = \hat{\mathcal{Q}}_{\mathrm{in}} t^{1/2}$ behaves similarly to the axisymmetric currents with upper-layer volume $V_{\mathrm{axi}} = \hat{\mathcal{Q}}_{\mathrm{in}} t$ that we have analysed in the body of the chapter. In both cases a balance between influx and spreading allows for a similarity solution in which the upper layer is characterised by a constant thickness (see Appendix B of Lister and Kerr, 1989). We sketch here the similarities and differences between the two-dimensional and axisymmetric analyses.

In the two-dimensional case the relevant similarity variable and non-dimensional influx are given by

$$\xi = x t^{-1/2} \left(\frac{3\mu_2}{\rho_1 g \hat{h}_\infty^3} \right)^{1/2}, \tag{2.34}$$

and

$$\mathcal{Q}_{\mathrm{in}} = \left(\frac{3\mu_2 \hat{\mathcal{Q}}_{\mathrm{in}}^2}{16\rho_1 g \hat{h}_\infty^5} \right)^{1/2}, \tag{2.35}$$

respectively. Since $\xi \propto t^{1/2}$ in both (2.10) and (2.34), the two-dimensional depth-integrated mass-conservation equations

$$\frac{\partial H}{\partial \tau} - \tfrac{1}{2}\xi \frac{\partial H}{\partial \xi} + \frac{\partial q_H}{\partial \xi} = 0, \qquad \frac{\partial D}{\partial \tau} - \tfrac{1}{2}\xi \frac{\partial D}{\partial \xi} + \frac{\partial q_D}{\partial \xi} = 0. \tag{2.36}$$

differ from the axisymmetric (2.11) only in the form of the divergence of the fluxes q_H and q_D. With the choice of non-dimensional influx, (2.35), the boundary conditions are identical to (2.13).

The fluxes q_H and q_D are the same as in the axisymmetric case (2.12), since the local analysis of the piece-wise parabolic velocity profiles is not influenced by the global geometry. Therefore, we recover the same flux function $\mathcal{F}$, (2.16a). This implies in particular that the local analysis of the regularisation of any shock via travelling-wave solutions is identical in the two geometries. Therefore, we obtain shocks if and only if $m > 3/2$, which have to obey the Oleinik entropy condition (2.24), and in the steady self-similar case a frontal shock is found with height λ_{crit} defined by (2.26).

As a final remark, in the two-dimensional case the origin is non-singular, and solutions do not exhibit the logarithmic singularity which occurs in the axisymmetric case. Nonetheless, the boundary condition (2.13b) is still automatically satisfied as before, due to a similar argument as at the end of §2.4.3. Numerical integration shows that the behaviour of the solutions is largely similar between the two different geometries except the mentioned singularity at the origin in the axisymmetric case. A tableau of two-dimensional solutions for a range of values for $\mathcal{Q}_{\text{in}}$ and m is shown in figure 2.10.

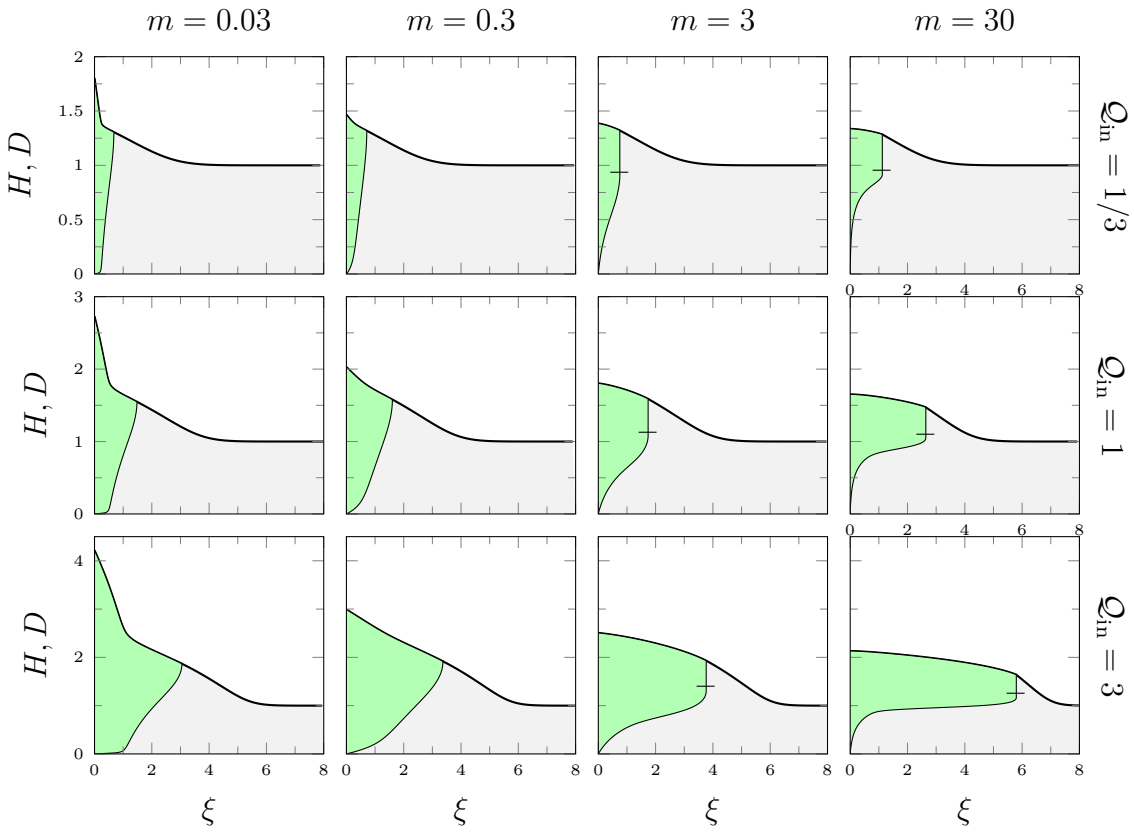

Fig. 2.10 Profiles of numerically calculated similarity solutions as functions ξ for influx rates $\mathcal{Q}_{\text{in}} \in \{1/3, 1, 3\}$ and viscosity ratios $m \in \{0.03, 0.3, 3, 30\}$ in the case of two-dimensional geometry, again showing the appearance of shocks for $m > 1.5$ but without the singularity at the origin. The horizontal tick shows the height of the shock.

Chapter 3

Linear stability analysis of single-layer gravity currents governed by the porous-medium equation using a scaling-invariant formalism

3.1 Introduction

Viscous gravity currents are flows driven by gravity, where effects of inertia can be neglected due to the high viscosity of the fluids involved. They occur in many physical situations and are of wide interest, for example, in geophysical or industrial settings (Huppert, 2006) such as lava flows (Griffiths, 2000) and ice-sheets (Schoof and Hewitt, 2013). Hence, there have been many theoretical and experimental investigations.

Viscous gravity currents should be contrasted with high-Reynolds-number gravity currents, whose rate of propagation is typically controlled at the nose with models often making use of a Froude-number condition. Viscous gravity currents, on the other hand, are generally not controlled at, or even influenced by, the nose. In fact, a common feature of viscous gravity currents is a singular behaviour at the nose, where the assumptions of the model break down — yet experiments confirm that the rate of propagation is very well predicted by these models. For example, Huppert (1982b) used lubrication theory, assuming a long thin current at late times, to derive similarity solutions for a single-layer current spreading over a horizontal surface. He analysed

both axisymmetric and planar geometries, and constant volume and volumes increasing as a power of time. All of the cases analysed exhibit a cube-root singularity at the nose, characteristic of an advancing contact line in lubrication theory, which locally violates the assumption of a long and thin current. However, Huppert (1982b) argued that away from the nose the solution is still valid as it is not dependent on the exact condition at the nose; experiments conducted by him confirmed this to great accuracy.

A problem related to the simple viscous gravity currents analysed by Huppert (1982b) is a gravity current in a saturated porous medium, where Darcy's law applies for low pore Reynolds numbers. This system also has a closed-form analytical self-similar solution for the case of a constant-volume release, which was found by Barenblatt (1952) and later Pattle (1959), and hence is commonly referred to as the Barenblatt–Pattle solution. The equation governing these flows is a simple nonlinear diffusion equation, commonly known as the porous-medium equation, which can be given in dimensionless form by

$$\frac{\partial h}{\partial \tau} = \boldsymbol{\nabla} \cdot \left(h^{\beta} \boldsymbol{\nabla} h \right). \tag{3.1}$$

The equation for a viscous gravity current is a special case ($\beta = 3$) of the porous-medium equation, and so is the equation for a gravity current in a homogeneous porous medium ($\beta = 1$). In fact, many other diffusive processes are governed by the same equation, such as, for example, radiative heat transport in fully ionized gasses ($\beta = 13/2$) or electron heat conduction in a plasma ($\beta = 5/2$) (Boyer, 1962).

Because of the wide-spread applicability of the porous-medium equation and its relatively simple nature, it has been studied extensively. For example, the approach to the self-similar Barenblatt–Pattle solution has been analysed to show that radially spreading currents with constant volume are stable to small perturbations, first by Grundy and McLaughlin (1982) for axisymmetric perturbations, and later by Mathunjwa and Hogg (2006) for non-axisymmetric perturbations. These constant-volume currents are fairly easy to study as they permit analytical solutions both for the base state and for the perturbations. Work on non-Newtonian gravity currents by Longo and Di Federico (2015) showed that the special case of a current in a homogeneous porous medium is stable even for volumes increasing in time. More generally, it may be reasonable to assume that any self-similar current governed by the general porous-medium equation and with increasing volume is also stable. This is plausible, both on physical grounds and from experimental observations of constant-flux currents. However, to the best of our knowledge no one has performed the linear stability analyses for this general case.

In their studies of the porous-medium equation, Gratton and Minotti (1990) developed a phase-plane formalism to analyse all possible self-similar solutions to the equation. This formalism is similar to the one developed for gas dynamics by Sedov (1959) and Courant and Friedrichs (1948), and effectively makes use of a scaling invariance of the equations. It reduces the second-order porous-medium equation to an autonomous first-order differential equation, whose singular points and possible integral curves are linked to a variety of possible boundary conditions (Gratton and Minotti, 1990). However, this formalism was only applied to the self-similar axisymmetric spreading and does not consider transient behaviour or instabilities.

The aim of this chapter is to establish a method, inspired by the phase-plane formalism of Gratton and Minotti (1990), to analyse the linear stability of porous-media gravity currents with volumes growing as powers of time, thereby further extending previous results about the stability of single-layer viscous gravity currents (Grundy and McLaughlin, 1982; Mathunjwa and Hogg, 2006). Ultimately, the method developed in this chapter is applicable to an even wider range of problems with some form of scaling invariance, such as the two-layer viscous gravity currents and the analysis of their stability in Chapter 5.

First, we consider the viscous gravity current with constant flux (Huppert, 1982b) as an illustrative example in §3.2. We contrast the usual approach to stability analysis to a novel method we develop in §3.3 using scaling invariance and a change of variables. The equations obtained are then solved numerically in §3.4. An analysis in §3.5 reveals two analytical solutions: one from shifting the temporal origin (§3.5.1), and a second for the asymptotic limit of large wavenumber (§3.5.2); the details of the latter are worked out in Appendix 3.B. The derivation for the more general porous-media gravity current is given in Appendix 3.A. Finally, in Appendix 3.C, we directly compare our results to those of Mathunjwa and Hogg (2006).

3.2 A viscous gravity current with constant influx — an illustrative example

We consider a viscous gravity current spreading radially from a point source over a horizontal rigid surface. The fluid is of viscosity μ and density ρ and it is introduced at a constant volumetric rate $\hat{\mathcal{Q}}_{\rm in}$ at the origin. We define the height $\widehat{h}(r,\theta,t)$ of the spreading current in plane-polar coordinates and its radial extent $r_*(\theta,t)$ as depicted in figure 3.1. Surface tension and inertial forces are assumed to be negligible. This is exactly the set-up studied by Huppert (1982b) and can be thought of as a limiting

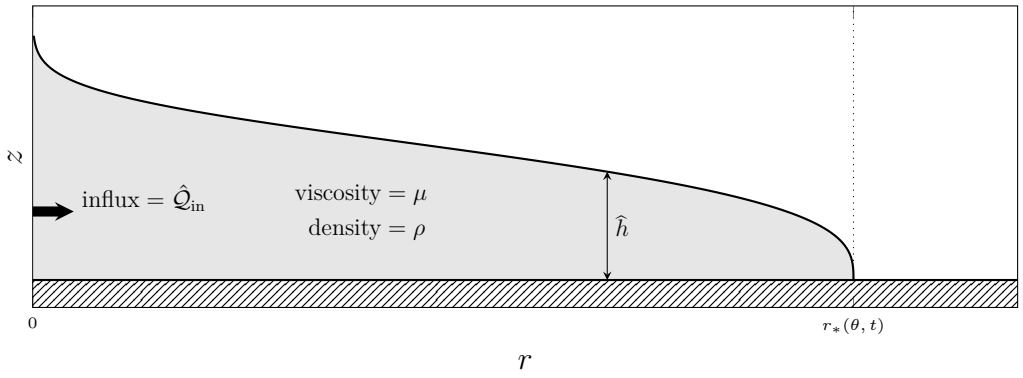

Fig. 3.1 A radial cross-section of a viscous gravity current with constant influx $\hat{\mathcal{Q}}_{\text{in}}$ of a fluid with density ρ and viscosity μ spreading over a rigid horizontal surface. The dynamic variables defined are the height of the current $\widehat{h}(r, \theta, t)$ and the radial extent $r_*(\theta, t)$.

case of the two-layer gravity currents discussed in Chapter 2 except that here we allow for azimuthal variation. Hence, the derivation will largely follow the same method as before.

After a short initial transient, the current becomes long and thin with the horizontal extent r_* greatly exceeding the vertical height $\widehat{h}$. In this limit, the pressure is hydrostatic to leading order and variations in $\widehat{h}$ result in a horizontal pressure gradient. This drives a flow with velocity $\widehat{\boldsymbol{u}}$ given by

$$\mu \frac{\partial^2 \widehat{\boldsymbol{u}}}{\partial z^2} = \boldsymbol{\nabla} \widehat{p} = \rho g \boldsymbol{\nabla} \widehat{h}, \tag{3.2}$$

where the gradient operator $\boldsymbol{\nabla}$ acts in the horizontal only and g is the acceleration due to gravity. Assuming no-slip at the bottom, $\widehat{\boldsymbol{u}} = 0$ at $z = 0$, and no-stress at the free upper surface, $\partial \widehat{\boldsymbol{u}}/\partial z = 0$ on $z = \widehat{h}$, equation (3.2) results in a quadratic velocity profile given by

$$\widehat{\boldsymbol{u}} = \frac{\rho g \boldsymbol{\nabla} \widehat{h}}{2\mu} \left(z^2 - 2\widehat{h} z \right). \tag{3.3}$$

Integrating this velocity profile over the height of the current leads to a local mass-conservation equation governing the evolution of $\widehat{h}$:

$$\frac{\partial \widehat{h}}{\partial t} + \boldsymbol{\nabla} \cdot \widehat{\boldsymbol{q}} = 0 \qquad \text{with} \qquad \widehat{\boldsymbol{q}} = -\frac{\rho g}{3\mu} \widehat{h}^3 \boldsymbol{\nabla} \widehat{h}, \tag{3.4}$$

where $\widehat{\boldsymbol{q}}$ is the integrated local flux of the current.

As (3.4) is a second-order system, we expect two boundary conditions: firstly, global mass conservation implies that

$$\int_0^{2\pi} \int_0^{r_*} \widehat{h}\, r \,\mathrm{d}r \,\mathrm{d}\theta = \hat{\mathcal{Q}}_{\mathrm{in}} t, \tag{3.5}$$

and secondly, the nose $r = r_*(\theta, t)$ defined by $\widehat{h}(r_*) = 0$ moves with a speed given by mass conservation at the nose, i.e.

$$(\boldsymbol{n} \cdot \boldsymbol{e}_r) \frac{\partial r_*}{\partial t} = \lim_{\widehat{h} \to 0} \left(\frac{\boldsymbol{n} \cdot \widehat{\boldsymbol{q}}}{\widehat{h}} \right), \tag{3.6}$$

where $\boldsymbol{n}$ is the unit normal to the front of the current and $\boldsymbol{e}_r$ is the unit radial vector. The right-hand side of (3.6) has to be considered as a limit, as both $\widehat{h} \to 0$ and $\boldsymbol{n} \cdot \widehat{\boldsymbol{q}} \to 0$ at the nose.

3.2.1 Self-similar spreading

Huppert (1982b) found a similarity solution, which may be written as a function of the similarity variable

$$\xi = \hat{\mathcal{Q}}_{\mathrm{in}}^{-3/8} \left(\frac{3\mu}{\rho g} \right)^{1/8} r t^{-1/2}. \tag{3.7}$$

In order to describe the evolution towards self-similarity, we also define a rescaled temporal variable $\tau = \log(t/\widehat{t})$, where $\widehat{t}$ is an arbitrary reference time scale. We then introduce a dimensionless height and dimensionless flux vector

$$h(\xi, \theta, \tau) = \left(\frac{\rho g}{3\mu \hat{\mathcal{Q}}_{\mathrm{in}}} \right)^{1/4} \widehat{h}, \qquad \boldsymbol{q}(\xi, \theta, \tau) = \hat{\mathcal{Q}}_{\mathrm{in}}^{5/8} \left(\frac{3\mu}{\rho g} \right)^{1/8} \widehat{\boldsymbol{q}} t^{-1/2}, \tag{3.8}$$

and write $\xi_*(\theta, t) = \xi(r_*, \theta, \tau)$ as the dimensionless extent of the current.

From (3.4) and using (3.7), the equations governing $h(\xi, \theta, \tau)$ and $\boldsymbol{q}(\xi, \theta, \tau)$ defined in (3.8) are given by

$$\frac{\partial h}{\partial \tau} - \tfrac{1}{2}\xi \frac{\partial h}{\partial \xi} = -\boldsymbol{\nabla} \cdot \boldsymbol{q}, \qquad \boldsymbol{q} = -h^3 \boldsymbol{\nabla} h. \tag{3.9}$$

These equations are autonomous in τ, and the Huppert similarity solution is a steady τ-independent solution. The term proportional to $-\xi/2$ results from the time-dependence of the similarity variable ξ in (3.7).

We write $\boldsymbol{q} = (q_\xi, q_\theta)$ for the radial and azimuthal components of the flux. We then eliminate the azimuthal flux q_θ to obtain two coupled partial differential equations for the dimensionless height h and the dimensionless radial flux q_ξ given by

$$\frac{\partial h}{\partial \tau} - \tfrac{1}{2}\xi\frac{\partial h}{\partial \xi} = -\frac{1}{\xi}\frac{\partial(\xi q_\xi)}{\partial \xi} + \frac{1}{\xi^2}\frac{\partial}{\partial \theta}\left(h^3\frac{\partial h}{\partial \theta}\right), \tag{3.10a}$$

$$q_\xi = -h^3\frac{\partial h}{\partial \xi}, \tag{3.10b}$$

$$\left(q_\theta = -\frac{h^3}{\xi}\frac{\partial h}{\partial \theta}\right). \tag{3.10c}$$

We derive two boundary conditions as before: firstly, the dimensionless version of global mass conservation (3.5) is given by

$$\int_0^{2\pi}\int_0^{\xi_*} h\,\xi\,\mathrm{d}\xi\,\mathrm{d}\theta = 1, \tag{3.11}$$

which is equivalent to a flux condition at the origin. Secondly, the dimensionless counterpart to (3.6), describing mass conservation at the nose, is given by

$$(\boldsymbol{n}\cdot\boldsymbol{e}_\xi)\left(\frac{\partial \xi_*}{\partial \tau} + \frac{\xi_*}{2}\right) = \lim_{h\to 0}\left(\frac{\boldsymbol{n}\cdot\boldsymbol{q}}{h}\right), \tag{3.12}$$

where the extra $\xi_*/2$ again results from the time-dependence of the similarity variable ξ and the resulting radial velocity in the time-dependent coordinate frame.

3.2.2 Linear perturbation expansion

Huppert (1982b) computed the self-similar steady-state solution of (3.10) subject to (3.11) and (3.12), and experiments suggest that it is the late-time limit for flow from a compact source. Here, we demonstrate its linear stability to small perturbations, using this calculation as an example to illustrate a number of analytical techniques that offer advantages over the standard approach.

The standard approach for a perturbation analysis is simply to expand the height, flux and nose position as

$$h(\xi,\theta,\tau) = H_0(\xi) + H_1(\xi)\mathrm{e}^{\mathrm{i}k\theta+\sigma\tau} + \cdots, \tag{3.13a}$$

$$q_\xi(\xi,\theta,\tau) = Q_0(\xi) + Q_1(\xi)\mathrm{e}^{\mathrm{i}k\theta+\sigma\tau} + \cdots, \tag{3.13b}$$

$$\xi_*(\theta,\tau) = \xi_{*0} + \xi_{*1}\mathrm{e}^{\mathrm{i}k\theta+\sigma\tau} + \cdots, \tag{3.13c}$$

where H_0, Q_0 and ξ_{*0} are the self-similar base-state height, flux and nose position, respectively, and H_1, Q_1 and ξ_{*1} are the corresponding linear perturbations, which we assume to be small. The dots denote higher-order corrections, which we neglect as much smaller than the linear perturbations. We assume without loss of generality that the azimuthal wavenumber is non-negative, i.e. $k \in \{0, 1, 2, \dots\}$. The growth rate of the perturbations is given by σ, and we want to show that all possible σ are negative, indicating decay of the perturbation and therefore stability.

We then substitute (3.13) into (3.10) and equate the different orders. This gives

$$\tfrac{1}{2}\xi H_0' = \frac{1}{\xi}\left(\xi Q_0\right)', \qquad Q_0 = -H_0^3 H_0', \tag{3.14a,b}$$

$$\sigma H_1 - \tfrac{1}{2}\xi H_1' = -\frac{1}{\xi}\left(\xi Q_1\right)' - \frac{k^2}{\xi^2} H_0^3 H_1, \qquad Q_1 = -H_0^2\left(3H_0' H_1 + H_0 H_1'\right), \tag{3.14c,d}$$

where primes denote differentiation with respect to the independent variable ξ. This can be slightly simplified to give

$$H_0' = -\frac{Q_0}{H_0^3}, \qquad \frac{1}{\xi}\left(\xi Q_0\right)' = -\frac{\xi Q_0}{2H_0^3}, \tag{3.15a,b}$$

$$\begin{pmatrix} H_1' \\ \frac{1}{\xi}\left(\xi Q_1\right)' \end{pmatrix} = \begin{pmatrix} \frac{3Q_0}{H_0^4} & -\frac{1}{\xi H_0^3} \\ \frac{3\xi Q_0}{2H_0^4} - \sigma - \frac{k^2 H_0^3}{\xi^2} & -\frac{1}{2H_0^3} \end{pmatrix} \begin{pmatrix} H_1 \\ \xi Q_1 \end{pmatrix}. \tag{3.15c}$$

The form of the coefficient matrix in (3.15c) shows that both the origin ($\xi = 0$) and the nose ($H_0 = 0$) are singular points of the differential equation.

The boundary conditions at the nose

By rescaling the variables and relaxing (3.11), we can assume without loss of generality that $\xi_{*0} = 1$, though we still have to allow for an unknown perturbation ξ_{*1} to this position. The rescaled version of (3.11) has a constant $\mathcal{Q}_{\text{in}}$ on the right-hand side in place of unity.

To expand the boundary condition (3.12), we note that

$$\boldsymbol{n} = \left[1 + \left(\frac{\partial \xi_*}{\partial \theta}\right)^2\right]^{-1/2} \begin{pmatrix} 1 \\ \frac{\partial \xi_*}{\partial \theta} \end{pmatrix} \sim \begin{pmatrix} 1 \\ \frac{\partial \xi_*}{\partial \theta} \end{pmatrix} + \cdots, \tag{3.16}$$

and hence $\boldsymbol{n} \cdot \boldsymbol{q} \approx q_\xi$ and $\boldsymbol{n} \cdot \boldsymbol{e}_\xi \approx 1$ with corrections being quadratic in the perturbation quantities and therefore negligible. Thus, we can expand (3.12) using (3.13) and

$\xi_{*0} = 1$, which gives

$$\lim_{\xi\to 1}\left(\frac{Q_0}{H_0}\right) = \tfrac{1}{2}, \tag{3.17a}$$

$$\lim_{\xi\to 1}\left(\frac{Q_0}{H_0}\left\{\frac{Q_1 + Q_0'\xi_{*1}}{Q_0} - \frac{H_1 + H_0'\xi_{*1}}{H_0}\right\}\right) = \left(\sigma + \tfrac{1}{2}\right)\xi_{*1}, \tag{3.17b}$$

where the definition of the nose position, $h(\xi_*) = 0$, also has to be expanded using (3.13), which gives

$$\lim_{\xi\to 1} H_0 = 0, \qquad \lim_{\xi\to 1}\left(H_1 + H_0'\xi_{*1}\right) = 0. \tag{3.17c,d}$$

The perturbation condition (3.17b) appears somewhat messy, and to simplify it, we first need to find expansions of the base state, derived from (3.15a,b) and (3.17a,c):

$$H_0 \sim \left(\tfrac{3}{2}(1-\xi)\right)^{1/3}\left(1 + \tfrac{1}{12}(1-\xi) + \cdots\right), \tag{3.18a}$$

$$Q_0 \sim \left(\tfrac{3}{2}(1-\xi)\right)^{1/3}\left(\tfrac{1}{2} + \tfrac{7}{24}(1-\xi) + \cdots\right). \tag{3.18b}$$

We note that both H_0 and Q_0 tend to zero at the nose, corresponding to a no-flux, zero-height nose in the steady limit. However, due to the cube-root singularity of the base-state variables, their derivatives diverge as $\xi \to 1$, which implies that the perturbation variables H_1 and Q_1 also diverge near the nose to allow for any shift in nose position, i.e. for nonzero ξ_{*1}. This makes the boundary condition at the nose somewhat more involved, but, using (3.18), we can combine and simplify (3.17) to

$$\lim_{\xi\to 1} H_0 = 0, \qquad \lim_{\xi\to 1}\left(\frac{Q_0}{H_0}\right) = \tfrac{1}{2}, \tag{3.19a,b}$$

$$\lim_{\xi\to 1}\left(\frac{Q_1}{H_1}\right) = \tfrac{1}{2}, \qquad \lim_{\xi\to 1}\left(\frac{Q_1}{Q_0} - \frac{H_1}{H_0}\right) = \left(\tfrac{3}{2} + 2\sigma\right)\xi_{*1}. \tag{3.19c,d}$$

We attempt to find the value of ξ_{*1} by expanding the perturbation variables near the nose using the base-state expansions (3.18), the differential equation (3.15c) and the boundary condition (3.19c):

$$\frac{H_1}{H_0} \sim \delta\left(\frac{1}{1-\xi} + \tfrac{5}{4} + 2\sigma + \cdots\right), \tag{3.20a}$$

$$\frac{Q_1}{Q_0} \sim \delta\left(\frac{1}{1-\xi} + \tfrac{23}{4} + 8\sigma + \cdots\right), \tag{3.20b}$$

where δ is the arbitrary amplitude of the linear perturbations. Equations (3.19d) and (3.20) then imply that

$$\xi_{*1} = 3\delta, \tag{3.21}$$

where the coefficient 3 is related to the exponent of the cube-root singularity of the base state.

We note that the solution of (3.19d), the condition defining ξ_{*1}, depends crucially on the cancellation of the diverging parts of the perturbation variables H_1 and Q_1 in (3.20). This would be numerically problematic to implement.

The boundary condition at the origin

By choice of scaling, we have two boundary conditions (3.19a,b) at the nose for the base state and the condition at the origin determines the constant $\mathcal{Q}_{\text{in}}$. However, for the perturbations we had to introduce a third variable, the nose position ξ_{*1}, and the second of the two perturbation boundary conditions (3.19c,d) is used to determine it. Therefore, we require a third boundary condition for the perturbations, which comes from a condition at the origin. Physically, the influx of fluid at the origin is fixed and hence should not be changed by the perturbations, i.e.

$$\lim_{\xi\to 0}(\xi Q_1) = 0. \tag{3.22}$$

(The extra factor of ξ is due to the cylindrical geometry, and compensates for the fact that the flux of fluid gets distributed over a cylinder of radius ξ.)

As the origin is a singular point of the equations, we need to find expansions for the possible behaviours of the perturbation flux near the origin to check whether (3.22) is sufficient to give a well-posed problem.

We first expand the base state near the origin to find a logarithmic singularity in the base-state height:

$$H_0 \sim \left[4\mathcal{Q}_{\text{in}} \log\left(\frac{c_\xi}{\xi}\right)\right]^{1/4} + \cdots, \qquad \xi Q_0 \sim \mathcal{Q}_{\text{in}} + \cdots, \tag{3.23}$$

where $\mathcal{Q}_{\text{in}}$ is a constant of integration related to the choice of rescaling $\xi_{*0} = 1$, and c_ξ is a second constant of integration. The next-order corrections, i.e. the dots, are $O(\xi^2)$ smaller than the leading order (up to logarithmic factors). We substitute this expansion of the base state near the origin into (3.15c) to find expansions for the

perturbation quantities near the origin, which for $k > 0$ are given by

$$\frac{H_1}{H_0} \sim \frac{-c_+\xi^k + c_-\xi^{-k}}{4k\log\left(\frac{c_\xi}{\xi}\right)} + \cdots \sim \frac{\xi Q_0}{kH_0^4}\left(-c_+\xi^k + c_-\xi^{-k}\right) + \cdots, \tag{3.24a}$$

$$\frac{Q_1}{Q_0} \sim c_+\xi^k + c_-\xi^{-k} + \cdots, \tag{3.24b}$$

where $c_\pm$ are integration constants. Hence, an appropriate boundary condition must give $c_- = 0$ to avoid an infinite perturbation to both height and flux. We see that the physically intuitive condition (3.22) is indeed sufficient as a boundary condition at the origin for $k > 0$.

If, however, $k = 0$ we get instead of (3.24) the expansions

$$\frac{H_1}{H_0} \sim \left(\tfrac{1}{4}\right)c_1 + \left(\frac{\xi Q_0}{H_0^4}\right)c_2 \cdots, \qquad \frac{Q_1}{Q_0} \sim c_1 + \cdots, \tag{3.25}$$

where the two constants $c_{1,2}$ are effectively obtained by writing $c_1 = (c_- - c_+)/k - (c_- + c_+)\log c_\xi$ and $c_2 = (c_- + c_+)$ in (3.24) and then taking the limit $k \to 0$. Note that the Q_1 terms associated with c_2 are all $O(\xi^2)$ and hence an appropriate boundary condition must give $c_1 = 0$. Therefore, (3.23) is sufficient as a boundary condition at the origin for $k = 0$ as well.

3.3 A new numerical approach

Unlike for constant-volume currents, the equations for a constant-flux current cannot be solved analytically, even for the base state, and we have to develop a numerical integration scheme. In this section we highlight issues with implementing the naive expansions presented above and suggest a different approach to avoid these issues numerically.

We need to integrate the differential equations (3.15) numerically with boundary conditions (3.19) at the nose, and choosing growth rates σ such that the boundary condition (3.22) is satisfied at the origin. Numerically, this system is far from ideal for several reasons:

- The nose is a singular point of the base-state equations, and the base-state derivatives diverge near this singularity.
- It is necessary to introduce a separate perturbation of the nose position. Perturbing the position of the singularity at the nose leads to a strongly diverging

perturbation height and flux to compensate for the diverging derivatives of the base state.

- We had to find expansions near the nose of both the base state and the perturbation quantities to find sensible boundary conditions (3.19) at the nose, including a value for the perturbation of the nose position ξ_{*1}. Though this can be done analytically, it does require extra work.

- There is an undetermined degree of freedom in the arbitrary amplitude of the perturbations δ, which needs to be eliminated through an extra artificial boundary condition in order to obtain a closed numerical scheme.

We could mitigate the first two points by initiating the numerical integration a small step away from the nose and using expansions near the nose such as (3.18) and (3.20). These expansions however depend on the undetermined amplitude δ, which would need to be fixed arbitrarily, for example $\delta = 1$. Choosing δ this way also addresses the final point made above regarding the artificial boundary condition. However, the diverging nature of the perturbation quantities still poses difficulties with numerical codes, leading to very small step sizes in shooting methods or convergence issues with continuation methods.

Therefore, we instead introduce a different set of variables, which avoids these problems and can be easily implemented using continuation software such as AUTO. There are three key ideas motivating our choice of new variables:

- We will exploit a scaling-invariance symmetry of the equations, by introducing two scaling-invariant variables. This change of variables results in equations which are autonomous with respect to $\log \xi$. Therefore, the two base-state equations for these new variables decouple in such a way that only a first-order system needs to be solved for the base state to find the corresponding perturbation equations. This is similar to the phase-plane method developed by Gratton and Minotti (1990), but extended to the perturbation problem.

- Instead of considering perturbations to the height for fixed position ξ, we will consider perturbations to the radial position for another fixed variable ζ related to the height. The result is that the radial position ξ becomes a dependent variable with its own base state and perturbation. This has the benefit of eliminating the singular behaviour at the nose.

- Instead of considering two physical perturbation quantities, we shift from Cartesian to polar perturbations, by introducing a perturbation amplitude $A(\zeta)$ and

phase angle $\varphi(\zeta)$. As the Cartesian equations are linear and homogeneous, the equation for $\varphi(\zeta)$ decouples from the equation for $A(\zeta)$ making $\varphi(\zeta)$ independent of the arbitrary scale δ.

In addition to the avoidance of singularities, these ideas have the benefit of reducing a fourth-order system with a free boundary condition to a second-order system with fixed boundary conditions, thereby significantly simplifying any integration scheme.

The only downside is that solutions are somewhat harder to interpret and the variables are physically less intuitive. Therefore, we shall try to present analytical results in terms of physical variables and we shall present our numerical results both in transformed variables and their physical counterparts.

3.3.1 Scaling invariance

On studying (3.10), we note that the equations remain unchanged under the rescalings

$$h \mapsto c^2 h, \qquad q_\xi \mapsto c^5 q_\xi, \qquad \xi \mapsto c^3 \xi, \tag{3.26}$$

where c is any non-zero constant. Hence, instead of the physical variables, it is advantageous to consider two scaling-invariant groups:

$$\vartheta = \frac{q_\xi}{\xi^{5/3}}, \qquad \zeta = \frac{h}{\xi^{2/3}}, \tag{3.27}$$

where we call ϑ the scaling-invariant flux and ζ the scaling-invariant height. These are similar to the variables used in Gratton and Minotti (1990), except that we are considering height and flux instead of height and average velocity and that we allow for θ and τ dependence.

Using these scaling-invariant variables, (3.10) becomes

$$\frac{\partial \zeta}{\partial \tau} - \tfrac{1}{2}\left(\xi \frac{\partial \zeta}{\partial \xi} + \tfrac{2}{3}\zeta\right) = -\left(\xi \frac{\partial \vartheta}{\partial \xi} + \tfrac{8}{3}\vartheta\right) + \tfrac{1}{4}\frac{\partial^2 \zeta^4}{\partial \theta^2}, \quad \vartheta = -\zeta^3\left(\xi \frac{\partial \zeta}{\partial \xi} + \tfrac{2}{3}\zeta\right). \tag{3.28}$$

We rewrite these equations as

$$\frac{\partial \vartheta}{\partial \log \xi} = -\left(\frac{16\zeta^3 + 3}{6\zeta^3}\right)\vartheta - \frac{\partial \zeta}{\partial \tau} + \tfrac{1}{4}\frac{\partial^2 \zeta^4}{\partial \theta^2}, \qquad \frac{\partial \zeta}{\partial \log \xi} = -\left(\frac{2\zeta^4 + 3\vartheta}{3\zeta^3}\right), \tag{3.29}$$

which are autonomous equations in $\log \xi$. We can then consider phase-plane trajectories, i.e. a flux–height relationship $\vartheta(\zeta, \theta, \tau)$, by dividing the two equations. Furthermore,

if we assume steady and axisymmetric behaviour $\vartheta(\zeta)$, as is appropriate for the base state, we obtain

$$\frac{\mathrm{d}\vartheta}{\mathrm{d}\zeta} = \left(\frac{16\zeta^3 + 3}{2\zeta^4 + 3\vartheta}\right)\frac{\vartheta}{2}. \tag{3.30}$$

This shows how, at least for the base state, the equations governing the flux–height relationship can be decoupled from the radial dependence by choice of appropriate (scaling-invariant) height and flux variables.

3.3.2 Changing the independent variable

We now change the independent variable from ξ (or equivalently from $\log\xi$) to ζ. To derive appropriate transformation laws for this change of variables, we apply the chain rule to the partial derivatives

$$\left(\frac{\partial}{\partial\zeta}\right)_{\theta,\tau} = \left(\frac{\partial\xi}{\partial\zeta}\right)_{\theta,\tau}\left(\frac{\partial}{\partial\xi}\right)_{\theta,\tau}, \tag{3.31a}$$

$$\left(\frac{\partial}{\partial\theta}\right)_{\zeta,\tau} = \left(\frac{\partial}{\partial\theta}\right)_{\xi,\tau} + \left(\frac{\partial\xi}{\partial\theta}\right)_{\zeta,\tau}\left(\frac{\partial}{\partial\xi}\right)_{\theta,\tau}, \tag{3.31b}$$

$$\left(\frac{\partial}{\partial\tau}\right)_{\zeta,\theta} = \left(\frac{\partial}{\partial\tau}\right)_{\xi,\theta} + \left(\frac{\partial\xi}{\partial\tau}\right)_{\zeta,\theta}\left(\frac{\partial}{\partial\xi}\right)_{\theta,\tau}, \tag{3.31c}$$

where the subscripts on the brackets signify which variables are being held constant. Inverting these relationships leads to the following transformation laws from the variables (ξ,θ,τ) to the variables (ζ,θ,τ):

$$\frac{\partial}{\partial\xi} \mapsto \frac{\partial}{\partial\zeta}\Big/\frac{\partial\xi}{\partial\zeta}, \tag{3.32a}$$

$$\frac{\partial}{\partial\theta} \mapsto \frac{\partial}{\partial\theta} - \left(\frac{\partial\xi}{\partial\theta}\Big/\frac{\partial\xi}{\partial\zeta}\right)\frac{\partial}{\partial\zeta}, \tag{3.32b}$$

$$\frac{\partial}{\partial\tau} \mapsto \frac{\partial}{\partial\tau} - \left(\frac{\partial\xi}{\partial\tau}\Big/\frac{\partial\xi}{\partial\zeta}\right)\frac{\partial}{\partial\zeta}. \tag{3.32c}$$

Using these transformations, and after some algebra, (3.29) becomes

$$\frac{\partial\vartheta}{\partial\zeta} = \left(\frac{16\zeta^3 + 3}{2\zeta^4 + 3\vartheta}\right)\frac{\vartheta}{2} + \frac{\partial\log\xi}{\partial\tau} - \zeta^3\frac{\partial^2\log\xi}{\partial\theta^2} + \underbrace{\frac{\partial}{\partial\zeta}\left(\zeta^3\left[\frac{\partial\log\xi}{\partial\theta}\right]^2\left[\frac{\partial\log\xi}{\partial\zeta}\right]^{-1}\right)}_{\text{negligible for linear perturbations}}, \tag{3.33a}$$

$$\frac{\partial \log \xi}{\partial \zeta} = \frac{-3\zeta^3}{2\zeta^4 + 3\vartheta}. \tag{3.33b}$$

In these new variables, the nose corresponds to $\zeta = 0$ as the height vanishes near the nose, while the physical origin, $\xi = 0$, corresponds to $\zeta \to \infty$ as the height diverges logarithmically near the origin.

We similarly transform the boundary condition at the nose, (3.12), by re-expressing the physical variables in terms of the scaling-invariant variables ϑ and ζ,

$$\frac{\partial \log \xi}{\partial \tau} + \tfrac{1}{2} = \lim_{\zeta \to 0} \left(\frac{\vartheta}{\zeta} \right). \tag{3.34}$$

Again, the only coupling to the radial dependence in this boundary condition via $\log \xi$ disappears for the steady base state.

Linear perturbation expansions

We then expand

$$\vartheta(\zeta, \theta, \tau) = \Theta_0(\zeta) + \Theta_1(\zeta) \mathrm{e}^{\mathrm{i}k\theta + \sigma\tau} + \cdots, \tag{3.35a}$$

$$\log \xi(\zeta, \theta, \tau) = \Lambda_0(\zeta) + \Lambda_1(\zeta) \mathrm{e}^{\mathrm{i}k\theta + \sigma\tau} + \cdots, \tag{3.35b}$$

and, substituting this expansion into (3.33), we obtain the equations

$$\Theta_0' = \left(\frac{16\zeta^3 + 3}{2\zeta^4 + 3\Theta_0} \right) \frac{\Theta_0}{2}, \qquad \Lambda_0' = \frac{-3\zeta^3}{2\zeta^4 + 3\Theta_0}, \tag{3.36a}$$

$$\Theta_1' = \underbrace{\frac{(3 + 16\zeta^3)\,\zeta^4}{(2\zeta^4 + 3\Theta_0)^2}}_{=\frac{\partial \Theta_0'}{\partial \Theta_0}} \Theta_1 + \left(\sigma + k^2 \zeta^3 \right) \Lambda_1, \qquad \Lambda_1' = \underbrace{\frac{9\zeta^3}{(2\zeta^4 + 3\Theta_0)^2}}_{=\frac{\partial \Lambda_0'}{\partial \Theta_0}} \Theta_1, \tag{3.36b}$$

where primes again denote differentiation with respect to the independent variable, which now is ζ.

As expected, the base-state equations decouple into an equation for the flux–height relationship given by $\Theta_0(\zeta)$ and an equation for the radial dependence given by $\Lambda_0(\zeta)$. This should be compared to (3.15a,b), the fully coupled equations of the physical base-state variables $H_0(\xi)$ and $Q_0(\xi)$. In particular, as we don't actually have to solve for Λ_0 to determine the perturbation equations, the transformed variables effectively lead to a reduction in order in the base-state equations by one, thereby simplifying matters.

The perturbation equations are simply partial derivatives of the base-state equations with an additional simple coupling term linked to the time dependence via the growth rate σ and to the azimuthal variation via the wavenumber k.

The boundary conditions at the nose

Substituting (3.35) into (3.34) gives an expansion of the boundary condition at the nose:

$$\lim_{\zeta\to 0}\left(\frac{\Theta_0}{\zeta}\right) = \tfrac{1}{2}, \qquad\qquad \lim_{\zeta\to 0}\left(\frac{\Theta_1}{\zeta\Lambda_1}\right) = \sigma. \tag{3.37}$$

Compared to (3.19d), this boundary condition for the transformed variables does not rely on the cancellation of diverging parts in the perturbations. In fact, a local analysis of (3.36) near $\zeta = 0$ shows that both the base state and the perturbations have Taylor series, which are given by

$$\Theta_0 \sim \tfrac{1}{2}\zeta + \tfrac{1}{2}\zeta^4 + O\left(\zeta^7\right), \tag{3.38a}$$

$$\Theta_1 \sim c_1\left[1 + \frac{4+6\sigma}{9}\zeta^3 + O\left(\zeta^6\right)\right] + c_2\left[\sigma\zeta + \frac{3k^2+4\sigma(1+\sigma)}{12}\zeta^4 + O\left(\zeta^7\right)\right], \tag{3.38b}$$

$$\Lambda_1 \sim c_1\left[2\zeta^2 - \frac{152-24\sigma}{45}\zeta^5 + O\left(\zeta^8\right)\right] + c_2\left[1 + \frac{4\sigma}{3}\zeta^3 + O\left(\zeta^6\right)\right], \tag{3.38c}$$

where $c_{1,2}$ are constants of integration associated with the different possible behaviours of the perturbations near the nose. The boundary condition (3.37b) then selects $c_1 = 0$ and we usually write $c_2 = \delta$ for the perturbation amplitude.

These expansions near the nose show one of the major benefits of the change of variables: the perturbation quantities behave non-singularly near the nose with well-defined Taylor series and a simple boundary condition $\Theta_1 = 0$ at $\zeta = 0$ as opposed to the diverging nature of the physical perturbation variables H_1 and Q_1.

Recovering the physical variables

To recover the physical perturbation variables, we write $X_0(\zeta) = \mathrm{e}^{\Lambda_0(\zeta)}$, which gives

$$\xi(\zeta,\theta,\tau) \sim X_0(\zeta)\Big(1 + \Lambda_1(\zeta)\mathrm{e}^{\mathrm{i}k\theta+\sigma\tau} + \cdots\Big)$$

$$\Rightarrow \qquad \zeta(\xi,\theta,\tau) \sim X_0^{-1}(\xi) - \frac{\Lambda_1 \circ X_0^{-1}(\xi)}{\Lambda_0' \circ X_0^{-1}(\xi)}\mathrm{e}^{\mathrm{i}k\theta+\sigma\tau} + \cdots. \tag{3.39}$$

Together with

$$h(\xi,\theta,\tau)=\xi^{2/3}\zeta, \qquad\qquad q_\xi(\xi,\theta,\tau)=\xi^{5/3}\vartheta, \tag{3.40}$$

this allows us to recover the physical variables in terms of the rescaled ones:

$$h(\xi,\theta,\tau)\sim\left[\underbrace{\xi^{2/3}\zeta}_{H_0}-\underbrace{\xi^{2/3}\frac{\Lambda_1(\zeta)}{\Lambda_0'(\zeta)}}_{H_1}\mathrm{e}^{\mathrm{i}k\theta+\sigma\tau}+\cdots\right]_{\zeta=X_0^{-1}(\xi)}, \tag{3.41a}$$

$$q_\xi(\xi,\theta,\tau)\sim\left[\underbrace{\xi^{5/3}\Theta_0(\zeta)}_{Q_0}+\underbrace{\xi^{5/3}\left(\Theta_1(\zeta)-\frac{\Theta_0'(\zeta)}{\Lambda_0'(\zeta)}\Lambda_1(\zeta)\right)}_{Q_1}\mathrm{e}^{\mathrm{i}k\theta+\sigma\tau}+\cdots\right]_{\zeta=X_0^{-1}(\xi)}. \tag{3.41b}$$

The boundary condition at the (physical) origin

To obtain a boundary condition for the rescaled perturbations at the physical origin, we could look for possible behaviours as $\zeta\to\infty$ by expanding (3.36). However, due to the logarithmic singularity of the height of the current, the algebra is inherently messy, and, for example, a simple expansion of (3.36a) as $\zeta\to\infty$ would give

$$\Theta_0'\sim\frac{8\zeta^3\Theta_0}{2\zeta^4+3\Theta_0} \quad\Rightarrow\quad \tfrac{3}{2}\Theta_0\left(\log c_\Theta+\log\Theta_0\right)\sim\zeta^4 \quad\Rightarrow\quad \Theta_0\sim\frac{\frac{2}{3}\zeta^4}{\mathrm{W}\left(\frac{2}{3}c_\Theta\zeta^4\right)}, \tag{3.42}$$

where W denotes the Lambert W-function and c_Θ is a constant of integration. Therefore, the search for perturbation expansions with this ansatz is very difficult. We note that (3.42) implies that Θ_0 grows as $O\left(\zeta^4\right)$ up to some essentially logarithmic factors given by the Lambert W-function, i.e. ζ^4/Θ_0 grows logarithmically.

Instead, we can simply use the expansion of the physical variables near the origin, (3.24) with $c_-=0$, together with the formulae relating the physical perturbation variables to the scaling-invariant perturbation variables, (3.41). This gives

$$\frac{H_1}{H_0}=\left(\frac{2\zeta^4+3\Theta_0}{3\zeta^3}\right)\frac{\Lambda_1}{\zeta}\sim-c_+\xi^k\frac{\xi Q_0}{4kH_0^4}=-c_+\xi^k\frac{\Theta_0}{k\zeta^4}, \tag{3.43a}$$

$$\frac{Q_1}{Q_0}=\frac{\Theta_1}{\Theta_0}+\tfrac{1}{2}\underbrace{\left(\frac{16\zeta^3+3}{3\zeta^3}\right)}_{\sim16/3+\cdots}\Lambda_1\sim c_+\xi^k. \tag{3.43b}$$

Taking the ratio of these expressions gives a boundary condition solely in terms of transformed variables

$$\frac{\Theta_1}{\Lambda_1} \sim -\left(\tfrac{2}{3}k\right)\zeta^4 - \left(k+\tfrac{8}{3}\right)\Theta_0 + \cdots \qquad \text{as} \qquad \zeta \to \infty, \tag{3.44}$$

where, up to some logarithmic factors, the corrections are $O\left(\zeta^{-3}\right)$ smaller than the leading-order terms, which is equivalent to the $O\left(\xi^2\right)$ corrections seen earlier.

We can check that using (3.24) with $c_- \neq 0$ gives a different expansion, which is essentially obtained by replacing k with $-k$, and therefore (3.44) does single out the correct solution. We can also check that (3.44) works for $k = 0$.

3.3.3 Cartesian vs. polar perturbation variables

Finally, we note that there is an undetermined degree of freedom associated with the amplitude, which motivates a change from Cartesian perturbations Θ_1, Λ_1 to polar perturbations φ, A defined by

$$\begin{aligned} \Theta_1 &= A\sin\varphi, \\ \Lambda_1 &= A\cos\varphi, \end{aligned} \qquad \Leftrightarrow \qquad \begin{aligned} \tan\varphi &= \frac{\Theta_1}{\Lambda_1}, \\ A^2 &= \Theta_1^2 + \Lambda_1^2. \end{aligned} \tag{3.45}$$

The equations governing the phase angle $\varphi(\zeta)$ and the amplitude $A(\zeta)$ are obtained from (3.36b) and are given by

$$\varphi' = \begin{pmatrix} \cos\varphi \\ -\sin\varphi \end{pmatrix}^{\mathsf{T}} \begin{pmatrix} \frac{\left(3+16\zeta^3\right)\zeta^4}{\left(2\zeta^4+3\Theta_0\right)^2} & \sigma + k^2\zeta^3 \\ \frac{9\zeta^3}{\left(2\zeta^4+3\Theta_0\right)^2} & 0 \end{pmatrix} \begin{pmatrix} \sin\varphi \\ \cos\varphi \end{pmatrix}, \tag{3.46a}$$

$$\frac{A'}{A} = \begin{pmatrix} \sin\varphi \\ \cos\varphi \end{pmatrix}^{\mathsf{T}} \begin{pmatrix} \frac{\left(3+16\zeta^3\right)\zeta^4}{\left(2\zeta^4+3\Theta_0\right)^2} & \sigma + k^2\zeta^3 \\ \frac{9\zeta^3}{\left(2\zeta^4+3\Theta_0\right)^2} & 0 \end{pmatrix} \begin{pmatrix} \sin\varphi \\ \cos\varphi \end{pmatrix}. \tag{3.46b}$$

We note that the equation for φ is decoupled from A, which is a result of the linear homogeneous nature of the equations for Θ_1 and Λ_1.

The boundary conditions for φ are obtained from (3.37) at the nose and (3.44) at the physical origin, which give

$$\varphi = 0 \qquad \text{at} \qquad \zeta = 0, \tag{3.47a}$$

$$\varphi(\infty) \sim n\pi - \tan^{-1}\left(\left[\tfrac{2}{3}k\right]\zeta^4 + \left[k+\tfrac{8}{3}\right]\Theta_0\right) \qquad \text{as} \qquad \zeta \to \infty, \tag{3.47b}$$

where $n \in \{0, 1, 2, \dots\}$ can be used as the index of the different eigenmodes, which reveals another advantage of introducing polar perturbations.

Finally, to find the growth rates σ, we only need to integrate (3.46a) with boundary conditions (3.47), where the base state $\Theta_0(\zeta)$ is obtained by integrating

$$\Theta_0' = \left(\frac{16\zeta^3 + 3}{2\zeta^4 + 3\Theta_0}\right)\frac{\Theta_0}{2} \qquad \text{with} \qquad \lim_{\zeta\to 0}\left(\frac{\Theta_0}{\zeta}\right) = \tfrac{1}{2}. \tag{3.48}$$

If we want to recover the physical quantities H_i and Q_i, we simply use the relations (3.45) and (3.41), which requires both the radial scale X_0 and the amplitude A. Both X_0 and A can be found analytically: integrating (3.36a) gives

$$X_0(\zeta) = \exp\left(-\int_0^\zeta \frac{3s^3}{2s^4 + 3\Theta_0(s)}\,\mathrm{d}s\right), \tag{3.49}$$

and integrating (3.46b) gives

$$A(\zeta) = \delta \exp\left(\int\left[\begin{pmatrix}\sin\varphi\\ \cos\varphi\end{pmatrix}^{\mathsf{T}}\begin{pmatrix}\frac{\left(3+16\zeta^3\right)\zeta^4}{\left(2\zeta^4+3\Theta_0\right)^2} & (\sigma + k^2\zeta^3)\\ \frac{9\zeta^3}{\left(2\zeta^4+3\Theta_0\right)^2} & 0\end{pmatrix}\begin{pmatrix}\sin\varphi\\ \cos\varphi\end{pmatrix}\right]\mathrm{d}\zeta\right), \tag{3.50}$$

where δ is an arbitrary scale for the amplitude. Note that the integrand in (3.50) is non-singular even if $\tan\varphi = \infty$ and hence (3.50) can be numerically integrated without any issues.

A word of caution

In general, the use of a perturbation phase angle simplifies the numerics significantly as the index n appears directly in the boundary conditions, there is no arbitrary amplitude, and we only have to integrate a first order (though now nonlinear) differential equation instead of two coupled differential equations for the perturbations. However, there are cases where a particular choice of perturbation quantities might be almost, or even exactly, correlated such that their phase angle varies only negligibly. In that case, all the information is in the variation of the amplitude and using φ as the only dependent variable might be badly conditioned. This can happen even in simple linear systems with constant coefficients, and manifests itself by the approach of the angle φ to a step function.

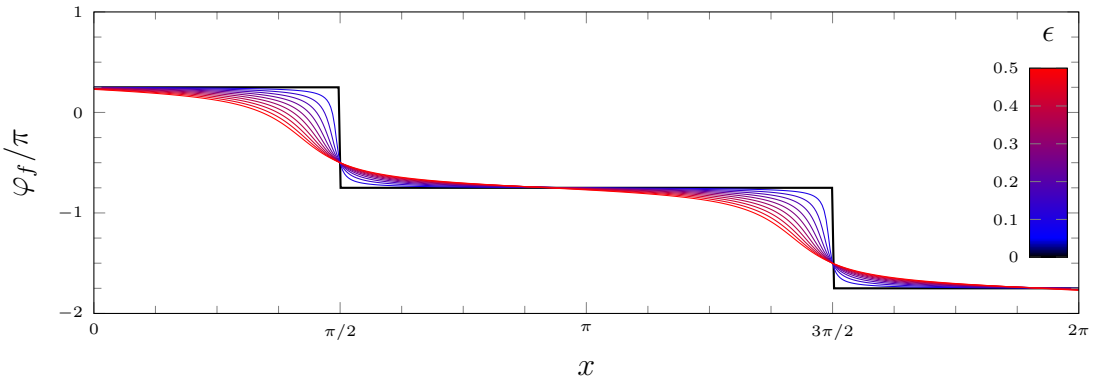

Fig. 3.2 Solutions to the model equation (3.51) in terms of the phase angle $\varphi_f(x)$ over the interval $x \in [0, 2\pi]$ for $x_0 = 0$ and a range of ϵ, showing that as $\epsilon \to 0$ the solutions approach a step function with $\tan\varphi_f = 1$.

For example, consider the simple system

$$\boldsymbol{f}'(x) = \begin{pmatrix} -\cot\epsilon & \csc\epsilon \\ -\csc\epsilon & \cot\epsilon \end{pmatrix} \cdot \boldsymbol{f}(x) \qquad \Rightarrow \qquad \boldsymbol{f}(x) \propto \begin{pmatrix} \cos(x - x_0) \\ \cos(x - x_0 + \epsilon) \end{pmatrix}$$
$$\Rightarrow \qquad \tan\varphi_f = \frac{\cos(x - x_0 + \epsilon)}{\cos(x - x_0)}, \tag{3.51}$$

where $\boldsymbol{f} : \mathbb{R} \to \mathbb{R}^2$ is a vector-valued function, $\epsilon \ll 1$ is a small positive constant and x_0 is an arbitrary constant of integration. Figure 3.2 shows the solution φ_f, where we have taken care to ensure continuity of φ_f by adding the correct multiples of π. This clearly shows that as $\epsilon \to 0$ the solutions approach a discontinuous step function with increasingly steep gradients near the 'steps'.

Having sounded a cautionary note, it turns out that the particular case of single-layer gravity currents does not suffer from this issue. We will confirm this retrospectively, by noting that the numerical solutions obtained are smooth with reasonable gradients.

3.4 Numerical solutions

In this section, we present numerical results for the stability of viscous gravity currents which we obtained using the scaling-invariant formalism derived above. We also include numerical results for the stability of porous-media gravity currents, which, as mentioned in the introduction, are governed by the more general porous-medium equation

$$\frac{\partial h}{\partial \tau} = \boldsymbol{\nabla} \cdot \left(h^\beta \boldsymbol{\nabla} h \right), \tag{3.52}$$

where β is a constant linked to the porosity and permeability structure of the porous medium. We generalise the problem in a second way, by considering currents with total volume V increasing in time as

$$V = \hat{\mathcal{Q}}_{\text{in}} t^{\alpha}, \tag{3.53}$$

where $\alpha > 0$ is a constant. For a detailed derivation of the resulting governing equations of a porous-media gravity current with a power-law volume using a scaling-invariant formalism as above, we refer to Appendix 3.A. We note one particular result given by the local behaviour at the nose

$$H_0, Q_0 \sim (1-\xi)^{1/\beta} \qquad \text{and} \qquad H_1, Q_1 \sim (1-\xi)^{1/\beta - 1} \qquad \text{as} \qquad \xi \to 1, \tag{3.54}$$

similar to (3.18) and (3.20). This indicates that the nose is non-singular for $\beta \leq 1$, with a linear base state and finite-valued perturbations for $\beta = 1$, and vanishing base state and perturbations for $\beta < 1$. Nonetheless, the scaling-invariant formalism including the use of phase angles and change of independent variable still provides a reduction in order and leads to numerically better conditioned equations especially near the origin.

There are several special cases of the parameters α and β which are of particular interest: firstly, we note that $\alpha = 1$ corresponds to a constant-flux current as analysed above, and that $\alpha = 0$ corresponds to a constant-volume current for which there is a closed-form analytic solution studied by Mathunjwa and Hogg (2006). Secondly, we note that $\beta = 3$ gives the same equation as for a viscous gravity current, and that $\beta = 1$ corresponds to a current in a homogeneous porous medium.

In the remainder of this section, and in particular in the figures 3.3 to 3.7, we will consider the cases of a viscous current ($\beta = 3$) and of a current in a homogeneous porous medium ($\beta = 1$), each time with a constant influx ($\alpha = 1$), as examples to illustrate the solutions.

Figure 3.3 shows numerical solutions for the base state contrasting the scaling-invariant variables and their physical counterparts. This highlights the bounded, non-singular nature of the transformed variables ζ/Θ_0 and X_0. The physical base-state variables on the other hand exhibit the expected logarithmic singularity of the height H_0 at the origin and also, in the case of $\beta = 3$, the cube-root singularity at the nose.

To confirm the validity of the solutions obtained numerically using the scaling-invariant formalism, we compare them to the base-state expansions (3.94) near the nose, which shows excellent agreement. For the case of $\beta = 3$, a further comparison

can be made by evaluating

$$\left(2\pi \int_0^1 H_0\, \xi \, \mathrm{d}\xi\right)^{-3/8} \approx 0.715, \tag{3.55}$$

which is the same as the value as obtained by Huppert (1982b) for the corresponding integral in the case of a constant-flux current ($\alpha = 1$), therefore supporting the validity of the numerical method.

Figure 3.4 shows the phase angles φ of the perturbations for the first three eigenmodes $n \in \{0, 1, 2\}$, clearly illustrating the relationship between the eigenmode index n and the number of revolutions by π in φ.

The corresponding physical perturbations H_1 and Q_1 are shown in figure 3.5. Here it can seen that the index n corresponds to the number of zeros in either H_1, or equivalently Q_1. As k increases the perturbations become more localised near the nose. At the nose the perturbations for $\beta = 3$ diverge as in (3.54), while the perturbations for $\beta = 1$ approach a constant, which has been chosen to be 1. Finally, as predicted by the expansions (3.24) and (3.25) at the origin, we note that the axisymmetric perturbations ($k = 0$) decay logarithmically instead of algebraically like ξ^k.

Figures 3.6 and 3.7 depict the growth rate σ for the first three eigenmodes $n \in \{0, 1, 2\}$ as a function of k and α, respectively. The perturbation modes become monotonically more stable with increasing n, k, or α. Physically, we note that more oscillatory behaviour, through larger k or larger n, decays quicker due to the diffusive spreading of the current, and larger α correspond to a thicker current again stabilising the flow. The overall least stable case is given by the fundamental mode $n = 0$ for an axisymmetric ($k = 0$) perturbation to a constant-volume current ($\alpha = 0$), which has growth rate $\sigma = 0$. Physically, this particular case corresponds to a small perturbation to the total volume, which does not decay (Mathunjwa and Hogg, 2006). All other perturbations are stable with negative growth rates $\sigma < 0$. We also note that the growth rate σ of the fundamental mode ($n = 0$) appears to be both linear in α and linear in k. In fact, based on the numerical results, it seems that $\sigma = -1 - k/2$ for $\alpha = 1$ and $\sigma = -\alpha$ for $k = 0$ are exact solutions for the growth rate. We confirm these results in the next section.

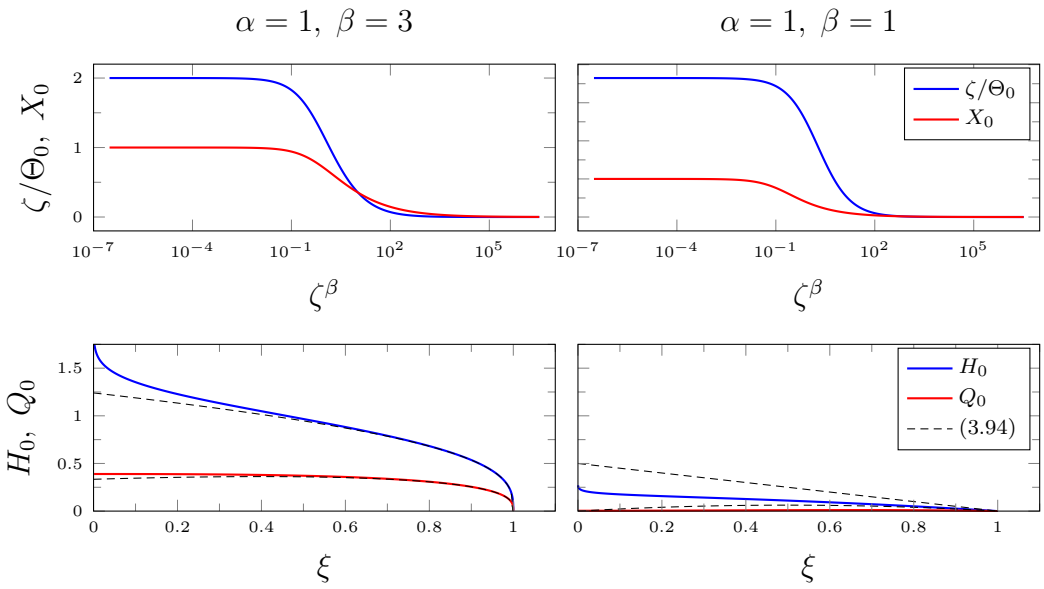

Fig. 3.3 Solution for the base state in terms of the scaling-invariant variables ζ/Θ_0 and $X_0 = \mathrm{e}^{\Lambda_0}$ as functions of ζ^β and the physical height H_0 and flux Q_0 as functions of ξ. There is good agreement with the local expansions (3.94) of the physical variables near the nose (dashed black).

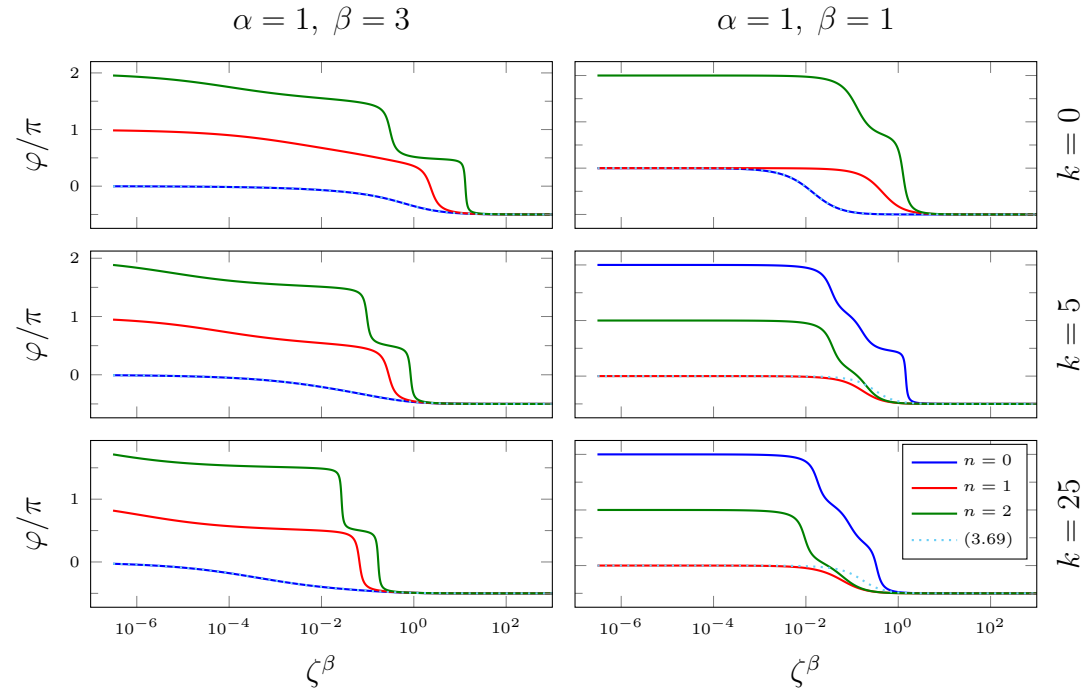

Fig. 3.4 The first three perturbation modes $n \in \{0, 1, 2\}$ in terms of the phase angle φ as a function of ζ^β for wavenumbers $k \in \{0, 5, 25\}$. The analytical solution (3.69) for the fundamental mode ($n = 0$) is indistinguishable from the numerical solution (dotted cyan).

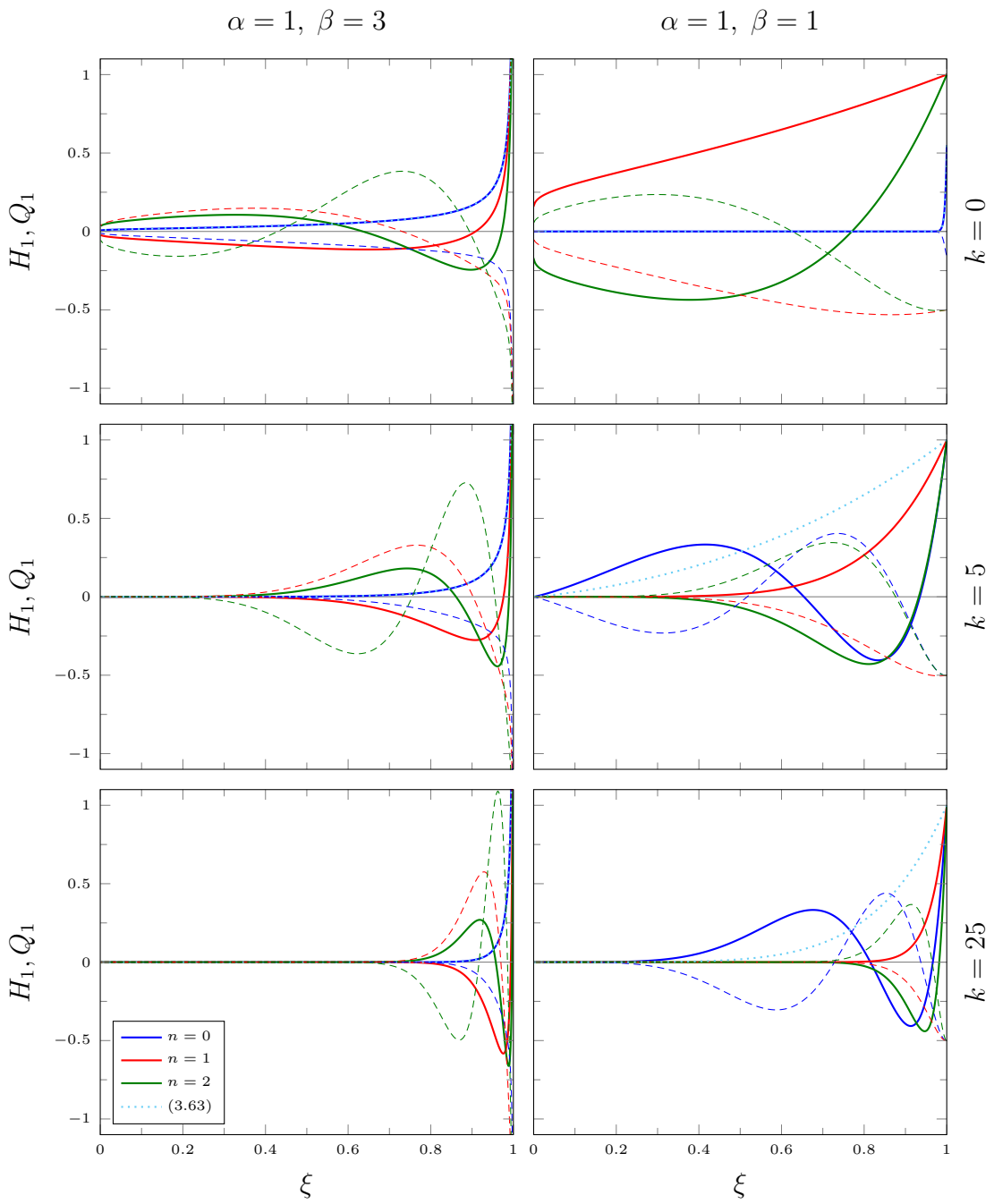

Fig. 3.5 The first three perturbation modes $n \in \{0, 1, 2\}$ in terms of the height perturbation H_1 (solid) and the flux perturbation Q_1 (dashed) as functions of the radial coordinate ξ for wavenumbers $k \in \{0, 5, 25\}$. The analytic solution (3.63) for the fundamental mode ($n = 0$) is indistinguishable from the numerical solution (dotted cyan).

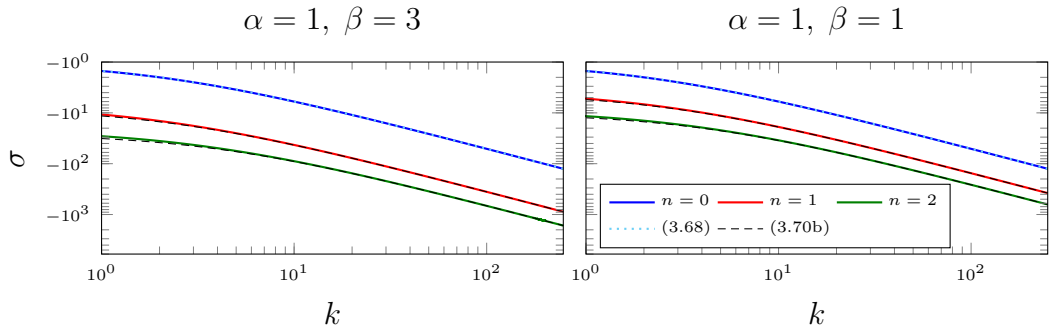

Fig. 3.6 The growth rates σ of the first three eigenmodes $n \in \{0, 1, 2\}$ as functions of the wavenumber k. The analytical solution (3.68) for the fundamental mode $n = 0$ is indistinguishable from the numerical result (dotted cyan), and the asymptotic solution (3.70b) for the large wavenumber k shows excellent agreement (dashed black).

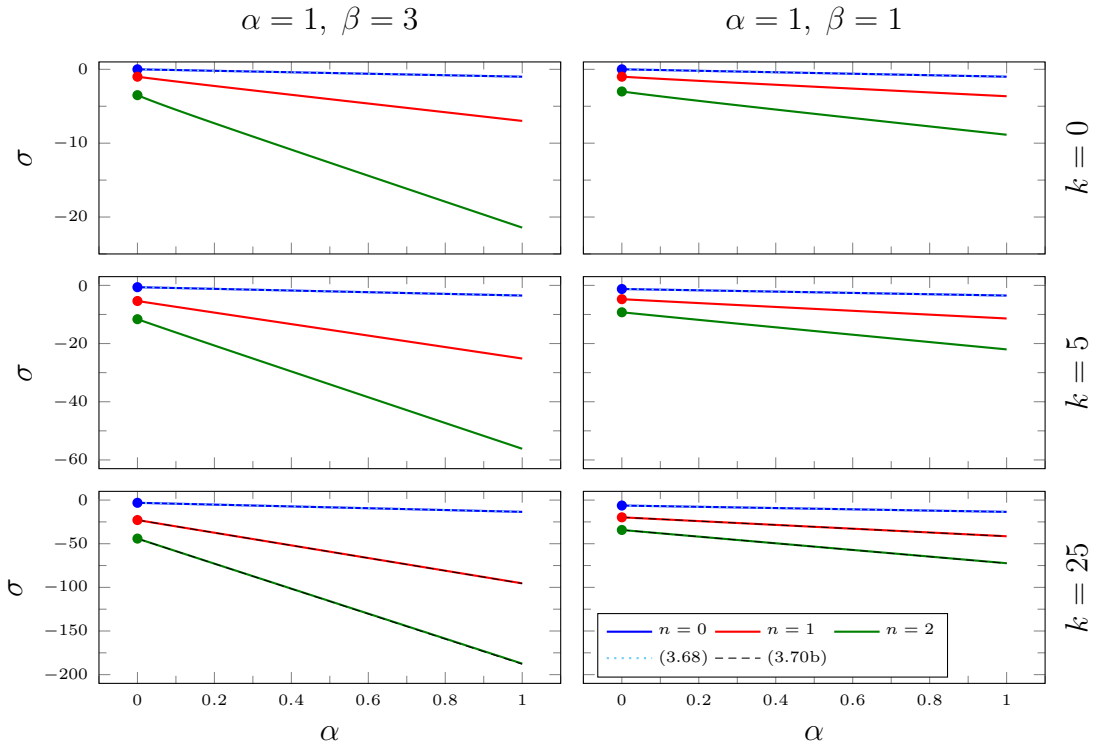

Fig. 3.7 The growth rates σ of the first three eigenmodes $n \in \{0, 1, 2\}$ as functions of the flux exponent α for wavenumbers $k \in \{0, 5, 25\}$. The analytical solution (3.68) for the fundamental mode $n = 0$ is indistinguishable from the numerical result (dotted cyan), and the asymptotic solution (3.70b) for the large wavenumber k shows excellent agreement for the case $k = 25$ (dashed black). Analytical results for $\alpha = 0$ obtained by Mathunjwa and Hogg (2006) are consistent (points).

3.5 Analytic results

3.5.1 The fundamental mode ($n = 0$)

We have just noted that the growth rate σ of the fundamental mode ($n = 0$) appears to be linearly related to both α and k. Motivated by this observation, we look for an analytic solution of the fundamental mode in terms of the base state variables H_0 and Q_0.

In Appendix 3.A we derive the governing equations (3.81) for a porous-media gravity current in terms of the physical variables and the corresponding boundary conditions. Expanding similar to (3.13) results in

$$H_0' = -\frac{Q_0}{H_0^\beta}, \qquad \frac{1}{\xi}\left(\xi Q_0\right)' = \gamma_h H_0 - \frac{\gamma_\xi \xi Q_0}{H_0^\beta}, \tag{3.56a,b}$$

for the base state,

$$H_1' = \left(\frac{\beta Q_0}{H_0^{1+\beta}}\right) H_1 - \frac{Q_1}{H_0^\beta}, \tag{3.56c}$$

$$\frac{1}{\xi}\left(\xi Q_1\right)' = \left(\{\gamma_h - \sigma\} - \frac{k^2 H_0^\beta}{\xi^2} + \frac{\beta\gamma_\xi \xi Q_0}{H_0^{1+\beta}}\right) H_1 - \left(\frac{\gamma_\xi}{H_0^\beta}\right) \xi Q_1, \tag{3.56d}$$

for the perturbations, and

$$\lim_{\xi\to 1} \frac{Q_1}{H_1} = \gamma_\xi, \qquad \lim_{\xi\to 0} \left(\xi Q_1\right) = 0, \tag{3.57}$$

for the boundary conditions, where γ_ξ and γ_h are constants defined in terms of α and β by

$$\gamma_\xi = \frac{1+\alpha\beta}{2(1+\beta)}, \qquad \gamma_h = \frac{1-\alpha}{1+\beta}. \tag{3.58}$$

For the case of a current in a porous medium, the radial similarity variable ξ and the dimensionless height h scale as

$$\xi \propto r t^{-\gamma_\xi}, \qquad h \propto \widehat{h} t^{\gamma_h}. \tag{3.59}$$

Shifting the temporal origin for a constant-flux current

For the case of a constant-flux current ($\alpha = 1$), we can consider shifting the temporal origin by $t \mapsto t + 2\delta$, where δ is a small constant and the factor 2 is for algebraic

convenience. As the flux is constant, and hence the total volume is given by $V = \hat{\mathcal{Q}}_{\text{in}} t$, this shift in temporal origin is equivalent to adding a small amount of extra fluid $V \mapsto V + 2\delta\hat{\mathcal{Q}}_{\text{in}}$. As time increases this extra fluid becomes insignificant compared to the additional fluid provided by the constant flux and therefore we expect the corresponding perturbation to be stable and decay.

Applying the shift of temporal origin to the radial similarity variable ξ, which scales like (3.59a) with $\gamma_\xi = 1/2$ as $\alpha = 1$, and expanding for small $\delta \ll 1$, yields a radial shift given by

$$\xi \mapsto \xi - \delta t^{-1}\xi + \cdots . \tag{3.60}$$

For a constant-flux current where $\alpha = 1$ such that $\gamma_h = 0$, (3.59b) shows that the height h has a constant scale in time. Similarly, we note from (3.56a) that ξq_ξ, which corresponds to the integrated flux through a cylinder of radius ξ, also has a constant scale in time. Therefore, a self-similar current with height $h = H_0(\xi)$ and flux $q_\xi = Q_0(\xi)$, when viewed in the new shifted temporal coordinate, is described by

$$h = H_0\left(\xi - \delta t^{-1}\xi + \cdots\right) \sim H_0(\xi) - \delta t^{-1}\xi H_0'(\xi) + \cdots , \tag{3.61a}$$

$$\xi q_\xi = (\xi Q_0)\left(\xi - \delta t^{-1}\xi + \cdots\right) \sim \xi Q_0(\xi) - \delta t^{-1}\xi\left(\xi Q_0\right)'(\xi) + \cdots . \tag{3.61b}$$

This can be interpreted as a perturbation to the base state $H_0(\xi)$ and $Q_0(\xi)$ given by

$$H_1 = -\xi H_0' = \frac{\xi Q_0}{H_0^\beta}, \qquad\qquad Q_1 = -\left(\xi Q_0\right)' = \frac{\xi}{2} H_1. \tag{3.62}$$

We note that the resulting perturbation flux Q_1 corresponds to the flux of a current with height H_1 moving at velocity $\xi/2$ associated with the time-dependence of the radial similarity coordinate ξ. From (3.61), we see that the perturbations (3.62) decay like $\mathrm{e}^{-\tau} \propto t^{-1}$, which corresponds to a growth rate given by $\sigma = -1$.

It can be easily checked that (3.62) with $\sigma = -1$ indeed satisfy the equations (3.56) and the boundary conditions (3.57).

Extension to non-axisymmetric perturbations for constant flux

We note the resemblance of the analytical solution (3.61a) to the expansion (3.25a) near the origin for the axisymmetric perturbation ($k = 0$). Motivated by this similarity, we look at the expansion (3.24) near the origin in the more general, non-axisymmetric

case ($k > 0$). We therefore propose the perturbation height

$$H_1 = \frac{\xi^{1+k} Q_0}{H_0^\beta}. \tag{3.63}$$

We note that the additional factor ξ^k appears similar to cylindrical harmonics without any vertical variation. We then substitute (3.63) and its derivative into (3.56c) and eliminate any base state derivatives H_0' and Q_0' by using (3.56a,b). After some algebra this results in the perturbation flux

$$Q_1 = \frac{\xi^{2+k} Q_0}{2H_0^\beta} - k\xi^k Q_0 = \left(\frac{\xi}{2} - \frac{kH_0^\beta}{\xi}\right) H_1. \tag{3.64}$$

We again recognise the term $\xi H_1/2$ as corresponding the the flux associated with a current of height H_1 flowing at the radial velocity associated with the time-dependence of the radial similarity coordinate ξ. To interpret the second term, we consider the azimuthal flux, which, in the case of a porous-media gravity current, is given by

$$q_\theta = -\frac{1}{\xi} h^\beta \frac{\partial h}{\partial \theta} = -\frac{\mathrm{i}kH_0^\beta H_1}{\xi} \mathrm{e}^{\mathrm{i}k+\sigma\tau} + \cdots. \tag{3.65}$$

Therefore, the second term in (3.64) has the same magnitude as the azimuthal flux and a phase shift of $\pi/2$. This leads to a flow pattern with k lines of inflow and k lines of outflow somewhat resembling a cobweb, especially for $k \geq 3$. In figure 3.8, these patterns are illustrated in plan view for wavenumbers $k \in \{1, 2, 3\}$.

In order to calculate the growth rate associated with these perturbations, we substitute (3.63) and (3.64) together with its derivative into (3.56d) and use (3.56a,b) to eliminate the base-state derivatives as before. After extensive algebra this results in the growth rate

$$\sigma = -1 - \tfrac{1}{2}k. \tag{3.66}$$

Again, it can be easily checked that (3.63) and (3.64) satisfy and the boundary conditions (3.57). Therefore, (3.63) and (3.64) together with (3.66) present an analytic solution for both the perturbation height H_1 and the perturbation flux Q_1 in terms of the base-state variables H_0 and Q_0 for the fundamental mode ($n = 0$) of a constant-flux current ($\alpha = 1$).

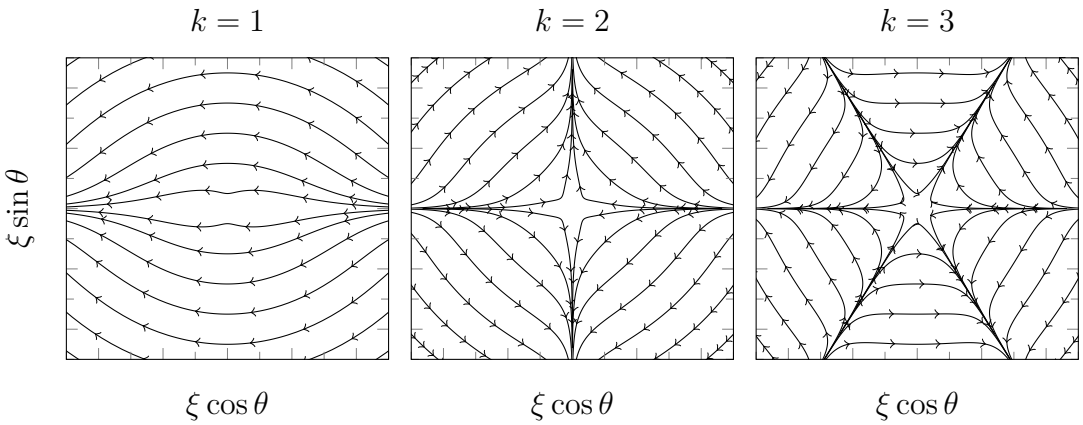

Fig. 3.8 The flow patterns in plan view corresponding to a flux with radial and azimuthal components of equal magnitude (not shown) and a phase shift of $\pi/2$, for the wavenumbers $k \in \{1, 2, 3\}$. This illustrates the non-axisymmetric component of the analytical solution for the fundamental mode (3.64).

The general fundamental mode

Somewhat surprisingly, we find that a relationship between Q_1 and H_1 similar to (3.64), given by

$$Q_1 = \left(\gamma_\xi \xi - \frac{k H_0^\beta}{\xi}\right) H_1, \tag{3.67}$$

is an analytic first integral for all possible values of α, not just for the constant-flux case $\alpha = 1$. We confirm this by substituting (3.67) and its derivative into (3.56d) using (3.56a-c) to eliminate both the base-state derivatives and H_1'. This, after extensive algebra, also results in the associated growth rate given by

$$\sigma = \underbrace{(\gamma_h - 2\gamma_\xi)}_{-\alpha} - \gamma_\xi k. \tag{3.68}$$

Physically, the first integral (3.67) has the same interpretation as before, i.e. a superposition of a current with height H_1 flowing at the coordinate velocity $\gamma_\xi \xi$ and of the same non-axisymmetric flow illustrated in figure 3.8.

In contrast to the constant-flux case ($\alpha = 1$), there is no analytic second integral to obtain the perturbation height H_1 and flux Q_1 in terms of the base-state variables H_0 and Q_0 only. Nonetheless, we could derive the growth rate (3.68) for the fundamental mode for all possible values of α.

For the purpose of comparing to the numerical results, we rephrase (3.68) in terms of the scaling-invariant perturbations by using equation (3.88) derived in Appendix 3.A. This gives

$$\tan\varphi = \frac{\Theta_1}{\Lambda_1} = \frac{\Theta_0'}{\Lambda_0'} - \frac{\gamma_\xi - k\zeta^\beta}{\Lambda_0'} = \left(\gamma_h + \frac{2\gamma_\xi}{\beta}\right)\zeta - \frac{k}{\beta}\left(2\zeta^{1+\beta} + \beta\Theta_0\right) - \left(2 + \frac{2}{\beta}\right)\Theta_0. \quad (3.69)$$

Comparing the analytical solution for the eigenmode profiles, both in terms of physical variables (3.63) and scaling-invariant variables (3.69), with the numerical profiles shows excellent agreement, see figures 3.4 and 3.5. Similarly, the analytic solution for the growth rate (3.68) is also in excellent agreement with the numerically computed growth rates. And finally, the analytic solution for $\alpha = 0$ obtained by Mathunjwa and Hogg (2006) gives the same result for the fundamental mode $n = 0$ (see Appendix 3.C for more details).

To summarise, we have found an analytic first integral (3.64) for the fundamental mode ($n = 0$) and its growth rate σ given by (3.68), which confirmed the numerical results that $\sigma \leq 0$ for $n = 0$. As seen in the numerics, the only case with zero growth rate $\sigma = 0$ is the case of axisymmetrically ($k = 0$) perturbing the total volume of a constant-volume current ($\alpha = 0$). In all other cases the analytic solution confirms that the fundamental mode is linearly stable with a negative growth rate $\sigma < 0$. Given the numerical results indicate that the fundamental mode is always the least stable mode, the analytic solution (3.64) with growth rate (3.68) implies that all gravity currents with volume $V \propto t^\alpha$, spreading within a porous medium with porosity and permeability (3.71), are stable for all parameters.

3.5.2 Stability of advancing fronts within the porous-medium equation — large wavenumber ($k \gg 1$)

A second case which we can solve analytically is the limit of large azimuthal wavenumber $k \to \infty$. As the wavenumber increases, the length scale of the perturbations in the azimuthal direction becomes small and, as a result, the perturbation becomes increasingly confined to a region near the nose. This was seen in the numerical results in §3.4.

As the perturbations for large k are confined to near the nose, they are no longer influenced by the radial geometry of the current, and therefore the asymptotic analysis

for large k is equivalent to a stability analysis of a generic advancing contact line within the framework of lubrication theory. This gives a good motivation to pursue the somewhat cumbersome algebra involved in finding an asymptotic solution for $k \to \infty$. The details of this analysis are given in Appendix 3.B. The final result is

$$H_1 \sim \delta \xi^k H_0^{1-\beta} \left\{ \mathrm{L}_n^{(\gamma_0)} \left(2k[1-\xi] \right) + \cdots \right\}, \tag{3.70a}$$

$$\sigma \sim -\gamma_\xi (1+2n\beta)k - \alpha - \frac{(1+2\alpha\beta)(1+n\beta)n}{1+\beta} + \cdots < 0, \tag{3.70b}$$

where δ is the perturbation amplitude, $\gamma_0 = 1/\beta - 1$ and $\mathrm{L}_n^{\gamma_0}$ is a generalised Laguerre polynomial. This asymptotic solution agrees very well with the numerical result, as seen in terms of the growth rate σ in figure 3.6. Comparing to the analytic result of Mathunjwa and Hogg (2006) for $\alpha = 0$ further confirms these asymptotic results (see Appendix 3.C for more details).

We conclude that an advancing front of a gravity current within a porous medium is stable to local perturbations of length scale k^{-1} with a growth rate scaling as $\sigma = O(k)$. Therefore, any perturbation on a small length scale such as, for example, the pore size, is negligible as hoped. As the equations describing viscous gravity currents mathematically are a special case of the equations describing gravity currents in a porous medium, the same stability result holds for advancing contact lines of viscous gravity currents.

3.6 Discussion & Conclusions

In this chapter, we have first re-derived equations governing the evolution of viscous gravity currents with constant influx (Huppert, 1982b), which we then used as an illustrative example to motivate rescaled variables. These new variables were found exploiting a scaling-invariance of the governing equations and overall led to a reduction in order from four to three. This extends the phase-plane formalism of Gratton and Minotti (1990), who analysed the self-similar base state only, to fully time-dependent systems including linear perturbation analyses. Furthermore, this change of variables meant that we could avoid perturbing the singular nose, which in the usual approach results in diverging perturbations at the nose with associated numerical issues. The new variables avoid these singularities altogether and were shown to have well-behaved Taylor series near the nose.

A further change of variables from Cartesian perturbations to polar perturbations allowed us to eliminate the arbitrary degree of freedom associated with the perturbation

amplitude, and meant that the index of the eigenmodes n appeared explicitly in the boundary conditions for the perturbation angle φ. Additionally, this corresponds to a further decrease in the order of the equations from three to two.

We extended this to currents governed by the porous-medium equation, introducing two new parameters: an exponent α associated with a power-law increase in total volume $V \propto t^\alpha$, and an exponent β associated with the properties of the porous medium (Mathunjwa and Hogg, 2006). The equations for viscous gravity currents are included as a special case with $\beta = 3$. In Appendix 3.A, we derived numerically well-suited equations by using equivalent variable rescalings as motivated by the example of the viscous gravity current. These were then easily solved using AUTO, a continuation and bifurcation software package. Comparing the numerically calculated base state to analytic expansions near the nose, and to the viscous gravity current as in Huppert (1982b), showed excellent agreement making us confident that the change of variables and the numerical implementation indeed resulted in the correct solutions.

For the perturbations, we found an analytic first integral and its associated growth rate σ, which we determined to correspond to the fundamental mode $n = 0$ and was shown to be stable, i.e. $\sigma < 0$, except for the particular case of perturbing the total volume of a constant-volume current ($\alpha = 0$ and $k = 0$) where $\sigma = 0$. We argued that the fundamental mode should be the least stable mode and hence we concluded that all viscous gravity currents in porous media are stable. Furthermore, we also computed asymptotics for large wavenumber $k \to \infty$ showing that $\sigma = O(k)$, which were effectively local travelling waves at the nose governed by the local behaviour of the base state at the nose and turned out to be stable for all parameters.

Comparison between the numerical solutions, the analytical solution for the fundamental mode $n = 0$, and the asymptotics for large wavenumber $k \to \infty$, all agreed excellently, further confirming the validity of our numerical method. In particular, the numerical solutions confirm that the fundamental mode is the least stable one and therefore that indeed viscous gravity currents in porous media are stable for all parameters. In general, the flow is more stable as the influx increases faster, i.e. for larger α, and similarly the flow is more stable to perturbations with large wavenumber k.

Finally, we compared our results to the analytical results of Mathunjwa and Hogg (2006) for the case of a constant-volume current ($\alpha = 0$), again showing excellent agreement, both with respect to the numerical results and the large-k asymptotics.

We conclude that viscous gravity currents in porous media with a volume $V \propto t^\alpha$ are stable for all parameters as long as the current remains long and thin. Furthermore,

we conclude that using scaling-invariant variables and polar perturbation variables to analyse these viscous gravity currents avoids the singular behaviour at the nose and involves the index of the eigenmode explicitly in the boundary conditions, thereby significantly simplifying the numerical analysis.

Appendix 3.A Porous-media gravity currents

3.A.1 Model description

We consider a gravity current spreading in a porous medium over an impermeable horizontal boundary. The porous medium is initially saturated with a fluid of density ρ and viscosity μ. A second, heavier fluid of density $\rho + \Delta\rho$ and viscosity μ is then injected at a volumetric rate of $\alpha\hat{\mathcal{Q}}_{\rm in}t^{\alpha-1}$ such that the total volume of injected fluid at time t is given by $V = \hat{\mathcal{Q}}_{\rm in}t^{\alpha}$. As for the viscous gravity current, we define the height $\widehat{h}(r,\theta,t)$ of the spreading current in polar coordinates and its radial extent $r_*(\theta,t)$, see figure 3.1.

The main difference is that we need to specify the properties of the porous medium. For this we assume that the porosity ϕ is homogeneous in the horizontal directions and that both the porosity $\phi(z)$ and the permeability $\kappa(\phi)$ are given by power laws in terms of the height z and the porosity ϕ respectively:

$$\phi(z) = \phi_0 z^{\beta_\phi}, \qquad\qquad \kappa(\phi) = \kappa_0\phi^{\beta_\kappa}, \tag{3.71}$$

where ϕ_0, κ_0 and $\beta_{\phi,\kappa}$ are constants. In particular, this includes the case of a linearly varying porosity if $\beta_\phi = 1$ and the case of a homogeneous porous medium if $\beta_\phi = 0$. For porous rock, typical values of the permeability exponent β_κ fall in the range $2 \leq \beta_\kappa \leq 10$ (Dullien, 1992; Fowler, 1997).

Equation (3.2) for lubrication flow applicable in §3.2 is now replaced by Darcy's law for a slow moving flow in a porous medium. For a long and thin current this still gives a hydrostatic pressure. Hence, the horizontal Darcy velocity (i.e. the discharge velocity) $\widehat{\boldsymbol{u}}$, which is proportional to the horizontal pressure gradient $\boldsymbol{\nabla}\widehat{p}$, is given by

$$\widehat{\boldsymbol{u}} = -\frac{\kappa}{\mu}\boldsymbol{\nabla}\widehat{p} = -\frac{\Delta\rho g\kappa}{\mu}\boldsymbol{\nabla}\widehat{h} = -\frac{\Delta\rho g\kappa_0\phi_0^{\beta_\kappa}}{\mu}z^{\beta_\kappa\beta_\phi}\boldsymbol{\nabla}\widehat{h}. \tag{3.72}$$

Integrating this velocity profile $\widehat{\boldsymbol{u}}$ gives the flux of fluid

$$\widehat{\boldsymbol{q}} = \int_0^{\widehat{h}} \widehat{\boldsymbol{u}}\,\mathrm{d}z = -\frac{\Delta\rho g\kappa_0\phi_0^{\beta_\kappa}}{(\beta_\kappa\beta_\phi+1)\,\mu}\widehat{h}^{\beta_\kappa\beta_\phi+1}\boldsymbol{\nabla}\widehat{h}, \tag{3.73}$$

which gives an evolution equation for the height h by considering local mass conservation in a porous medium

$$\phi\big(\widehat{h}\big)\frac{\partial\widehat{h}}{\partial t} + \boldsymbol{\nabla}\cdot\widehat{\boldsymbol{q}} = 0. \tag{3.74}$$

Introducing the variable $\bar{h}(r,\theta,t) = \phi\big(\widehat{h}\big)\widehat{h} = \phi_0\widehat{h}^{\beta_\phi+1}$ and some algebra results in the well-known porous-medium equation

$$\frac{\partial\bar{h}}{\partial t} = \mathcal{D}\boldsymbol{\nabla}\cdot\left(\bar{h}^\beta\boldsymbol{\nabla}\bar{h}\right), \tag{3.75}$$

where we introduced two constants

$$\mathcal{D} = \left(\frac{\Delta\rho g\kappa_0}{(\beta_\kappa\beta_\phi+1)\,\mu}\right)\phi_0^{\frac{\beta_\kappa-2}{\beta_\phi+1}}, \qquad \beta = \frac{1-(1-\beta_\kappa)\,\beta_\phi}{1+\beta_\phi}. \tag{3.76}$$

Equation (3.75) is a nonlinear diffusion equation with diffusivity $\mathcal{D}\bar{h}^\beta$. In particular, we recognise that if $\beta_\phi = 0$, i.e. $\beta = 1$, we recover the porous-medium equation for a homogeneous medium (Lyle et al., 2005). If $\beta = 3$ the equation is equivalent to equation (3.4) for a viscous gravity current. The porous-medium equation (3.75) can also be applied, for example, as a nonlinear heat conduction equation to radiative heat transport in a fully ionized gas ($\beta = 13/2$) or to electron heat conduction in a plasma ($\beta = 5/2$), and many other physical systems (Vázquez, 2007).

The boundary conditions are given by a global mass conservation integral

$$\int_0^{2\pi}\int_0^{r_*}\bar{h}\,r\,\mathrm{d}r\,\mathrm{d}\theta = \hat{\mathcal{Q}}_{\mathrm{in}}t^\alpha, \tag{3.77}$$

and a nose at $r = r_*$ defined by a vanishing height $\bar{h}_* = \bar{h}\,(r_*) = 0$ with velocity given as a limit by mass conservation at the nose

$$(\boldsymbol{n}\cdot\boldsymbol{e}_r)\,\frac{\partial r_*}{\partial t} = \lim_{\bar{h}\to 0}\left(\frac{\boldsymbol{n}\cdot\widehat{\boldsymbol{q}}}{\bar{h}}\right) \qquad \text{with flux} \qquad \widehat{\boldsymbol{q}} = -\mathcal{D}\bar{h}^\beta\boldsymbol{\nabla}\bar{h}. \tag{3.78}$$

3.A.2 Self-similar spreading and linear perturbations

There exists a well-known similarity solution to (3.75) with boundary conditions (3.77) and (3.78), similar to the fully analytical Barenblatt–Pattle solution in the case of constant-volume currents. A scaling analysis of these equations reveals that appropriate similarity variables can be defined by

$$\xi = \left(\hat{\mathcal{Q}}_{\rm in}^{\beta}\mathcal{D}\right)^{-\frac{1}{2(1+\beta)}} rt^{-\gamma_\xi} \qquad \text{where} \qquad \gamma_\xi = \frac{1+\alpha\beta}{2(1+\beta)}, \tag{3.79a}$$

$$h(\xi,\theta,\tau) = \left(\frac{\mathcal{D}}{\hat{\mathcal{Q}}_{\rm in}}\right)^{\frac{1}{1+\beta}} \bar{h}t^{\gamma_h} \qquad \text{where} \qquad \gamma_h = \frac{1-\alpha}{1+\beta}, \tag{3.79b}$$

and we define $\tau = \log(t/\hat{t})$ as in §3.2 and again write $\xi_*(\theta,\tau) = \xi(r_*,\theta,\tau)$ for the dimensionless radial extent in similarity space. To ensure that the approximation of a long and thin current is satisfied at late times, i.e. that ultimately $r_* \gg \hat{h} \propto \bar{h}^{1/(\beta_\phi+1)}$, we need to have $\gamma_h/(\beta_\phi+1) < \gamma_\xi$ so that the radial extent grows faster than the height. This restricts the possible choices of α for given β_ϕ and β_κ, but otherwise has no impact on the further analysis.

With these definitions (3.79), equation (3.75) becomes

$$\frac{\partial h}{\partial\tau} - \gamma_h h - \gamma_\xi\xi\frac{\partial h}{\partial\xi} = -\boldsymbol{\nabla}\cdot\boldsymbol{q} \qquad \text{with dimensionless flux} \qquad \boldsymbol{q} = -h^\beta\boldsymbol{\nabla}h, \tag{3.80}$$

where the horizontal gradient operator $\boldsymbol{\nabla}$ now applies to similarity space. As before, we then write $\boldsymbol{q} = (q_\xi, q_\theta)$ for the radial and azimuthal components of the flux giving

$$\frac{\partial h}{\partial\xi} = -\frac{q_\xi}{h^\beta}, \tag{3.81a}$$

$$\frac{1}{\xi}\frac{\partial(\xi q_\xi)}{\partial\xi} = \gamma_h h - \frac{\partial h}{\partial\tau} - \gamma_\xi\frac{\xi q_\xi}{h^\beta} + \frac{1}{(1+\beta)\xi^2}\frac{\partial^2 h^{1+\beta}}{\partial\theta^2}, \tag{3.81b}$$

$$\left(q_\theta = -\frac{1}{\xi}h^\beta\frac{\partial h}{\partial\theta}\right). \tag{3.81c}$$

The boundary conditions are given in terms of the self-similar variables by

$$h = 0 \qquad \text{at} \qquad \xi = \xi_*, \tag{3.82a}$$

$$(\boldsymbol{n}\cdot\boldsymbol{e}_r)\left(\frac{\partial\xi_*}{\partial\tau} + \gamma_\xi\xi_*\right) = \lim_{h\to0}\left(\frac{\boldsymbol{n}\cdot\boldsymbol{q}}{h}\right), \tag{3.82b}$$

$$\int_0^{2\pi}\int_0^{\xi_*} h\,\xi\,\mathrm{d}\xi\,\mathrm{d}\theta = 1. \tag{3.82c}$$

Equivalent to our discussion before, we could rescale the variables to shift the nose position to $\xi_* = 1$ at the expence of introducing a coefficient $\mathcal{Q}_{\text{in}}$ on the right-hand side of (3.82c).

Similar to (3.27), we introduce scaling-invariant flux and height variables, ϑ and ζ respectively, which are now given by

$$\vartheta = \frac{q_\xi}{\xi^{1+2/\beta}}, \qquad\qquad \zeta = \frac{h}{\xi^{2/\beta}}. \tag{3.83}$$

We then eliminate h and q_ξ in favour of their scaling-invariant counterparts and transform to ζ as the independent variable using the transformation laws (3.32). After some extensive algebra, we obtain

$$\frac{\partial\vartheta}{\partial\zeta} = \left(\frac{\left\{2(1+\beta)\zeta^\beta + \beta\gamma_\xi\right\}\vartheta - \beta\gamma_h\zeta^{1+\beta}}{2\zeta^{1+\beta} + \beta\vartheta}\right) + \frac{\partial\log\xi}{\partial\tau} - \zeta^\beta\frac{\partial^2\log\xi}{\partial\theta^2} + \cdots, \tag{3.84a}$$

$$\frac{\partial\log\xi}{\partial\zeta} = \frac{-\beta\zeta^\beta}{2\zeta^{1+\beta} + \beta\vartheta}, \tag{3.84b}$$

where the dots represent terms which are quadratic in $\partial\log\xi/\partial\theta$ and hence negligible when linearly perturbing an axisymmetric base state.

We expand similarly to (3.35) and introduce the perturbation angle $\tan\varphi = \Theta_1/\Lambda_1$ as before, which gives

$$\varphi' = \begin{pmatrix}\cos\varphi\\ -\sin\varphi\end{pmatrix}\cdot\begin{pmatrix}\frac{\left(4(1+\beta)\zeta^\beta+\beta\right)\zeta^{1+\beta}}{\left(2\zeta^{1+\beta}+\beta\Theta_0\right)^2} & \sigma + k^2\zeta^\beta\\ \frac{\beta^2\zeta^\beta}{\left(2\zeta^{1+\beta}+\beta\Theta_0\right)^2} & 0\end{pmatrix}\cdot\begin{pmatrix}\sin\varphi\\ \cos\varphi\end{pmatrix}, \tag{3.85}$$

where $\Theta_0(\zeta)$ satisfies

$$\Theta_0' = \frac{\left\{2(1+\beta)\zeta^\beta + \beta\gamma_\xi\right\}\Theta_0 - \beta\gamma_h\zeta^{1+\beta}}{2\zeta^{1+\beta} + \beta\Theta_0}. \tag{3.86}$$

The boundary conditions are derived similarly to (3.37) at the nose and (3.44) at the origin and are given by

$$\lim_{\zeta\to0}\left(\frac{\Theta_0}{\zeta}\right) = \gamma_\xi, \qquad\qquad \varphi(0) = 0, \tag{3.87a,b}$$

$$\varphi \sim n\pi - \tan^{-1}\left(\underbrace{\left\{2+\frac{2}{\beta}\right\}\Theta_0 + \frac{k}{\beta}\left\{2\zeta^{1+\beta}+\beta\Theta_0\right\}}_{O\left(\zeta^{1+\beta}\right)} - \underbrace{\gamma_h\zeta+\cdots}_{O(\zeta)}\right) \quad \text{as} \quad \zeta\to\infty. \tag{3.87c}$$

Similarly to (3.41), the physical heights H_0, H_1 and fluxes Q_0, Q_1 are given by

$$h(\xi,\theta,\tau) \sim \left[\underbrace{\xi^{2/\beta}z}_{H_0} - \underbrace{\xi^{2/\beta}\frac{\Lambda_1(z)}{\Lambda_0'(z)}}_{H_1}\mathrm{e}^{\mathrm{i}k\theta+\sigma\tau}+\cdots\right]_{z=X_0^{-1}(\xi)}, \tag{3.88a}$$

$$q_\xi(\xi,\theta,\tau) \sim \left[\underbrace{\xi^{1+2/\beta}\Theta_0(z)}_{Q_0} + \underbrace{\xi^{1+2/\beta}\left(\Theta_1(z)-\Theta_0'(z)\frac{\Lambda_1(z)}{\Lambda_0'(z)}\right)}_{Q_1}\mathrm{e}^{\mathrm{i}k\theta+\sigma\tau}+\cdots\right]_{z=X_0^{-1}(\xi)}, \tag{3.88b}$$

where the radial scale $X_0(\zeta)$ is given similarly to (3.49) by

$$X_0(\zeta) = \mathrm{e}^{\Lambda_0} = \exp\left(-\int_0^\zeta \frac{\beta s^\beta}{2s^{1+\beta}+\beta\Theta_0(s)}\,\mathrm{d}s\right), \tag{3.89}$$

and the perturbation amplitude $A(\zeta)$ similarly to (3.50) by

$$A(\zeta) = \delta\exp\left(\int\left[\begin{pmatrix}\sin\varphi\\ \cos\varphi\end{pmatrix}\cdot\begin{pmatrix}\frac{\left(4(1+\beta)\zeta^\beta+\beta\right)\zeta^{1+\beta}}{\left(2\zeta^{1+\beta}+\beta\Theta_0\right)^2} & \left(\sigma+k^2\zeta^\beta\right)\\ \frac{\beta^2\zeta^\beta}{\left(2\zeta^{1+\beta}+\beta\Theta_0\right)^2} & 0\end{pmatrix}\cdot\begin{pmatrix}\sin\varphi\\ \cos\varphi\end{pmatrix}\right]\mathrm{d}\zeta\right), \tag{3.90}$$

with arbitrary perturbation amplitude δ.

Appendix 3.B Asymptotic limit of large wavenumber ($k \gg 1$)

For ease of interpreting the results, we will consider physical perturbation quantities in this appendix. It is advantageous to work with a single dependent variable only, and hence we solve (3.56c) for the perturbation flux Q_1 giving

$$Q_1 = \left(\frac{\beta Q_0}{H_0}\right)H_1 - H_0^\beta H_1', \tag{3.91}$$

which we then use to eliminate Q_1 in (3.56d). This results in a second-order differential equation for the perturbation height H_1 only:

$$H_1'' + \left(\frac{1}{\xi} + \frac{\gamma_\xi \xi}{H_0^\beta} + 2\beta\frac{H_0'}{H_0}\right) H_1' + \left(\frac{\gamma_h - \sigma}{H_0^\beta} - \frac{k^2}{\xi^2} + \beta\frac{H_0'}{H_0}\left[\frac{(\xi Q_0)'}{\xi Q_0} - \frac{H_0'}{H_0}\right]\right) H_1 = 0. \tag{3.92}$$

The appropriate behaviours at the boundaries are found similarly to (3.20a) near the nose and (3.24a) near the origin, and are given by

$$H_1 \sim c_1 H_0^{1-\beta} \qquad \text{as} \qquad \xi \to 1, \tag{3.93a}$$

$$H_1 \sim c_2 \frac{\xi Q_0}{H_0^\beta} \xi^k \qquad \text{as} \qquad \xi \to 0, \tag{3.93b}$$

where $c_{1,2}$ are arbitrary multiplicative constants related to the amplitude δ, and related to each other via a nonlinear integration across the interior domain $0 < \xi < 1$.

For large azimuthal wavenumber, $k \gg 1$, we expect the perturbations to be confined to a region near the nose of radial extent $O(1/k)$, provided that the order n is not too large. This warrants the introduction of a local variable η which we define by $\xi = 1 - \eta/2/k$.

Then, as we are considering the perturbation equations locally to the nose, all that matters is the expansion of the base state near the nose and not the full solution of the base state. This expansion is obtained similarly to (3.18), and in terms of the local variable η it is given by

$$H_0 \sim \left(\frac{\gamma_\xi \beta \eta}{2k}\right)^{1/\beta} \left(1 - \frac{(1-\alpha\beta)\eta}{4\beta(1+\alpha\beta)k} + O\left(k^{-2}\right)\right), \tag{3.94a}$$

$$\xi Q_0 \sim \left(\frac{\gamma_\xi \beta \eta}{2k}\right)^{1/\beta} \left(\gamma_\xi - \frac{(1+4\beta-\alpha\beta)\eta}{8\beta(1+\beta)k} + O\left(k^{-2}\right)\right). \tag{3.94b}$$

We then expand H_1 and σ in powers of k

$$H_1 = \xi^k H_0^{1-\beta} \sum_{i=0}^{\infty} f_i(\eta) k^{-i}, \qquad\qquad \sigma = \sum_{i=0}^{\infty} \sigma_i k^{1-i}, \tag{3.95}$$

where without loss of generality the amplitude of H_1 was chosen to be $O(1)$, while it turns out that $\sigma = O(k)$ is the correct scaling for the growth rate. The pre-factor $\xi^k H_0^{1-\beta}$ was chosen to simplify the analysis and can be motivated by the behaviour at

the two boundaries, (3.93). We note that locally this pre-factor is given by

$$\xi^k H_0^{1-\beta} \sim \left(1-\frac{\eta}{2k}\right)^k \left(\frac{2k}{\gamma_\xi \beta \eta}\right)^{1-1/\beta} \sim \mathrm{e}^{-\eta/2} \left(\frac{2k}{\gamma_\xi \beta \eta}\right)^{1-1/\beta} \quad \text{as} \quad k \to \infty. \tag{3.96}$$

3.B.1 Leading order solution: f_0 and σ_0

First, to simplify the algebra, we write

$$\sigma_0 = -\gamma_\xi(1+2n\beta), \tag{3.97}$$

where we will show that n has to be a non-negative integer corresponding to the index of the perturbation.

For f_0 we obtain a second order linear homogeneous differential equation

$$\eta f_0'' + \left(\frac{1}{\beta} - \eta\right) f_0' + n f_0 = 0. \tag{3.98}$$

This can be recognised as Kummer's equation which has two linearly independent solutions given for $\beta \neq 1$ in terms of generalised Laguerre polynomials:

$$f_0 = c_1 \, \mathrm{L}_n^{(\gamma_0)}(\eta) + c_2 \eta^{-\gamma_0} \, \mathrm{L}_{n+\gamma_0}^{(-\gamma_0)}(\eta), \tag{3.99}$$

where $\gamma_0 = 1/\beta - 1 \neq 0$ and $c_{1,2}$ are constants. If $\beta = 1$ and hence $\gamma_0 = 0$, the two solutions are identical, but it turns out they happen to satisfy both boundary conditions given by (3.93).

The boundary condition at the nose (3.93a) gives

$$\eta\left(1 - 2\frac{f_0'}{f_0}\right) \to 0 \qquad \text{as} \qquad \eta \to 0, \tag{3.100}$$

which implies that $c_2 = 0$.

Looking at expansions towards the physical origin, i.e. as $\eta \to \infty$, gives

$$f_0 \sim c_1 \left(\frac{\sin(n\pi)}{\pi} \eta^{-n-\gamma_0} \mathrm{e}^\eta \left[-\frac{\Gamma(1+n+\gamma_0)}{\eta} + \cdots \right] \right.$$
$$\left. + (-1)^n \eta^n \left[\frac{1}{\Gamma(1+n)} - \frac{n+\gamma_0}{\Gamma(n)\eta} \cdots \right] \right). \tag{3.101}$$

Hence, unless $\sin(n\pi) = 0$ we get exponential growth and therefore we must have $n \in \mathbb{Z}$.

Furthermore, we note that if n is a negative integer we would get $\mathrm{L}_n^{(\gamma_0)}(\eta) = 0$. This might seem worrying as we would only be left with the trivial solution. However, we could have rescaled c_1 by a constant factor of $\Gamma(1+n)$, turning the Laguerre polynomial into a confluent hypergeometric function which is non-trivial even for negative integer n. As $\sin(n\pi)/\pi = -\left[\Gamma(-n)\Gamma(1+n)\right]^{-1}$ we see from (3.101) that this rescaled f_0 no longer decays as $\eta \to \infty$. Therefore, apart from being an integer, n must also be non-negative.

Hence, the leading order solution is given by a generalised Laguerre polynomial of degree n:

$$f_0 = \delta\, \mathrm{L}_n^{(\gamma_0)}(\eta), \qquad\qquad \sigma_0 = -\gamma_\xi(1+2n\beta), \tag{3.102}$$

with $n \in \{0, 1, 2, \cdots\}$ and $\gamma_0 = 1/\beta - 1$.

3.B.2 First order correction: f_1 and σ_1

For f_1 we obtain a second order linear inhomogeneous differential equation, which has the same homogeneous part as the equation for f_0. Therefore, the complementary solutions for f_1 are the same as (3.99), which simply corresponds to the arbitrary choice of amplitude for our perturbations. Hence, we are only interested in the particular integral for f_1 due to the forcing from f_0. The equation for f_1 is

$$\begin{aligned}\eta f_1'' + \left(\frac{1}{\beta} - \eta\right) f_1' + n f_1 = &\left(\tfrac{1}{2}\eta^2 + \frac{1 + 2\beta - 5\alpha\beta + 2\alpha\beta^2}{4\beta(1+\alpha\beta)}\eta\right) f_0' \\ &+ \left(\frac{\alpha}{1+\alpha\beta} + \frac{4\alpha - n(1-\alpha\beta)}{4(1+\alpha\beta)}\eta + \frac{(1+\beta)}{\beta(1+\alpha\beta)}\sigma_1\right) f_0.\end{aligned} \tag{3.103}$$

We note that the forcing on the right-hand side of this equation is a polynomial of degree $n+1$ and hence, expecting a polynomial solution for f_1 as well, we propose a series solution as a particular integral and we write

$$f_1 = \sum_{i=0}^{\infty} a_i \eta^i, \qquad RHS = \sum_{i=0}^{\infty} b_i \eta^i \ \text{ where } b_i = 0 \text{ for all } i > n+1. \tag{3.104}$$

This then gives the recurrence relationship

$$a_i = \frac{b_{i-1} + (i-1-n)a_{i-1}}{i(i+\gamma_0)}. \tag{3.105}$$

We note that as $b_i = 0$ for $i > n+1$ we can split the series solution for f_1 into two parts

$$f_1 = \sum_{i=0}^{n+1} a_i \eta^i + a_{n+2} \sum_{i=n+1}^{\infty} \frac{(n+2)(n+2+\gamma_0)(1)^{(i-1-n)}}{(n+2)^{(i-1-n)}(n+2+\gamma_0)^{(i-1-n)}} \eta^i \tag{3.106}$$

$$= \sum_{i=0}^{n+2} a_i \eta^i + a_{n+2}\eta^{n+1}(n+2)(n+2+\gamma_0)\,{}_2\mathrm{F}_2\left(1,1;n+2,n+2+\gamma_0;\eta\right) \tag{3.107}$$

$$\sim a_{n+2}\Gamma(n+3)\Gamma(n+3+\gamma_0)\eta^{-n-\gamma_0-1}\mathrm{e}^{\eta} + \cdots, \tag{3.108}$$

where we have used the rising factorial $x^{(n+1)} = x(x+1)(x+2)\cdots(x+n)$. In the last step we have expanded the generalised hypergeometric function ${}_2\mathrm{F}_2$ as $\eta \to \infty$, which shows that we need $a_{n+2} = 0$ to avoid an exponentially growing solution. This will give a condition on σ_1.

To obtain an expression for a_{n+2}, we note that a_{n+1} is independent of a_n and hence

$$a_{n+2} = \frac{b_{n+1}}{(n+2)(n+2+\gamma_0)} + \frac{b_n}{(n+2)(n+1)(n+2+\gamma_0)(n+1+\gamma_0)}. \tag{3.109}$$

Therefore, we only need to find b_n and b_{n+1}. This can be done by using the explicit formula for the generalised Laguerre polynomials

$$\mathrm{L}_n^{(\gamma_0)}(\eta) = \sum_{i=0}^{n} \binom{n+\gamma_0}{n-i} \frac{(-\eta)^i}{i!} = \frac{(-1)^n}{n!}\eta^n - \frac{(-1)^n(n+\gamma_0)}{(n-1)!}\eta^{n-1} + \cdots, \tag{3.110}$$

which gives

$$b_{n+1} = \frac{(-1)^n}{n!}\left(\frac{n}{2} + \frac{4\alpha - n(1-\alpha\beta)}{4(1+\alpha\beta)}\right), \tag{3.111a}$$

$$b_n = \frac{(-1)^n}{n!}\left(\frac{n+2n\beta+(4-5n)\alpha\beta+2n\alpha\beta^2}{4\beta(1+\alpha\beta)} + \frac{(1+\beta)}{\beta(1+\alpha\beta)}\sigma_1 + \frac{n(n+\gamma_0)}{2}\right) - n(n+\gamma_0)b_{n+1}. \tag{3.111b}$$

Solving $a_{n+2} = 0$ with these finally gives the first order correction to the growth rate as

$$\sigma_1 = -\alpha - \frac{(1+2\alpha\beta)(1+n\beta)n}{1+\beta}. \tag{3.112}$$

The first order correction f_1 to the perturbation height is given by some polynomial of degree $n+1$.

3.B.3 Higher order corrections

A similar method can be employed to find all higher-order corrections, as the homogeneous part of the equation will always be the same, and the forcing will always be a polynomial of some finite degree. Therefore, the solution can again be split into a polynomial plus a generalised hypergeometric function, which grows exponentially as $\eta \to \infty$. The difficult task then is to work out the pre-factor of this generalised hypergeometric function from the forcing. Setting this pre-factor to zero then determines the according σ_i.

Appendix 3.C Currents with constant volume — Mathunjwa and Hogg (2006)

Mathunjwa and Hogg (2006) analytically solved the constant-volume case $\alpha = 0$ for all β. For this case the base state is given analytically by

$$H_0 = \left(\frac{\beta}{4(1+\beta)}\left(1-\xi^2\right)\right)^{1/\beta}, \tag{3.113a}$$

$$Q_0 = \frac{\xi}{2(1+\beta)}\left(\frac{\beta}{4(1+\beta)}\left(1-\xi^2\right)\right)^{1/\beta}. \tag{3.113b}$$

For the perturbations Mathunjwa and Hogg (2006) found analytical solutions in terms of Jacobi polynomials $\mathrm{P}_n^{(a,b)}$

$$H_1 = \xi^k H_0^{1-\beta}\,\mathrm{P}_n^{(\gamma_0,k)}\Big|_{2\xi^2-1}, \tag{3.114a}$$

$$\sigma = -\frac{2\beta n(n+k)+2n+k}{2(1+\beta)}, \tag{3.114b}$$

where $\gamma_0 = 1/\beta - 1$ as in Appendix 3.B. The corresponding perturbation flux is still given by (3.91), i.e.

$$Q_1 = \left(\frac{Q_0}{H_0} - \frac{kH_0^\beta}{\xi} - H_0^\beta \frac{\mathrm{d}}{\mathrm{d}\xi} \log \left\{ \mathrm{P}_n^{(\gamma_0,k)} \Big|_{2\xi^2-1} \right\} \right) H_1. \tag{3.115}$$

In particular, we note that for $n = 0$ we obtain $\mathrm{P}_0^{(a,b)} = 1$ and hence we recover the fundamental perturbation mode (3.64).

Furthermore, to compare (3.114a), the solution found by Mathunjwa and Hogg (2006), to (3.70), the asymptotic solution for large k, we can express the two solutions as hypergeometric functions:

$$\alpha = 0, \text{ general } k: \quad \xi^{-k} H_0^{\beta-1} H_1 = \mathrm{P}_n^{(\gamma_0,k)} \Big|_{2\xi^2-1} \propto {}_2\mathrm{F}_1 \left(-n, n + \frac{1}{\beta} + k; \frac{1}{\beta}; 1 - \xi^2 \right), \tag{3.116a}$$

$$k \to \infty, \text{ general } \alpha: \qquad \xi^{-k} H_0^{\beta-1} H_1 \sim \mathrm{L}_n^{(\gamma_0,k)} \Big|_{\eta} \propto {}_1\mathrm{F}_1 \left(-n; \frac{1}{\beta}; \eta \right). \tag{3.116b}$$

Now note that in the limit $k \to \infty$ using the definition $\xi = 1 - \eta/2k$ we find that

$$1 - \xi^2 = \frac{\eta}{k} - \frac{\eta^2}{4k^2} \sim \frac{\eta}{k}, \tag{3.117}$$

and that the following relation holds for hypergeometric functions:

$${}_2\mathrm{F}_1 \left(a, b; c; \frac{z}{b} \right) \to {}_1\mathrm{F}_1(a; c; z) \qquad \text{as} \qquad b \to \infty. \tag{3.118}$$

This hence shows that the large-k asymptotics found for general α agree with the analytical solutions obtained by Mathunjwa and Hogg (2006) for $\alpha = 0$. In fact, we note that to leading order the large-k asymptotics are independent of α except through dependence on the base state H_0 as they are simply the local travelling-wave solutions near the nose.

Chapter 4

Linear stability of constant-flux intrusions in a Hele-Shaw cell with negligible surface tension under the assumption of an Oleinik shock

4.1 Introduction

The Hele-Shaw cell, consisting of two parallel rigid plates with a small separation, was first introduced in 1897 by Hele-Shaw to visualise two-dimensional laminar potential flow past objects. Nowadays, flows in these cells continue to be of wide interest, for example, as a model for two-dimensional viscous flows in porous media, and hence there is a large body of literature relating to theoretical and experimental investigations of flows in Hele-Shaw cells (Richardson, 1989).

Most commonly, the analysis of flows in Hele-Shaw cells makes use of depth-averaged quantities neglecting the exact cross-sectional structure of the flow by assuming that all ambient fluid gets expelled (or that only a fixed layer of constant thickness gets left behind). This effectively results in Laplace's equation for the pressure, similar to currents in porous media which are governed by Darcy's law and the continuity equation, and which allows for the use of conformal mappings to study the resulting flows. This method has led to many analytical solutions and results concerning existence and regularity of general solutions (Gustafsson and Vasil'ev, 2000). However, it turns out that the equations governing the interfaces can be ill-posed and additional physical effects such as surface tension are crucial in regularising the equations. Two examples

of this are receding viscous fronts which tend to form singular cusps, and an intruding finger in a long rectangular Hele-Shaw cell whose width is not uniquely determined by the standard equations (Saffman and Taylor, 1958).

For example, Saffman and Taylor (1958) first analysed an instability of a moving horizontal interface in a vertical Hele-Shaw cell. They included surface tension and gravitational effects and they assumed that the intruding fluid expelled all of the ambient fluid (although they mentioned that similar results hold if a constant-thickness layer of ambient fluid is left behind). This effectively ignores the cross-sectional structure of the intrusions, focussing only on the radial structure. Their key result is that, as long as the intruding fluid is less viscous, there is a critical velocity of the interface above which an instability forms. Surface tension stabilises the short wavelengths, leading to a most-unstable wavelength proportional to the square-root of the surface tension. Hence, in the limit of zero surface tension, the short wavelength perturbations grow the fastest with an infinitely fast rate. In fact, zero surface tension is a singular limit of the boundary conditions, as it neglects the derivatives related to the curvature. Saffman and Taylor (1958) confirmed their analysis experimentally by forcing air into a glycerol-filled Hele-Shaw cell, and due to their work, this fingering instability is now commonly referred to as the Saffman–Taylor fingering instability.

We are interested here in the case of negligible surface tension, which, for example, arises when studying miscible fluids. For such intrusions into Hele-Shaw cells with miscible fluids, Wooding (1969) first described an instability similar to the Saffman–Taylor instability for immiscible fluids, but did not attempt a perturbation analysis. Later, Paterson (1985) considered an inviscid intrusion spreading from a point source into a miscible ambient with negligible diffusion. He also neglected the cross-sectional structure by assuming that the ambient leaves only an immobile film of constant thickness behind. He noted that a standard linear stability analysis assuming only in-plane flow, again leads to a singular result. To mitigate this, he proposed an analysis based on minimising dissipation, which he calculated from the full three-dimensional stress tensor, i.e. including radial and azimuthal stresses. Only by incorporating these additional physics in his model could he avoid the singular nature of zero surface tension, and he predicted the fastest growing wavelength to be a fixed multiple of the plate separation. Paterson (1985) confirmed this result through experimental observations of water intrusions into glycerol.

More recently, Yang and Yortsos (1997) resolved the cross-sectional structure of intrusion with negligible diffusion and negligible surface tension, but they ignored the radial structure by making use of axisymmetric similarity solutions. We recall

from Chapter 2 that their analysis revealed a flat shock front for sufficiently less viscous intrusions. They argued that, in order to calculate the shock height, a fully three-dimensional Stokes flow near the nose would have to be considered. Instead, they ad hoc proposed a shock height given by a tangent construction based on the flux function given by the ratio of intruding to total fluid flux. Experiments (Petitjeans and Maxworthy, 1996) and numerical models (Chen and Meiburg, 1996; Rakotomalala et al., 1996) cited by them suggest that this value for the shock height underestimates the true value for flows in a Hele-Shaw cell, and to the best of our knowledge the exact nature of these shocks and how their height is determined is not yet fully understood. However, in Chapter 2 we also discovered similar shocks in equal-density two-layer gravity currents, where we could derive an Oleinik entropy condition determining the shock height from considering small but finite density differences as a regularising mechanism. The value obtained by using this physically motivated regularisation mechanism matches exactly the value obtained by Yang and Yortsos (1997). We note that there is a correspondence between intrusions in a Hele-Shaw cell and equal-density two-layer gravity current with small influx (see Chapter 5 for a rigorous asymptotic analysis), and hence in this chapter we will assume that shocks in a Hele-Shaw cell are indeed governed by the Oleinik entropy condition.

Lajeunesse et al. (1997, 1999, 2001) and later Bischofberger et al. (2014) conducted experiments in Hele-Shaw cells with negligible diffusion and negligible surface tension, and found an instability to the front of the intrusion above a critical viscosity ratio. The critical viscosity ratio for the onset of the instability was very similar to the critical viscosity ratio derived by Yang and Yortsos (1997) for the formation of shocks in the axisymmetric flows. Hence, both Lajeunesse et al. (1997, 1999, 2001) and Bischofberger et al. (2014) suggested that the existence of a flat shock front and the associated jump in pressure gradient are crucial to the development of a fingering instability similar to the classical Saffman–Taylor instability. Further, Lajeunesse et al. (1997, 1999, 2001) argued that at late times flat frontal shocks locally resemble the flow geometry originally studied by Saffman and Taylor (1958), and that therefore the same instability mechanism should be applicable. Neither Lajeunesse et al. (1997, 1999, 2001) or Bischofberger et al. (2014) attempted a theoretical analysis of the instability mechanism though. The related case of the instability of a miscible intrusion where diffusion between the intruding and ambient fluid is not neglected, has been analysed numerically by Goyal and Meiburg (2006). In this case however, there is no self-similar base state, and their results were limited to finite Péclet numbers.

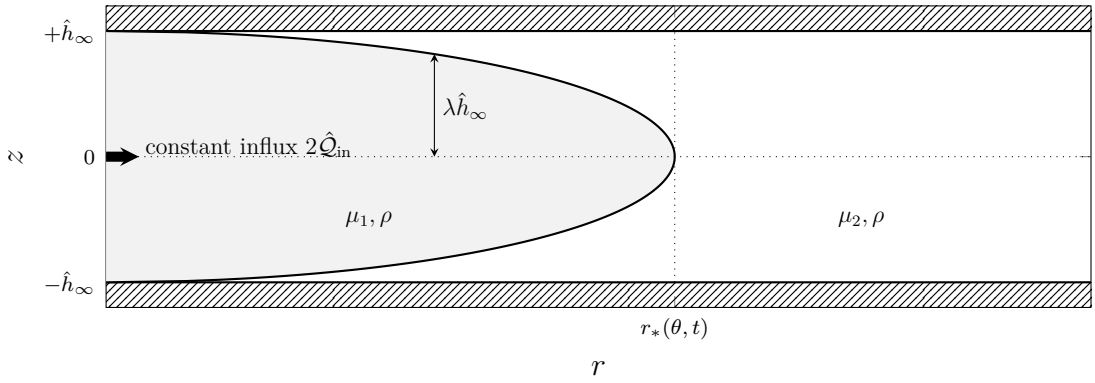

Fig. 4.1 A radial cross-section of an equal-density intrusion into a Hele-Shaw cell with gap thickness $2\hat{h}_\infty$ and with constant influx $2\hat{\mathcal{Q}}_{\text{in}}$. The dynamic variables defined are the fluid fraction $\lambda(r, \theta, t)$ and the radial extent $r_*(\theta, t)$, and the fluid properties are the common density ρ and the two viscosities $\mu_{1,2}$, which give rise to a viscosity ratio of ambient to intruding fluid $m = \mu_2/\mu_1$.

To the best of our knowledge, no linear stability analysis of self-similar intrusions into a Hele-Shaw cell with negligible diffusion and negligible surface tension has been performed, taking into account both the radial and cross-sectional structure. Therefore, it is our aim in this chapter to perform such a linear stability analysis. We shall assume a shock governed by the Oleinik entropy condition as motivated above.

The set-up of the model and its assumptions are described in §4.2, which leads to a closed system of ordinary differential equations. Analytical solutions can be found for the special cases of axisymmetric flows and equal-viscosity flows which are described in §4.3.1 and §4.3.2, respectively. These solutions motivate a change of variables set out in §4.4, and the resulting equations for the general case are solved numerically in §4.5. Finally, we consider large azimuthal wavenumber in §4.6 using the WKB method to investigate the singular nature of the instability in the absence of a short-wavelength regularisation. In Appendix 4.A, we analyse the same limit, but using a local expansion approach in order to confirm the WKB results.

4.2 Model description

We consider radial flow emanating from a point source in a Hele-Shaw cell consisting of two infinite parallel horizontal rigid plates separated by a constant distance $2\hat{h}_\infty$. The space between the plates is initially filled with some fluid of viscosity μ_2 when a second fluid of viscosity μ_1 is introduced at the origin with constant volumetric rate $2\hat{\mathcal{Q}}_{\text{in}}$. The fluid densities are the same, or equivalently we neglect gravitational effects.

As shown in figure 4.1, we use cylindrical polar coordinates to define the horizontal extent of the current $r_*(\theta,t)$ and the vertical thickness of the intrusion $2\hat{h}_\infty\lambda(r,\theta,t)$. Hence, $\lambda(r,\theta,t)$ is the relative fluid fraction. Surface tension and diffusion are assumed to be negligible.

After a short initial transient, the horizontal extent of the current is significantly greater than the vertical extent, $r_* \gg \hat{h}_\infty$. In this limit, the vertical velocity is negligible and the horizontal velocity $\widehat{\boldsymbol{u}}(r,z,t)$ is related to the horizontal pressure gradient $\boldsymbol{\nabla}\widehat{p}$ by the lubrication approximation of Stokes equation,

$$\mu\frac{\partial^2\widehat{\boldsymbol{u}}}{\partial z^2} = \boldsymbol{\nabla}\widehat{p}. \tag{4.1}$$

The boundary conditions

$$\widehat{\boldsymbol{u}} = \boldsymbol{0} \text{ at } z = \pm\hat{h}_\infty, \quad [\widehat{\boldsymbol{u}}]^+_- = 0 \text{ at } z = \pm\hat{h}_\infty\lambda, \quad \left[\mu\frac{\partial\widehat{\boldsymbol{u}}}{\partial z}\right]^+_- = 0 \text{ at } z = \pm\hat{h}_\infty\lambda, \tag{4.2}$$

impose no-slip at the top and bottom, and velocity and stress continuity at the interfaces between the fluids, respectively. Solving (4.1) with boundary conditions (4.2), we obtain the velocity profile

$$\widehat{\boldsymbol{u}} = \frac{\boldsymbol{\nabla}\widehat{p}}{2\mu_2}\left(mz^2 - \hat{h}_\infty^2\left\{1+(m-1)\lambda^2\right\}\right) \quad \text{for} \quad 0 < |z|/\hat{h}_\infty < \lambda, \tag{4.3a}$$

$$\widehat{\boldsymbol{u}} = \frac{\boldsymbol{\nabla}\widehat{p}}{2\mu_2}\left(z^2 - \hat{h}_\infty^2\right) \quad \text{for} \quad \lambda < |z|/\hat{h}_\infty < 1, \tag{4.3b}$$

where the flow profile is characterised in terms of the dimensionless viscosity ratio $m = \mu_2/\mu_1$ and the fluid fraction λ.

For $r < r_*(\theta,t)$ we obtain two local mass-conservation equations by integrating the velocity profile (4.3) both over the vertical thickness of the intrusion and the total gap of the Hele-Shaw cell:

$$\frac{\partial\lambda}{\partial t} = \frac{\hat{h}_\infty^2}{3\mu_2}\boldsymbol{\nabla}\cdot\left(\mathcal{M}\mathcal{F}\boldsymbol{\nabla}\widehat{p}\right), \qquad 0 = \boldsymbol{\nabla}\cdot\left(\boldsymbol{\nabla}\widehat{p}\right), \tag{4.4}$$

where the mobility function $\mathcal{M}(\lambda)$ and flux function $\mathcal{F}(\lambda)$ are given by

$$\mathcal{M} = 1+(m-1)\lambda^3 \qquad \text{and} \qquad \mathcal{F} = \frac{3\lambda+(2m-3)\lambda^3}{2+2(m-1)\lambda^3}, \tag{4.5}$$

respectively.

The first of these equations determines the evolution of λ from local mass conservation of the intruding fluid, while the second equation gives the pressure gradient $\boldsymbol{\nabla}\widehat{p}$ from the constraint imposed on the divergence of the total flux by the fixed rigid plates of the Hele-Shaw cell.

Ahead of the nose of the current, $r > r_*(\theta, t)$, there is no intruding fluid and hence the pressure obeys Laplace's equation:

$$0 = \boldsymbol{\nabla}^2\widehat{p}. \tag{4.6}$$

We impose zero pressure gradient in the far-field, i.e. $\boldsymbol{\nabla}\widehat{p} \to 0$ as $r \to \infty$, and a given influx of fluid $\hat{\mathcal{Q}}_{\text{in}}$ at the origin, which can be written as

$$\hat{\mathcal{Q}}_{\text{in}} = \frac{2\pi m\hat{h}_\infty^3}{3\mu_2}\lim_{r\to 0}\left(r\boldsymbol{e}_r\cdot\boldsymbol{\nabla}\widehat{p}\right), \tag{4.7}$$

where $\boldsymbol{e}_r$ is the radially outward unit vector. We also impose $\lambda = 1$ at $r = 0$, such that there is no ambient fluid present at the source of the intruding fluid.

At $r = r_*(\theta, t)$, the normal flux of intruding fluid through the nose has to match the velocity of the nose giving

$$\frac{\partial r_*}{\partial t} = \frac{\hat{h}_\infty^3\left(\boldsymbol{n}\cdot\boldsymbol{\nabla}\widehat{p}\right)}{6\mu_2\left(\boldsymbol{n}\cdot\boldsymbol{e}_r\right)}\left\{3 + (2m-3)\lambda_*^2\right\}, \tag{4.8}$$

where $\boldsymbol{n}$ is the normal to the perimeter $r = r_*(\theta, t)$ of the intrusion and λ_*, possibly non-zero in the case of a shock, is the limiting value of λ as $r \to r_*$. Furthermore, at $r = r_*(\theta, t)$ we need to impose continuity of pressure and continuity of total normal flux through the nose, giving

$$[\widehat{p}]_-^+ = 0, \qquad \left[\frac{\hat{h}_\infty^3\left(\boldsymbol{n}\cdot\boldsymbol{\nabla}\widehat{p}\right)}{3\mu_2}\left\{1 + (m-1)\lambda^3\right\}\right]_-^+ = 0 \qquad \text{at} \qquad r = r_*, \tag{4.9}$$

respectively.

The boundary conditions governing the interfacial shape $\lambda(r, \theta, t)$ are somewhat complicated by the fact that (4.4a) is a nonlinear hyperbolic equation for λ, and, as such, may not have a unique solution. For example, there can be regions where the interface is horizontal, i.e. $\lambda = \text{const}$, or vertical shocks where λ is discontinuous. We will assume that any shock which might occur, with a discontinuity in λ jumping from

λ_l to λ_r, is governed by the Oleinik entropy condition (see Chapter 2):

$$\frac{\mathcal{F}(\lambda_r) - \mathcal{F}(\lambda_i)}{\lambda_r - \lambda_i} \leq \frac{\mathcal{F}(\lambda_r) - \mathcal{F}(\lambda_l)}{\lambda_r - \lambda_l} \leq \frac{\mathcal{F}(\lambda_i) - \mathcal{F}(\lambda_l)}{\lambda_i - \lambda_l}, \tag{4.10}$$

for all λ_i with $\lambda_r \leq \lambda_i \leq \lambda_l$. This entropy condition is in fact sufficient to ensure a unique solution.

Equations (4.4)–(4.10) give a complete system of equations describing the evolution of a radially spreading intrusion of constant flux into a Hele-Shaw cell neglecting diffusion, surface tension, and gravity.

4.2.1 Self-similar spreading

We first note that the fluid fraction λ is already dimensionless. A scaling analysis of (4.4a) and (4.7), governing the evolution of the relative fluid fraction and global mass conservation respectively, suggests a dimensionless pressure p and a radial similarity variable ξ given by

$$\xi = \left(\frac{2\pi\hat{h}_\infty}{\hat{\mathcal{Q}}_{\text{in}}}\right)^{1/2} rt^{-1/2}, \qquad p(\xi,\theta,t) = \left(\frac{2\pi\hat{h}_\infty^3}{3\mu_2\hat{\mathcal{Q}}_{\text{in}}}\right)\widehat{p}(r,\theta,t). \tag{4.11}$$

with $\xi_* = \xi(r_*, t)$ for the non-dimensional radial extent of the current. In order to describe the evolution towards self-similarity, we define a rescaled temporal variable $\tau = \log(t/\widehat{t})$, where $\widehat{t}$ is an arbitrary reference time scale. The local mass-conservation equations (4.4) and (4.6) then lead to a nonlinear dimensionless system of partial differential equations which consists of a third-order system up to the nose coupled to a second-order system beyond the nose. For $\xi < \xi_*$ this is given by

$$\frac{\partial\lambda}{\partial\tau} - \tfrac{1}{2}\xi\frac{\partial\lambda}{\partial\xi} = -\boldsymbol{\nabla}\cdot(\mathcal{F}\boldsymbol{q}), \qquad \boldsymbol{\nabla}\cdot\boldsymbol{q} = 0, \qquad \boldsymbol{q} = -\mathcal{M}\boldsymbol{\nabla}p, \tag{4.12}$$

where $\boldsymbol{q}(\xi,\theta,\tau)$ is the depth-integrated total flux.

For $\xi > \xi_*$ we simply have,

$$\boldsymbol{\nabla}^2 p = 0, \qquad \boldsymbol{q} = -\boldsymbol{\nabla}p. \tag{4.13}$$

The boundary conditions on (4.12) and (4.13) can be expressed in the dimensionless variables as

$$\text{influx at the origin:} \quad \xi\,(\boldsymbol{e}_\xi \cdot \boldsymbol{q}) \to 1 \quad \text{as} \quad \xi \to 0, \tag{4.14a}$$

$$\text{no flow at infinity:} \quad \boldsymbol{q} \to \boldsymbol{0} \quad \text{as} \quad \xi \to \infty, \tag{4.14b}$$

$$\text{mass conservation at the nose:} \quad \frac{\partial \xi_*}{\partial \tau} = \frac{\mathcal{F}\,(\boldsymbol{n}\cdot\boldsymbol{q})}{\lambda\,(\boldsymbol{n}\cdot\boldsymbol{e}_\xi)} - \tfrac{1}{2}\xi \quad \text{at} \quad \xi = \xi_*, \tag{4.14c}$$

$$\text{continuity of pressure:} \quad [p]^+_- = 0 \quad \text{at} \quad \xi = \xi_*, \tag{4.14d}$$

$$\text{continuity of normal flux:} \quad [\boldsymbol{n}\cdot\boldsymbol{q}]^+_- = 0 \quad \text{at} \quad \xi = \xi_*, \tag{4.14e}$$

where $\partial\xi_*/\partial\tau$ is the dimensionless speed of the nose in similarity space and to ensure uniqueness we require (4.10) for any shock .

If the evolution of the system becomes self-similar and independent of τ at late times, then (4.12) reduces to a system of coupled ordinary differential equations, and the boundary conditions are the same as (4.14) only with a zero nose speed, $\partial\xi_*/\partial\tau = 0$.

4.3 Kinematic wave solutions

4.3.1 Axisymmetric flows

If the flow is axisymmetric, i.e. $\partial/\partial\theta = 0$, we immediately see that $\boldsymbol{q} = (1/\xi, 0)$, due to the incompressibility of the fluid and the influx at the origin. Therefore, (4.12) becomes

$$\frac{\partial\lambda}{\partial\tau} = \left(\tfrac{1}{2}\xi - \frac{\mathcal{F}'}{\xi}\right)\frac{\partial\lambda}{\partial\xi}, \tag{4.15}$$

where $\mathcal{F}'(\lambda)$ denotes $\partial\mathcal{F}/\partial\lambda$. We recognise this equation governing the evolution of $\lambda(\xi,\tau)$ as a simple quasi-linear one-dimensional advection equation. Hence, we can use the method of characteristics to construct an analytical solution for any given initial condition $\lambda(\xi,0) = \lambda_{\text{init}}(\xi)$. For this we construct characteristic curves $\xi_c(\tau)$ such that

$$\frac{\mathrm{d}\xi_c}{\mathrm{d}\tau} = \frac{\mathcal{F}'}{\xi_c} - \tfrac{1}{2}\xi_c \qquad \Leftrightarrow \qquad \left(\xi_c^2 - 2\mathcal{F}'\right)\mathrm{e}^{\tau} = \text{const.} \tag{4.16}$$

Along these characteristic curves (4.15) implies that λ is a constant and hence determined by its initial value λ_{init} at $\tau = 0$. This leads to the general solution

$$\lambda(\xi, \tau) = \lambda_{\text{init}} \left(\left\{ \xi^2 \mathrm{e}^{\tau} + 2\mathcal{F}' \left(1 - \mathrm{e}^{\tau}\right) \right\}^{1/2} \right), \tag{4.17}$$

which is implicit in λ as $\mathcal{F}$ depends on λ, and hence it would have to be inverted to find λ explicitly in terms of ξ and τ. In general, this inversion is not possible analytically. However, we note that if we invert the initial condition by defining $\xi_{\text{init}}(\lambda) = \lambda_{\text{init}}^{-1}(\lambda)$ then we can solve (4.17) explicitly for $\xi(\lambda, \tau)$:

$$\xi(\lambda, \tau) = \left\{ \xi_{\text{init}}^2 \mathrm{e}^{-\tau} + 2\mathcal{F}' \left(1 - \mathrm{e}^{-\tau}\right) \right\}^{1/2}. \tag{4.18}$$

This shows that the fluid fraction λ is a more convenient independent variable than the radial distance ξ, and suggests a change of variable from $\lambda(\xi, \theta, \tau)$ to $\xi(\lambda, \theta, \tau)$.

Equation (4.18) shows that as $\tau \to \infty$ the flow becomes self-similar for any initial condition $\xi_{\text{init}}(\lambda)$ and the shape of the interface approaches the steady shape $\xi = X_0(\lambda)$ given by

$$X_0 = \left(2\mathcal{F}'\right)^{1/2}. \tag{4.19}$$

The corresponding pressure for this self-similar late-time limit is obtained from integrating (4.12c), which results in a self-similar pressure $p = P_0(\lambda)$ given by

$$P_0 = -\int \frac{1}{\xi \mathcal{M}} \, \mathrm{d}\xi = -\int \frac{\mathcal{F}''}{2\mathcal{M}\mathcal{F}'} \, \mathrm{d}\lambda. \tag{4.20}$$

As we are interested in the linear stability of intrusions into a Hele-Shaw cell, we expand (4.18) to linear order when $\tau \to \infty$, to obtain

$$\xi \sim X_0 + \frac{\xi_{\text{init}}^2 - X_0^2}{2X_0} \mathrm{e}^{-\tau} + \cdots. \tag{4.21}$$

This result shows that any axisymmetric perturbations left over from the initial condition decay as $O\left(\mathrm{e}^{-\tau}\right)$, and hence the associated growth rate is $\sigma = -1$.

We note that due to the form of $\mathcal{F}$ for $m > 3/2$, the steady solution (4.19) is non-monotonic over the domain $\lambda \in [0, 1]$ and the time-dependent solution (4.18) evolves to become so. However, full numerical studies indicate that a non-monotonic interface is not physical (Chen and Meiburg, 1996; Yang and Yortsos, 1997), and

therefore we have to restrict the solution to some domain $\lambda \in [0, \lambda_r] \cup [\lambda_l, 1]$, with a vertical discontinuity, i.e. a shock, at $\lambda \in [\lambda_r, \lambda_l]$.

To find the heights $\lambda_{r,l}$ and position ξ_s of this shock, we note that the non-monotonic interface given by (4.18) for $\lambda \in [0, 1]$ has the correct volume at any time τ due to the mass-conserving evolution underlying (4.18). Therefore, the heights $\lambda_{r,l}$ are determined by making a vertical cut such that the overall volume of the current at that point in time τ is not altered. Hence, the shock position ξ_s and heights $\lambda_{r,l}$ are given by

$$\xi_s^2 = \xi^2(\lambda_l) = \xi^2(\lambda_r) = \frac{1}{\lambda_l - \lambda_r} \int_{\lambda_r}^{\lambda_l} \xi^2 \, \mathrm{d}\lambda. \tag{4.22}$$

At some finite time the shock extends to the mid-plane, i.e. $\lambda_r = 0$, and from then onwards only the shock height $\lambda_s = \lambda_l$ varies to approach the final steady-state shock height λ_{crit}. By substituting the steady solution (4.19) into (4.22) we find that λ_{crit} satisfies $\mathcal{F}' = \mathcal{F}/\lambda$ as in Chapter 2, and therefore is given by

$$\lambda_{\mathrm{crit}} = \begin{cases} 2\left(\frac{2}{3}m - 1\right)^{-1/2} \sinh\left[\frac{1}{3}\sinh^{-1}\left\{(m-1)^{-1}\left(\frac{2}{3}m - 1\right)^{3/2}\right\}\right], & m > 3/2. \\ 0, & m \leq 3/2, \end{cases} \tag{4.23}$$

Considering the late-time limit of the integral expression (4.22) and the expansion (4.21) yields the linear perturbation to the shock height λ_s and the shock position ξ_s

$$\lambda_s = \lambda_{\mathrm{crit}} + \frac{1}{2\mathcal{F}_*''}\left(\frac{1}{\lambda_{\mathrm{crit}}}\int_0^{\lambda_{\mathrm{crit}}} \xi_{\mathrm{init}}^2(\lambda)\,\mathrm{d}\lambda - \xi_{\mathrm{init}}^2(\lambda_{\mathrm{crit}})\right)\mathrm{e}^{-\tau} + \cdots, \tag{4.24}$$

$$\xi_s = X_{0*} + \frac{1}{2X_0(\lambda_{\mathrm{crit}})}\left(\frac{1}{\lambda_{\mathrm{crit}}}\int_0^{\lambda_{\mathrm{crit}}} \xi_{\mathrm{init}}^2\,\mathrm{d}\lambda - X_0^2(\lambda_{\mathrm{crit}})\right)\mathrm{e}^{-\tau} + \cdots, \tag{4.25}$$

where $X_{0*} = (2\mathcal{F}_*')^{1/2}$ and $\mathcal{F}_*'$ and $\mathcal{F}_*''$ are evaluated at λ_{crit}. The form of (4.24) and (4.25) shows that including shock dynamics does not affect the decay of axisymmetric perturbation being $O(\mathrm{e}^{-\tau})$ with a growth rate $\sigma = -1$.

Figure 4.2 shows the time-dependent analytic solution (4.18) for a viscosity ratio $m = 5$ and for the example initial condition $\xi_{\mathrm{init}} = (2/3)\left(1 - \lambda^{1/2}\right)$. We observe that, at approximately $\tau = 0.22$, a shock begins to form at point **A**. This shock then grows in both vertical directions until it reaches the mid-plane at point **B**. After this, only the lower boundary of the shock continues to evolve towards the final steady state at point **N**, where $\lambda_s = \lambda_{\mathrm{crit}}$. This final point is only reached as $\tau \to \infty$.

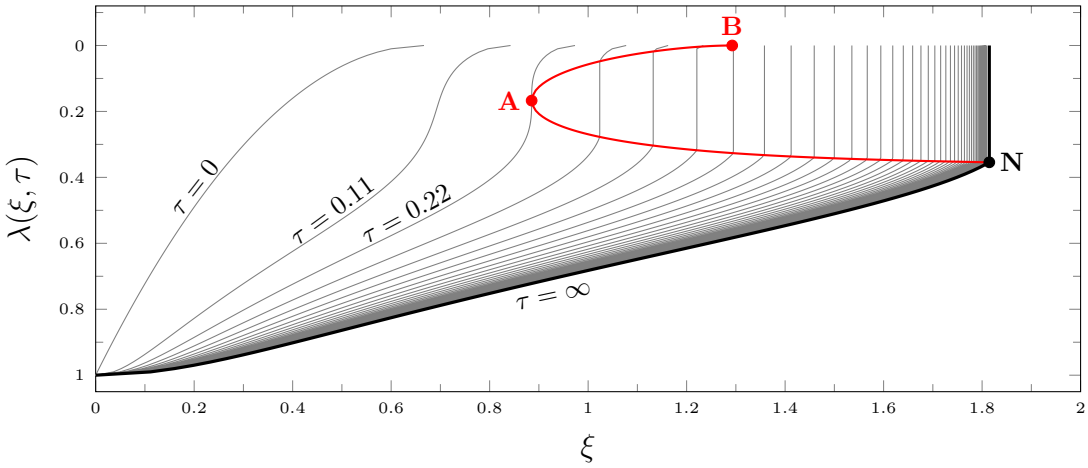

Fig. 4.2 A time-series of axisymmetric interfacial shapes $\lambda(\xi, \tau)$ given by (4.18) for a viscosity ratio $m = 5$ and initial condition $\xi_{\text{init}} = 2/3\left(1 - \lambda^{1/2}\right)$. The shapes are shown at equal time intervals $\Delta\tau = 0.11$. The boundaries of the shock are highlighted and points of interest **A**,**B** and **N** are marked (see text). Note we have reversed the λ-axis to aid physical interpretation and comparison to the gravity currents in Chapter 2.

Note in particular the distinction to the advection of an interface in an externally fixed gravity current as presented in Chapter 2: in the gravity-current case we also observed the points **A** and **B**. However, we observed an additional point **C**, where, after a finite time, the shock height reaches $\lambda_s = \lambda_{\text{crit}}$. Following **C** the shock height ceases to evolve due to the constraint of the Oleinik entropy condition. Instead, the evolution from **C** to **N** is governed by non-horizontal characteristics emanating from the shock, carrying the information of a constrained shock height to the rest of the interface.

Mathematically, this difference between the Hele-Shaw case in this chapter and the gravity-current case in Chapter 2 is a consequence of the lack of a source term in the governing advection equation (4.15). This results in purely horizontal characteristics along which λ is constant.

To summarise, we have shown in this section that intrusions into a Hele-Shaw cell with or without a shock (or equivalently the flow in the low-flux limit of a two-layer gravity current) are stable to axisymmetric perturbations, with all perturbations decaying like $\mathrm{e}^{-\tau} = \widehat{t}/t$.

4.3.2 Equal-viscosity flow ($m = 1$)

If the viscosities of the two fluids are equal, i.e. $m = 1$ and therefore $\mathcal{M} = 1$, the equations for the pressure and for the evolution of the interface decouple. In this case,

the pressure is given by Laplace's equation $\boldsymbol{\nabla}^2 p = 0$ in the entire domain, and the interface is simply a passive tracer line advected along the flow according to

$$\frac{\partial \lambda}{\partial \tau} - \tfrac{1}{2}\xi \frac{\partial \lambda}{\partial \xi} = \tfrac{3}{2}\left(1-\lambda^2\right)\boldsymbol{\nabla}\lambda \cdot \boldsymbol{\nabla} p. \tag{4.26}$$

The axisymmetric influx at the origin results in an axisymmetric pressure gradient and therefore an axisymmetric flux throughout the entire domain given by $\boldsymbol{q} = -\boldsymbol{\nabla} p = \boldsymbol{e}_\xi/\xi$. Substituting this flux into (4.26) results in

$$\frac{\partial \lambda}{\partial \tau} = \left(\tfrac{1}{2}\xi - \frac{3}{2\xi}\left\{1-\lambda^2\right\}\right)\frac{\partial \lambda}{\partial \xi}, \tag{4.27}$$

which we recognise as similar to (4.15) with $m = 1$. The difference between (4.27) and (4.15) is that in the former λ depends on the azimuthal angle θ, while the latter is fully axisymmetric. However, there is no interaction between the different θ-directions, and hence we can still use the same solution method as in §4.3.1 for each θ individually resulting in

$$\xi(\lambda, \theta, \tau) = \left\{\xi_{\text{init}}^2 \mathrm{e}^{-\tau} + 2\mathcal{F}'\left(1-\mathrm{e}^{-\tau}\right)\right\}^{1/2}, \tag{4.28}$$

where $\xi_{\text{init}}(\lambda, \theta)$ is the initial condition now depending on θ. As $m = 1$, we do not get any shocks.

We conclude that equal-viscosity flows are linearly stable with perturbations again decaying like $\mathrm{e}^{-\tau} = \widehat{t}/t$ with growth rate $\sigma = -1$.

4.4 Equations for the general case — a change of independent variable

Motivated by the analytic convenience of the fully time-dependent solution (4.18) for axisymmetric flows in §4.3.1 and similar considerations to those seen in the previous chapter, we analyse non-axisymmetric perturbations using the fluid fraction λ as the independent variable instead of the radial distance ξ. To transform the variables, we

apply the chain rule to the partial derivatives

$$\left(\frac{\partial}{\partial\lambda}\right)_{\theta,\tau} = \left(\frac{\partial\xi}{\partial\lambda}\right)_{\theta,\tau}\left(\frac{\partial}{\partial\xi}\right)_{\theta,\tau}, \tag{4.29a}$$

$$\left(\frac{\partial}{\partial\theta}\right)_{\lambda,\tau} = \left(\frac{\partial}{\partial\theta}\right)_{\xi,\tau} + \left(\frac{\partial\xi}{\partial\theta}\right)_{\lambda,\tau}\left(\frac{\partial}{\partial\xi}\right)_{\theta,\tau}, \tag{4.29b}$$

$$\left(\frac{\partial}{\partial\tau}\right)_{\lambda,\theta} = \left(\frac{\partial}{\partial\tau}\right)_{\xi,\theta} + \left(\frac{\partial\xi}{\partial\tau}\right)_{\lambda,\theta}\left(\frac{\partial}{\partial\xi}\right)_{\theta,\tau}, \tag{4.29c}$$

where the subscripts on the brackets signify which variables are being held constant. Inverting these relationships leads to the following transformation laws from the variables (ξ,θ,τ) to the variables (λ,θ,τ):

$$\frac{\partial}{\partial\xi} \mapsto \frac{\partial}{\partial\lambda}\Big/\frac{\partial\xi}{\partial\lambda}, \tag{4.30a}$$

$$\frac{\partial}{\partial\tau} \mapsto \frac{\partial}{\partial\tau} - \left(\frac{\partial\xi}{\partial\tau}\Big/\frac{\partial\xi}{\partial\lambda}\right)\frac{\partial}{\partial\lambda}, \tag{4.30b}$$

$$\frac{\partial}{\partial\theta} \mapsto \frac{\partial}{\partial\theta} - \left(\frac{\partial\xi}{\partial\theta}\Big/\frac{\partial\xi}{\partial\lambda}\right)\frac{\partial}{\partial\lambda}. \tag{4.30c}$$

Writing $\boldsymbol{q} = (q_\xi, q_\theta)$ for the radial flux q_ξ and the azimuthal flux q_θ, the transformation laws (4.30) applied to (4.12) result in

$$\frac{\partial\xi}{\partial\tau} + \left(\tfrac{1}{2}\xi - \mathcal{F}'q_\xi\right) = \frac{\mathcal{M}\mathcal{F}'}{\xi^2}\left\{\frac{\partial p}{\partial\theta} - \left(\frac{\partial\xi}{\partial\theta}\Big/\frac{\partial\xi}{\partial\lambda}\right)\frac{\partial p}{\partial\lambda}\right\}\frac{\partial\xi}{\partial\theta}, \tag{4.31a}$$

$$\frac{\partial(\xi q_\xi)}{\partial\lambda} = \frac{\partial\xi}{\partial\lambda}\left[\frac{\partial}{\partial\theta} - \left(\frac{\partial\xi}{\partial\theta}\Big/\frac{\partial\xi}{\partial\lambda}\right)\frac{\partial}{\partial\lambda}\right]\left\{\frac{\mathcal{M}}{\xi}\left[\frac{\partial p}{\partial\theta} - \left(\frac{\partial\xi}{\partial\theta}\Big/\frac{\partial\xi}{\partial\lambda}\right)\frac{\partial p}{\partial\lambda}\right]\right\}, \tag{4.31b}$$

$$q_\xi\frac{\partial\xi}{\partial\lambda} = -\mathcal{M}\frac{\partial p}{\partial\lambda}, \tag{4.31c}$$

where we have eliminated the azimuthal flux q_θ by using

$$q_\theta = -\frac{\mathcal{M}}{\xi}\left(\frac{\partial p}{\partial\theta} - \left(\frac{\partial\xi}{\partial\theta}\Big/\frac{\partial\xi}{\partial\lambda}\right)\frac{\partial p}{\partial\lambda}\right). \tag{4.32}$$

4.4.1 Linear perturbation expansion

To perform a linear stability analysis, we propose a steady axisymmetric base state and small normal-mode perturbations

$$\xi(\lambda,\theta,\tau) = X_0(\lambda) + X_1(\lambda)\mathrm{e}^{\mathrm{i}k\theta+\sigma\tau} + \cdots\,, \tag{4.33a}$$

$$p(\lambda,\theta,\tau) = P_0(\lambda) + P_1(\lambda)\mathrm{e}^{\mathrm{i}k\theta+\sigma\tau} + \cdots\,, \tag{4.33b}$$

$$(\xi q_\xi)(\lambda,\theta,\tau) = \Phi_0(\lambda) + \Phi_1(\lambda)\mathrm{e}^{\mathrm{i}k\theta+\sigma\tau} + \cdots\,, \tag{4.33c}$$

where σ is the growth rate of the perturbations and k is the azimuthal wavenumber, which we assume to be positive, $k \in \{0,1,2,\dots\}$, without loss of generality. The dots stand for any higher order terms, which we neglect within the frame work of a linear stability analysis. We note that we have expanded ξq_ξ instead of just q_ξ as this significantly simplifies the algebra: the extra factor ξ in ξq_ξ resulting from the divergence in (4.31b) is now no longer just an independent variable, but itself would be perturbed, leading to excessive terms in the equations for the perturbations.

The analytic solution for the axisymmetric base state is given, as in §4.3.1, by

$$X_0 = (2\mathcal{F}')^{1/2}, \qquad P_0 = -\int \frac{\mathcal{F}''}{2\mathcal{M}\mathcal{F}'}\,\mathrm{d}\lambda, \qquad \Phi_0 = 1. \tag{4.34}$$

At the order of linear perturbations, we obtain the equations

$$\left(\tfrac{1}{2}+\sigma\right)X_1 = \frac{\mathcal{F}'\Phi_0}{X_0}\left(\frac{\Phi_1}{\Phi_0} - \frac{X_1}{X_0}\right) = \left(\frac{\mathcal{F}'}{2}\right)^{1/2}\Phi_1 - \tfrac{1}{2}X_1, \tag{4.35a}$$

$$\Phi_1' = -k^2\mathcal{M}\left(\frac{X_0'}{X_0}P_1 - \frac{P_0'}{X_0}X_1\right) = -\frac{k^2\mathcal{F}''}{2\mathcal{F}'}\left(\mathcal{M}P_1 + \frac{X_1}{X_0}\right), \tag{4.35b}$$

$$P_1' = -\frac{X_0'\Phi_0}{\mathcal{M}X_0}\left(\frac{\Phi_1}{\Phi_0} + \frac{X_1'}{X_0'} - \frac{X_1}{X_0}\right) = -\frac{\mathcal{F}''}{2\mathcal{M}\mathcal{F}'}\left(\Phi_1 + \frac{X_1'}{X_0'} - \frac{X_1}{X_0}\right). \tag{4.35c}$$

Equation (4.35a) can be easily solved for X_1 giving

$$(1+\sigma)X_1 = \left(\frac{X_0}{2}\right)\Phi_1 = \left(\frac{\mathcal{F}'}{2}\right)^{1/2}\Phi_1, \tag{4.36}$$

which, as long as $\sigma \neq -1$, we can use to eliminate X_1 in (4.35b,c), leaving us with two equations for two unknown variables P_1 and Φ_1:

$$\begin{pmatrix} \mathcal{M}P_1' \\ \Phi_1' \end{pmatrix} = \mathcal{X}(\lambda) \begin{pmatrix} \frac{k^2}{2(1+\sigma)} & \frac{k^2}{4(1+\sigma)^2} - 1 \\ -k^2 & -\frac{k^2}{2(1+\sigma)} \end{pmatrix} \cdot \begin{pmatrix} \mathcal{M}P_1 \\ \Phi_1 \end{pmatrix}, \tag{4.37}$$

where we have introduced the function

$$\mathcal{X}(\lambda) = \frac{X_0'}{X_0} = \frac{\mathcal{F}''}{2\mathcal{F}'} = \frac{1 - 2(m-1)\lambda^3}{\lambda + (m-1)\lambda^4} = \frac{3 - 2\mathcal{M}}{\lambda\mathcal{M}}. \tag{4.38}$$

If $\sigma = -1$ on the other hand, (4.36) implies that $\Phi_1 = 0$. From (4.35) we obtain after some algebra, that in order to have non-zero perturbations we must have either axisymmetric perturbations with $k = 0$ (§4.3.1), or equal-viscosity fluids with $m = 1$ such that $\mathcal{M} = 1$ (§4.3.2). As we have already found solutions for both of these cases, we assume from now on that $\sigma \neq -1$ such that (4.37) holds.

4.4.2 Boundary conditions

The perturbation equations (4.37) are a linear second-order system of homogeneous ordinary differential equations and hence we expect two boundary conditions. Physically these are given by a condition on the perturbation flux at the origin $\xi = 0$, and a matching condition to the flux and pressure distribution ahead of the nose.

These boundary conditions are also homogeneous and so any constant rescaling of a solution is also a solution, i.e. if P_1, Φ_1 satisfy (4.37) so does $\delta P_1, \delta\Phi_1$ for an arbitrary amplitude scale δ. Therefore, (4.37) with its boundary conditions is an eigenvalue problem, where we will find an infinite discrete spectrum of eigenvalues $\sigma(k)$ for which both boundary conditions can be satisfied simultaneously.

Mathematically, to obtain the boundary conditions, we compute local expansions near the origin to find an appropriate boundary condition from (4.14a), and we solve the system ahead of the nose analytically to find a matching condition via (4.14d) and (4.14e).

Origin condition

The origin $\xi = 0$ corresponds to $\lambda = 1$, where the intruding fluid fills the the channel. This is a singular point of the equations since

$$\mathcal{X} \sim -\tfrac{1}{2}(1-\lambda)^{-1} + \frac{9-8m}{4m} + \cdots, \tag{4.39}$$

as $\lambda \to 1$.

Using this expansion in (4.37), we can find the leading-order terms as $\lambda \to 1$ for two linearly independent solutions for P_1 and Φ_1. For $k > 0$ these are

$$P_1 = \left(\frac{1}{k} - \frac{1}{2(1+\sigma)}\right)\frac{c_-}{m}(1-\lambda)^{-k/2} - \left(\frac{1}{k} + \frac{1}{2(1+\sigma)}\right)\frac{c_+}{m}(1-\lambda)^{k/2} + \cdots, \tag{4.40a}$$

$$\Phi_1 = c_-(1-\lambda)^{-k/2} + c_+(1-\lambda)^{k/2} + \cdots, \tag{4.40b}$$

where $c_\pm$ are constants of integration. If we also expand $X_0 = (2\mathcal{F}')^{1/2}$ as $\lambda \to 1$,

$$X_0 \sim \left(\frac{6}{m}(1-\lambda)\right)^{1/2} + \cdots, \tag{4.41}$$

we can see that the two solutions in (4.40) are asymptotically proportional to $\xi^{\pm k}$, which we recognise from the analysis near the origin of single-layer gravity currents in Chapter 3.

For the physical boundary condition, we must reject the solution that diverges, by setting $c_- = 0$. For $c_- = 0$ and $c_+ \neq 0$ equation (4.40) gives decaying perturbations, i.e. $P_1 \to 0$ and $\Phi_1 \to 0$ as $\lambda \to 1$, which matches the physical condition that the perturbations do not alter the given influx at the origin. Another way to write the boundary condition at the origin is to consider the ratio of pressure to flux perturbation, which gives

$$\lim_{\lambda\to 1}\frac{P_1}{\Phi_1} = -\frac{1}{m}\left(\frac{1}{k} + \frac{1}{2(1+\sigma)}\right). \tag{4.42}$$

Matching onto region ahead of the nose

Ahead of the nose the pressure obeys Laplace's equation and the flux is given by $\boldsymbol{q} = -\boldsymbol{\nabla} p$. This is linear and hence can be solved for the base state and perturbations separately.

From (4.34) we know that the base-state flux is given by $q_\xi = 1/\xi$. This results from a base-state pressure given by $p = -\log\xi$, with a possible constant ambient pressure which can be set to zero without loss of generality.

For the perturbations we propose a pressure proportional to $\mathrm{e}^{\mathrm{i}k\theta}$ as in the expansions (4.33), which leads to $p \propto \xi^{\pm k}$. Then, (4.14b), which imposes a decaying pressure gradient as $\xi \to \infty$, rejects the ξ^k solution and therefore we obtain $p \propto \xi^{-k}$ for the perturbation pressure ahead of the nose.

Combining these results for the base-state and perturbation pressure, and finding the corresponding radial fluxes, results in

$$p(\xi,\theta,\tau) = -\log\xi + \delta\xi^{-k}\mathrm{e}^{\mathrm{i}k\theta+\sigma\tau} + \cdots, \tag{4.43a}$$

$$\xi q_\xi(\xi,\theta,\tau) = 1 + \delta k\xi^{-k}\mathrm{e}^{\mathrm{i}k+\sigma\tau} + \cdots, \tag{4.43b}$$

where δ is the small amplitude of the perturbations ahead of the nose.

The boundary conditions are then given by demanding continuity of both radial flux and pressure at the nose. For this we need to evaluate the pressure and flux just behind and ahead of the nose from (4.33b,c) and (4.43), respectively. We assume that the shock height λ_* is not perturbed, which we will justify in §4.4.3. Hence, the nose position is given either by $\lambda = \lambda_*$ or equivalently by $\xi = X_0(\lambda_*) + X_1(\lambda_*)\,\mathrm{e}^{\mathrm{i}k\theta+\sigma\tau}$ as in (4.33a). Using these expressions for the position of the nose, together with (4.33b,c) and (4.43), then gives the linearised continuity conditions for the perturbation pressure and flux

$$P_1 + X_0^{-1}X_1 = \delta X_0^{-k}, \qquad \Phi_1 = \delta k X_0^{-k}, \tag{4.44}$$

evaluated at $\lambda = \lambda_*$. We then use (4.36) to eliminate X_1 giving

$$P_1 = \delta X_0^{-k}\left(1 - \frac{k}{2(1+\sigma)}\right), \qquad \Phi_1 = \delta k X_0^{-k}. \tag{4.45}$$

The amplitude δ can be eliminated between these two continuity conditions to yield the desired boundary condition for (4.37) at the nose:

$$\frac{P_1}{\Phi_1} = \frac{1}{k} - \frac{1}{2(1+\sigma)} \qquad \text{at} \qquad \lambda = \lambda_*. \tag{4.46}$$

4.4.3 Perturbing the shock height — mass conservation at the nose

Suppose we wanted to allow for the perturbation of the shock height $\lambda_* = \lambda_{\text{crit}}$. A priori one would argue that this is physically possible and hence should affect the eigenmodes and their growth rates. However, we shall show in this section that in fact linear perturbations to the shock height can only occur with growth rate $\sigma = -1$, which correspond to either axisymmetric or equal-viscosity flows (see §4.3.1 and §4.3.2 respectively).

To perturb the shock height, we expand λ_* as

$$\lambda_* = \lambda_{\text{crit}} + \lambda_1 \mathrm{e}^{\mathrm{i}k\theta+\sigma\tau} + \cdots , \tag{4.47}$$

in line with the expansions (4.33). This then gives the nose position $\xi_* = \xi(\lambda_*, \theta, \tau)$ as

$$\xi_* = X_0|_{\lambda_{\text{crit}}} + (X_1 + X_0'\lambda_1)|_{\lambda_{\text{crit}}} \mathrm{e}^{\mathrm{i}k\theta+\sigma\tau} + \cdots . \tag{4.48}$$

We then want to substitute this expansion of the nose position into the boundary condition (4.14c), which governs mass conservation through the nose. Before we proceed with this though, we note that the unit normal $\boldsymbol{n}$ can be expanded as

$$\boldsymbol{n} = \left[1 + \left(\frac{\partial \xi_*}{\partial \theta}\right)^2\right]^{-1/2} \begin{pmatrix} 1 \\ \frac{\partial \xi_*}{\partial \theta} \end{pmatrix} \sim \begin{pmatrix} 1 \\ \frac{\partial \xi_*}{\partial \theta} \end{pmatrix} + \cdots , \tag{4.49}$$

and hence $\boldsymbol{n}\cdot\boldsymbol{q} \approx q_\xi$ and $\boldsymbol{n}\cdot\boldsymbol{e}_\xi \approx 1$ with corrections being quadratic in the perturbation quantities and therefore negligible.

Then, by using (4.48) and (4.49), we expand (4.14c) giving

$$0 = \left(\frac{\mathcal{F}_{\text{crit}}}{\lambda_{\text{crit}}}\right)\frac{\Phi_0}{X_0} - \frac{X_0}{2}, \tag{4.50a}$$

$$\sigma(X_1 + X_0'\lambda_1) = \frac{X_0}{2}\left(\frac{\Phi_1}{\Phi_0} - \frac{X_1 + X_0'\lambda_1}{X_0} + \left[\frac{\mathcal{F}_{\text{crit}}'}{\mathcal{F}_{\text{crit}}} - \frac{1}{\lambda_{\text{crit}}}\right]\lambda_1\right) - \frac{X_1 + X_0'\lambda_1}{2}, \tag{4.50b}$$

where all quantities are evaluated at $\lambda = \lambda_{\text{crit}}$. We note that the Oleinik condition (4.23), which defines the base-state shock height λ_{crit}, implies that $\lambda_{\text{crit}}\mathcal{F}_{\text{crit}}' = \mathcal{F}_{\text{crit}}$. Furthermore, the base-state flux is given by $\Phi_0 = 1$ from (4.34) and we can eliminate X_1 and Φ_1 by using (4.36). Therefore, (4.50b) becomes

$$(1 + \sigma)X_0'\lambda_1 = 0, \tag{4.51}$$

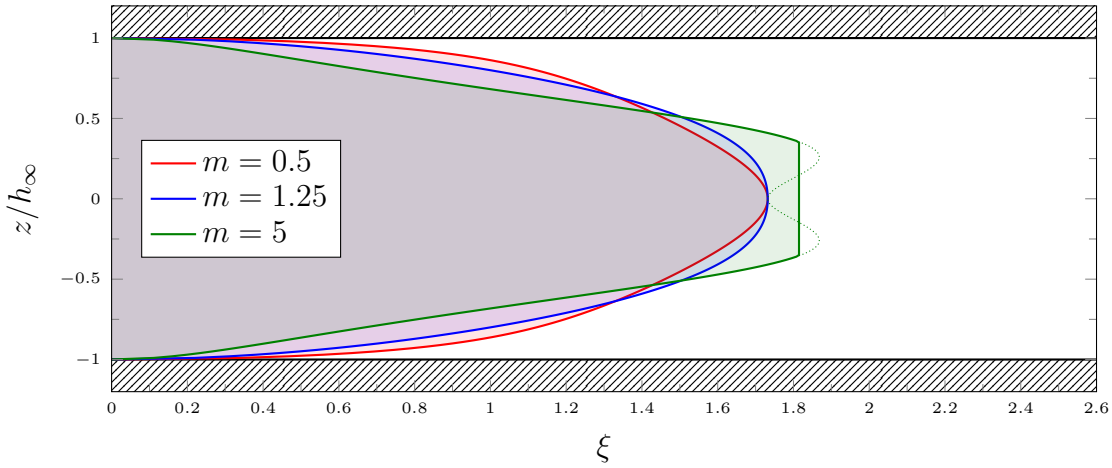

Fig. 4.3 Base-state profiles (solid) of the intrusions, $\xi_0(\lambda)$, for viscosity ratios $m \in \{0.5, 1.25, 5\}$ including the non-monotonic profile for $m = 5$ (dotted) if the shock were to be ignored.

and, as $X_0' \neq 0$ at the nose, we must either have $\sigma = -1$ or $\lambda_1 = 0$. If $\sigma = -1$ we have already shown in §4.4.1 that either $k = 0$ or $m = 1$ and we have found analytical solutions for these cases in §4.3.1 and §4.3.2, respectively.

We conclude that normal-mode perturbations of the shock height, must have a growth rate of $\sigma = -1$, and therefore are stable and decay. Therefore, we do not consider these modes and instead assume that the shock height is not perturbed.

4.5 Numerical results

We can solve (4.37) with boundary conditions (4.42) and (4.46) numerically using the continuation software package AUTO.

Figure 4.3 shows the analytical base-state profiles (4.34) for $m \in \{0.5, 1.25, 5\}$ including the non-monotonic profile for $m = 5 > 3/2$ if the shock were to be ignored.

Figure 4.4 shows the first three eigenmodes $n \in \{0, 1, 2\}$ in terms of P_1 and Φ_1 for azimuthal wavenumbers $k \in \{1, 5, 25, 100\}$ and viscosity ratios $m \in \{0.15, 1.25, 5\}$ as functions of the radial similarity variable ξ. These solution profiles show that there are three distinct cases: firstly, if the intruding fluid is more viscous $m < 1$, we observe that the signs of P_1 and Φ_1 are the same and hence we can describe the two perturbation variables as in phase with each other. As the wavenumber k increases, the perturbations become more localised at some interior position between the origin and the nose. Also, while for small k we find that $|P_1| > |\Phi_1|$ we observe that as k become large this reverses. Secondly, if the intruding fluid is less viscous, but not sufficiently so for the

base state to have developed a shock, $1 < m < 3/2$, we observe that the signs of P_1 and Φ_1 are now the opposite and hence we can describe the two perturbation variables as out of phase by π. Similarly, as the wavenumber k increases, the perturbations become more localised. However, now this localisation occurs at the nose. We also note that in this case $|P_1| > |\Phi_1|$ even for large k, i.e. the pressure perturbations are always larger than the flux perturbations. Finally, if the intruding fluid is sufficiently less viscous such that the base state does develop a shock, $m > 3/2$, we observe out-of-phase perturbations which become localised near the nose as k becomes large. In this case, we also observe, similar to the first case of a more viscous intrusion, that as k increases the perturbations switch from $|P_1| > |\Phi_1|$ to $|P_1| < |\Phi_1|$.

Figure 4.5 shows the growth rates σ of the first three eigenmodes labelled by an integer index $n \in \{0, 1, 2\}$ as functions of the azimuthal wavenumber k. The depicted viscosity ratios $m \in \{0.15, 1.25, 5\}$ were chosen to fall into the three cases: more viscous intrusion, less viscous without shock, and less viscous with shock, as discussed above. In the first case, $m = 0.15$, figure 4.5 shows that the perturbations have growth rates of $\sigma < -1$, with the fundamental mode $n = 0$ being the most stable perturbation mode. As k increases the perturbations becomes more stable. In the second case, $m = 1.25$, we observe that the first three perturbation modes are stable over the range of k depicted in figure 4.5 with growth rates $-1 < \sigma < 0$. Now the fundamental mode $n = 0$ is the most unstable perturbation mode and as k increases the perturbations become less stable, with the growth rates possibly approaching constant values as $k \to \infty$. The final case, $m = 5$, is similar to the second case, except that the fundamental mode $n = 0$ now becomes unstable at approximately $k \approx 18$ after which the growth rate diverges as $k \to \infty$. This divergence for large k is to be expected as the model used is based on lubrication theory thereby neglecting the vertical structure, which becomes significant once the azimuthal length scale $1/k$ becomes comparable to the length scale associated with the vertical shock λ_*.

To confirm that $m_{\text{crit}} = 3/2$ is indeed the critical viscosity ratio for the stability, and therefore that the occurrence of shocks in the base state is crucial to form an instability, we compute the curve of marginal stability $\sigma = 0$ in terms of k as a function of m, see figure 4.6. This shows that indeed for $m > 3/2$ there is always a sufficiently large k such that the flow becomes unstable, while for $m < 3/2$ the perturbations are stable for all k. For comparison figure 4.6 also depicts asymptotic results derived in the large-wavenumber limit $k \to \infty$, which agree excellently with the numerical results and further confirm that indeed $m_{\text{crit}} = 3/2$.

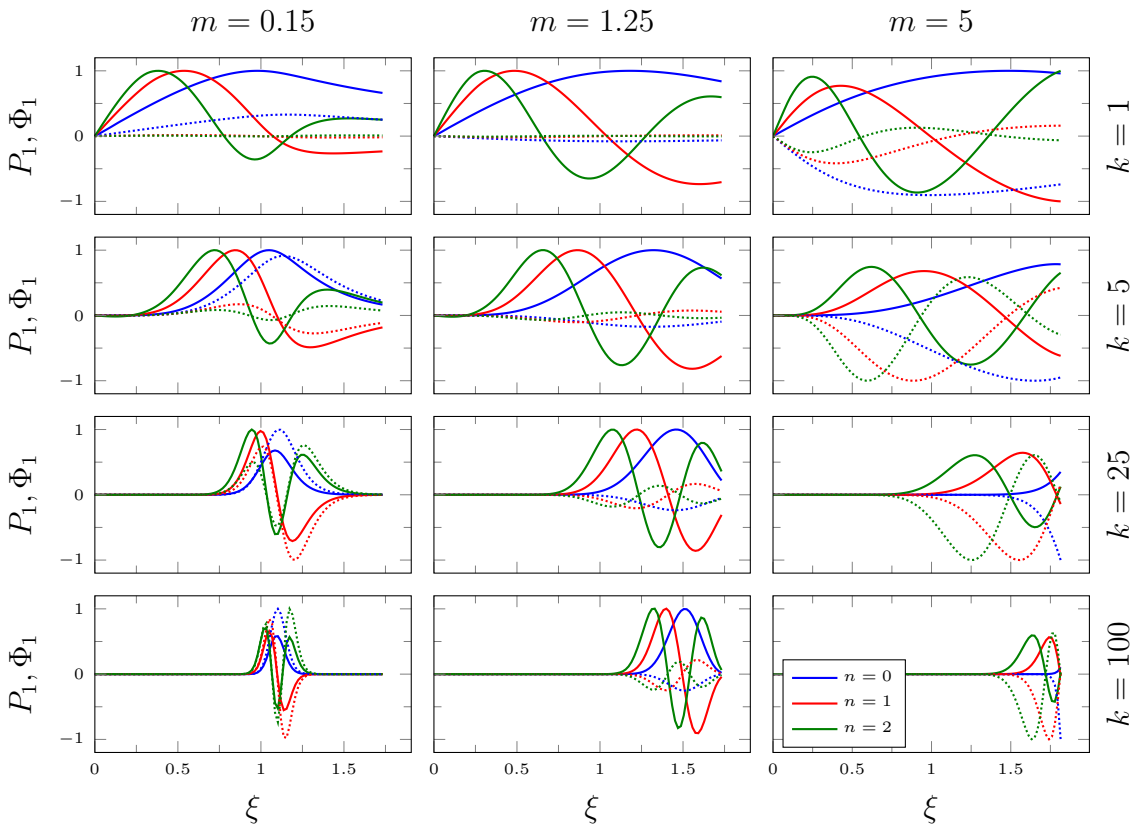

Fig. 4.4 Numerical solutions for the first three eigenmodes $n \in \{0, 1, 2\}$ in terms of the perturbation pressure P_1 (solid) and perturbation flux Φ_1 (dotted) for wavenumbers $k \in \{1, 5, 25, 100\}$ and viscosity ratios $m \in \{0.15, 1.25, 5\}$.

We note that physically n is equal to the number of zeros of the perturbations and therefore corresponds in some way to a radial length scale, while k defines an azimuthal length scale. Hence, as $n \to \infty$ for fixed k the azimuthal structure becomes insignificant in comparison to the radial structure and therefore the growth rate approaches that of a kinematic wave solution as in §4.3 resulting in $\sigma \to -1$. Figure 4.5 matches this trend and we can compute further eigenmodes, which do indeed confirm this conjecture.

To summarise, the numerical results confirm the conjecture of previous studies, that the vertical shocks occurring for $m > 3/2$ give rise to an instability comparable to the Saffman–Taylor instability, and also that more viscous intrusions $m < 1$ are stable. Additionally, they provide a theoretical basis for experimental observations that less viscous intrusions with $1 < m < 3/2$ are stable, which should be contrasted to the classical Saffman–Taylor instability. Finally, these results show that there is only a single unstable eigenmode, namely the fundamental mode $n = 0$, while all other perturbations decay in time and are stable.

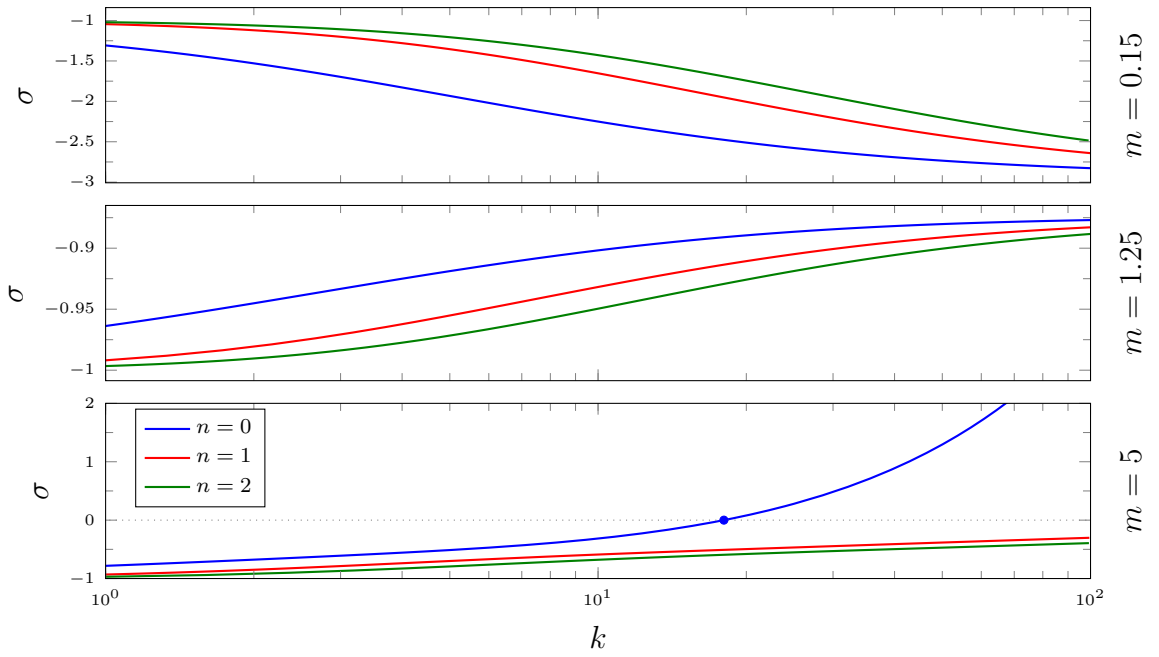

Fig. 4.5 The growth rates σ corresponding to the first three eigenmodes $n \in \{0, 1, 2\}$ with viscosity ratios $m \in \{0.15, 1.25, 5\}$ as a function of the azimuthal wavenumber k on a log-axis. For $m = 5$, the fundamental mode $n = 0$ is unstable if k exceeds a certain value of marginal stability where $\sigma = 0$ (blue dot).

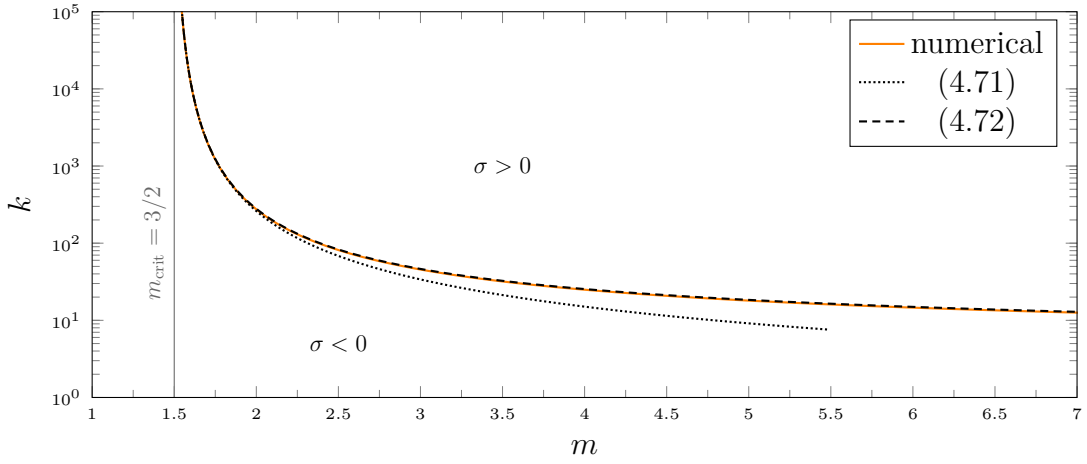

Fig. 4.6 The marginal-stability contour $\sigma = 0$ for the fundamental mode $n = 0$ on a (m, k)-diagram compared to two formulae for the asymptotic curves (4.71) and (4.72) obtained by the two methods in §4.6.2.

4.6 The limit of large azimuthal wavenumber ($k \gg 1$) for $m > 3/2$

For the unstable cases with a shock ($m > 3/2$), we perform an asymptotic analysis for large azimuthal wavenumber $k \gg 1$ to confirm the nature of the instability as $m \to 3/2$. For this analysis, it is advantageous to work with a single dependent variable only, and hence we solve the Φ_1'-part of (4.37) for the perturbation pressure P_1 resulting in

$$\mathcal{M}P_1 = -\frac{\Phi_1'}{k^2\mathcal{X}} - \frac{\Phi_1}{2(1+\sigma)}, \tag{4.52}$$

which we then use to eliminate P_1 in (4.37) resulting in a second order differential equation for the perturbation flux Φ_1:

$$\Phi_1'' - \left(\frac{\mathcal{X}'}{\mathcal{X}} + \frac{\mathcal{M}'}{\mathcal{M}}\right)\Phi_1' - k^2\left(\mathcal{X}^2 + \frac{\mathcal{X}\mathcal{M}'}{2(1+\sigma)\mathcal{M}}\right)\Phi_1 = 0. \tag{4.53}$$

Similarly, we obtain boundary conditions from eliminating P_1 from (4.46) at the nose, and from selecting perturbations which decay towards the origin as discussed in §4.4.2:

$$\left(\frac{\mathcal{M}_* - 1}{2(1+\sigma)} - \frac{\mathcal{M}_*}{k}\right)\Phi_1 - \left(\frac{1}{k^2\mathcal{X}_*}\right)\Phi_1' = 0 \quad \text{at} \quad \lambda = \lambda_*, \tag{4.54a}$$

$$\Phi_1 \to 0 \quad \text{as} \quad \lambda \to 1. \tag{4.54b}$$

We note that defining P_1 via (4.52) also shows that, as $k \to \infty$, the perturbation flux and pressure are exactly out of phase by π for $\sigma > -1$ (i.e. for $m > 1$), and in phase for $\sigma < -1$ (i.e. for $m < 1$).

To find asymptotic solutions for the perturbations in the limit $k \to \infty$, we use the WKB method, as we expect oscillatory behaviour in a confined region near the nose (recall $m > 3/2$) and decaying behaviour away from it. In Appendix 4.A we analyse the same limit $k \to \infty$, but using a local asymptotic expansion instead of the WKB method, in order to independently confirm the results.

4.6.1 WKB method

For the WKB analysis, we write $\Phi_1 = \mathrm{e}^{S(\lambda)}$ and expand $S(\lambda) = kS_0(\lambda) + S_1(\lambda) + \cdots$. Substituting this expansion into (4.53) gives differential equations for the S_i at the

different orders of k:

$$O\left(k^2\right): \qquad S_0' = \pm\left(\mathcal{X}^2 + \frac{\mathcal{X}\mathcal{M}'}{2(1+\sigma)\mathcal{M}}\right)^{1/2}, \tag{4.55a}$$

$$O(k): \qquad S_1' = \tfrac{1}{2}\left(\frac{\mathcal{X}'}{\mathcal{X}} + \frac{\mathcal{M}'}{\mathcal{M}}\right) - \frac{S_0''}{2S_0'}. \tag{4.55b}$$

We then integrate these resulting in

$$O\left(k^2\right): \quad S_0 = \pm\int\left(\mathcal{X}^2 + \frac{\mathcal{X}\mathcal{M}'}{2(1+\sigma)\mathcal{M}}\right)^{1/2}\mathrm{d}\lambda, \tag{4.56a}$$

$$O(k): \quad S_1 = c - \tfrac{1}{2}\log\left|\frac{S_0'}{\mathcal{M}\mathcal{X}}\right| = c + \tfrac{1}{2}\log|\mathcal{M}| - \tfrac{1}{4}\log\left|1 + \frac{\mathcal{M}'}{2(1+\sigma)\mathcal{M}\mathcal{X}}\right|, \tag{4.56b}$$

where c is a constant of integration for S_1. The constant of integration for S_0 is hidden in the choice of bounds on the indefinite integral in (4.56a).

We note that the solution for S_0 is either real or purely imaginary resulting from a positive or negative $(S_0')^2$. As $\Phi_1 \propto \mathrm{e}^{kS_0}$, this corresponds to exponential or oscillatory behaviour for the perturbations, respectively. We define a turning point $\lambda_\circ$ as a zero of $(S_0')^2$, which therefore corresponds to a point where the behaviour of the perturbations switches between exponential and oscillatory. Expanding $(S_0')^2 = 0$ by using (4.55a) and substituting the definitions of $\mathcal{M}$ and $\mathcal{X} = \mathcal{F}''/(2\mathcal{F}')$ from (4.5), results in

$$\begin{aligned}\sigma &= -1 - \frac{\mathcal{M}_\circ'}{2\mathcal{X}_\circ\mathcal{M}_\circ} \\ &= -1 - \frac{3(m-1)\left(1-\lambda_\circ\right)\lambda_\circ\left(1+\lambda_\circ+2(m-1)\lambda_\circ^2\right)}{2(2m-3) - 12(m-1)\lambda_\circ - 4(m-1)(2m-3)\lambda_\circ^3 + 6(m-1)^2\lambda_\circ^4}.\end{aligned} \tag{4.57}$$

We note two special cases for this: firstly, if $\lambda_\circ = 1$ we get $\sigma = -1$ and, secondly, if $\lambda_\circ = \lambda_{\mathrm{crit}}$ we can show that $\sigma = 0$. The second observation can be derived by recalling that λ_{crit} satisfies $\lambda\mathcal{F}' = \mathcal{F}$. Some algebra then reveals that (4.57) is zero for such a λ_{crit}. Therefore, for a turning point to exist within the current ($\lambda_{\mathrm{crit}} < \lambda_\circ < 1$), we must have $-1 < \sigma < 0$. This implies that any eigenmode with oscillations (i.e. $n \geq 1$) must be stable in the limit of large k. Note that all perturbations have an exponentially decaying region towards the origin, and therefore oscillatory behaviour requires the existence of a turning point.

Figure 4.7 shows σ given by (4.57) as a function of m, for various turning-point positions with $\lambda_* < \lambda_\circ < 1$ resulting in $-1 < \sigma < 0$. From the figure we deduce that for any combination of m and σ with $-1 < \sigma < 0$, there exists exactly one turning

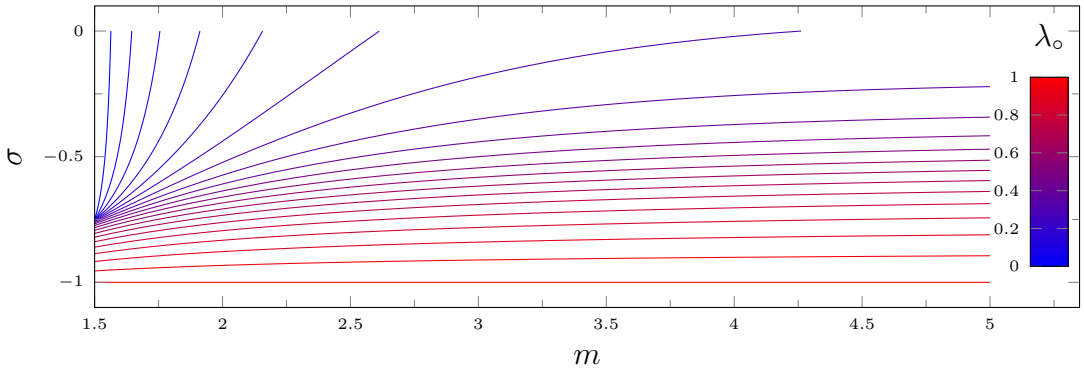

Fig. 4.7 Contours of the turning point $\lambda_\circ$ as a function of the viscosity ratio m and the growth rate σ. The domain is restricted to $m > 3/2$ and $-1 < \sigma < 0$, which ensures that $\lambda_{\text{crit}} < \lambda_\circ < 1$ (see text).

point. Therefore, all modes with oscillations ($n \geq 1$) have exactly one oscillatory region towards the nose and an exponential region towards the origin separated by a single turning point.

Without oscillatory region: the fundamental mode ($n = 0$)

Firstly, let us suppose that $\sigma > 0$ and therefore that the solution is exponentially decaying over the entire domain without any turning point within $\lambda_* < \lambda_\circ < 1$. We choose the negative root for S_0 in (4.56a) to ensure decay rather than growth towards the origin, which results in an asymptotic solution for the perturbation flux given by

$$\Phi_1 \sim \delta \mathcal{M}^{1/2} \left(1 + \frac{\mathcal{M}'}{2(1+\sigma)\mathcal{M}\mathcal{X}}\right)^{-1/4} \exp\left(-k \int_{\lambda_*}^{\lambda} \left[\mathcal{X}^2 + \frac{\mathcal{X}\mathcal{M}'}{2(1+\sigma)\mathcal{M}}\right]^{1/2} \mathrm{d}\lambda\right), \tag{4.58}$$

where $\delta = \mathrm{Re}(c)$ is the constant amplitude. In this case $\mathrm{Im}(c) = 0$ to provide a real solution for Φ_1.

Enforcing the boundary condition (4.54a) at the nose directly on this exponential solution (4.58) results in the condition

$$0 = \frac{\mathcal{M}_* - 1}{2(1+\sigma)} - \frac{1}{k}\left(\mathcal{M}_* + \frac{S_0'(\lambda_*)}{\mathcal{X}_*}\right) - \frac{S_1'(\lambda_*)}{k^2 \mathcal{X}_*} + O\left(k^{-3}\right), \tag{4.59}$$

which determines the growth rate σ in terms of the viscosity ratio m and the azimuthal wavenumber k.

Substituting S_0' and S_1' from (4.55) and some rearranging results in an expansion for the growth rate σ:

$$\begin{aligned}\sigma &= \frac{(\mathcal{M}_* - 1)\,k}{2\,(\mathcal{M}_* + 1)} + \left(-1 - \frac{\mathcal{M}_*'}{2\,(\mathcal{M}_* + 1)^2\,\mathcal{X}_*}\right) + O\left(k^{-1}\right) \\ &= \underbrace{\left(\frac{(m-1)\lambda_*^3}{4 + 2(m-1)\lambda_*^3}\right)}_{>0} k + \left(-1 + \frac{1 + (m-1)\lambda_*^3}{\left(2 + (m-1)\lambda_*^3\right)^2}\right) + O\left(k^{-1}\right), \end{aligned} \tag{4.60}$$

where we have used $\mathcal{M}_*' = -2\mathcal{X}_*\mathcal{M}_*$, which can be derived from the definition of $\lambda_* = \lambda_{\text{crit}}$ satisfying $\lambda\mathcal{F}' = \mathcal{F}$. We note that this looks very much like a result obtained through a local series expansion, and in fact we obtain the exact same series in Appendix 4.A.

Therefore, we have shown that the growth rate (4.60) of the fundamental mode $n = 0$ is positive, and grows like $O(k)$ for large k. This implies that, as long as $m > 3/2$, there is always at least one unstable mode, with the most unstable behaviour at $k \to \infty$ confirming the numerical results. In fact, the asymptotic result (4.60) for the growth rate σ of the fundamental mode $n = 0$ compares very well to the numerical result, see §4.6.3 and in particular figure 4.8.

We finally note that, as S_0 and S_1 depend on σ, which is given in terms of an expansion in k (4.60), the solution (4.58) is not strictly speaking well-ordered. Therefore, we substitute (4.60) into (4.58), which results in the now well-ordered expansion

$$\Phi_1 \sim \delta\mathcal{M}^{1/2} \exp\left(k\int_{\lambda_*}^{\lambda} \mathcal{X}\,\mathrm{d}\lambda + \frac{\mathcal{M}_* + 1}{2\,(\mathcal{M}_* - 1)}\int_{\lambda_*}^{\lambda} \frac{\mathcal{M}'}{\mathcal{M}}\,\mathrm{d}\lambda\right) \sim \tilde{\delta}\mathcal{M}^{\frac{\mathcal{M}_*}{\mathcal{M}_* - 1}} X_0^k + O\left(k^{-1}\right), \tag{4.61}$$

where we have recalled that $\mathcal{X} = X_0'/X_0$, and where $\tilde{\delta}$ is a rescaled constant amplitude. This shows that $\Phi_1 \sim \xi^k$ near the origin, thereby recovering the behaviour of the perturbations near the origin previously derived in §4.4.2.

With oscillatory region: higher modes ($n \geq 1$)

Now suppose $0 < \sigma < -1$ such that there is a turning point with $\lambda_{\text{crit}} < \lambda_\circ < 1$. Similarly to (4.58), the perturbation flux Φ_1 decays exponentially towards the origin where $\lambda > \lambda_\circ$, but now there also is a oscillatory solution towards the nose where $\lambda_* < \lambda < \lambda_\circ$. We split our analysis into these two regions and obtain the perturbation

flux Φ_1 as

$$\Phi_1 \sim \delta_1 \mathcal{M}^{1/2} \left(-1 - \frac{\mathcal{M}'}{2(1+\sigma)\mathcal{M}\mathcal{X}} \right)^{-1/4} \sin\left(\alpha - k \int_{\lambda_\circ}^{\lambda} \left[-\mathcal{X}^2 - \frac{\mathcal{X}\mathcal{M}'}{2(1+\sigma)\mathcal{M}} \right]^{1/2} \mathrm{d}\lambda \right) \quad \text{for } \lambda_* \leq \lambda < \lambda_\circ, \tag{4.62a}$$

$$\Phi_1 \sim \delta_2 \mathcal{M}^{1/2} \left(1 + \frac{\mathcal{M}'}{2(1+\sigma)\mathcal{M}\mathcal{X}} \right)^{-1/4} \exp\left(-k \int_{\lambda_\circ}^{\lambda} \left[\mathcal{X}^2 + \frac{\mathcal{X}\mathcal{M}'}{2(1+\sigma)\mathcal{M}} \right]^{1/2} \mathrm{d}\lambda \right) \quad \text{for } \lambda_\circ < \lambda \leq 1, \tag{4.62b}$$

where $\delta_i = \mathrm{Re}\,(c_i)$ are the constant amplitudes and $\alpha = \mathrm{Im}\,(c_1)$ is a constant phase shift. Again we must have $\mathrm{Im}\,(c_2) = 0$ to ensure a real solution in the decaying region.

As typical for the WKB method, we need to match the two regions across the turning point $\lambda_\circ$ via Airy functions giving the phase shift α and a condition relating the amplitudes δ_i:

$$\alpha = \tfrac{1}{4}\pi, \qquad \delta_1 = 2\delta_2. \tag{4.63}$$

We then need to evaluate the nose boundary condition (4.54a), which to leading order gives $\Phi_1 \sim O\left(k^{-1}\right) \ll 1$ at the nose $\lambda \to \lambda_*$. Hence,

$$k \int_{\lambda_*}^{\lambda_\circ} \left[-\mathcal{X}^2 - \frac{\mathcal{X}\mathcal{M}'}{2(1+\sigma)\mathcal{M}} \right]^{1/2} \mathrm{d}\lambda = \left(n - \tfrac{1}{4} \right) \pi, \tag{4.64}$$

where $n \in \{1, 2, 3, \dots\}$ is a positive integer corresponding to the eigenmode index. For each viscosity ratio m, this is a relationship between the turning point $\lambda_\circ$ and the growth rate σ, which, together with (4.57), can be used to determine both $\lambda_\circ$ and σ in terms of m.

The two equations (4.57) and (4.64) are not particularly easy to interpret. Therefore, we instead attempt to find an expansion for the growth rate σ as $k \to \infty$ in terms of powers of k. This is done by first assuming that $\lambda_\circ - \lambda_* \ll 1$ such that all oscillations are confined to a region very close to the nose, and then expanding (4.57):

$$\sigma = -1 - \left(\underbrace{\left[\frac{\mathcal{M}'}{2\mathcal{X}\mathcal{M}} \right]_*}_{-1} + \left[\frac{\mathcal{M}'}{2\mathcal{X}\mathcal{M}} \right]_*' (\lambda_\circ - \lambda_*) + \cdots \right) = -\left[\frac{\mathcal{M}'}{2\mathcal{X}\mathcal{M}} \right]_*' (\lambda_\circ - \lambda_*) + \cdots . \tag{4.65}$$

This shows that σ and $\lambda_\circ - \lambda_* \ll 1$ have the same order of magnitude and therefore $|\sigma| \ll 1$. We then consider the second equation (4.64), which contains an integral over the interval $\lambda \in [\lambda_*, \lambda_\circ]$, where therefore $\lambda - \lambda_* \ll 1$. By using this together with $|\sigma| \ll 1$, we expand the integrand of (4.64) resulting in

$$\begin{aligned}\left[-\mathcal{X}^2 - \frac{\mathcal{X}\mathcal{M}'}{2(1+\sigma)\mathcal{M}}\right]^{1/2} \\ = |\mathcal{X}_*| \left(-1 - \left\{ \underbrace{\left[\frac{\mathcal{M}'}{2\mathcal{X}\mathcal{M}}\right]_*}_{-1} + \underbrace{\left[\frac{\mathcal{M}'}{2\mathcal{X}\mathcal{M}}\right]_*'}_{-\sigma/(\lambda_\circ-\lambda_*)} (\lambda-\lambda_*) + \cdots \right\} \{1-\sigma+\cdots\} \right)^{1/2} \\ = |\mathcal{X}_*| \, (-\sigma)^{1/2} \left(1 - \frac{\lambda-\lambda_*}{\lambda_\circ-\lambda_*} + \cdots\right)^{1/2}. \quad (4.66)\end{aligned}$$

Therefore, in the limit of a turning point close to the nose $\lambda_\circ - \lambda_* \ll 1$, (4.64) is given to leading order by

$$\left(n - \tfrac{1}{4}\right)\pi = k\,|\mathcal{X}_*|\,(-\sigma)^{1/2} \underbrace{\int_{\lambda_*}^{\lambda_\circ} \left(1 - \frac{\lambda-\lambda_*}{\lambda_\circ-\lambda_*}\right)^{1/2} \mathrm{d}\lambda}_{=\frac{2}{3}(\lambda_\circ-\lambda_*)} + \cdots, \quad (4.67)$$

resulting in the eigenvalues

$$\sigma = -\left(\frac{2\pi}{3\,|\mathcal{X}_*|}\left[n-\tfrac{1}{4}\right]\left[\frac{\mathcal{M}'}{2\mathcal{X}\mathcal{M}}\right]_*'\right)^{2/3} k^{-2/3} + \cdots < 0. \quad (4.68)$$

This shows that $\sigma = O\left(k^{-2/3}\right)$ and hence $|\sigma| \ll 1$ confirming our assumption $\lambda_\circ - \lambda_* \ll 1$ in the limit of large k. We again note that a similar expansion is obtained by a local asymptotic expansion in Appendix 4.A.

This shows that all non-fundamental perturbation modes $n \geq 1$ have a negative growth rate $\sigma < 0$ and are therefore stable in the limit of large k. It also confirms that the perturbations indeed become localised near the nose for $m > 3/2$, with an associated length scale $\lambda_\circ - \lambda_* = O\left(k^{-2/3}\right)$.

4.6.2 Estimating marginal stability

To confirm that the onset of instability indeed occurs at $m = 3/2$, we want to investigate the curve of marginal stability, i.e. the relationship between the wavenumber k and the viscosity ratio m defined by a most unstable eigenmode with zero growth rate $\sigma = 0$.

We recall that the most unstable eigenmode is always the fundamental mode $n = 0$ with a growth rate which is asymptotically given by (4.60), and therefore we want to solve

$$0 = \left(\frac{(m-1)\lambda_*^3}{4 + 2(m-1)\lambda_*^3} \right) k + \left(-1 + \frac{1 + (m-1)\lambda_*^3}{(2 + (m-1)\lambda_*^3)^2} \right) + O\left(k^{-1}\right), \tag{4.69}$$

in terms of either $k(m)$ or $m(k)$.

Firstly, as we expect the critical viscosity ratio for the onset of instability to be given by $m_{\text{crit}} = 3/2$, we propose a series expansion for m as follows

$$m = \tfrac{3}{2} + m_1 k^{-1/3} + m_2 k^{-2/3} + m_3 k^{-1} + O\left(k^{-4/3}\right). \tag{4.70}$$

The reason we chose powers of $k^{-1/3}$ instead of simply k^{-1}, is to accommodate for the λ_*^3 terms in (4.69) and the fact that $\lambda_* = O(m - 3/2)$ as $m \to 3/2$, which can be derived from the definition (4.23). Substituting the expansion (4.70) into (4.69) results in equations at the various orders in k which are easily solved to obtain a series solution for $m(k)$ given by

$$m = \tfrac{3}{2} + \tfrac{9}{8}\left(\frac{k}{6}\right)^{-1/3} + \tfrac{27}{16}\left(\frac{k}{6}\right)^{-2/3} + \tfrac{243}{128}\left(\frac{k}{6}\right)^{-1} + O\left(k^{-4/3}\right). \tag{4.71}$$

Alternatively, if we assume that all higher-order terms in (4.69) remain small compared to the two leading-order terms, even as $m \to 3/2$, we can neglect those terms to obtain an approximate solution for $k(m)$ given by

$$0 \approx \left(\frac{(m-1)\lambda_*^3}{4 + 2(m-1)\lambda_*^3} \right) k + \left(-1 + \frac{1 + (m-1)\lambda_*^3}{(2 + (m-1)\lambda_*^3)^2} \right)$$
$$\Rightarrow \qquad k \approx 2 + \frac{3}{(m-1)\lambda_*^3} - \frac{1}{2 + (m-1)\lambda_*^3}. \tag{4.72}$$

This is consistent with $m_{\text{crit}} = 3/2$, since $\lambda_* \to 0$ as $m \to 3/2$ resulting in $k \to \infty$, which implies that for $m = 3/2$ there are no marginally stable eigenmodes and certainly no unstable ones either.

Although, the second method makes assumptions on higher-order terms, which we did not calculate, it does provide a remarkably good approximation to the curve of marginal stability, even for relatively small wavenumber k, see figure 4.6. We also note that (4.72) is equivalent to (4.71) to the order shown.

4.6.3 Comparison between asymptotics and numerics

Figure 4.8 compares the numerical and asymptotic growth rates σ as functions of k for the first three eigenmodes $n \in \{0, 1, 2\}$ with viscosity ratio $m = 5$. The figure shows excellent agreement of the asymptotic results obtained via the WKB method, which are given by (4.60) for the fundamental solution $n = 0$, and by (4.64) together with (4.57) for all higher modes $n \geq 1$. The figure also shows the results of using a local asymptotic expansion obtained in Appendix 4.A, which for the fundamental mode $n = 0$ were exactly the same as the WKB results, and for all higher modes $n \geq 1$ related to the large-k expansion (4.68) of the WKB results. As a consequence, the local-asymptotic-expansion results compare well to the WKB results for very large k, however, we were unable to extend the full numerical results to similarly large k to allow any direct comparison between the numerical and local-asymptotic-expansion results. This shows that the WKB method is much better suited to approximate the large-k limit compared to the method of using a local asymptotic expansions, with results being valid over a much wider range of k. We note the sharp dip exhibited by the growth rate of the fundamental mode $n = 0$ at approximately $k = 18$, which is due to a zero in the growth rate $\sigma = 0$ and the choice of logarithmically scaled axes.

Figure 4.9 compares the numerical and asymptotic WKB solutions for the first three eigenmodes $n \in \{0, 1, 2\}$, with viscosity ratio $m = 5$ and wavenumber $k = 100$, in terms of the physical variables P_1 and Φ_1 and their ratio P_1/Φ_1. We see that the WKB method predicts the the profiles very well, except near the singular region of the turning point $\lambda_\circ$, which is expected when using this method. To avoid these turning-point singularities, we would need to include the local Airy-function behaviour.

4.7 Discussion & Conclusions

In this chapter, we have derived the equations for the evolution of a fluid intruding into a Hele-Shaw cell filled with another fluid of the same density but differing viscosity, neglecting both diffusion and surface tension. We have utilised a change of variables to the relative fluid fraction λ as independent variable, allowing us to derive better conditioned equations with explicit analytic solutions for the base state. We have recovered the same shock structure for the axisymmetric steady base state, as reported by Yang and Yortsos (1997), for an intruding fluid which is sufficiently less viscous than the ambient fluid ($m > 3/2$).

Numerically solving for the linear perturbations revealed that the occurrence of a shock in the base state is crucial for an instability to form. In the model presented, all

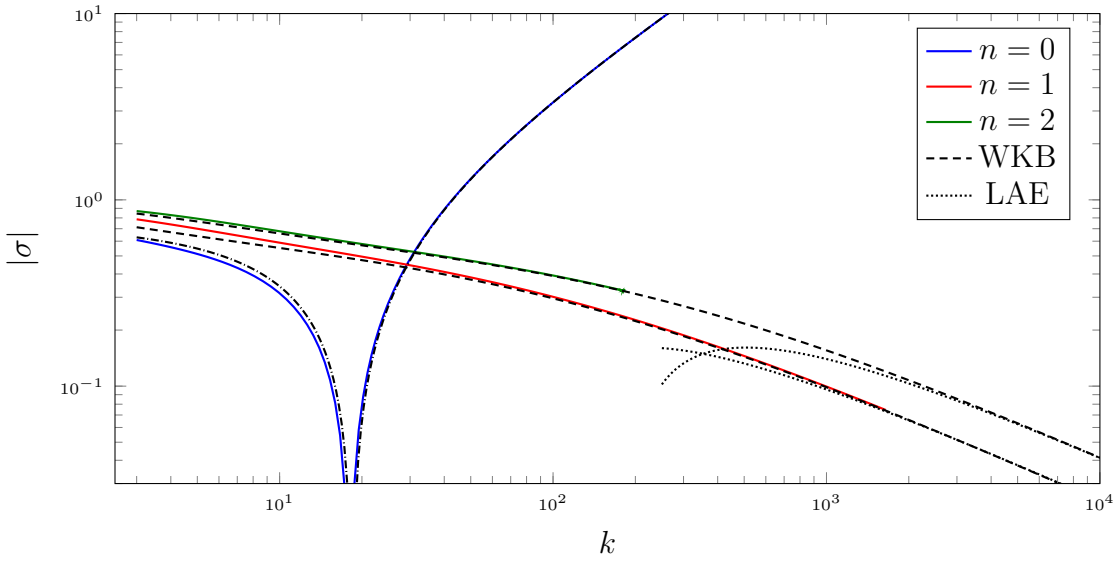

Fig. 4.8 Comparison of the numerically computed growth rate σ as a function of k for $n \in \{0, 1, 2\}$ and $m = 5$ (solid colour) with the corresponding WKB solution (dashed) and the local-asymptotic-expansion result (LAE; dotted).

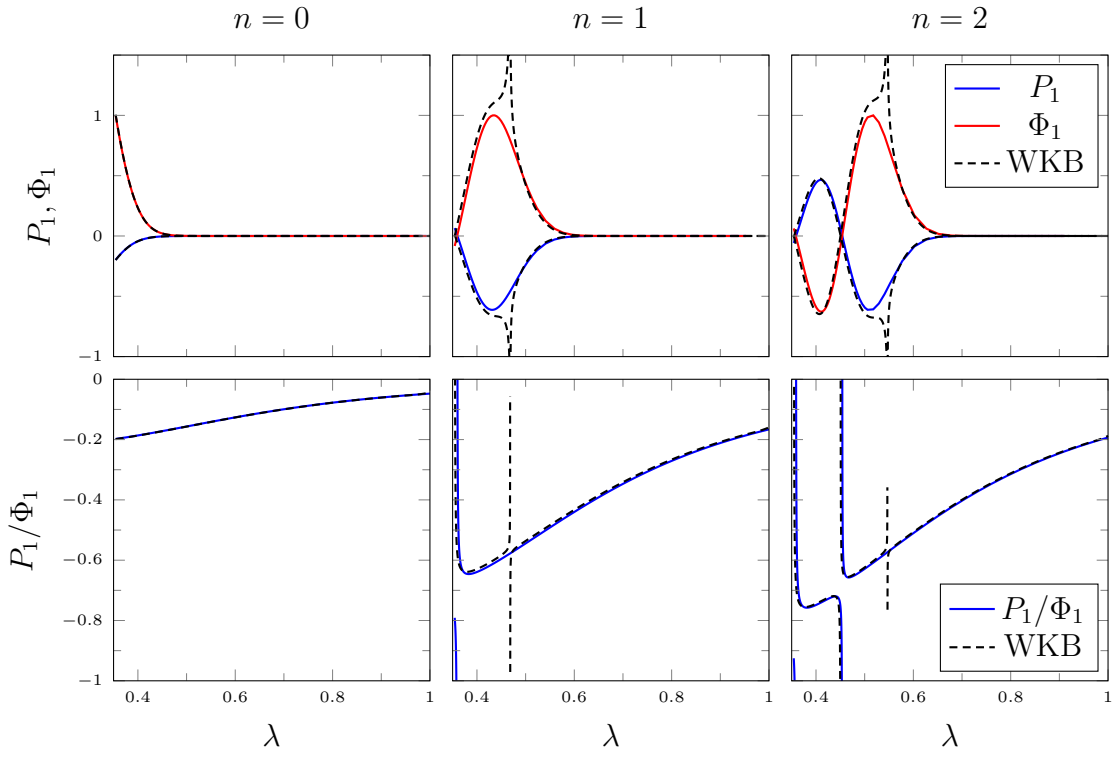

Fig. 4.9 Comparison between the full numerical solutions (solid colour) and the WKB solutions (dashed black) both for the physical variables P_1 and Φ_1 and their ratio P_1/Φ_1 for the first three eigenmodes $n \in \{0, 1, 2\}$, where we have chosen $m = 5$ and $k = 50$.

flows with a viscosity ratio $m < 3/2$ and hence without a shock were shown to be stable, while all flows with a viscosity ratio $m > 3/2$ and hence with a shock were shown to be unstable. In particular, this means that the theory developed in this chapter predicts that some intrusions of less viscous fluid are in fact stable, as long as $1 < m < 3/2$. We note that the theory predicts at most a single unstable eigenmode, given by the fundamental eigenmode corresponding to perturbations without any zeros, all other modes were shown to be stable for all m and k. We have furthermore shown that, as long as $m > 3/2$, the fundamental mode is most unstable for infinite wavenumber $k \to \infty$. Therefore, we unfortunately cannot predict a finite value for the most unstable wavenumber, which could have been compared to experimental results. We argue that this behaviour as $k \to \infty$ is not physical, and that in fact, for large wavenumber, the lubrication approximation breaks down requiring the consideration of the full Stokes equation near the nose. However, we argue that the theory presented here can still be used to predict the overall nature of the onset of instability, in particular the link of instability to the occurrence of shocks occurring for viscosity ratios above a critical value $m_{\text{crit}} = 3/2$ which is larger than the classical Saffman–Taylor value of $m_{\text{crit}} = 1$.

Apart from the numerical solutions, we have also found a fully analytical solution for the time-dependent partial differential equations, valid both in the case of axisymmetric flows ($k = 0$) and the case of equal-viscosity flows ($m = 1$). Late-time expansions of the time dependent solutions revealed a degenerate eigenspectrum for the linear perturbation, in that the only eigenvalue is $\sigma = -1$, with an arbitrary shape for the perturbations given by the particular initial conditions. Furthermore, we could show that $\sigma = -1$ is a necessary condition for linearly perturbing the shock height, and from the analytical solution we derived an expression for the shock-height perturbation in terms of the initial condition.

Finally, in the unstable cases ($m > 3/2$) we also found asymptotic solutions for large azimuthal wavenumber $k \to \infty$, using both a WKB ansatz and local asymptotic expansions . These asymptotic results confirmed that $k \to \infty$ is the most unstable wavenumber, and that the critical viscosity ratio is indeed $m = 3/2$, which we could show by deriving a curve of marginal stability where $\sigma = 0$ in (m, k)-space. Whilst the WKB asymptotics were shown to agree very well with the full numerical results, we could not continue the numerical solutions to sufficiently large values of k to compare them to the local-asymptotic-expansion results. However, the WKB results and local-asymptotic-expansion results were shown to agree with one another as long as k is sufficiently large, thereby confirming that using local asymptotic expansions

provides the correct scalings for very large k. In fact, we derived the leading-order local-asymptotic-expansion results from expanding the WKB results for large k.

Overall, we confirmed the previously stated hypothesis that the shocks in Hele-Shaw currents of negligible diffusion and negligible surface tension are crucial for the development of instabilities. In particular, we have shown that currents of less viscous intrusions with $1 < m < 3/2$ are stable, confirming previous experimental results. Similar to issues faced in the classical Saffman–Taylor analysis, we unfortunately could not make any predictions for the most unstable wavenumber.

Appendix 4.A Large wavenumber — local asymptotic expansions

In this appendix, we again consider the limit of large azimuthal wavenumber $k \to \infty$, but now, instead of finding solutions via the WKB method, we use local asymptotic expansions. This is motivated by the observation that for large k the perturbations become localised at the nose, and we can hence restrict our analysis to near the nose, assuming decaying behaviour away from the nose.

For the method of local asymptotic expansions, we expand both the perturbation flux Φ_1 and the growth rate σ as series in powers of k, and we introduce a suitable local variable η. The amplitude of the perturbations, and hence scaling order of Φ_1, is arbitrary and therefore can be chosen to be $O(1)$ for convenience. The particular scaling of the growth rate is crucial in determining which modes we find as it is related to the length scale of the extent of the local region near the nose.

4.A.1 The fundamental mode: $\sigma = O(k)$

For the fundamental mode ($n = 0$), we expect the perturbations to be confined to a small region near the nose with size $\lambda - \lambda_* = O\left(k^{-1}\right)$ as this corresponds to the length scale of the azimuthal oscillations. We therefore introduce the local variable η by writing $\lambda = \lambda_* + \eta/k$ and we expect $\sigma = O(k)$. These assumptions lead to series expansions given by

$$\Phi_1(\eta) = \sum_{j=0}^{\infty} k^{-j} f_j(\eta) = f_0 + k^{-1} f_1 + k^{-2} f_2 + \cdots , \tag{4.73a}$$

$$\sigma = \sum_{j=0}^{\infty} k^{1-j} \sigma_j = k\sigma_0 + \sigma_1 + k^{-1}\sigma_2 + \cdots . \tag{4.73b}$$

We substitute this expansion into (4.53) resulting in second-order differential equations for the f_i at the various orders of k:

$$O(1): \qquad f_0'' - \mathcal{X}_*^2 f_0 = 0, \tag{4.74a}$$

$$O\left(k^{-1}\right): \qquad f_1'' - \mathcal{X}_*^2 f_1 = \left(2\mathcal{X}_*\mathcal{X}_*'\eta - \frac{\mathcal{X}_*\mathcal{M}_*'}{2\sigma_0\mathcal{M}_*}\right) f_0 + \left(\frac{\mathcal{X}_*'}{\mathcal{X}_*} + \frac{\mathcal{M}_*'}{\mathcal{M}_*}\right) f_0'. \tag{4.74b}$$

For f_0 we immediately see that the solutions are given by exponentials $\mathrm{e}^{\pm\mathcal{X}_*\eta}$. We recall the boundary condition (4.54b), which implies that we need to select the decaying exponential. To determine which exponential decays, we need to compute the sign of $\mathcal{X}_*$: as $\mathcal{X} = X_0'/X_0$ and as X_0 increases towards the nose while λ decreases towards the nose, we deduce that $\mathcal{X}_* < 0$. By using this, and also ensuring decay of f_1 we obtain the results

$$f_0 = \delta \exp\left(\mathcal{X}_*\eta\right), \qquad f_1 = \left(\frac{\mathcal{X}_*'}{2}\eta^2 + \frac{(1+2\sigma_0)\,\mathcal{M}_*'}{4\sigma_0\mathcal{M}_*}\eta\right) f_0, \tag{4.75}$$

where δ is a constant of integration equal to the amplitude. We have neglected the complementary solution for f_1, as it would be of exactly the same form as f_0, thereby simply corresponding to an $O\left(k^{-1}\right)$ correction of the amplitude δ.

We then need to impose the boundary condition (4.54a) at the nose, which determines the coefficients of the expansion of the growth rate σ:

$$\sigma_0 = \frac{\mathcal{M}_* - 1}{2\left(\mathcal{M}_* + 1\right)}, \qquad \sigma_1 = -1 - \frac{\mathcal{M}_*'}{2\left(\mathcal{M}_* + 1\right)^2\mathcal{X}_*}. \tag{4.76}$$

This is exactly the same result as (4.60), which was obtained by means of the WKB method for the limit of large wavenumber $k \to \infty$ in §4.6.1.

Finally, we note that in general we expect the f_i for $i \geq 1$ to be given by polynomials of order $2i$ multiplied by the leading-order solution f_0. The complementary solution for any f_i will always be the same, namely just f_0, and hence can always be ignored. This could be used to easily obtain higher-order corrections.

4.A.2 Higher modes: $\sigma = O\left(k^{-2/3}\right)$

For the higher modes, we also expect the perturbations to be confined to a small region near the nose. However, due to the radial oscillations in the perturbations there is a further length scale, and it turns out the appropriate size of the boundary layer is $\lambda - \lambda_* = O\left(k^{-2/3}\right)$, as derived in the WKB analysis, see (4.68). Hence, we introduce

a local variable η by writing $\lambda = \lambda_* + k^{-2/3}\eta$ and expand

$$\Phi_1(\eta) = \sum_{j=0}^{\infty} k^{-2j/3} f_j(\eta) = f_0 + k^{-2/3} f_1 + \cdots, \tag{4.77a}$$

$$\sigma = \sum_{j=0}^{\infty} k^{-2(1+j)/3} \sigma_j = k^{-2/3}\sigma_0 + k^{-4/3}\sigma_1 + \cdots. \tag{4.77b}$$

Again substituting into (4.53) we get equations for the f_i:

$$O(1): \qquad f_0'' - \mathcal{X}_*^2 (\sigma_0 + \mathcal{Y}_*\eta) f_0 = 0, \tag{4.78a}$$

$$O\left(k^{-2/3}\right): \qquad f_1'' - \mathcal{X}_*^2 (\sigma_0 + \mathcal{Y}_*\eta) f_1 = -\left(2\mathcal{X}_* + \frac{\mathcal{X}_*'}{\mathcal{X}_*}\right) f_0' + \\ + \mathcal{X}_*^2 \left(\sigma_1 - \left(\sigma_0 - \frac{2\mathcal{X}_*'}{\mathcal{X}_*}\eta\right)(\sigma_0 + \mathcal{Y}_*\eta) + \frac{1}{2}\mathcal{Y}_*'\eta^2\right) f_0, \tag{4.78b}$$

where we have introduced $\mathcal{Y}(\lambda) = (\mathcal{M}'/\mathcal{M}/\mathcal{X}/2)'$ for algebraic convenience. We note that $\mathcal{M}_*'/\mathcal{M}_*/\mathcal{X}_*/2 = -1$ as mentioned in §4.6.1.

The leading-order equation for f_0 can be recognised as equivalent to a shifted form of Airy's equation. Hence, using (4.54b) to single out the decaying solutions, we get

$$f_0 = \delta \,\mathrm{Ai}\left(\left(-\mathcal{X}_*\right)^{2/3} \left(\mathcal{Y}_*\right)^{1/3} \left[\eta + \frac{\sigma_0}{\mathcal{Y}_*}\right]\right), \tag{4.79a}$$

$$f_1 = \tfrac{1}{10}\left(\frac{\mathcal{X}_*'}{\mathcal{X}_*} - \frac{\mathcal{Y}_*'}{\mathcal{Y}_*} - 10\mathcal{X}_*\right)\eta f_0 + \left(\frac{\sigma_1}{\mathcal{Y}_*} - \frac{\sigma_0^2}{\mathcal{Y}_*}\left\{\tfrac{1}{3} - \frac{4\mathcal{Y}_*'}{15\left(\mathcal{Y}_*\right)^2} + \frac{4\mathcal{X}_*'}{15\mathcal{X}_*\mathcal{Y}_*}\right\}\right. \\ \left. - \left\{\tfrac{1}{3} + \frac{2\mathcal{Y}_*'}{15\left(\mathcal{Y}_*\right)^2} - \frac{\mathcal{X}_*'}{15\mathcal{X}_*\mathcal{Y}_*}\right\}\sigma_0\eta + \left\{\frac{\mathcal{Y}_*'}{\mathcal{Y}_*} + \frac{4\mathcal{X}_*'}{\mathcal{X}_*}\right\}\frac{\eta^2}{10}\right) f_0', \tag{4.79b}$$

where again δ is the constant amplitude and we recall that $\mathcal{X}_* < 0$. As before, we have neglected the complementary solution for f_1.

The boundary condition at the nose (4.54a) simply becomes $f_0 = 0$ at $\eta = 0$, and hence the growth rate σ_0 of the n^{th} eigenmode is related to z_n, the n^{th} root of the Airy function $\mathrm{Ai}(z)$, by

$$\sigma_0 = -z_n \left(\frac{\mathcal{Y}_*'}{-\mathcal{X}_*}\right)^{2/3}. \tag{4.80}$$

Similarly, the next-order correction boundary condition at the nose gives $f_1 = 0$, which leads to

$$\sigma_1 = \sigma_0^2 \left(\tfrac{1}{3} - \frac{4\mathcal{Y}_*''}{15\left(\mathcal{Y}_*'\right)^2} + \frac{4\mathcal{X}_*'}{15\mathcal{X}_*\mathcal{Y}_*'} \right). \tag{4.81}$$

To compare with the WKB result, we note that if n is sufficiently large, such that z_n is sufficiently large, we can estimate the Airy function as a phase-shifted sine and therefore we get

$$z_n \approx -\left[\left(n - \tfrac{1}{4}\right) \frac{3\pi}{2} \right]^{2/3} \qquad \Rightarrow \qquad \sigma_0 \approx -\left[\left(\tfrac{1}{4} - n\right) \frac{3\pi\mathcal{Y}_*'}{2\mathcal{X}_*} \right]^{2/3}, \tag{4.82}$$

which is exactly the same as (4.68). We note that even for $n = 1$ this approximation for z_1 is less than 0.8% off and therefore it is in fact a reasonable approximation for any $n \geq 1$.

Chapter 5

Linear stability analysis of a two-layer viscous gravity current with constant influx rate and equal densities

5.1 Introduction

Finally, in this chapter, we theoretically investigate an instability observed experimentally in two-layer viscous gravity currents using the same set-up as mentioned in Chapter 2. As before, the experiments were carried out by Box, Gell and Neufeld. An example time-series of a finger-like pattern developing is shown in figure 5.1 indicating a fairly large-wavenumber instability. Our aim is to model this instability, and, in particular, to find conditions on the physical parameters which led to a stable or unstable flow pattern. For this, we consider the linear stability of equal-density two-layer viscous gravity currents spreading from a point source of constant influx. This combines aspects of all previous chapters, and hence we summarise the relevant key results here. For an outline of the relevant literature, we direct the reader to the introductions of the previous chapters.

Firstly, in Chapter 2, we analysed the axisymmetric self-similar spreading of two-layer equal-density gravity currents. The solutions we obtained will be the base state for the linear stability analysis of this chapter. In particular, we recall the key result that, for sufficiently less viscous intruding fluids ($m > 3/2$), the equations predict shocks at the nose of the current. This behaviour was identified as a consequence of

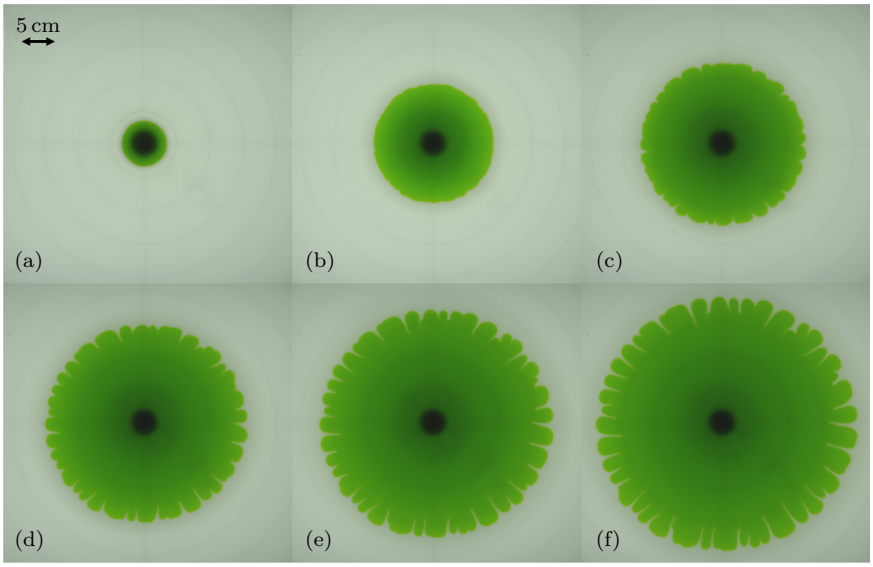

Fig. 5.1 An example time-series of the finger-like pattern developing in the experiments with parameters $m \approx 9.77$ and $\mathcal{Q}_{\text{in}} \approx 62.0$. The time interval between the successive pictures (a) – (f) was 25 s and the first picture was taken 5 s after the beginning of the experiment.

the hyperbolic nature of the equations for equal-density fluids. The height λ_{crit} of these shocks was obtained by imposing an Oleinik entropy condition, which we derived from considering small density differences as a regularising mechanism. We also note that, when considering the time-dependent evolution of the interface between the two fluids, simplified by assuming a prescribed evolution of the top surface, we found that this shock height was in fact attained within finite time. This implies that in a linear stability analysis we do not need to consider perturbing the shock height.

Then, in Chapter 3, we considered the simpler case of single-layer gravity currents with various types of influxes, which we found to be stable for all parameters. In order to conduct the linear stability analysis, we defined scaling-invariant variables, similar to Gratton and Minotti (1990) but including azimuthal and temporal variations. A further simplification was obtained by introducing perturbation phase angles instead of the usual Cartesian perturbation variables. These two variable changes reduced the order of the differential equations by two, regularised the singularity at the nose, and eliminated the arbitrary amplitude of the perturbations. Hence, these variables were found to be very useful for implementing numerical integration schemes, for example, with continuation software such as AUTO. As the equations governing two-layer gravity currents share many features with the equations governing single-layer gravity currents, we will use similar variable transformations. A further result of Chapter 3 was an

analytic solution for axisymmetric perturbations to constant-influx currents, found by considering a small shift in the temporal origin. We then extended this solution to non-axisymmetric perturbations as well. As the currents considered in this chapter have a constant-influx source, we can expect to find an analytic solution by a similar method.

Finally, in Chapter 4, we departed from gravity currents and instead considered intrusions into Hele-Shaw cells assuming both negligible diffusion and negligible surface tension. The reason we did so is the fact that the equation governing the evolution of the interface in a two-layer gravity current is very similar to the equation governing the evolution of the interface between the two fluids in a Hele-Shaw cell. For example, the two systems exhibit the same shock structure. Our linear stability analysis of intrusions into Hele-Shaw cells found that the flow is stable unless there are shocks ($m > 3/2$), in which case the fundamental perturbation mode becomes unstable for sufficiently large k. In fact, lacking any small-wavelength regularising mechanism such as surface tension, our theory predicted rapid growth of perturbations in the limit $k \to \infty$. This is a well-known issue for fingering instabilities in Hele-Shaw cells, which, we argued, does not invalidate the qualitative prediction of the relation between shocks and instability. We note that once again the shock height λ_{crit} could not be perturbed within the framework of a normal-mode analysis, except in the degenerate case of kinematic wave perturbations with $\sigma = -1$, which occur for axisymmetric or equal-viscosity flows. We expect two-layer equal-density viscous gravity currents to contain features both similar to single-layer gravity currents which are stable (top-surface evolution), and similar to intrusions in Hele-Shaw cells (interfacial evolution) which may become unstable. As a result, we expect any instability of two-layer gravity currents to resemble the instability of intrusions in Hele-Shaw cells.

The overarching aim of this chapter is to model the experimentally observed instability and predict the particular physical parameters which lead to instability. In order to derive the equations for a linear stability analysis of two-layer equal-density viscous gravity currents, we aim to utilise a scaling-invariant method similar to Chapter 3. Finally, we also aim to investigate the relationship of the observed instability to the well-known Saffman–Taylor instability in Hele-Shaw cells.

The set-up of the model and its assumptions are described in §5.2, which leads to a closed system of ordinary differential equations for the base state and linear perturbations. We then solve the resulting equations numerically in §5.3 and compare the obtained results to experiments (§5.3.1). Appendix 5.A presents the details of a scaling-invariant reformulation of the equations (§5.A.1) and boundary conditions

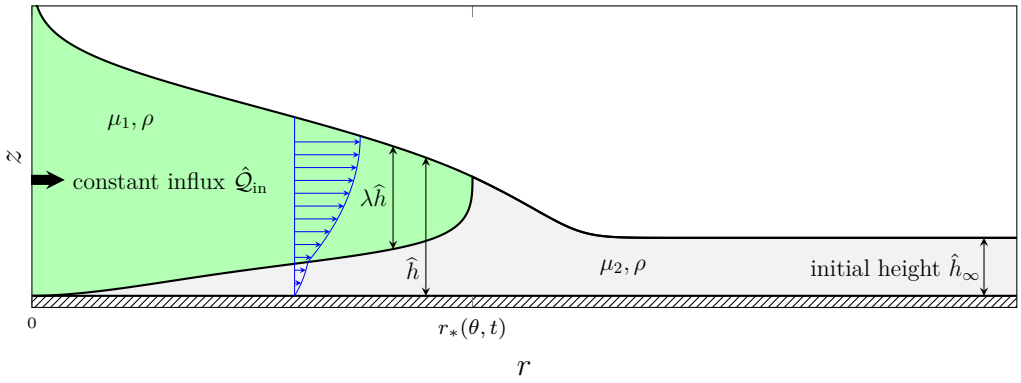

Fig. 5.2 A radial cross-section of a two-layer equal-density viscous gravity current with constant influx $\hat{\mathcal{Q}}_{\text{in}}$ of a fluid with viscosity μ_1 spreading over a layer of ambient fluid with viscosity μ_2 and initial height $\hat{h}_\infty$ on a rigid horizontal surface. The dynamic variables defined are the total height of the current $\hat{h}(r, \theta, t)$, the relative fluid fraction $\lambda(r, \theta, t)$ and the radial extent $r_*(\theta, t)$.

(§5.A.2), and the introduction of phase-angle perturbation variables (§5.A.3). In Appendix 5.B, we formally derive the equations for single-layer viscous gravity currents (§5.B.1) and intrusions into Hele-Shaw cells (§5.B.2) as asymptotic limits of the general theory, and we compare these to the full numerical solutions (§5.B.3). Additionally, in Appendix 5.C, we find two analytic solutions for the perturbations, one by considering a small shift in temporal origin as with single-layer gravity currents (§5.C.1), and a second for perturbing only the interface for the case of equal viscosities (§5.C.2).

5.2 Model description

Much of this section contains material very similar to that seen in Chapters 2 and 3. We reproduce it here so that this chapter forms a self-contained and coherent narrative.

As in Chapter 2, we consider a viscous two-layer axisymmetric gravity current spreading from a point source over a rigid horizontal surface. The upper fluid is introduced at a constant volumetric rate $\hat{\mathcal{Q}}_{\text{in}}$ at the origin and spreads radially over a lower layer of fluid, which initially covers the entire horizontal plane with a constant thickness $\hat{h}_\infty$, see figure 5.2. The fluids have viscosities μ_i, where $i = 1$ corresponds to the upper, intruding fluid and $i = 2$ to the lower, lubricating fluid, and we assume the densities are equal and given by ρ. Using cylindrical polar coordinates, we define the total height $\hat{h}(r, \theta, t)$ and the fluid fraction of upper-layer fluid $\lambda(r, \theta, t)$ such that the upper-layer thickness is given by $\lambda\hat{h}$. We define the horizontal radial extent of the current $r_*(\theta, t)$. As before, surface tension and diffusion are assumed to be negligible.

This is essentially the same situation as in Chapter 2, except that we now include azimuthal dependence through θ, and we neglect density differences from the beginning.

After a short initial transient, the horizontal extent of the current is significantly greater than the vertical extent, $r_* \gg \widehat{h}$. In this limit the vertical velocity is negligible and the pressure $\widehat{p}$ is hydrostatic. As the fluids have equal densities, the horizontal pressure gradient is simply given by

$$\boldsymbol{\nabla}\widehat{p} = \rho g \boldsymbol{\nabla}\widehat{h}, \tag{5.1}$$

where g is the acceleration due to gravity and $\boldsymbol{\nabla}$ acts in the horizontal (r, θ) directions only. This pressure gradient drives a flow with horizontal velocity $\widehat{\boldsymbol{u}}$, which is determined by

$$\mu \frac{\partial^2 \widehat{\boldsymbol{u}}}{\partial z^2} = \boldsymbol{\nabla}\widehat{p} = \rho g \boldsymbol{\nabla}\widehat{h}, \tag{5.2}$$

with boundary conditions given by no-slip at the bottom, no-stress at the top surface, and velocity and stress continuity at the interface between the fluids:

$$\widehat{\boldsymbol{u}} = \mathbf{0} \text{ at } z = 0, \qquad \frac{\partial \widehat{\boldsymbol{u}}}{\partial z} = \mathbf{0} \text{ at } z = \widehat{h}, \tag{5.3a}$$

$$[\widehat{\boldsymbol{u}}]_-^+ = \mathbf{0} \text{ at } z = (1-\lambda)\widehat{h}, \qquad \left[\mu \frac{\partial \widehat{\boldsymbol{u}}}{\partial z}\right]_-^+ = \mathbf{0} \text{ at } z = (1-\lambda)\widehat{h}. \tag{5.3b}$$

Solving (5.2) with (5.3) gives the velocity profile

$$\widehat{\boldsymbol{u}} = \frac{\rho g \boldsymbol{\nabla}\widehat{h}}{2\mu_2}\left\{z^2 - 2\widehat{h}z\right\} \qquad \text{for} \quad 0 < z/\widehat{h} < 1-\lambda, \tag{5.4a}$$

$$\widehat{\boldsymbol{u}} = \frac{\rho g \boldsymbol{\nabla}\widehat{h}}{2\mu_2}\left\{m\left(z^2 - 2\widehat{h}z\right) + (m-1)\left(1-\lambda^2\right)\widehat{h}^2\right\} \quad \text{for} \quad 1-\lambda < z/\widehat{h} < 1, \tag{5.4b}$$

where $m = \mu_2/\mu_1$ is the ratio of lower-layer to upper-layer viscosity. This piecewise-parabolic velocity profile can be integrated over the whole vertical height and over the depth of the upper layer, which gives two local mass-conservation equations for $r < r_*$:

$$\frac{\partial \widehat{h}}{\partial t} = \frac{\rho g}{3\mu_2}\boldsymbol{\nabla}\cdot\left(\mathcal{M}\widehat{h}^3\boldsymbol{\nabla}\widehat{h}\right), \qquad \frac{\partial \lambda\widehat{h}}{\partial t} = \frac{\rho g}{3\mu_2}\boldsymbol{\nabla}\cdot\left(\mathcal{F}\mathcal{M}\widehat{h}^3\boldsymbol{\nabla}\widehat{h}\right), \tag{5.5}$$

where the mobility $\mathcal{M}(\lambda)$ and the ratio of upper-layer flux to total flux $\mathcal{F}(\lambda)$ are given by

$$\mathcal{M}(\lambda) = 1 + (m-1)\lambda^3, \qquad \mathcal{F}(\lambda) = \frac{3\lambda + (2m-3)\lambda^3}{2 + 2(m-1)\lambda^3}. \tag{5.6}$$

For $r > r_*$ there is only lubricating fluid and we recover the equation for a classical single-layer gravity current:

$$\frac{\partial \widehat{h}}{\partial t} = \frac{\rho g}{3\mu_2} \boldsymbol{\nabla} \cdot \left(\widehat{h}^3 \boldsymbol{\nabla} \widehat{h} \right). \tag{5.7}$$

This is also equivalent to simply setting $\lambda = 0$ in (5.5a).

For the boundary conditions, we introduce the unit vector normal to the front of the current $\boldsymbol{n}$, the radial outward-pointing vector $\boldsymbol{e}_r$, and the critical shock height

$$\lambda_{\text{crit}}(m) = \begin{cases} 2\left(\frac{2}{3}m - 1\right)^{-1/2} \sinh\left[\frac{1}{3}\sinh^{-1}\left\{(m-1)^{-1}\left(\frac{2}{3}m-1\right)^{3/2}\right\}\right], & m > 3/2, \\ 0, & m \leq 3/2, \end{cases} \tag{5.8}$$

derived in Chapter 2 as the Oleinik shock height. With these, the boundary conditions for the system (5.5) and (5.7) are given by: a fixed initial height in the far-field

$$\widehat{h} \to \hat{h}_\infty; \tag{5.9a}$$

global mass-conservation for the upper and lower fluids

$$\hat{\mathcal{Q}}_{\text{in}} t = \int_0^{2\pi} \int_0^{r_*} \lambda \widehat{h}\, r \,\mathrm{d}r \,\mathrm{d}\theta = \int_0^{2\pi} \int_0^{r_*} \left(h - \hat{h}_\infty\right) r \,\mathrm{d}r \,\mathrm{d}\theta; \tag{5.9b}$$

a nose with shock height $\lambda_* = \lambda(r_*) = \lambda_{\text{crit}}$ from (5.8) and velocity given by mass conservation at the nose

$$(\boldsymbol{e}_r \cdot \boldsymbol{n}) \frac{\partial r_*}{\partial t} = \frac{\rho g}{3\mu_2} \mathcal{F}\mathcal{M}\widehat{h}^2 \left(\boldsymbol{n} \cdot \boldsymbol{\nabla}\widehat{h}\right); \tag{5.9c}$$

and continuity both of the total height and the total normal flux at the nose

$$\left[\widehat{h}\right]_-^+ = \left[\mathcal{M}\widehat{h}^3 \left(\boldsymbol{n} \cdot \boldsymbol{\nabla}\widehat{h}\right)\right]_-^+ = 0. \tag{5.9d}$$

5.2.1 Self-similar spreading

As in Chapter 2, the case of radially spreading two-layer gravity currents admits a similarity solution governed by a constant characteristic thickness (Lister and Kerr, 1989). It is natural to define a dimensionless total height $h = \widehat{h}/\hat{h}_\infty$ and write the solution in terms of the similarity variable

$$\xi = \left(\frac{3\mu_2}{\rho g \hat{h}_\infty^3}\right)^{1/2} r t^{-1/2}, \tag{5.10}$$

which can be found from a scaling analysis of (5.5a) using $\hat{h}_\infty$ as the characteristic height scale for $\widehat{h}$. In order to describe the evolution towards self-similarity, we define a rescaled temporal variable $\tau = \log(t/\widehat{t})$, where $\widehat{t}$ is an arbitrary reference time scale. We write $\xi_*(\theta,\tau) = \xi(r_*,\theta,\tau)$ for the non-dimensional radial extent of the current. We note that λ is already dimensionless, being defined as the fluid fraction of upper-layer fluid.

The local mass-conservation equations (5.5) and (5.7) for $\xi < \xi_*$ then lead to a nonlinear dimensionless system of partial differential equations given by

$$\frac{\partial h}{\partial \tau} - \tfrac{1}{2}\xi\frac{\partial h}{\partial \xi} + \boldsymbol{\nabla}\cdot\boldsymbol{q} = 0, \tag{5.11a}$$

$$\frac{\partial \lambda h}{\partial \tau} - \tfrac{1}{2}\xi\frac{\partial \lambda h}{\partial \xi} + \boldsymbol{\nabla}\cdot(\mathcal{F}\boldsymbol{q}) = 0, \tag{5.11b}$$

$$\boldsymbol{q} = -\mathcal{M}h^3\boldsymbol{\nabla}h, \tag{5.11c}$$

where $\boldsymbol{q}(\xi,\theta,\tau)$ is the depth-integrated total fluid flux vector. We write $\boldsymbol{q} = (q_\xi, q_\theta)$ for the radial and azimuthal components of the total flux and substitute it into (5.11). Eliminating the azimuthal flux q_θ from the resulting equations gives

$$\frac{\partial h}{\partial \tau} - \tfrac{1}{2}\xi\frac{\partial h}{\partial \xi} + \frac{1}{\xi}\frac{\partial \xi q_\xi}{\partial \xi} = \frac{1}{\xi^2}\frac{\partial}{\partial \theta}\left(\mathcal{M}h^3\frac{\partial h}{\partial \theta}\right), \tag{5.12a}$$

$$\frac{\partial \lambda h}{\partial \tau} - \tfrac{1}{2}\xi\frac{\partial \lambda h}{\partial \xi} + \frac{1}{\xi}\frac{\partial \mathcal{F}\xi q_\xi}{\partial \xi} = \frac{1}{\xi^2}\frac{\partial}{\partial \theta}\left(\mathcal{F}\mathcal{M}h^3\frac{\partial h}{\partial \theta}\right), \tag{5.12b}$$

$$q_\xi = -\mathcal{M}h^3\frac{\partial h}{\partial \xi} \qquad \left(q_\theta = -\frac{\mathcal{M}h^3}{\xi}\frac{\partial h}{\partial \theta}\right). \tag{5.12c}$$

For $\xi > \xi_*$ we can either nondimensionalise (5.7) or set $\lambda = 0$ and $\mathcal{M} = \mathcal{F} = 1$ above, which leads to

$$\frac{\partial h}{\partial \tau} - \tfrac{1}{2}\xi\frac{\partial h}{\partial \xi} + \frac{1}{\xi}\frac{\partial \xi q_\xi}{\partial \xi} = \frac{1}{\xi^2}\frac{\partial}{\partial \theta}\left(h^3\frac{\partial h}{\partial \theta}\right), \tag{5.13a}$$

$$q_\xi = -h^3\frac{\partial h}{\partial \xi} \qquad \left(q_\theta = -\frac{h^3}{\xi}\frac{\partial h}{\partial \theta}\right). \tag{5.13b}$$

Similarly to Chapter 2, we express the boundary conditions (5.9) in terms of the dimensionless variables:

$$\text{global mass conservation:} \quad \int_0^{2\pi}\int_0^{\xi_*} \lambda h\,\xi\,\mathrm{d}\xi\,\mathrm{d}\theta = \mathcal{Q}_{\text{in}}, \tag{5.14a}$$

$$\text{fixed initial height at infinity:} \quad h \to 1 \quad \text{as} \quad \xi \to \infty, \tag{5.14b}$$

$$\text{Oleinik shock height at the nose:} \quad \lambda = \lambda_{\text{crit}} \quad \text{at} \quad \xi = \xi_*, \tag{5.14c}$$

$$\text{mass conservation at nose:} \quad (\boldsymbol{n}\cdot\boldsymbol{e}_\xi)\left(\frac{\partial \xi_*}{\partial \tau} + \tfrac{1}{2}\xi_*\right) = \frac{\mathcal{F}\,(\boldsymbol{n}\cdot\boldsymbol{q})}{\lambda h} \quad \text{at} \quad \xi = \xi_*, \tag{5.14d}$$

$$\text{continuity of total height:} \quad [h]^+_- = 0 \quad \text{at} \quad \xi = \xi_*, \tag{5.14e}$$

$$\text{continuity of normal total flux:} \quad [\boldsymbol{n}\cdot\boldsymbol{q}]^+_- = 0 \quad \text{at} \quad \xi = \xi_*, \tag{5.14f}$$

where $\partial\xi_*/\partial\tau$ is the dimensionless speed of the nose in similarity space and

$$\mathcal{Q}_{\text{in}} = \frac{3\mu_2\hat{\mathcal{Q}}_{\text{in}}}{2\pi\rho g\hat{h}_\infty^4} \tag{5.15}$$

is the dimensionless volumetric influx.

As noted in Chapter 2, the dimensionless influx $\mathcal{Q}_{\text{in}}$ can be related to the ratio of the height scale for a single-layer current (Huppert, 1982b) and the far-field height.

If, at late times, the evolution of the system becomes self-similar and independent of τ, then (5.12) and (5.13) reduce to the coupled ordinary differential equations analysed in Chapter 2, where the boundary conditions are the same as (5.14) with a zero nose speed, $\partial\xi_*/\partial\tau = 0$. We want to investigate for which values of the physical parameters $\mathcal{Q}_{\text{in}}$ and m this occurs, and for which values the self-similar state is unstable to small perturbations.

5.2.2 Changing variables

At this point, we have derived the governing equations (5.12) and (5.13), and could attempt a linear stability analysis based on the physical variables h, q_ξ and λ. However, in Chapter 2, we established that the interfacial position λ of an axisymmetric two-layer viscous gravity current has a square-root singularity at the nose of the current and hence the slope of the interface diverges there. As discussed in Chapter 3, perturbing the nose position of such a singular base state with infinite gradient leads to diverging perturbations, which are numerically problematic. In Chapter 3, we developed a method to mitigate this by utilising the scaling-invariant symmetry of the equations

$$h \mapsto c^2 h, \qquad q_\xi \mapsto c^5 q_\xi, \qquad \xi \mapsto c^3 \xi, \tag{5.16}$$

where c is any non-zero constant, resulting in the scaling-invariant flux and height variables

$$\vartheta = \frac{q_\xi}{\xi^{5/3}}, \qquad \zeta = \frac{h}{\xi^{2/3}}, \tag{5.17}$$

and by changing the independent variable from the radial position ξ to the height variable ζ. This had the additional benefit of reducing the order of the equations. Here we use a similar scaling invariance but choose λ instead of ζ as the independent variable, as it is the interfacial position rather than the top surface that is singular at the nose. Beyond the nose, we use ζ as the independent variable, as the current is effectively a single-layer viscous gravity current similar to Chapter 3. This use of ζ is not needed to mitigate problems with singularities, but is done to maintain the benefit of reduced-order equations and to facilitate a fully scaling-invariant matching across the nose. All the algebraic details of these changes of variables are given in Appendix 5.A and follow similar lines to those already seen in Chapter 3.

A scaling-invariant form of the influx parameter $\mathcal{Q}_{\text{in}}$

When discussing the axisymmetric base state in Chapter 2, we introduced two dimensionless physical parameters that control the evolution of a two-layer equal-density viscous gravity current. These are the viscosity ratio m, which is scaling-invariant, and the dimensionless influx $\mathcal{Q}_{\text{in}}$, which depends on a particular choice of scaling such that $H_0 \to 1$.

To fully utilise the benefits of the scaling-invariance symmetry, we need to replace $\mathcal{Q}_{\text{in}}$ by a scaling-invariant parameter. We choose $\mathcal{Z}_{\text{in}} = \zeta(\lambda_*)$, the unperturbed scaling-

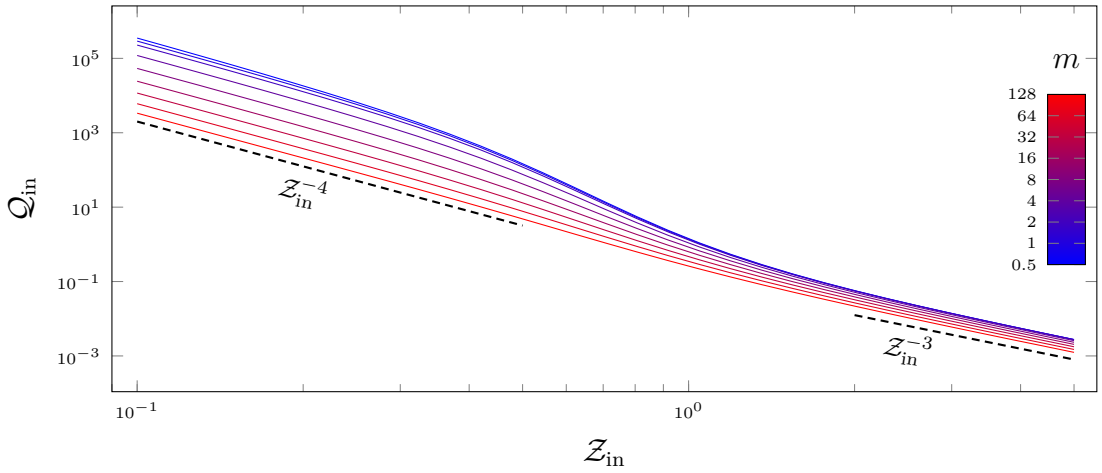

Fig. 5.3 The dimensionless scaling-dependent influx $\mathcal{Q}_{\text{in}}$ as a function of the scaling-invariant height at the nose $\mathcal{Z}_{\text{in}}$ for a range of viscosity ratios m. As comparison, the asymptotic scalings $\mathcal{Q}_{\text{in}} \sim \mathcal{Z}_{\text{in}}^{-4}$ and $\mathcal{Q}_{\text{in}} \sim \mathcal{Z}_{\text{in}}^{-3}$ obtained from (5.83) in the single-layer limit (§5.B.1) and from (5.98) in the Hele-Shaw limit (§5.B.2), respectively.

invariant height at the nose, to be this parameter. To enable comparison between physical experiments and theoretical results, and to facilitate physical interpretation, we calculated the dependence of $\mathcal{Z}_{\text{in}}$ on $\mathcal{Q}_{\text{in}}$ for a range of fixed m. This is shown in figure 5.3, revealing that there is a one-to-one relationship between $\mathcal{Z}_{\text{in}}$ and $\mathcal{Q}_{\text{in}}$ for each m, with large $\mathcal{Z}_{\text{in}}$ corresponding to small influxes $\mathcal{Q}_{\text{in}}$ and vice versa.

Asymptotic limits

There are two asymptotic limits of a two-layer current, which are of particular interest to us. Firstly, if the influx of intruding fluid is sufficiently large ($\mathcal{Q}_{\text{in}} \gg 1$), or if the ambient fluid is sufficiently more viscous ($m \gg 1$), then we expect the ambient fluid has insufficient time to be displaced and thus it remains approximately undisturbed with the intruding fluid sliding on top. This effectively leads to a single-layer current spreading on top of the ambient fluid layer and hence corresponds to the analysis of Chapter 3. Secondly, if the influx of intruding fluid is sufficiently small ($\mathcal{Q}_{\text{in}} \ll 1$), we expect the top surface to remain approximately flat, as there is sufficient time for it to settle under gravity. Hence, the no-stress boundary at the top surface is comparable to the horizontal mid-plane in a Hele-Shaw cell intrusion, which, due to its symmetry, is also a no-stress boundary. Therefore, we expect the limit $\mathcal{Q}_{\text{in}} \ll 1$ to correspond to the analysis of Hele-Shaw intrusions in Chapter 4.

Figure 5.4 shows the base states of a two-layer viscous gravity current with viscosity ratio $m = 5$ in the limits of large and small influxes and compares them to the base

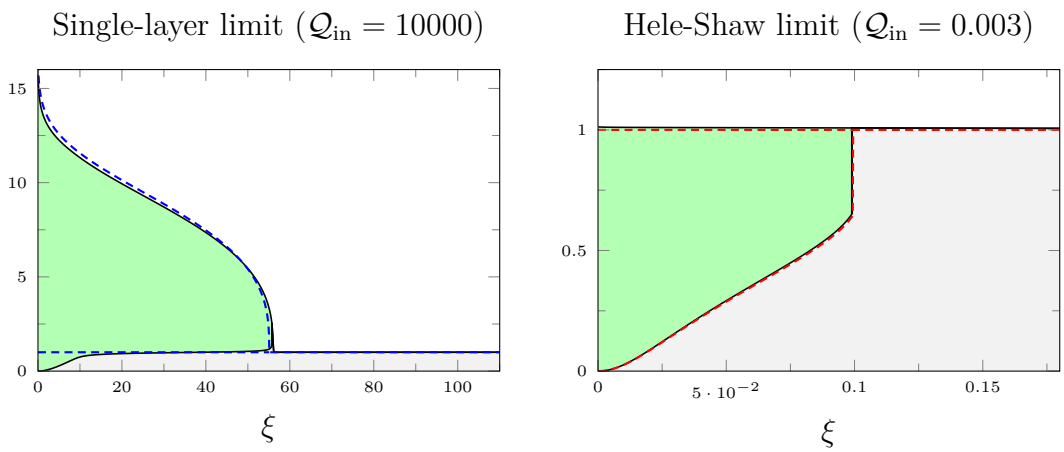

Fig. 5.4 Illustrative example profiles (solid lines) for the top surface and interface for two-layer currents with viscosity ratio $m = 5$ and a large ($\mathcal{Q}_{\text{in}} = 10000$) and small ($\mathcal{Q}_{\text{in}} = 0.003$) influx. The profiles compare very well to a single-layer current profile and a Hele-Shaw intrusion profile (dashed lines), respectively.

states of a single-layer current and a Hele-Shaw intrusion. The figure clearly illustrates the correspondence between the full two-layer dynamics and the physically motivated asymptotic limits.

Mathematically, the governing equations of a single-layer current and an intrusion in a Hele-Shaw cell can be derived formally as asymptotic limits of the two-layer equations (5.12). This is done in Appendix 5.B, where we also derive the exact conditions on $\mathcal{Q}_{\text{in}}$ and m, under which the asymptotic limits are applicable. One particular result is that $\mathcal{Q}_{\text{in}} \sim \mathcal{Z}_{\text{in}}^{-4}$ and $\mathcal{Q}_{\text{in}} \sim \mathcal{Z}_{\text{in}}^{-3}$ in the limits of large and small $\mathcal{Q}_{\text{in}}$, respectively, which figure 5.3 shows, agrees excellently with the numerical results.

5.3 Numerical results

Using the continuation software package AUTO, we solved numerically the scaling-invariant equations governing linear perturbations of a two-layer viscous gravity current, which are detailed in Appendix 5.A. We are mainly concerned here with solutions to these perturbation equations, and we refer to Chapter 2 for solutions to the base-state equations.

For $\sigma < -1$, some of the allowed perturbation modes (the advective modes in (5.63)) are strongly divergent like $\xi^{8(1+\sigma)\log\xi}$ and dominant over the ξ^{-k} gravity-current modes that should be excluded on physical grounds (see §5.A.2). As a result, it is very difficult to get reliable results numerically for $\sigma < -1$. However, these are stable by

definition and, as we are interested in finding conditions for instability, we will not pursue results for $\sigma < -1$ and will focus instead on $\sigma > -1$.

Figure 5.5 shows the numerical solutions for the first three eigenmodes $n \in \{0, 1, 2\}$ in terms of the absolute values of the physical perturbation variables $|H_1|$, $|Q_1|$ and $|\lambda_1|$ with a viscosity ratio $m = 5$, a scaling-invariant nose height $\mathcal{Z}_{\text{in}} = 1$ and an azimuthal wavenumber $k = 15$ as functions of the radial similarity variable ξ. There are several interesting general features to note. Firstly, the perturbation λ_1 to the interface always diverges at the nose. This is due to the fact that the base-state interface has a square-root singularity with infinite gradient at the nose and hence perturbing the nose position requires a divergent interfacial perturbation. This is directly analogous to our discussion of single-layer gravity currents with a cube-root singularity at the nose in Chapter 3, and we recall that one of the key reasons for changing independent variables was to avoid such singular behaviour. Secondly, towards the origin, the solutions decay rapidly, proportional to $\xi^k = \xi^{15}$ as expected (see §5.A.2). And thirdly, the solutions for the first three eigenmodes are nearly identical beyond the nose, up to a rescaling of their amplitude. This indicates that the different modes are mainly distinguished by the effects of the full two-layer dynamics of the current before the nose. Towards the far-field, the solutions also decay as expected.

When comparing the different eigenmodes, we note that the fundamental mode $n = 0$ behaves differently to the higher modes, as it varies monotonically over the region before the nose. Hence, the amplitude of the fundamental mode is maximal near the nose indicating that it is predominantly associated with perturbing the position and dynamics of the nose. Physically, the fundamental mode is the most important mode to explain fingering, as all the other modes are stable for all parameters, which indicates that the nose dynamics of the fundamental mode are crucial in the mechanism of the instability. The higher-order modes $n = 1$ and $n = 2$ have maximal amplitudes in the interior of the current which are orders of magnitude larger than their amplitudes near the nose (making the use of logarithmically scaled axes in figure 5.5 necessary). This can be explained as a frozen-in relic of the larger amplitudes which used to be around when the perturbation was larger, which got predominantly advected towards the origin due to the nature of the equations governing the interfacial evolution. We explore this phenomena in detail in Appendix Z (at the end of this thesis), where we consider two linear perturbation analyses of an illustrative toy problem with an advection–diffusion equation in which the velocity distribution shares some of the features of the base-state interfacial velocity.

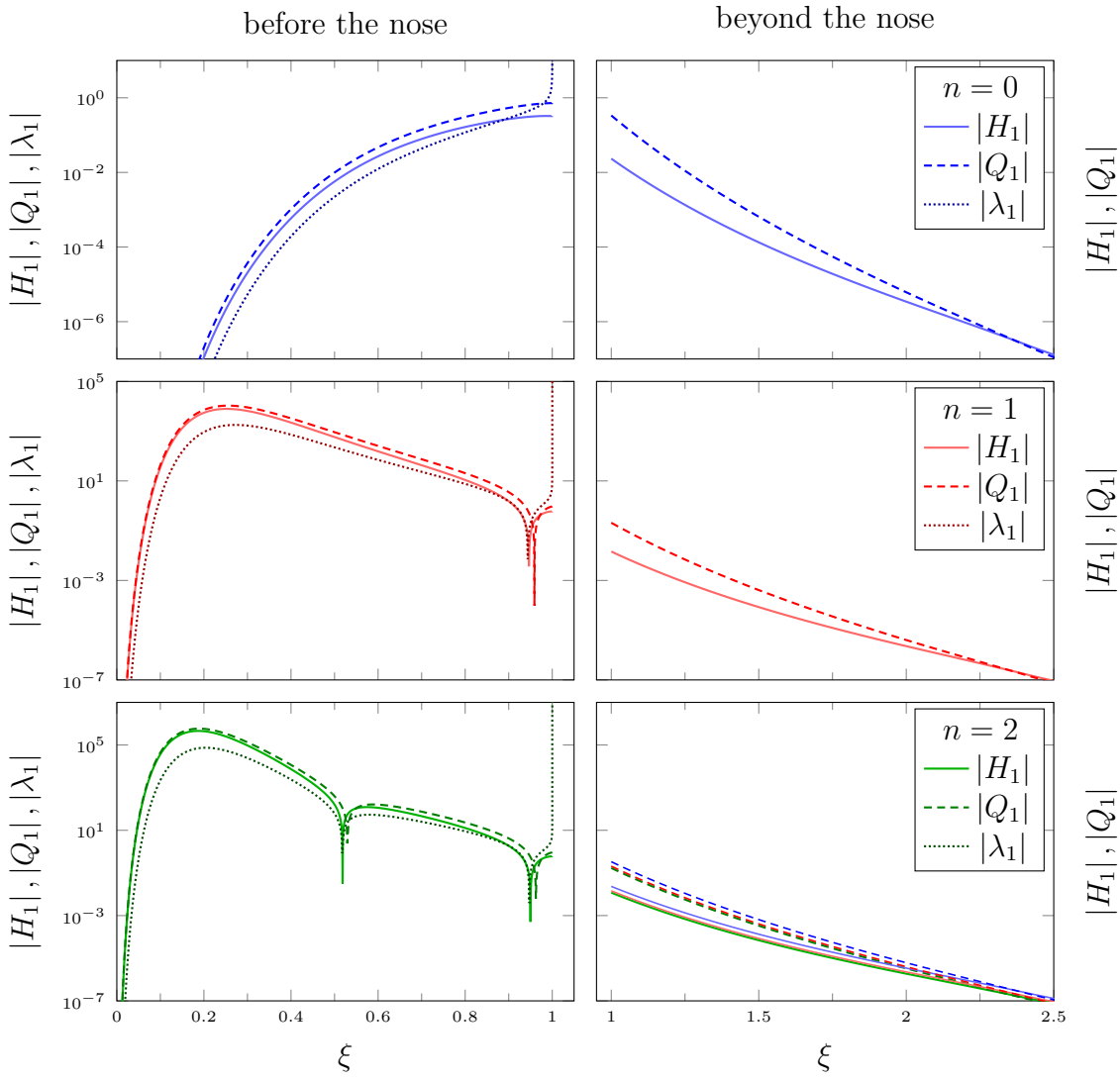

Fig. 5.5 Numerical solutions for the first three eigenmodes $n \in \{0, 1, 2\}$ in terms of the absolute values of the physical perturbations to the total height $|H_1|$ (solid), the total flux $|Q_1|$ (dashed), and the relative fluid fraction $|\lambda_1|$ (dotted) with wavenumber $k = 15$ and viscosity ratio $m = 5$. Beyond the nose, the different modes are nearly identical up to a rescaling of their amplitudes

We used the continuation capabilities of AUTO to explore the dependencies of the growth rate σ on the other physical parameters. These are the key results:

Firstly, figure 5.6 shows the growth rate σ for $m = 5$ and $k = 15$ as a function of the input parameter $\mathcal{Z}_{\text{in}}$. For small $\mathcal{Z}_{\text{in}}$ (large $\mathcal{Q}_{\text{in}}$), all modes are stable with growth rates $\sigma < -1$ consistent with the results for single-layer viscous gravity currents in Chapter 3. For $\mathcal{Z}_{\text{in}} \to \infty$ ($\mathcal{Q}_{\text{in}} \to 0$), the Hele-Shaw limit becomes applicable, and indeed the growth rates for large $\mathcal{Z}_{\text{in}}$ show very good agreement with the values calculated in Chapter 4, which are stable for $m = 5$ and $k = 15$. Significantly, there is a finite interval $0.42 < \mathcal{Z}_{\text{in}} < 1.07$, where the fundamental mode $n = 0$ has $\sigma > 0$ and is unstable. Between the two points of marginal stability, the fundamental mode is most unstable at $\mathcal{Z}_{\text{in}} \approx 0.56$ with growth rate $\sigma \approx 0.17$. We interpret the observation that intermediate values of $\mathcal{Q}_{\text{in}}$ (intermediate $\mathcal{Z}_{\text{in}}$) are most unstable reflecting the fact that these give comparable depths of intruding and ambient fluids and hence maximal effect to the viscosity contrast.

Secondly, figure 5.7 shows the growth rate σ for input parameter $\mathcal{Z}_{\text{in}} = 1$ and wavenumber $k = 15$ as a function of the viscosity ratio m. This shows that over the range of m considered, all three eigenmodes monotonically become less stable with increasing m. The only mode that actually becomes unstable ($\sigma > 0$) is the fundamental mode $n = 0$, with the marginally stable transition occurring at $m \approx 3.40$. For sufficiently large m, we would again expect stability as the single-layer limit becomes applicable. However, as seen in figure 5.12, this is expected only for $m \gtrsim 10^5$ which was beyond the reach of our numerical implementation.

And finally, figure 5.8 shows the growth rate σ for input parameter $\mathcal{Z}_{\text{in}} = 1$ and viscosity ratio $m = 5$ as a function of the wavenumber k. This shows that the fundamental mode $n = 0$ seems to have a growth rate $\sigma = -1$ at $k = 0$ and becomes less stable with increasing k. It becomes marginally stable ($\sigma = 0$) at $k \approx 14.61$ and then the growth rate seemingly diverges with $\sigma \to \infty$ as $k \to \infty$. The higher modes $n = 1$ and $n = 2$ behave differently in that they have $\sigma < -1$ for both large and small k, reaching maximal growth rates $\sigma \approx -0.69$ and $\sigma \approx -0.79$ at wavenumbers $k \approx 8.64$ and $k \approx 10.83$, respectively.

We then computed curves of marginal stability for the fundamental mode, which we give in terms of the input parameter $\mathcal{Z}_{\text{in}}$ as a function of the viscosity ratio m for a number of fixed values for the wavenumber k. The results are shown in figure 5.9, which shows that, independent of the particular wavenumber k, the curves of marginal stability have a similar qualitative structure: as $\mathcal{Z}_{\text{in}} \to 0$ they diverge to $m = \infty$, while as $\mathcal{Z}_{\text{in}} \to \infty$ they each approach a constant value of m which compares very well to

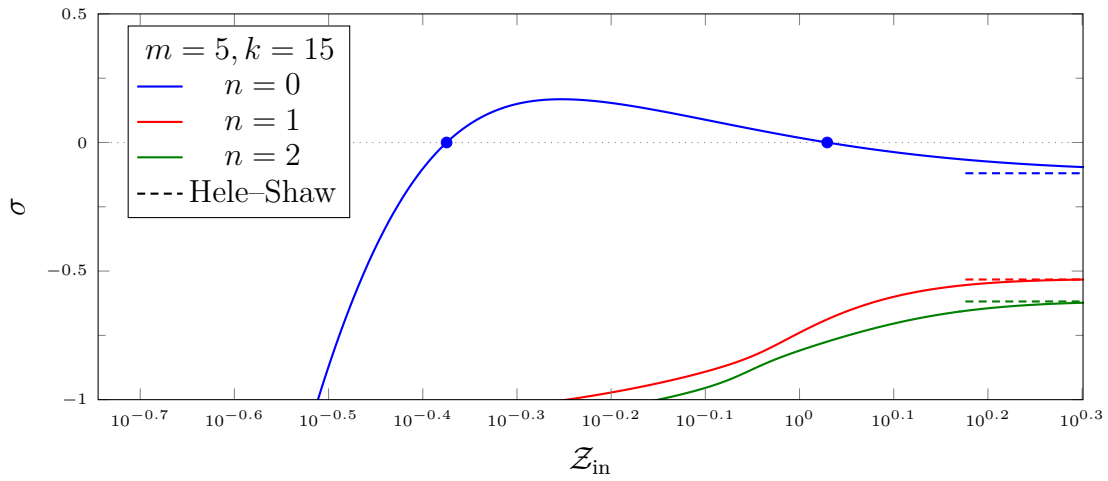

Fig. 5.6 The growth rates σ corresponding to the first three eigenmodes $n \in \{0, 1, 2\}$ as a function of the input parameter $\mathcal{Z}_{\text{in}}$ with viscosity ratio $m = 5$ and wavenumber $k = 15$. The fundamental mode $n = 0$ is unstable ($\sigma > 0$) if $\mathcal{Z}_{\text{in}}$ lies between the two points of marginal stability where $\sigma = 0$ (blue dots). In the limit $\mathcal{Z}_{\text{in}} \to \infty$ the growth rates tend to the values (dashed) for the perturbation modes of an intrusion in a Hele-Shaw cell studied in Chapter 4.

the corresponding values obtained for intrusions into Hele-Shaw cells in Chapter 4. For intermediate values of $\mathcal{Z}_{\text{in}}$ the marginal-stability curves are somewhat C-shaped, such that for each wavenumber k there is a minimal m where $\sigma = 0$, which occurs at some finite nonzero $\mathcal{Z}_{\text{in}}$. Below this minimal value of m, perturbations with that k are stable for all $\mathcal{Z}_{\text{in}}$, and above this m, there is an interval of $\mathcal{Z}_{\text{in}}$, potentially extending to $\mathcal{Z}_{\text{in}} = \infty$, within which perturbations with that k are unstable.

The conclusion from figure 5.9 is that intermediate influxes $\mathcal{Q}_{\text{in}}$, corresponding to intermediate $\mathcal{Z}_{\text{in}}$, are the most unstable for given values k and m (see §5.3.1). However, without any regularising physical mechanisms to stabilise the large-wavenumber perturbations ($k \to \infty$), figure 5.9 also suggests that for any $m > 3/2$ we can find an unstable mode if we choose k sufficiently large. This is similar to the results for intrusions into Hele-Shaw cells in Chapter 4.

5.3.1 Comparison of theory and experiments

As mentioned in Chapter 2, Box, Gell and Neufeld conducted experiments with glycerol in a square tank with an experimental set-up as described in Dauck et al. (2019). For sufficiently more viscous ambient fluids and certain flow rates, they observed the flow

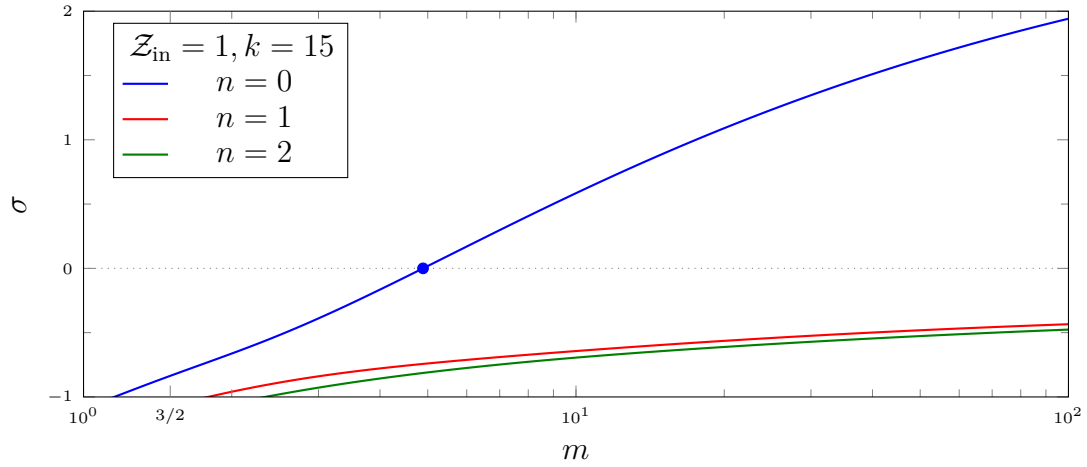

Fig. 5.7 The growth rates σ corresponding to the first three eigenmodes $n \in \{0, 1, 2\}$ as a function of the viscosity ratio m with input parameter $\mathcal{Z}_{\text{in}} = 1$ and wavenumber $k = 15$. The fundamental mode $n = 0$ is unstable if m is sufficiently large with marginal stability where $\sigma = 0$ (blue dot).

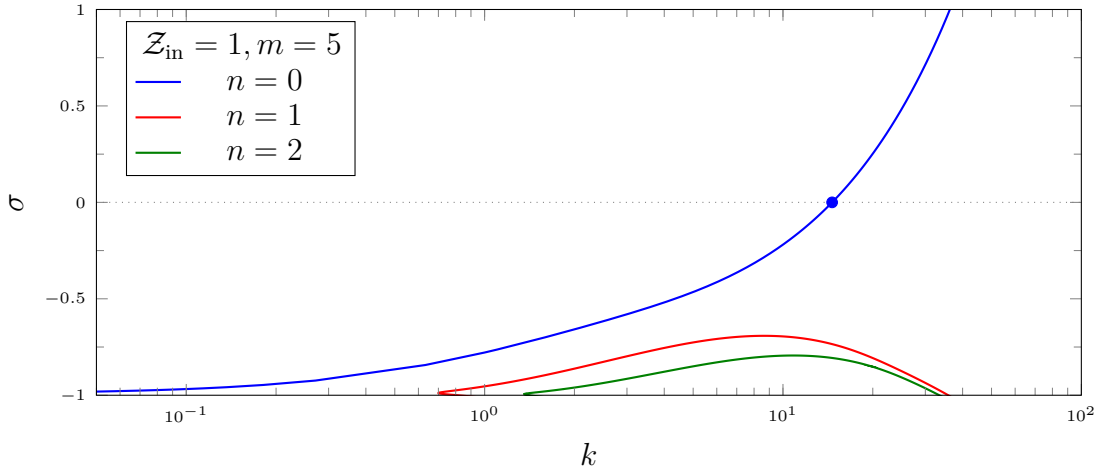

Fig. 5.8 The growth rates σ corresponding to the first three eigenmodes $n \in \{0, 1, 2\}$ as a function of the wavenumber k with input parameter $\mathcal{Z}_{\text{in}} = 1$ and viscosity ratio $m = 5$. The fundamental mode $n = 0$ is unstable if k exceeds a certain value with marginal stability where $\sigma = 0$ (blue dot).

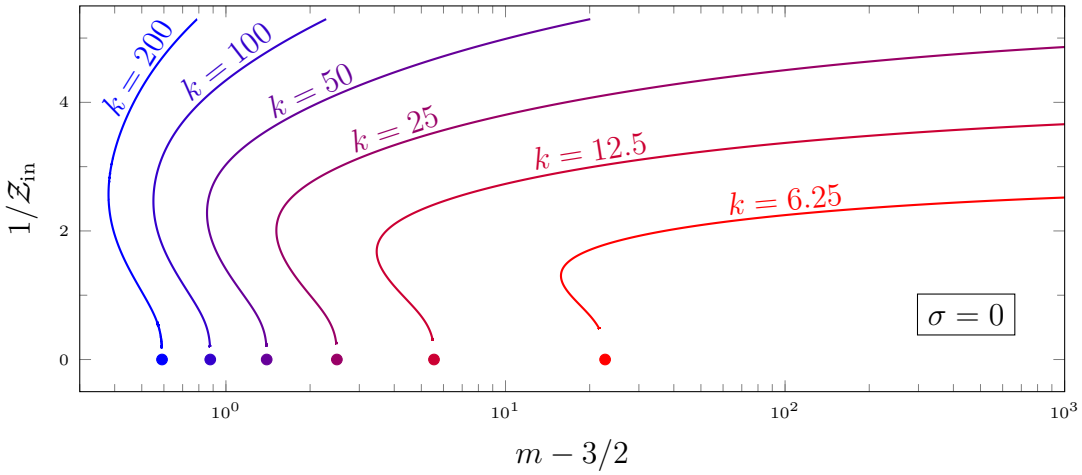

Fig. 5.9 The marginal-stability contours ($\sigma = 0$) of the fundamental mode for a range of wavenumbers $k \in \{6.25, 12.5, 25.50, 100, 200\}$. The axes are chosen for convenience. As $\mathcal{Z}_{\text{in}} \to \infty$, the curves of marginal stability tend to the points of marginal stability for the same values of k (coloured dots) for an intrusion in a Hele-Shaw cell studied in Chapter 4.

to become unstable and develop a finger-like pattern. An example time-series of such an unstable case was shown in figure 5.1.

Figure 5.10 compares the result of these experiments to the curves of marginal stability $\sigma = 0$ for fixed wavenumbers $k \in \{12.5, 25, 50, 100, 200\}$, as in figure 5.9. This shows that, similar to the theoretical results, the experiments suggest a C-shaped region of instability. In other words, experimentally the most unstable cases occur at intermediate $\mathcal{Z}_{\text{in}}$ corresponding to intermediate influxes $\mathcal{Q}_{\text{in}}$, while both large and small $\mathcal{Z}_{\text{in}}$ seem to be stable in the experiments. As discussed in §5.2.2, small $\mathcal{Z}_{\text{in}} \ll 1$ correspond to large influxes $\mathcal{Q}_{\text{in}} \gg 1$ and vice versa. Physically, large influxes $\mathcal{Q}_{\text{in}} \gg 1$ lead to the intruding fluid spilling on top of the barely perturbed ambient fluid effectively creating a single-layer gravity current (see §5.B.1), which we know from Chapter 3 is stable. On the other hand, small influxes $\mathcal{Q}_{\text{in}} \ll 1$ result in a nearly flat top surface, which can be compared to Hele-Shaw flows (see §5.B.2). In contrast to the experimental results, we would expect this limit to be unstable, both from the numerical results in §5.3 and from the analysis of intrusions into Hele-Shaw cells in Chapter 4. However, we note that small influxes $\mathcal{Q}_{\text{in}}$ correspond physically to a slow moving and thin current, and to a small shock height in dimensional terms. Also, small $\mathcal{Q}_{\text{in}}$ requires larger k for an instability. All of these factors suggest that diffusion between the miscible fluids might have played a stabilising role (at small influx rates), which cannot be neglected.

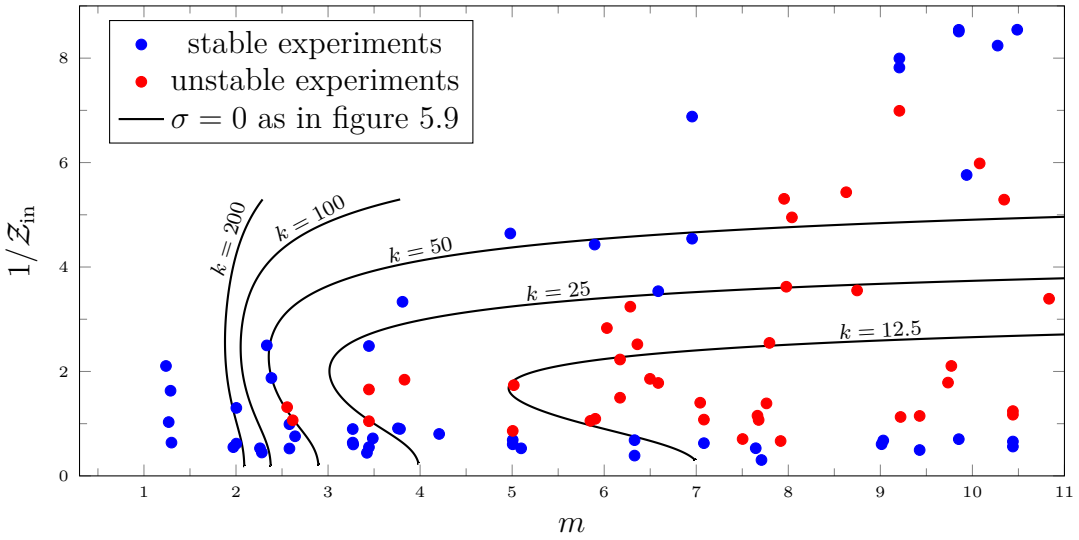

Fig. 5.10 Comparison of experimental stability results to the marginal-stability curves $\sigma = 0$ for fixed k as in figure 5.9.

In addition, the experiments were conducted over finite times within a finite tank, and it was not always clear whether a current had become unstable on these scales.

A key result derived in this chapter is that, for fixed viscosity ratio $m > 3/2$ and wavenumber k, the most unstable case is given by intermediate $\mathcal{Z}_{\rm in}$ and correspondingly by intermediate influxes $\mathcal{Q}_{\rm in}$. Qualitatively, this agrees very well with the experimental data, implying that key aspects of the relevant physics are captured by our analysis. A quantitative comparison is not possible, as the present model based on lubrication theory and neglecting diffusion does not allow to select a finite most unstable wavenumber k.

5.4 Discussion & Conclusions

In this chapter we have successfully developed a theoretical model which describes a fingering instability of a viscous gravity current spreading over a uniform ambient fluid layer from a constant-flux point source. This was motivated by experimental observations of others, which saw the formation of finger-like patterns in such flows for sufficiently more viscous ambient fluids. The theoretical model was based on a linear stability analysis using scaling-invariant variables similar to Chapter 3, and the resulting equations were solved numerically using the continuation software package AUTO.

The numerical results for a two-layer current with a shock ($m > 3/2$) revealed only one potentially unstable eigenmode, the fundamental mode $n = 0$. This mode was

shown to become more unstable and grow more rapidly as the wavenumber increases ($k \to \infty$). As a result, there is instability for all $m > 3/2$ at sufficiently large k. Conversely, the numerical results for a two-layer current without a shock ($m < 3/2$) clearly indicate that those currents are stable. These results were identified as very similar to the results of Chapter 4, which considers the linear stability of an intrusion into a Hele-Shaw cell. Therefore, we conclude that the instability observed in the case of a two-layer viscous gravity current is governed by the same physical mechanism as the instability of a miscible Hele-Shaw-cell intrusion, namely the jump in mobility and hence pressure gradient at the frontal shock. In some sense, this is the same as the immiscible Saffman–Taylor instability, though the latter is regularised by surface tension at large wavenumber and the critical viscosity ratio $m_{\text{crit}} = 1$ differs from the critical viscosity ratio $m_{\text{crit}} = 3/2$ found here.

In the limit of small influxes, we could also directly compare the results of this chapter to the calculations in Chapter 4, which revealed very good agreement. One feature not present in the stability analysis of an intrusion into a Hele-Shaw cell is the dependency of the growth rates on the influx $\mathcal{Q}_{\text{in}}$. In particular, for any given wavenumber k, we found a C-shaped curve of marginal stability on a $(m, \mathcal{Q}_{\text{in}})$-diagram indicating that intermediate influxes $\mathcal{Q}_{\text{in}}$ are the most unstable. This agrees well qualitatively with experiments, but due to the lack of a regularising mechanism for large k, no quantitative comparison is possible.

There are two analytic solutions to the equations, one obtained from considering a small shift in the temporal origin (as we did in Chapter 3 for single-layer currents), and a second from considering perturbations only to the interface in the case of an equal-viscosity flow. These are derived in appendices 5.C.1 and 5.C.2 respectively.

Finally, we established the cases of single-layer viscous gravity currents studied in Chapter 3 and intrusions into Hele-Shaw cells studied in Chapter 4 as formal asymptotic limits for large and small influxes, respectively.

Overall, our model qualitatively confirms an instability in two-layer gravity currents, based on a similar mechanism to the well-known Saffman–Taylor instability in immiscible intrusions in Hele-Shaw cells. Future work adding in additional physics into the model, such as a fully three-dimensional Stokes flow at the nose, diffusion or surface tension of the top-surface, could hopefully provide improved quantitative predictions on the exact parameters leading to instability. In contrast to the equal-density currents in this chapter, a further interesting case to study would be a two-layer viscous gravity current where the intruding fluid is less dense than the ambient fluid, hence creating an additional buoyancy force. In that case, the interface is no longer governed by

a hyperbolic advection equation but instead becomes diffusive in nature due to the pressure gradient resulting from slopes in the interface. We would expect that for sufficiently large density differences, the current is stabilised by the resulting buoyancy forces, similar perhaps to Kowal and Worster (2019b). An intriguing open question is whether the additional buoyancy forces are sufficient to stabilise large-wavenumber perturbations, even for overall unstable cases, which would allow prediction of a most unstable wavenumber.

Appendix 5.A Changing variables

For numerical purposes, we introduce several changes of variables, similar to methods developed in Chapter 3. The details are presented in this appendix.

5.A.1 Scaling-invariant equations

We first transform the differential equations (5.12) and (5.13) into scaling-invariant form and change the independent variable to mitigate the singular nature of the nose.

Before the nose ($\xi < \xi_*$)

Equation (5.12a) describes a single-layer viscous gravity current with an evolving mobility $\mathcal{M}(\lambda)$ that is coupled to the advecting interface position λ by (5.12b). Hence, similar to the equation for a single-layer gravity current discussed in Chapter 3, these equations remain unchanged under the rescalings

$$h \mapsto c^2 h, \qquad q_\xi \mapsto c^5 q_\xi, \qquad \xi \mapsto c^3 \xi, \tag{5.18}$$

where c is any non-zero constant. This motivates the introduction of scaling-invariant variables

$$\vartheta = \frac{q_\xi}{\xi^{5/3}}, \qquad \zeta = \frac{h}{\xi^{2/3}}, \tag{5.19}$$

where we again call ϑ the scaling-invariant flux and ζ the scaling-invariant height. The fluid fraction λ is already scaling-invariant.

Substituting (5.19) into the governing equations (5.12) gives

$$\frac{\partial\zeta}{\partial\tau} - \tfrac{1}{2}\left(\frac{\partial\zeta}{\partial\Lambda} + \tfrac{2}{3}\zeta\right) + \left(\frac{\partial\vartheta}{\partial\Lambda} + \tfrac{8}{3}\vartheta\right) = \frac{\partial}{\partial\theta}\left(\mathcal{M}\zeta^3\frac{\partial\zeta}{\partial\theta}\right), \tag{5.20a}$$

$$\frac{\partial\lambda\zeta}{\partial\tau} - \tfrac{1}{2}\left(\frac{\partial\lambda\zeta}{\partial\Lambda} + \tfrac{2}{3}\lambda\zeta\right) + \left(\frac{\partial\mathcal{F}\vartheta}{\partial\Lambda} + \tfrac{8}{3}\mathcal{F}\vartheta\right) = \frac{\partial}{\partial\theta}\left(\mathcal{F}\mathcal{M}\zeta^3\frac{\partial\zeta}{\partial\theta}\right), \tag{5.20b}$$

$$\vartheta = -\mathcal{M}\zeta^3\left(\frac{\partial\zeta}{\partial\Lambda} + \tfrac{2}{3}\zeta\right), \tag{5.20c}$$

where, for convenience, we have introduced $\Lambda = \log\xi$.

We now change the independent variable from ξ to λ by writing $\xi = \xi(\lambda,\theta,\tau)$ or, equivalently, from Λ to λ by writing $\Lambda = \Lambda(\lambda,\theta,\tau)$. To transform the governing equations, we apply the chain rule to the partial derivatives

$$\left(\frac{\partial}{\partial\lambda}\right)_{\theta,\tau} = \left(\frac{\partial\Lambda}{\partial\lambda}\right)_{\theta,\tau}\left(\frac{\partial}{\partial\Lambda}\right)_{\theta,\tau}, \tag{5.21a}$$

$$\left(\frac{\partial}{\partial\theta}\right)_{\lambda,\tau} = \left(\frac{\partial}{\partial\theta}\right)_{\Lambda,\tau} + \left(\frac{\partial\Lambda}{\partial\theta}\right)_{\lambda,\tau}\left(\frac{\partial}{\partial\Lambda}\right)_{\theta,\tau}, \tag{5.21b}$$

$$\left(\frac{\partial}{\partial\tau}\right)_{\lambda,\theta} = \left(\frac{\partial}{\partial\tau}\right)_{\Lambda,\theta} + \left(\frac{\partial\Lambda}{\partial\tau}\right)_{\lambda,\theta}\left(\frac{\partial}{\partial\Lambda}\right)_{\theta,\tau}, \tag{5.21c}$$

where the subscripts on the brackets signify which variables are being held constant. Inverting these relationships leads to the following transformation laws from the variables (Λ,θ,τ) to the variables (λ,θ,τ):

$$\frac{\partial}{\partial\Lambda} \mapsto \frac{\partial}{\partial\lambda}\Big/\frac{\partial\Lambda}{\partial\lambda}, \tag{5.22a}$$

$$\frac{\partial}{\partial\theta} \mapsto \frac{\partial}{\partial\theta} - \left(\frac{\partial\Lambda}{\partial\theta}\Big/\frac{\partial\Lambda}{\partial\lambda}\right)\frac{\partial}{\partial\lambda}, \tag{5.22b}$$

$$\frac{\partial}{\partial\tau} \mapsto \frac{\partial}{\partial\tau} - \left(\frac{\partial\Lambda}{\partial\tau}\Big/\frac{\partial\Lambda}{\partial\lambda}\right)\frac{\partial}{\partial\lambda}. \tag{5.22c}$$

We can then use the transformation laws (5.22) and the new variables ϑ and ζ defined in (5.19) to rewrite (5.12). But first, we focus on the right-hand side of (5.12a)

to simplify the nested θ derivatives. We find that

$$\frac{\partial}{\partial\theta}\left(\mathcal{M}\zeta^3\frac{\partial\zeta}{\partial\theta}\right)\mapsto\left(\frac{\partial}{\partial\theta}-\left\{\frac{\partial\Lambda}{\partial\theta}\Big/\frac{\partial\Lambda}{\partial\lambda}\right\}\frac{\partial}{\partial\lambda}\right)\left(\mathcal{M}\zeta^3\left\{\frac{\partial\zeta}{\partial\theta}-\left\{\frac{\partial\Lambda}{\partial\theta}\Big/\frac{\partial\Lambda}{\partial\lambda}\right\}\frac{\partial\zeta}{\partial\lambda}\right\}\right)$$
$$=\mathcal{M}\zeta^3\left(\frac{\partial^2\zeta}{\partial\theta^2}-\left\{\frac{\partial\zeta}{\partial\lambda}\Big/\frac{\partial\Lambda}{\partial\lambda}\right\}\frac{\partial^2\Lambda}{\partial\theta^2}\right)+O\left(\frac{\partial}{\partial\theta}\times\frac{\partial}{\partial\theta}\right),\quad(5.23)$$

and we note that the final term, which contains all the products of two azimuthal derivatives, is negligible both for an axisymmetric solution and for a linear perturbation to an axisymmetric solution. Therefore, (5.12) after some algebra becomes

$$\left(\frac{\partial\zeta}{\partial\tau}-\tfrac{1}{3}\zeta+\tfrac{8}{3}\vartheta\right)\frac{\partial\Lambda}{\partial\lambda}-\left(\frac{\partial\Lambda}{\partial\tau}+\tfrac{1}{2}\right)\frac{\partial\zeta}{\partial\lambda}+\frac{\partial\vartheta}{\partial\lambda}$$
$$=\mathcal{M}\zeta^3\left(\frac{\partial\Lambda}{\partial\lambda}\frac{\partial^2\zeta}{\partial\theta^2}-\frac{\partial\zeta}{\partial\lambda}\frac{\partial^2\Lambda}{\partial\theta^2}\right)+O\left(\frac{\partial}{\partial\theta}\times\frac{\partial}{\partial\theta}\right),\quad(5.24a)$$

$$\left(\frac{\partial\lambda\zeta}{\partial\tau}-\tfrac{1}{3}\lambda\zeta+\tfrac{8}{3}\mathcal{F}\vartheta\right)\frac{\partial\Lambda}{\partial\lambda}-\left(\frac{\partial\Lambda}{\partial\tau}+\tfrac{1}{2}\right)\frac{\partial\lambda\zeta}{\partial\lambda}+\frac{\partial\mathcal{F}\vartheta}{\partial\lambda}$$
$$=\mathcal{F}\mathcal{M}\zeta^3\left(\frac{\partial\Lambda}{\partial\lambda}\frac{\partial^2\zeta}{\partial\theta^2}-\frac{\partial\zeta}{\partial\lambda}\frac{\partial^2\Lambda}{\partial\theta^2}\right)+O\left(\frac{\partial}{\partial\theta}\times\frac{\partial}{\partial\theta}\right),\quad(5.24b)$$

$$\frac{\partial\Lambda}{\partial\lambda}=-\left(\frac{3\mathcal{M}\zeta^3}{2\mathcal{M}\zeta^4+3\vartheta}\right)\frac{\partial\zeta}{\partial\lambda}.\quad(5.24c)$$

We then expand the scaling-invariant variables in terms of an axisymmetric steady base state and linear normal-mode perturbations, which we assume to be small compared to the base state:

$$\vartheta(\lambda,\theta,\tau)=\Theta_0(\lambda)+\Theta_1(\lambda)\mathrm{e}^{\mathrm{i}k\theta+\sigma\tau}+\cdots,\quad(5.25)$$
$$\zeta(\lambda,\theta,\tau)=Z_0(\lambda)+Z_1(\lambda)\mathrm{e}^{\mathrm{i}k\theta+\sigma\tau}+\cdots,\quad(5.26)$$
$$\Lambda(\lambda,\theta,\tau)=\Lambda_0(\lambda)+\Lambda_1(\lambda)\mathrm{e}^{\mathrm{i}k\theta+\sigma\tau}+\cdots.\quad(5.27)$$

Substituting this expansion into (5.24), we firstly obtain nonlinear equations for the base state

$$\Theta_0' = \frac{Z_0 - 2\mathcal{F}'\Theta_0}{\mathcal{F} - \lambda}\left(\tfrac{1}{2} + \tfrac{8}{3}\mathcal{M}Z_0^3\right), \tag{5.28a}$$

$$Z_0' = \frac{Z_0 - 2\mathcal{F}'\Theta_0}{\mathcal{F} - \lambda}\left(1 + \frac{2\mathcal{M}Z_0^4}{3\Theta_0}\right), \tag{5.28b}$$

$$\Lambda_0' = \frac{Z_0 - 2\mathcal{F}'\Theta_0}{\mathcal{F} - \lambda}\left(-\frac{\mathcal{M}Z_0^3}{\Theta_0}\right), \tag{5.28c}$$

and, secondly, a linear system for the perturbations

$$\begin{pmatrix}\Theta_1'\\ Z_1'\\ \Lambda_1'\end{pmatrix} = \boldsymbol{M}\cdot\begin{pmatrix}\Theta_1\\ Z_1\\ \Lambda_1\end{pmatrix}, \tag{5.29}$$

where the matrix $\boldsymbol{M}$ is given in terms of the base state as

$$\begin{aligned}\boldsymbol{M} = \begin{pmatrix}\frac{\partial}{\partial\Theta_0}\\ \frac{\partial}{\partial Z_0}\\ \frac{\partial}{\partial\Lambda_0}\end{pmatrix} \otimes \begin{pmatrix}\Theta_0'\\ Z_0'\\ \Lambda_0'\end{pmatrix} + k^2\mathcal{M}Z_0^3\begin{pmatrix}0 & -\Lambda_0' & Z_0'\\ 0 & 0 & 0\\ 0 & 0 & 0\end{pmatrix}\\ - \frac{2\sigma\mathcal{M}Z_0^3}{\Theta_0}\begin{pmatrix}0 & -\frac{8}{3}\Theta_0\Lambda_0' & \frac{\Theta_0}{2\mathcal{M}(\lambda-\mathcal{F})Z_0^2} + \frac{8}{3}\Theta_0\left(Z_0' + \frac{Z_0}{\lambda-\mathcal{F}}\right)\\ 0 & Z_0' & -\frac{Z_0'}{\Lambda_0'}\left(Z_0' + \frac{Z_0}{\lambda-\mathcal{F}}\right)\\ 0 & \Lambda_0' & -\left(Z_0' + \frac{Z_0}{\lambda-\mathcal{F}}\right)\end{pmatrix},\end{aligned} \tag{5.30}$$

and $\otimes$ denotes the outer product $\boldsymbol{a}\otimes\boldsymbol{b} = \boldsymbol{a}\cdot\boldsymbol{b}^\intercal$. We note that (5.30) is already moderately complex, and after substituting the base-state derivatives (5.28) and expanding the outer product, the resulting matrix is exceedingly unwieldy.

Beyond the nose ($\xi > \xi_*$)

Beyond the nose, where $\xi > \xi_*$ and effectively $\lambda = 0$, we simply have a single-layer gravity current as in Chapter 3. Hence, the same symmetry holds as before the nose ($\xi < \xi_*$) and we can define the same scaling-invariant variables ϑ and ζ as in (5.19). We then change independent variables. However, since $\lambda = 0$, we choose ζ instead as

the independent variable. This leads to transformation laws similar to (5.22) given by

$$\frac{\partial}{\partial\Lambda} \mapsto \frac{\partial}{\partial\zeta}\Big/\frac{\partial\Lambda}{\partial\zeta}\,, \tag{5.31a}$$

$$\frac{\partial}{\partial\theta} \mapsto \frac{\partial}{\partial\theta} - \left(\frac{\partial\Lambda}{\partial\theta}\Big/\frac{\partial\Lambda}{\partial\zeta}\right)\frac{\partial}{\partial\zeta}, \tag{5.31b}$$

$$\frac{\partial}{\partial\tau} \mapsto \frac{\partial}{\partial\tau} - \left(\frac{\partial\Lambda}{\partial\tau}\Big/\frac{\partial\Lambda}{\partial\zeta}\right)\frac{\partial}{\partial\zeta}, \tag{5.31c}$$

where $\Lambda = \log\xi$, which transform the governing equations (5.13), or equivalently (5.20a,c) with $\mathcal{M} = 1$, into

$$\frac{\partial\vartheta}{\partial\zeta} + \left(\tfrac{8}{3}\vartheta - \tfrac{1}{3}\zeta\right)\frac{\partial\Lambda}{\partial\zeta} - \tfrac{1}{2} - \frac{\partial\Lambda}{\partial\tau} + \zeta^3\frac{\partial^2\Lambda}{\partial\theta^2} = O\left(\frac{\partial}{\partial\theta}\times\frac{\partial}{\partial\theta}\right), \tag{5.32a}$$

$$\frac{\partial\Lambda}{\partial\zeta} = \frac{-3\zeta^3}{2\zeta^4 + 3\vartheta}, \tag{5.32b}$$

where again the terms quadratic in azimuthal derivatives are negligible.

We expand similarly to before in terms of base-state and perturbation variables:

$$\vartheta(\zeta,\theta,\tau) = \widetilde{\Theta}_0(\zeta) + \widetilde{\Theta}_1(\zeta)\mathrm{e}^{\mathrm{i}k\theta+\sigma\tau} + \cdots\,, \tag{5.33a}$$

$$\Lambda(\zeta,\theta,\tau) = \widetilde{\Lambda}_0(\zeta) + \widetilde{\Lambda}_1(\zeta)\mathrm{e}^{\mathrm{i}k\theta+\sigma\tau} + \cdots\,, \tag{5.33b}$$

leading to governing equations given for the base state by

$$\widetilde{\Theta}_0' = \left(\frac{16\zeta^3+3}{2\zeta^4+3\widetilde{\Theta}_0}\right)\frac{\widetilde{\Theta}_0}{2}, \qquad\qquad \widetilde{\Lambda}_0' = \frac{-3\zeta^3}{2\zeta^4+3\widetilde{\Theta}_0}, \tag{5.34}$$

and for the perturbations by

$$\widetilde{\Theta}_1' = \frac{(16\zeta^3+3)\,\zeta^4}{\left(2\zeta^4+3\widetilde{\Theta}_0\right)^2}\widetilde{\Theta}_1 + \left(\sigma + k^2\zeta^3\right)\widetilde{\Lambda}_1, \qquad \widetilde{\Lambda}_1' = \frac{9\zeta^3}{\left(2\zeta^4+3\widetilde{\Theta}_0\right)^2}\widetilde{\Theta}_1. \tag{5.35}$$

Recovering the physical variables

We also wish to recover the equivalent physical perturbation height $H_1(\xi)$, flux $Q_1(\xi)$ and, where appropriate, interfacial position $\lambda_1(\xi)$. Firstly, we consider the system

before the nose, where we write $X_0(\lambda) = \mathrm{e}^{\Lambda_0(\lambda)}$ giving

$$\xi(\lambda,\theta,\tau) \sim X_0(\lambda)\Big(1 + \Lambda_1(\lambda)\mathrm{e}^{\mathrm{i}k\theta+\sigma\tau} + \cdots\Big)$$
$$\Rightarrow \qquad \lambda(\xi,\theta,\tau) \sim X_0^{-1}(\xi) - \frac{\Lambda_1 \circ X_0^{-1}(\xi)}{\Lambda_0' \circ X_0^{-1}(\xi)}\mathrm{e}^{\mathrm{i}k\theta+\sigma\tau} + \cdots, \quad (5.36)$$

which, together with

$$h(\xi,\theta,\tau) = \xi^{2/3}\zeta, \qquad\qquad q_\xi(\xi,\theta,\tau) = \xi^{5/3}\vartheta, \quad (5.37)$$

allows us to recover the physical variables in terms of the rescaled ones:

$$h(\xi,\theta,\tau) \sim \left[\underbrace{\xi^{2/3}Z_0(\lambda)}_{H_0} + \underbrace{\xi^{2/3}\left(Z_1(\lambda) - \frac{Z_0'(\lambda)}{\Lambda_0'(\lambda)}\Lambda_1(\lambda)\right)}_{H_1}\mathrm{e}^{\mathrm{i}k\theta+\sigma\tau} + \cdots\right]_{\lambda=X_0^{-1}(\xi)}, \quad (5.38a)$$

$$q_\xi(\xi,\theta,\tau) \sim \left[\underbrace{\xi^{5/3}\Theta_0(\lambda)}_{Q_0} + \underbrace{\xi^{5/3}\left(\Theta_1(\lambda) - \frac{\Theta_0'(\lambda)}{\Lambda_0'(\lambda)}\Lambda_1(\lambda)\right)}_{Q_1}\mathrm{e}^{\mathrm{i}k\theta+\sigma\tau} + \cdots\right]_{\lambda=X_0^{-1}(\xi)}, \quad (5.38b)$$

$$\lambda(\xi,\theta,\tau) \sim \left[\underbrace{\lambda}_{\lambda_0} - \underbrace{\frac{\Lambda_1(\lambda)}{\Lambda_0'(\lambda)}}_{\lambda_1}\mathrm{e}^{\mathrm{i}k\theta+\sigma\tau} + \cdots\right]_{\lambda=X_0^{-1}(\xi)}. \quad (5.38c)$$

Beyond the nose, we similarly obtain

$$h(\xi,\theta,\tau) \sim \left[\underbrace{\xi^{2/3}s}_{H_0} - \underbrace{\xi^{2/3}\frac{\widetilde{\Lambda}_1(\zeta)}{\widetilde{\Lambda}_0'(\zeta)}}_{H_1}\mathrm{e}^{\mathrm{i}k\theta+\sigma\tau} + \cdots\right]_{\zeta=\widetilde{X}_0^{-1}(\xi)}, \quad (5.39a)$$

$$q_\xi(\xi,\theta,\tau) \sim \left[\underbrace{\xi^{5/3}\widetilde{\Theta}_0(\zeta)}_{Q_0} + \underbrace{\xi^{5/3}\left(\widetilde{\Theta}_1(\zeta) - \frac{\widetilde{\Theta}_0'(\zeta)}{\widetilde{\Lambda}_0'(\zeta)}\widetilde{\Lambda}_1(\zeta)\right)}_{Q_1}\mathrm{e}^{\mathrm{i}k\theta+\sigma\tau} + \cdots\right]_{\zeta=\widetilde{X}_0^{-1}(\xi)}, \quad (5.39b)$$

where now we have $\widetilde{X}_0(\zeta) = \mathrm{e}^{\widetilde{\Lambda}_0(\zeta)}$. Equation (5.39) is exactly the same as in Chapter 3 since the system beyond the nose of a two-layer gravity current is just a single-layer gravity current.

5.A.2 Scaling-invariant boundary conditions

After having transformed the differential equations into scaling-invariant form, we now consider scaling-invariant forms of the boundary conditions (5.14). These are the conditions we use:

- the far-field condition:

$$\lim_{\zeta\to 0}\left(\frac{\widetilde{\Theta}_1}{\zeta\widetilde{\Lambda}_1}\right)=\tfrac{1}{3}, \tag{5.40}$$

- the continuity conditions at the nose:

$$\Theta_0=\widetilde{\Theta}_0, \qquad \Lambda_0=\widetilde{\Lambda}_0, \tag{5.41a,b}$$
$$\Theta_1=\widetilde{\Theta}_1+Z_1\widetilde{\Theta}_0', \qquad \Lambda_1=\widetilde{\Lambda}_1+Z_1\widetilde{\Lambda}_0', \tag{5.41c,d}$$

- the no-flux conditions at the nose:

$$\frac{\Theta_0}{Z_0}=\frac{\lambda_*}{2\mathcal{F}_*}, \qquad \frac{\Theta_1}{\Theta_0}-\frac{Z_1}{Z_0}=2\sigma\Lambda_1, \tag{5.42}$$

- and the condition at the origin:

$$\lim_{\lambda\to 1}\left\{\left(\frac{\Theta_1}{\Theta_0}+\tfrac{8}{3}\Lambda_1\right)+\frac{mkZ_0^4}{\Theta_0}\left(\frac{Z_1}{Z_0}+\tfrac{2}{3}\Lambda_1\right)+k\Lambda_1\right\}=0, \tag{5.43}$$

Their derivations are discussed in detail in the sections below.

First, we consider the position of the boundary points in terms of the transformed independent variables, λ (before) and ζ (beyond the nose), which are as follows: the physical origin is at $\lambda=1$ where the intruding fluid occupies the whole current depth. The physical far-field is at $\zeta=0$ where the height is finite ($h\to 1$) and the radial variable is large ($\xi\to\infty$). When viewed from beyond, the nose is at $\zeta=\zeta_*$, where we need to be careful to allow for perturbation of its position:

$$\zeta_*=Z_0\left(\lambda_*\right)+Z_1\left(\lambda_*\right)\mathrm{e}^{\mathrm{i}k\theta+\sigma\tau}+\cdots, \tag{5.44}$$

where $Z_0\left(\lambda_*\right)=\mathcal{Z}_{\mathrm{in}}$ is the scaling-independent input parameter replacing the scaling-dependent influx $\mathcal{Q}_{\mathrm{in}}$. Alternatively, when viewed from before, the nose is at $\lambda=\lambda_*<1$, where $\lambda_*=\lambda_{\mathrm{crit}}$ from (5.8), which is nonzero if there is a shock. We assume that the value λ_* at the nose is not perturbed, as this would correspond to perturbations to

the shock height, which are excluded. This is justified by the discussion in §2.4, where we noted that the shock height is attained within a finite time and therefore always has an unperturbed height in the linear perturbation regime (see also the discussion in §4.4.3 regarding perturbations of the shock height in Hele-Shaw cells).

We also note that all boundary points are, in fact, singular points of the nonlinear governing equations and hence, to confirm that a proposed boundary condition does indeed restrict the solution space as desired, expansions of generic solutions near these points need to be evaluated.

The boundary condition at the far-field

By studying (5.34a), we find that there are three possible behaviours for the base state $\widetilde{\Theta}_0(\zeta)$ as $\zeta \to 0$ given to leading order by

$$\widetilde{\Theta}_0 \sim c_\infty, \qquad \widetilde{\Theta}_0 \sim \tfrac{1}{2}\zeta \qquad \text{or} \qquad \widetilde{\Theta}_0 \sim c_\infty \mathrm{e}^{-\frac{1}{4}\zeta^{-3}}, \tag{5.45}$$

where $c_\infty > 0$ is a positive constant of integration.

Physically, we expect $\vartheta \to 0$ exponentially since $q_\xi \to 0$ exponentially faster than $\xi \to 0$. In fact, it can be shown that the first two cases above correspond to single-layer gravity currents of finite extent, with or without a sink at the nose, respectively. The third case corresponds to a single-layer gravity current of infinite extent with a finite height at infinity, and therefore, we impose that $\widetilde{\Theta}_0$ behaves like (5.45c) as $\zeta \to 0$. Substituting this base-state behaviour into (5.35) leads to a confluent hypergeometric equation for the perturbations $\widetilde{\Theta}_1$ and $\widetilde{\Lambda}_1$ with solutions given to leading order as $\zeta \to 0$ by

$$\widetilde{\Theta}_1 \sim c_1\zeta^{3\sigma}\mathrm{e}^{-\frac{1}{4}\zeta^{-3}} + c_2\zeta^{4-3\sigma}, \qquad \widetilde{\Lambda}_1 \sim 3c_1\zeta^{3\sigma-1}\mathrm{e}^{-\frac{1}{4}\zeta^{-1}} - \frac{3c_2}{4\sigma}\zeta^{-3\sigma}, \tag{5.46}$$

where c_1 and c_2 are two constants of integration. The solution associated with c_1 always decays exponentially, while the solution associated with c_2 decays only algebraically for $\sigma < 0$ and grows otherwise.

Physically, we expect the perturbations to decay in the far-field, and in fact we argue that this decay needs to be exponential, reflecting the decay of the base state. Simple algebraic decay would correspond to a significant change in the nature of the far-field. Therefore, we have $c_2 = 0$, and hence a suitable boundary condition is

$$\lim_{\zeta\to 0}\left(\frac{\widetilde{\Theta}_1}{\zeta\widetilde{\Lambda}_1}\right) = \tfrac{1}{3}. \tag{5.47}$$

The continuity condition at the nose

Physically, the top-surface height and the total flux have to be continuous at the nose as given by the boundary condition (5.14f). In terms of the scaling-invariant variables this condition simply translates into ϑ and ζ being continuous. We recall that the nose is at

$$\lambda_* = \lambda_{\mathrm{crit}} \qquad \text{and} \qquad \zeta_* = \mathcal{Z}_{\mathrm{in}} + Z_1\left(\lambda_{\mathrm{crit}}\right) \mathrm{e}^{\mathrm{i}k\theta+\sigma\tau} + \cdots , \tag{5.48}$$

in terms of the independent variables before and beyond the nose, respectively. We also note that the nose is a well-defined physical position and thus the radial variables $\Lambda_0(\lambda)$ and $\widetilde{\Lambda}_0(\zeta)$ must agree at the nose. We conclude that the continuity conditions for the base state are

$$\Theta_0 = \widetilde{\Theta}_0, \qquad\qquad \Lambda_0 = \widetilde{\Lambda}_0, \tag{5.49}$$

and for the perturbations are

$$\Theta_1 = \widetilde{\Theta}_1 + Z_1\widetilde{\Theta}_0', \qquad\qquad \Lambda_1 = \widetilde{\Lambda}_1 + Z_1\widetilde{\Lambda}_0', \tag{5.50}$$

where all Θ_i and Λ_i are evaluated at $\lambda = \lambda_{\mathrm{crit}}$, and all $\widetilde{\Theta}_i$ and $\widetilde{\Lambda}_i$ at $\zeta = \mathcal{Z}_{\mathrm{in}}$.

The no-flux condition at the nose

A further boundary condition at the nose is obtained from local mass conservation of upper-layer fluid as given by (5.14d). Before we transform this boundary condition into the scaling-invariant variables, we note that the unit normal $\boldsymbol{n}$ is given by

$$\boldsymbol{n} = \left[1 + \left(\frac{\partial \xi_*}{\partial \theta}\right)^2\right]^{-1/2} \begin{pmatrix} 1 \\ \frac{\partial \xi_*}{\partial \theta} \end{pmatrix} \sim \begin{pmatrix} 1 \\ \frac{\partial \xi_*}{\partial \theta} \end{pmatrix} + O\left(\frac{\partial}{\partial\theta} \times \frac{\partial}{\partial\theta}\right), \tag{5.51}$$

and hence $\boldsymbol{n}\cdot\boldsymbol{q} \approx q_\xi$ and $\boldsymbol{n}\cdot\boldsymbol{e}_\xi \approx 1$ with corrections being quadratic in the perturbation quantities and therefore negligible. As a consequence, (5.14d) is given in terms of the transformed variables by

$$\frac{\partial \Lambda}{\partial \tau} + \tfrac{1}{2} = \frac{\mathcal{F}\vartheta}{\lambda\zeta} + O\left(\frac{\partial}{\partial\theta} \times \frac{\partial}{\partial\theta}\right). \tag{5.52}$$

By using the expansions (5.25), we then get separate conditions for the base state and perturbations given by

$$\frac{\Theta_0}{Z_0} = \frac{\lambda_*}{2\mathcal{F}_*}, \qquad \frac{\Theta_1}{\Theta_0} - \frac{Z_1}{Z_0} = 2\sigma\Lambda_1, \tag{5.53}$$

at $\lambda = \lambda_*$.

This seems like a straightforward derivation of a local mass-conservation condition at the nose. However, the nose is a singular point of the hyperbolic advection equation for the interface (which is given by the difference of (5.20a) and (5.20b)). Therefore, we have to check whether (5.53) is indeed a sufficient boundary condition appropriately restricting the solutions. For this purpose, we first calculate local expansions of the base state near $\lambda = \lambda_*$ by using (5.28) and (5.53a), and introducing a constant of integration $\Lambda_* = \log \xi_*$ related to the radial scale of the nose position. Then we use (5.29) to find all possible behaviours of the perturbations. This analysis is significantly affected by whether or not there is a shock and hence we consider two cases:

- For $m \leq 3/2$ there is no shock, $\lambda_* = 0$, and we obtain the base-state expansions

$$\Theta_0 \sim \tfrac{1}{3}\mathcal{Z}_{\text{in}} + (3-2m)\mathcal{Z}_{\text{in}}\left(\frac{3+16\mathcal{Z}_{\text{in}}^3}{9+36\mathcal{Z}_{\text{in}}^3}\right)\lambda^2 + \cdots, \tag{5.54a}$$

$$Z_0 \sim \mathcal{Z}_{\text{in}} + 2(3-2m)\mathcal{Z}_{\text{in}}\left(\frac{1+2\mathcal{Z}_{\text{in}}^3}{3+12\mathcal{Z}_{\text{in}}^3}\right)\lambda^2 + \cdots, \tag{5.54b}$$

$$\Lambda_0 \sim \Lambda_* - (3-2m)\left(\frac{2\mathcal{Z}_{\text{in}}^3}{1+4\mathcal{Z}_{\text{in}}^3}\right)\lambda^2 + \cdots, \tag{5.54c}$$

  and the perturbation expansions

$$\Theta_1 \sim c_1 - c_3\left(\frac{3+16\mathcal{Z}_{\text{in}}^3}{18\mathcal{Z}_{\text{in}}^2}\right)\lambda^{-12\mathcal{Z}_{\text{in}}^3(\sigma-\sigma_{\text{crit}})} + \cdots, \tag{5.55a}$$

$$Z_1 \sim c_2 - c_3\left(\frac{1+2\mathcal{Z}_{\text{in}}^3}{3\mathcal{Z}_{\text{in}}^2}\right)\lambda^{-12\mathcal{Z}_{\text{in}}^3(\sigma-\sigma_{\text{crit}})} + \cdots, \tag{5.55b}$$

$$\Lambda_1 \sim \frac{3c_2 - c_2}{2\sigma\mathcal{Z}_{\text{in}}} + c_3\lambda^{-12\mathcal{Z}_{\text{in}}^3(\sigma-\sigma_{\text{crit}})} + \cdots, \tag{5.55c}$$

  where the c_i are constants of integration and we have introduced a critical growth rate given by $\sigma_{\text{crit}} = -1 - \mathcal{Z}_{\text{in}}^{-3}/12$.

- If on the other hand $m > 3/2$ such that there is a shock with height $\lambda_* = \lambda_{\text{crit}} > 0$, we get the base-state expansions

$$\Theta_0 \sim \frac{\mathcal{Z}_{\text{in}}}{2\mathcal{F}'_*} - \frac{\mathcal{Z}_{\text{in}}\mathcal{F}''_*\left(3 + 16\mathcal{M}_*\mathcal{Z}_{\text{in}}^3\right)}{12\left(\mathcal{F}_* - \lambda_*\right)\mathcal{F}'_*}\left(\lambda - \lambda_*\right)^2 + \cdots, \tag{5.56a}$$

$$Z_0 \sim \mathcal{Z}_{\text{in}} - \frac{\mathcal{Z}_{\text{in}}\mathcal{F}''_*\left(3 + 4\mathcal{M}_*\mathcal{F}'_*\mathcal{Z}_{\text{in}}^3\right)}{6\left(\mathcal{F}_* - \lambda_*\right)\mathcal{F}'_*}\left(\lambda - \lambda_*\right)^2 + \cdots, \tag{5.56b}$$

$$\Lambda_0 \sim \Lambda_* + \frac{\mathcal{Z}_{\text{in}}^3\mathcal{M}_*\mathcal{F}''_*}{\mathcal{F}_* - \lambda_*}\left(\lambda - \lambda_*\right)^2 + \cdots, \tag{5.56c}$$

  and the perturbation expansions

$$\Theta_1 \sim c_1 + \cdots, \qquad Z_1 \sim c_2 + \cdots, \qquad \Lambda_1 \sim \frac{3c_2 - c_2}{2\sigma\mathcal{Z}_{\text{in}}} + c_3 + \cdots, \tag{5.57}$$

  where all $\mathcal{M}_*$, $\mathcal{F}_*$ and their derivatives are evaluated at $\lambda_* = \lambda_{\text{crit}}$ and the c_i are again constants of integration.

Therefore, if $m > 3/2$ and there is a shock, the perturbations have well-defined Taylor series near the nose and the boundary condition (5.53b) implies that $c_3 = 0$, thereby restricting the solution space by one degree of freedom. However, if $m \leq 3/2$ and there is no shock, then (5.53b) can be satisfied in two ways: either by $c_3 = 0$ as before, or, by $\sigma \leq \sigma_{\text{crit}}$ such that all perturbations vanish at the nose. We refer to a discussion of a hyperbolic toy model with zero-velocity boundaries in Appendix Z. There we find similarly that the upstream boundary condition is satisfied automatically, and we mitigate this by requiring that the perturbations have Taylor series at the nose recovering a discrete spectrum of eigenmodes. Applying this reasoning to the problem at hand would give

$$\sigma = \sigma_{\text{crit}} - \frac{n}{12\zeta_*^3} = -1 - \frac{n+1}{12\zeta_*^3}, \tag{5.58}$$

where $n \in \{0, 1, 2, \dots\}$ is a non-negative integer index of the eigenmodes.

The boundary condition at the origin

For a viscous gravity current spreading from a point source, lubrication theory leads to a logarithmic singularity at the point source. Therefore, it is very difficult to obtain an expansion in terms of the inverted variables, as this would involve Lambert W-functions (see Chapter 3). Instead, we consider Θ_0, Z_0 and λ as functions of the logarithmic radial variable Λ_0 or equivalently of $\eta = c_\xi - \Lambda_0$, where c_ξ is a constant of integration of

the base state. Using η instead of Λ_0 as independent variable has the benefit of 'hiding' the constant c_ξ and thereby simplifying the analysis and its results. We expand

$$\xi^{8/3}\Theta_0 \sim \mathcal{Q}_{\text{in}} - \tfrac{1}{16}\omega\eta^{-3/4} f_\Theta(\eta)\xi^2 + O\left(\xi^4\right), \tag{5.59a}$$

$$\xi^{2/3} Z_0 \sim \omega\eta^{1/4} - \frac{1}{4m}\omega^{-2}\eta^{-1/2} f_Z(\eta)\xi^2 + O\left(\xi^4\right), \tag{5.59b}$$

$$\lambda \sim 1 - \tfrac{2}{3}\omega^{-3}\eta^{1/4} f_\lambda(\eta)\xi^2 + O\left(\xi^4\right), \tag{5.59c}$$

where we have introduced a rescaled flux $\omega = (4\mathcal{Q}_{\text{in}}/m)^{1/4}$ and ξ is given by $\xi = \mathrm{e}^{\Lambda_0}$. The functions $f_i(\eta)$ are then determined by the differential equations

$$\frac{\mathrm{d}f_\Theta}{\mathrm{d}\eta} = \left(2 + \frac{3}{4\eta}\right) f_\Theta - 2, \tag{5.60a}$$

$$\frac{\mathrm{d}f_\lambda}{\mathrm{d}\eta} = \left(\frac{8\eta - 2 + (1-8\eta) f_\lambda}{4\eta(1-f_\lambda)}\right) f_\lambda, \tag{5.60b}$$

$$\frac{\mathrm{d}f_Z}{\mathrm{d}\eta} = \left(\frac{1}{4\eta}\right) f_\Theta - 2(m-1) f_\lambda + \left(2 - \frac{1}{4\eta}\right) f_Z, \tag{5.60c}$$

with appropriate boundary conditions that ensure a well-ordered asymptotic series, i.e. $f_i = o\left(\xi^2\right)$ as $\xi \to 0$. From these equations and boundary conditions we obtain an analytic solution for f_Θ in terms of a generalised exponential integral function $E_{3/4}$, while for f_λ and f_Z we obtain series solutions as $\eta \to \infty$ corresponding to $\xi \to 0$:

$$f_\Theta = 2\eta \mathrm{e}^{2\eta} E_{3/4}(2\eta) \qquad \Rightarrow \qquad f_\Theta \sim 1 - \frac{3}{8\eta} + \frac{21}{64\eta^2} + \cdots, \tag{5.61a}$$

$$f_\lambda \sim 1 - \frac{1}{8\eta} - \frac{1}{64\eta^2} + \cdots, \tag{5.61b}$$

$$f_Z \sim (m-1) - \frac{1}{8\eta} - \frac{m-7}{64\eta^2} + \cdots. \tag{5.61c}$$

We note that to obtain the asymptotic expansion of $\Lambda_0(\lambda)$ as $\lambda \to 1$ we would have to invert $\eta^{1/4} f_1^\lambda(\eta)\xi^2$. We confirm that to leading order this would mean inverting $\log\left(c_\xi/\xi\right)^{1/4}\xi^2$ resulting in Lambert W-functions.

We can substitute the expansions (5.59) of the base state near the origin and the corresponding series solutions (5.61) into the equation (5.29) of the perturbations. After plenty of algebra this results in expansions of the perturbations, where we find two distinct types of expansions: one proportional to $\xi^{\pm k}$ associated with the diffusive

behaviour of a gravity current,

$$\frac{\Theta_1}{\Theta_0} \sim g_\Theta^\pm \mathrm{e}^{\pm k\eta} \quad \text{where} \qquad g_\Theta^\pm = -\frac{2(1-3\sigma)}{3} - \frac{4\sigma^2 - (\pm k - 2)^2}{\pm 6k(1+\sigma)\eta} + \cdots , \tag{5.62a}$$

$$\frac{Z_1}{Z_0} \sim g_Z^\pm \mathrm{e}^{\pm k\eta} \quad \text{where} \qquad g_Z^\pm = -\tfrac{2}{3} - \frac{\pm 2k(5+3\sigma) - k^2 - 8(1+\sigma)(2+\sigma)}{\pm 24k(1+\sigma)\eta} + \cdots , \tag{5.62b}$$

$$\Lambda_1 \sim g_\Lambda^\pm \mathrm{e}^{\pm k\eta} \quad \text{where} \qquad g_\Lambda^\pm = 1 + \frac{4\sigma^2 - (\pm k - 2)^2}{\pm 16k(1+\sigma)\eta} + \cdots , \tag{5.62c}$$

and a second one associated with the hyperbolic advection of the interface

$$\frac{\Theta_1}{\Theta_0} \sim g_\Theta^\circ \eta^{\frac{3}{2}+\sigma} \mathrm{e}^{-8(1+\sigma)\eta^2 + 2(3+\sigma)\eta} \quad \text{where} \qquad g_\Theta^\circ = -\tfrac{8}{3} + \frac{2+3\sigma}{3\eta} + \cdots , \tag{5.63a}$$

$$\frac{Z_1}{Z_0} \sim g_\Theta^\circ \eta^{\frac{3}{2}+\sigma} \mathrm{e}^{-8(1+\sigma)\eta^2 + 2(3+\sigma)\eta} \quad \text{where} \qquad g_Z^\circ = -\tfrac{2}{3} - \frac{1-3\sigma}{12\eta} + \cdots , \tag{5.63b}$$

$$\Lambda_1 \sim g_\Lambda^\circ \eta^{\frac{3}{2}+\sigma} \mathrm{e}^{-8(1+\sigma)\eta^2 + 2(3+\sigma)\eta} \quad \text{where} \qquad g_\Lambda^\circ = 1 - \frac{2+3\sigma}{8\eta} + \cdots . \tag{5.63c}$$

We note that, while the advective type (5.63) is well-behaved for all parameters k and σ, the gravity-current type (5.62) is singular at $k = 0$ and $\sigma = -1$. Therefore, these cases would have to be considered separately, which shall be omitted here as it is a simple exercise in more algebra.

In general, any solution for the perturbation variables has to be a linear combination of the three different types of expansions in (5.62) and (5.63) and therefore we can write

$$\begin{pmatrix} \Theta_1/\Theta_0 \\ Z_1/Z_0 \\ \Lambda_1 \end{pmatrix} = \boldsymbol{C} \cdot \begin{pmatrix} c_+ \\ c_- \\ c_\circ \end{pmatrix}, \tag{5.64}$$

where c_i are constants and $\boldsymbol{C}$ is the appropriate matrix of expansions (5.62) and (5.63).

A suitable boundary condition is then given by enforcing $c_+ = 0$, as this type of expansion is proportional to $\mathrm{e}^{+k\eta} \propto \xi^{-k}$, which diverges near the origin. We note that although, for $\sigma < -1$, the expansion (5.63) associated with $c_\circ$ also diverges rapidly, we do not exclude it, as it corresponds to a hyperbolic perturbation mode. We refer to Appendix Z, where we discuss similarly diverging perturbation modes of a hyperbolic toy model with zero-velocity boundaries, and we conclude that such diverging modes need to be interpreted with care and are only valid locally near the upstream boundary, given here by the nose.

Therefore, we obtain the boundary condition

$$0 = \begin{pmatrix} 1 \\ 0 \\ 0 \end{pmatrix}^{\mathsf{T}} \cdot \boldsymbol{C}^{-1} \cdot \begin{pmatrix} \Theta_1/\Theta_0 \\ Z_1/Z_0 \\ \Lambda_1 \end{pmatrix}, \tag{5.65}$$

which can be simplified to

$$\frac{\Theta_1}{\Theta_0} + \left(\frac{g_\Lambda^- g_\Theta^\circ - g_\Lambda^\circ g_\Theta^-}{g_Z^- g_\Lambda^\circ - g_Z^\circ g_\Lambda^-} \right) \frac{Z_1}{Z_0} + \left(\frac{g_\Theta^- g_Z^\circ - g_\Theta^\circ g_Z^-}{g_Z^- g_\Lambda^\circ - g_Z^\circ g_\Lambda^-} \right) \Lambda_1 = 0, \tag{5.66}$$

and finally by using (5.62) and (5.63) we obtain

$$\left(\frac{\Theta_1}{\Theta_0} + \tfrac{8}{3}\Lambda_1 \right) + \frac{mkZ_0^4}{\Theta_0} \left(\frac{Z_1}{Z_0} + \tfrac{2}{3}\Lambda_1 \right) + k\Lambda_1 = 0, \tag{5.67}$$

where we have eliminated η by using $Z_0^4/\Theta_0 \sim 4\eta/m$. We note that this result is exact up to $O(\xi^2)$ corrections and valid for all values of k and σ. Thereby, this avoids the singular behaviour of the $g_i^\pm$ at $k = 0$ or $\sigma = -1$.

5.A.3 Phase-angle perturbation variables

Before the nose, we have a third-order perturbation system with the three perturbation variables Θ_1, Z_1 and Λ_1. Therefore, similarly to the plane-polar perturbations introduced for single-layer gravity currents in Chapter 3, we now introduce spherical polar perturbation variables given by an amplitude $A(\lambda)$, a latitudinal phase angle $\varphi(\lambda)$, and a longitudinal phase angle $\psi(\lambda)$. It is important to note that any two-variable parametrisation of a sphere has at least one singular point, which could pose difficulties to an integration scheme based on continuation software such as AUTO. Therefore, it is crucial to choose φ and ψ appropriately. Numerical investigation revealed that phase angles based straightforwardly on the Cartesian perturbation variables Θ_1, Z_1 and Λ_1 are numerically poorly conditioned. Instead, motivated by recurring terms both in the governing equations (5.20) and the origin boundary condition (5.43), we write

$$\frac{\Theta_1}{\Theta_0} + \tfrac{8}{3}\Lambda_1 = A\sin\varphi\cos\psi, \qquad \frac{Z_1}{Z_0} + \tfrac{2}{3}\Lambda_1 = A\sin\psi, \qquad \Lambda_1 = A\cos\varphi\cos\psi. \tag{5.68}$$

Numerical solutions show that this particular choice works very well without ever running into either of the two singular points at the poles of the spherical polar coordinate map (see figure 5.11). We shall show later that this choice of phase angles is

also associated with an analytic solution derived from considering shifts of the temporal origin (see §5.C.1).

From (5.29), we derive the governing equations in terms of these phase angles defined in (5.68) resulting in

$$\begin{pmatrix} \varphi' \\ \psi' \\ A'/A \end{pmatrix} = \begin{pmatrix} \cos\varphi\sec\psi & 0 & -\sin\varphi\sec\psi \\ -\sin\varphi\sin\psi & \cos\psi & -\cos\varphi\sin\psi \\ \sin\varphi\cos\psi & \sin\psi & \cos\varphi\cos\psi \end{pmatrix} \cdot \boldsymbol{M}_{\varphi} \cdot \begin{pmatrix} \sin\varphi\cos\psi \\ \sin\psi \\ \cos\varphi\cos\psi \end{pmatrix}, \tag{5.69}$$

where the phase-angle derivative matrix $\boldsymbol{M}_{\varphi}$ is given by

$$\boldsymbol{M}_{\varphi} = \frac{1}{\mathcal{F}-\lambda} \begin{pmatrix} -\frac{1}{2}\mathcal{X} & \frac{1}{2}\mathcal{X} + k^2\frac{\mathcal{X}(\mathcal{X}-2\mathcal{F}')}{\mathcal{Y}^2} & (1+\sigma)\mathcal{X} + k^2\frac{\mathcal{X}-2\mathcal{F}'}{\mathcal{Y}} \\ -\frac{2\mathcal{F}'}{\mathcal{X}} & \frac{2\mathcal{F}'}{\mathcal{X}} - 2\sigma\frac{\mathcal{X}-2\mathcal{F}'}{\mathcal{Y}} & 4(1+\sigma)\frac{\mathcal{F}'}{\mathcal{X}} \\ \frac{\mathcal{X}}{\mathcal{Y}} & \frac{6\mathcal{F}'-4\mathcal{X}}{\mathcal{Y}} + 2\sigma\frac{\mathcal{X}(\mathcal{X}-2\mathcal{F}')}{\mathcal{Y}^2} & -4(1+\sigma)\frac{\mathcal{F}'}{\mathcal{Y}} \end{pmatrix}. \tag{5.70}$$

Here we have introduced $\mathcal{X} = Z_0/\Theta_0$ and $\mathcal{Y} = \mathcal{M}^{-1}Z_0^{-3}$ to simplify notation. We note that this altered derivative matrix $\boldsymbol{M}_{\varphi}$ is significantly less complicated than the original derivative matrix $\boldsymbol{M}$ in (5.30) once fully expanded.

Beyond the nose, we have a simple single-layer gravity current, and hence we can introduce plane-polar perturbation variables $\tilde{A}$ and $\tilde{\varphi}$ as in Chapter 3. Again, we base these on the analytic solution in §5.C.1:

$$\frac{\widetilde{\Theta}_1}{\zeta} + \left(\frac{8\widetilde{\Theta}_0}{3\zeta} - \tfrac{1}{3}\right)\tilde{\Lambda}_1 = \tilde{A}\sin\tilde{\varphi}, \qquad\qquad \tilde{\Lambda}_1 = \tilde{A}\cos\tilde{\varphi}. \tag{5.71}$$

For numerical convenience, we consider these as functions of ζ^3, resulting in the governing equation

$$\frac{\mathrm{d}\tilde{\varphi}}{\mathrm{d}\zeta^3} = \frac{1+\sigma}{3\zeta^3} + \tfrac{1}{3}k^2 - \frac{3\zeta^3\sin\tilde{\varphi} + \left(3\widetilde{\mathcal{X}}^2 + \zeta^3 - 12\zeta^3\widetilde{\mathcal{X}} - 4\zeta^6\right)\cos\tilde{\varphi}}{\zeta^3\left(2\zeta^3 + 3\widetilde{\mathcal{X}}\right)^2}\sin\tilde{\varphi}, \tag{5.72a}$$

$$\frac{\mathrm{d}\log\tilde{A}}{\mathrm{d}\zeta^3} = \left(\frac{1+\sigma}{6\zeta^3} + \tfrac{1}{6}k^2\right)\sin(2\tilde{\varphi}) + \frac{2 - 16\widetilde{\mathcal{X}} + 3\sin(2\tilde{\varphi})}{2\left(2\zeta^3 + 3\widetilde{\mathcal{X}}\right)^2} - \frac{3\widetilde{\mathcal{X}}^2 + \zeta^3 - 12\zeta^3\widetilde{\mathcal{X}} - 4\zeta^6}{\zeta^3\left(2\zeta^3 + 3\widetilde{\mathcal{X}}\right)^2}\sin^2\tilde{\varphi}, \tag{5.72b}$$

where we have introduced $\widetilde{\mathcal{X}} = \zeta/\widetilde{\Theta}_0$ for convenience of notation.

Boundary conditions

We express the boundary conditions derived in §5.A.2 in terms of these newly defined phase angles φ, ψ and $\widetilde{\varphi}$ given by (5.68) and (5.71). This results in

- the far-field condition from (5.40):

$$\widetilde{\varphi} \to 0 \qquad \text{as} \qquad \zeta^3 \to 0, \tag{5.73a}$$

- the continuity condition at the nose from (5.41c,d) substituting the base-state derivatives (5.28), using (5.42a) and defining an integer index $n \in \mathbb{Z}$:

$$\tan\left(\widetilde{\varphi} - n\pi\right) = \left(\tfrac{1}{3}\mathcal{Z}_{\text{in}}^3 + \frac{\lambda_*}{4\mathcal{F}_*'}\right)\left(\frac{2\sin\varphi - \left(\frac{2\mathcal{F}_*'}{\lambda_*}\right)\tan\psi}{\cos\varphi + \mathcal{Z}_{\text{in}}^3\left(\frac{2\mathcal{F}_*'}{\lambda_*}\right)\tan\psi}\right) \quad \text{at } \lambda = \lambda_* \text{ and } \zeta = \mathcal{Z}_{\text{in}}, \tag{5.73b}$$

- the no-flux condition at the nose from (5.42):

$$\tan\psi = \sin\varphi - 2(1+\sigma)\cos\varphi \qquad \text{at} \qquad \lambda = \lambda_*, \tag{5.73c}$$

- and the condition at the origin from (5.43) :

$$\left(\frac{k\mathcal{X}}{\mathcal{Y}}\right)\tan\psi + \sin\varphi + k\cos\varphi \to 0 \qquad \text{as} \qquad \lambda \to 1. \tag{5.73d}$$

A final boundary condition is needed to link the two amplitudes A and $\widetilde{A}$. This is derived from (5.41c,d) by using (5.34) together with (5.42a) which results in

$$\frac{\widetilde{A}}{A} = \left|\frac{\frac{\lambda_*}{2\mathcal{F}_*}\sin\varphi\cos\psi - \frac{1}{2}\sin\psi}{\sin\widetilde{\varphi}}\right| \qquad \text{at} \qquad \lambda = \lambda_* \qquad \text{and} \qquad \zeta = \zeta_*. \tag{5.73e}$$

Analytical solutions

As indicated above, the particular choice of the phase angles given in (5.68) and (5.71) is directly associated to an analytic solution derived in §5.C.1. As a result, we note that

$$\varphi = -\tan^{-1}k, \qquad \psi = 0, \qquad \tan\widetilde{\varphi} = -k\left(\frac{\widetilde{\Theta}_0}{\zeta} + \tfrac{2}{3}\zeta^3\right), \tag{5.74}$$

with growth rate $\sigma = -1 - k/2$ can be shown to satisfy equations (5.69) and (5.72), and the boundary conditions (5.73).

A second analytic solution derived for equal viscosities $m = 1$ in §5.C.2, which only perturbs the interface, is given in terms of phase angles before the nose by

$$\tan\varphi = -\tfrac{1}{2}\mathcal{Y}, \qquad \tan\psi = -\frac{\mathcal{Y}}{\mathcal{X}}\cos\varphi. \tag{5.75}$$

Numerical solutions

Figure 5.11 shows the numerical solutions for the same first three eigenmodes $n \in \{0, 1, 2\}$ with a viscosity ratio $m = 5$, a scaling-invariant nose height $\mathcal{Z}_{\text{in}} = 1$ and an azimuthal wavenumber $k = 15$ as in figure 5.5, but now in terms of the phase angles φ, ψ, and $\bar{\varphi}$ as functions of the radial similarity variable ξ. This clearly shows that considering the phase angle is numerically much better conditioned, with smooth and non-singular solutions. We also note that the index n corresponds directly to the number of revolutions by π of the latitudinal angle φ before the nose. The longitudinal angle ψ varies only very little up to the nose, remaining small in value, which indicates that our choice of spherical polar coordinates for the perturbation variables before the nose was indeed a good one. Finally, we remark that, as before, the three eigenmodes ($n \in \{0, 1, 2\}$) are almost identical beyond the nose, confirming our observation that the physical perturbation variables in figure 5.5 are approximately identical up to a rescaling of the amplitude.

Appendix 5.B Asymptotic limits

There are two asymptotic regimes of a two-layer equal-density viscous gravity current, in which we recover either a single-layer viscous gravity current as in Chapter 3 or an intrusion in a Hele-Shaw cell as in Chapter 4. This appendix analyses these two regimes and the exact conditions on the influx $\mathcal{Q}_{\text{in}}$ and the viscosity ratio m for which they apply.

5.B.1 The single-layer limit

Under certain circumstances, the lower layer of the two-layer viscous gravity current remains largely undisturbed and the upper-layer fluid forms a single-layer viscous gravity current on top of it. This can occur in two cases:

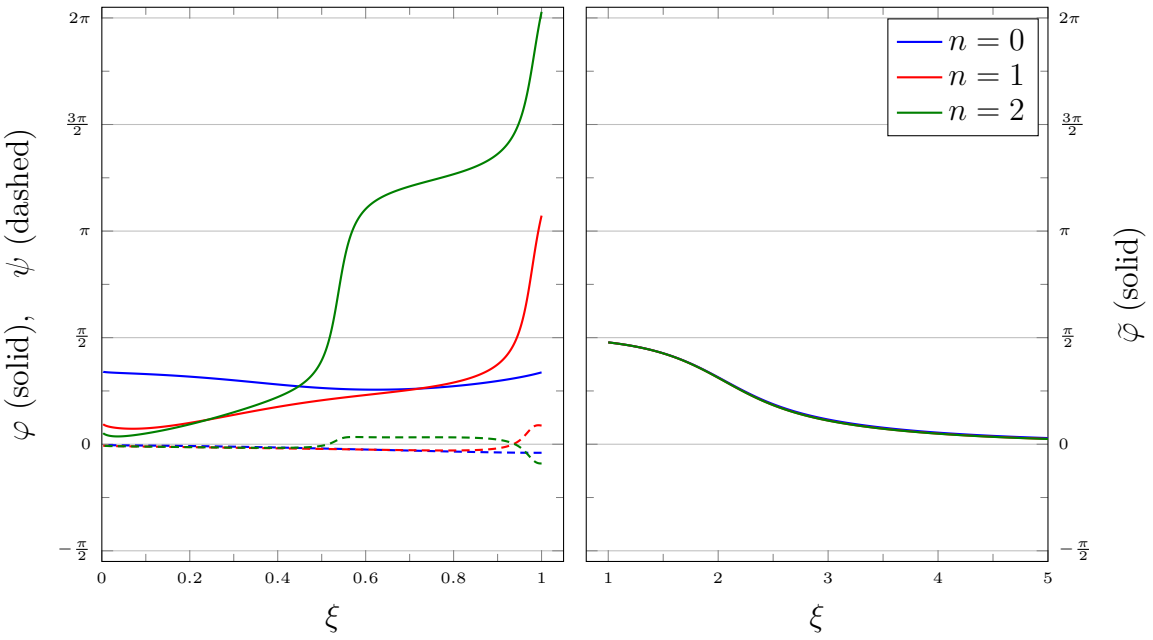

Fig. 5.11 Numerical solutions for the first three eigenmodes $n \in \{0, 1, 2\}$ in terms of the latitudinal perturbation angles φ, $\tilde{\varphi}$ (solid) and the longitudinal perturbation angle ψ (dashed) with viscosity ratio $m = 5$ and wavenumber $k = 15$.

- If the influx of introduced upper-layer fluid is very high ($\mathcal{Q}_{\text{in}} \gg 1$), the lower-layer fluid has insufficient time to move out of the way of the fast flowing upper-layer fluid. Hence, the lower-layer fluid remains nearly undisturbed while the upper-layer fluid flows on top of it similar to a single-layer viscous gravity current. However, if the lower-layer fluid is not viscous enough to support the weight of the upper-layer fluid, this ceases to be valid.

- Alternatively, if the viscosity ratio is very large ($m \gg 1$), the upper-layer fluid similarly spreads on top of the lower-layer fluid. This occurs as the lower-layer fluid is sufficiently viscous compared to the upper-layer fluid to be approximated as nearly rigid. However, this only remains valid if the influx of new fluid is not too small, which would give the lower-layer fluid more time give way to the pressure of the upper-layer fluid.

Both physical explanations presented above rely on the fact that the bulk of fluid flow occurs in the the upper-layer fluid. In other words we would like to say that ratio of upper-layer to total flux is given by $\mathcal{F}(\lambda) \sim 1$. To examine this we can rewrite the

flux function $\mathcal{F}(\lambda)$ as an infinite geometric series

$$\mathcal{F}(\lambda) = 1 + \frac{(1-\lambda)^2(2+\lambda)}{2\,(1-\lambda^3)} \sum_{n=1}^{\infty} \left(\frac{\lambda^3 - 1}{m\lambda^3} \right)^n . \tag{5.76}$$

From inspecting this series, we can see that as long as

$$\frac{1-\lambda^3}{\lambda^3} \ll m, \tag{5.77}$$

we do indeed obtain $\mathcal{F}(\lambda) \sim 1$. If (5.77) holds then $\mathcal{M}(\lambda) \sim m\lambda^3$, which together with $\mathcal{F}(\lambda) \sim 1$ transforms the governing equations (5.11) as

$$\frac{\partial h}{\partial \tau} - \tfrac{1}{2}\xi \frac{\partial h}{\partial \xi} + \boldsymbol{\nabla} \cdot \boldsymbol{q} = 0, \tag{5.78a}$$

$$\frac{\partial \lambda h}{\partial \tau} - \tfrac{1}{2}\xi \frac{\partial \lambda h}{\partial \xi} + \boldsymbol{\nabla} \cdot \boldsymbol{q} = 0, \tag{5.78b}$$

$$\boldsymbol{q} = -m(\lambda h)^3 \boldsymbol{\nabla} h. \tag{5.78c}$$

Taking the difference of the first two equations leads to a pure advection equation for the height of the interface $(1-\lambda)h$ given by

$$\left(\frac{\partial}{\partial \tau} - \tfrac{1}{2}\xi \frac{\partial}{\partial \xi} \right) (1-\lambda)h = 0. \tag{5.79}$$

Initially, the top surface is horizontal and there is no upper-layer fluid, and hence $(1-\lambda)h \to 1$ as $\tau \to -\infty$ (which corresponds to $t = 0$ given the definition $\tau = \log(t/\hat{t})$). Now, as (5.79) is a pure advection equation, the interface must be horizontal with height $(1-\lambda)h = 1$ at all times and therefore $\boldsymbol{\nabla} h = \boldsymbol{\nabla}(\lambda h)$. Using this in (5.78) we finally obtain equations for the upper-layer thickness λh and for the corresponding flux $\boldsymbol{q}$:

$$\frac{\partial \lambda h}{\partial \tau} - \tfrac{1}{2}\xi \frac{\partial \lambda h}{\partial \xi} + \boldsymbol{\nabla} \cdot \boldsymbol{q} = 0, \qquad \boldsymbol{q} = -m(\lambda h)^3 \boldsymbol{\nabla}(\lambda h), \tag{5.80}$$

which we easily recognise as the governing equation of a single-layer viscous gravity current of height λh.

The boundary conditions are simply obtained from (5.14) and are given by a nose at $\xi = \xi_*$, which is defined by the upper-layer thickness being zero $\lambda h = 0$, and mass

conservation both globally and locally near the nose, which are given by

$$\int_0^{2\pi}\int_0^{\xi_*} \lambda h\,\xi\,\mathrm{d}\xi\,\mathrm{d}\theta = \mathcal{Q}_{\mathrm{in}}, \qquad (\boldsymbol{n}\cdot\boldsymbol{e}_\xi)\left(\frac{\partial\xi_*}{\partial\tau}+\tfrac{1}{2}\xi_*\right) = \frac{1}{\lambda h}\,(\boldsymbol{n}\cdot\boldsymbol{q}) \text{ at } \xi=\xi_*, \tag{5.81}$$

respectively. Here $\boldsymbol{n}$ is the unit vector normal to the front of the current and we have used the fact that, as $\lambda \to 0$ at the nose, we must have $h \to 1$ to satisfy $(1-\lambda)h = 1$.

A key result of single-layer viscous gravity currents is the nose position ξ_*, which was calculated by Huppert (1982b) as

$$\xi_* \approx 0.715\,(2\pi\mathcal{Q}_{\mathrm{in}})^{3/8}\,m^{1/8}, \tag{5.82}$$

in terms of the variables used here (see also Chapter 3). This is a good parameter with which to compare the full numerical solutions to the asymptotic ones (see §5.B.3). Additionally, by using this result, we can derive an approximate scaling for the input parameter $\mathcal{Z}_{\mathrm{in}}$:

$$\mathcal{Z}_{\mathrm{in}} \sim 0.790\mathcal{Q}_{\mathrm{in}}^{-1/4}m^{1/12}, \tag{5.83}$$

as the height at the nose is simply given by the height of the undisturbed ambient layer resulting in $H = 1$. We confirmed this scaling in figure 5.3, giving us confidence both in the asymptotic correspondence and in the numerical results.

Region of validity

To determine the range of $\mathcal{Q}_{\mathrm{in}}$ and m over which this asymptotic approximation is valid, we revisit the condition (5.77). From $(1-\lambda)h = 1$ this condition can be rewritten in terms of the upper-layer thickness λh:

$$\frac{(1+\lambda h)^3-(\lambda h)^3}{(\lambda h)^3} = \left(\frac{1}{\lambda h}\right)^3 + 3\left(\frac{1}{\lambda h}\right)^2 + 3\left(\frac{1}{\lambda h}\right) \ll m. \tag{5.84}$$

However, we do not yet know how λh scales with $\mathcal{Q}_{\mathrm{in}}$ and m. Therefore, we consider the axisymmetric steady case and introduce rescaled variables x and $H(x)$

$$\xi = \left(\mathcal{Q}_{\mathrm{in}}^{3/8}m^{1/8}x_*\right)x, \qquad \lambda h = \left(\frac{\mathcal{Q}_{\mathrm{in}}}{m}\right)^{1/4}x_*^{2/3}H(x), \tag{5.85}$$

where x_* is a constant such that $H(1) = 0$, i.e. the nose is at $\xi_* = \mathcal{Q}_{\rm in}^{3/8} m^{1/8} x_*$. From (5.80) this gives the system

$$\tfrac{1}{2}x^2 H' + \left(H^3 H'\right)' = 0, \qquad H = 0 \text{ and } H^2 H' = -\tfrac{1}{2} \text{ at } x = 1, \tag{5.86}$$

for $H(x)$. Then x_* is given by (5.81) and, after numerically solving for $H(x)$, we find that

$$x_* = \left(2\pi \int_0^1 H\, x \,\mathrm{d}x\right)^{-3/8} \approx 1.424 = O(1), \tag{5.87}$$

which is equivalent to the result of Huppert (1982b). Crucially, it is independent of the physical parameters $\mathcal{Q}_{\rm in}$ and m. In fact, both the equation and the boundary conditions for $H(x)$ are independent of the physical parameters $\mathcal{Q}_{\rm in}$ and m and hence we can assume that $H = O(1)$ as well. Therefore, substituting the definition (5.85b) of $H(x)$ into (5.84) gives

$$\frac{x_*^2 H^{-3}}{(\mathcal{Q}_{\rm in}^3 m)^{1/4}} + \frac{3x_*^{4/3} H^{-2}}{(\mathcal{Q}_{\rm in} m)^{1/2}} + \frac{3x_*^{2/3} H^{-1}}{(\mathcal{Q}_{\rm in} m^3)^{1/4}} \ll 1. \tag{5.88}$$

Note that if both the first and the third terms on the left hand side of this expression are small, the middle term is automatically small as well. Therefore, using $H = O(1)$ we deduce that (5.88) is equivalent to the relation

$$\mathcal{Q}_{\rm in}^{-1} m^{-3} \ll 1 \ll \mathcal{Q}_{\rm in}^3 m, \tag{5.89}$$

which have to be simultaneously satisfied for the two-layer gravity current to be approximated by a single-layer gravity current.

The flux-dominated regime vs. the viscosity-dominated regime

Recall that initially we had two distinct physical reasons for the formation of a single-layer current on top of an undisturbed lower-layer: either $\mathcal{Q}_{\rm in} \gg 1$ and the influx is so high that the lower-layer fluid has insufficient time to move out of the way (flux-dominated), or $m \gg 1$ and the lower-layer fluid is so viscous that it can be treated as effectively rigid (viscosity-dominated). The two cases are similar, in that the total flux is mainly due to the upper-layer flux, i.e. $\mathcal{F} \sim 1$, but a crucial difference is that in the flux-dominated case we have mainly upper-layer fluid, i.e. $\lambda \sim 1$ with $h \gg 1$,

while in the viscosity-dominated case we have mainly lower-layer fluid, i.e. $h \sim 1$ and therefore $\lambda \ll 1$. The transition between these two regimes occurs when $\mathcal{Q}_{\text{in}} \sim m$.

In fact, we can express λ and h in terms of H by using $(1-\lambda)h = 1$ and (5.85b), which gives

$$h = 1 + \left(\frac{\mathcal{Q}_{\text{in}}}{m}\right)^{1/4} x_*^{-2/3} H, \qquad \lambda = \frac{H}{\left(\frac{\mathcal{Q}_{\text{in}}}{m}\right)^{-1/4} x_*^{2/3} + H}. \tag{5.90}$$

Then, considering the flux-dominated limit with $\mathcal{Q}_{\text{in}}^{-1/3} \ll m \ll \mathcal{Q}_{\text{in}}$, this gives

$$h \sim \left(\frac{\mathcal{Q}_{\text{in}}}{m}\right)^{1/4} x_*^{-2/3} H \gg 1, \qquad \lambda \sim 1 - \left(\frac{\mathcal{Q}_{\text{in}}}{m}\right)^{-1/4} x_*^{2/3} H^{-1} \sim 1, \tag{5.91}$$

and, considering the viscosity-dominated regime with $m^{-1/3} \ll \mathcal{Q}_{\text{in}} \ll m$, it gives

$$h \sim 1 + \left(\frac{\mathcal{Q}_{\text{in}}}{m}\right)^{1/4} x_*^{-2/3} H \sim 1, \qquad \lambda \sim \left(\frac{\mathcal{Q}_{\text{in}}}{m}\right)^{1/4} x_*^{-2/3} H \ll 1, \tag{5.92}$$

confirming our physical argument above.

5.B.2 The Hele-Shaw limit

Another asymptotic regime is given by a small volumetric influx rate $\mathcal{Q}_{\text{in}} \ll 1$. Physically, we expect this to lead to a current with small radial extent $\xi_* \ll 1$ and, as the current is flowing very slowly, we also expect the top-surface to have sufficient time to settle under gravity. This leads to the scaling $h \sim 1$ for the total height, since $h \to 1$ at infinity. Mass conservation of a current with approximately horizontal top surface then implies that the flux scales as $\boldsymbol{q} \sim \mathcal{Q}_{\text{in}}/\xi$. Substituting these scalings for the height and flux into the governing equation (5.11a) leads to the scaling $\xi \sim \mathcal{Q}_{\text{in}}^{1/2}$ for the radial variable, which is indeed small such that $\xi_* \ll 1$.

Motivated by this scaling analysis, we introduce a rescaled radial variable $\eta = \mathcal{Q}_{\text{in}}^{-1/2}\xi$, such that $\eta = O(1)$ over the current, and we expand in terms of the small influx $\mathcal{Q}_{\text{in}}$

$$h(\xi,\theta,\tau) = h_0(\eta,\theta,\tau) + \mathcal{Q}_{\text{in}} h_1(\eta,\theta,\tau) + \cdots, \tag{5.93a}$$

$$\mathcal{Q}_{\text{in}}^{-1/2}\boldsymbol{q}(\xi,\theta,\tau) = \boldsymbol{q}_0(\eta,\theta,\tau) + \mathcal{Q}_{\text{in}}\boldsymbol{q}_1(\eta,\theta,\tau) + \cdots, \tag{5.93b}$$

$$\lambda(\xi,\theta,\tau) = \lambda_0(\eta,\theta,\tau) + \mathcal{Q}_{\text{in}}\lambda_1(\eta,\theta,\tau) + \cdots, \tag{5.93c}$$

where we have also assumed that $\lambda = O(1)$, which is reasonable as $\lambda = 1$ at the origin and $\lambda = \lambda_{\text{crit}}$ at the nose. Substituting these expansions into the governing equations (5.11) gives to leading order

$$\frac{\partial h_0}{\partial \tau} - \tfrac{1}{2}\eta \frac{\partial h_0}{\partial \eta} + \boldsymbol{\nabla} \cdot \boldsymbol{q}_0 = 0, \tag{5.94a}$$

$$\frac{\partial \lambda_0 h_0}{\partial \tau} - \tfrac{1}{2}\eta \frac{\partial \lambda_0 h_0}{\partial \eta} + \boldsymbol{\nabla} \cdot (\mathcal{F} \boldsymbol{q}_0) = 0, \tag{5.94b}$$

$$-\mathcal{M} h_0^3 \boldsymbol{\nabla} h_0 = 0, \tag{5.94c}$$

where $\mathcal{M}$ and $\mathcal{F}$ are evaluated at λ_0, and $\boldsymbol{\nabla}$ is the gradient operator in the rescaled coordinates. The last of these equations gives that $h_0 = h_0(\tau)$ only. However, as $h_0 \to 1$ at infinity, this implies that $h_0 = 1$. Equation (5.94) reduces to

$$\boldsymbol{\nabla} \cdot \boldsymbol{q}_0 = 0, \qquad \frac{\partial \lambda_0}{\partial \tau} - \tfrac{1}{2}\eta \frac{\partial \lambda_0}{\partial \eta} + \mathcal{F}_0' \boldsymbol{q}_0 \cdot \boldsymbol{\nabla} \lambda_0 = 0. \tag{5.95}$$

We then consider the next-order correction to the flux equation (5.11c) which gives

$$\boldsymbol{q}_0 = -\mathcal{M}_0 \boldsymbol{\nabla} h_1, \tag{5.96}$$

where we have substituted $h_0 = 1$.

We recognise (5.95) together with (5.96) as the equations governing an intrusion into a Hele-Shaw cell as in Chapter 4, if we write $p = (4h_1)^{1/4}$ for the pressure. This equivalence is due to the fact that the mid-plane in a Hele-Shaw cell can be considered a no-stress boundary, similarly to the top surface of a gravity current. Hence, if this top surface happens to be flat and horizontal to leading order, as is the case for a very low influx rate, the two systems can be considered equivalent.

Again, we consider the nose position ξ_* of an intrusion into a Hele-Shaw cell, which was calculated by Yang and Yortsos (1997) as

$$\xi_* = (2\mathcal{F}_*' \mathcal{Q}_{\text{in}})^{1/2}, \tag{5.97}$$

with $\mathcal{F}_*'$ evaluated at the assumed Oleinik shock height λ_* (see also Chapter 4). As before, this parameter can be used to compare the full numerical solutions to the asymptotic ones (see §5.B.3). The corresponding scaling for the input parameter $\mathcal{Z}_{\text{in}}$ is given this time by

$$\mathcal{Z}_{\text{in}} \sim (2\mathcal{F}_*' \mathcal{Q}_{\text{in}})^{-1/3}, \tag{5.98}$$

as the height at the nose is again given by $h_0 = 1$. Figure 5.3 confirms this scaling, again giving confidence both in the asymptotic correspondence and in the numerical results.

Region of validity

There were two assumptions made on which the asymptotic limit was based: firstly, we assumed that the extent of the current is small, i.e. $\xi_* \ll 1$. And secondly, less obviously, we assumed that the logarithmically singular boundary layer near the origin is small compared to the extent of the upper-layer fluid current so that we indeed have $h \sim 1$.

Turning to the first assumption: from our analysis of the axisymmetric steady case in a Hele-Shaw cell, we recall that η_* is given by $\eta_*^2 = 2\mathcal{F}'_{\text{crit}}$. Therefore, to ensure $\xi_* \ll 1$ we need to check whether $2\mathcal{Q}_{\text{in}}\mathcal{F}'_{\text{crit}} \ll 1$. If there is no shock, i.e. $m \leq 3/2$, we have $\mathcal{F}'_{\text{crit}} = 3/2$ and hence we get $3\mathcal{Q}_{\text{in}} \ll 1$ which is true by the assumption of $\mathcal{Q}_{\text{in}} \ll 1$. However, if there is a shock, i.e. $m > 3/2$, the expression for $\mathcal{F}'_{\text{crit}}$ is more involved, and we can show from the definitions (5.6b) and (5.8) that

$$\mathcal{F}'_{\text{crit}} \sim \tfrac{1}{3}(4m)^{1/3} + \cdots \qquad \text{for} \qquad m \gg 1. \tag{5.99}$$

Therefore, we require that $2(4m)^{1/3}\mathcal{Q}_{\text{in}} \ll 3$, or equivalently $m \ll \mathcal{Q}_{\text{in}}^{-3}$.

Physically, as m increases towards $m \sim \mathcal{Q}_{\text{in}}^{-3} \gg 1$, the lower-layer fluid becomes increasingly viscous, so that the upper-layer fluid is forced on top of the increasingly rigid lower-layer fluid. Hence, the top surface can no longer remain flat, since the rigidity of the lower-layer fluid causes the upper-layer fluid to approximately form a single-layer gravity current on top of the lower-layer fluid. Note that this marks the transition to the single-layer limit considered earlier.

The second assumption is slightly more involved: we know that near the origin the height has a logarithmic singularity given by

$$h \sim \left(-\frac{4\mathcal{Q}_{\text{in}}}{m}\log\xi\right)^{1/4}, \tag{5.100}$$

and hence the point $\xi_\circ$ where $h \sim 1$ within this boundary layer is given by

$$\xi_\circ \sim \mathrm{e}^{-m/4\mathcal{Q}_{\text{in}}}. \tag{5.101}$$

Therefore, to ensure that $\xi_\circ \ll \xi_*$ we need $m \gg \mathcal{Q}_{\text{in}}$.

Physically, as m decreases towards $m \sim \mathcal{Q}_{\text{in}} \ll 1$, the lower-layer fluid becomes increasingly less viscous compared to the upper-layer fluid. As a result, the lower-layer fluid supports an increasingly large shear and hence can form a very thin film. The upper-layer fluid is therefore able to expel nearly all lower-layer fluid from a region near the origin, which now extends significantly compared to the overall extent of the upper-layer fluid. The condition $m \gg \mathcal{Q}_{\text{in}}$ guarantees that any such region of near-total expulsion of lower-layer fluid is very small, and that the viscosity of the lower-layer fluid very quickly resists the weight of the upper-layer fluid, which is trying to push it out of the way.

In conclusion, the region in parameter space in which a two-layer gravity current approximates an intrusion into a Hele-Shaw cell is given by

$$\mathcal{Q}_{\text{in}} \ll m \ll \mathcal{Q}_{\text{in}}^{-3}. \tag{5.102}$$

5.B.3 Comparison of asymptotic and numerical solutions

We confirm numerically the validity of the two asymptotic approximations derived above (§5.B.1 and §5.B.2), by using the predicted dimensionless radial extent ξ_* as a single parameter for comparison. We first calculate its value by numerically integrating the full equations governing a two-layer viscous gravity current as described in §5.3 (or in Chapter 2), and then use the results (5.82) and (5.97) within their individual regions of validity (5.89) and (5.102). The results of this comparison are shown in figure 5.12, where we consider contours of constant ξ_* in terms of the physical parameters $\mathcal{Q}_{\text{in}}$ and m. We observe that indeed, sufficiently far from the boundaries between the regions of validity the contours between the full numerical solutions and their asymptotic approximations agree very well, which is also confirmed by the shaded regions of 1 % relative deviation. We note that, in the Hele-Shaw limit (red), the asymptotic value (5.97) is always an overestimate. In the single-layer limit, the asymptotic value (5.82) can be either an overestimate or an underestimate, leading to spurious cases of relatively small $\mathcal{Q}_{\text{in}}$ and m where the ξ_* values agree by sheer coincidence (the blue-shaded spike in the figure).

Figure 5.13 shows a few examples of the solution profiles for the top surface and interface, comparing them to the appropriate asymptotic approximations. Plots **A** and **B** correspond to the flux-dominated and viscosity-dominated cases of the single-layer limit, respectively. Plot **C** corresponds to the Hele-Shaw limit. All cases show excellent agreement giving confidence both in the asymptotic analysis and the numerical integration. The final plot **D** corresponds to an intrusion into a low-viscosity ambient

$m \ll 1$, and is characterised by the near-total expulsion of all ambient fluid near the origin and a protrusion of upper-layer fluid towards the nose, where extensional-flow theory may be more appropriate than the lubrication theory used.

Finally, we note that, similar to Appendix 2.A in Chapter 2, we could consider currents with two-dimensional geometry spreading from a line source as opposed to a point source. Similar asymptotic analysis and comparisons can be done in this geometry resulting in an equivalent correspondence to single-layer currents for small $\mathcal{Q}_{\text{in}}$ or large m and to intrusions into Hele-Shaw cells for small $\mathcal{Q}_{\text{in}}$.

Appendix 5.C Analytic solutions

For two-layer equal-density viscous gravity currents, there are two cases in which we can find analytic solutions. Firstly, as we are considering constant-flux currents, a small shift in the temporal origin is equivalent to a small extra amount of intruding fluid. In §3.5.1 we found an analytic solution using a similar method for the case of constant-flux single-layer viscous gravity currents. Secondly, in the case of equal viscosities ($m = 1$) the evolution of the interface is decoupled from the evolution of the top surface, and we can look for perturbations of the interface only, leaving the top surface unperturbed.

5.C.1 Shifting the temporal origin — the 'single-layer' fundamental solution

Firstly, we attempt to find an analytic solution by shifting the temporal origin as we did for a single-layer gravity current with constant influx in §3.5.1. We take

$$t \mapsto t + 2\delta\widehat{t}, \tag{5.103}$$

where δ is a small perturbation amplitude and $\widehat{t}$ is the arbitrary time scale from the definition of τ used here together with an additional factor of 2 for algebraic convenience.

For constant-flux currents, we can also interpret a small temporal shift as adding a small extra quantity of intruding fluid. Then, as time increases, this extra quantity becomes negligible compared to the fluid introduced via the constant flux, leading us to expect a decaying perturbation solution.

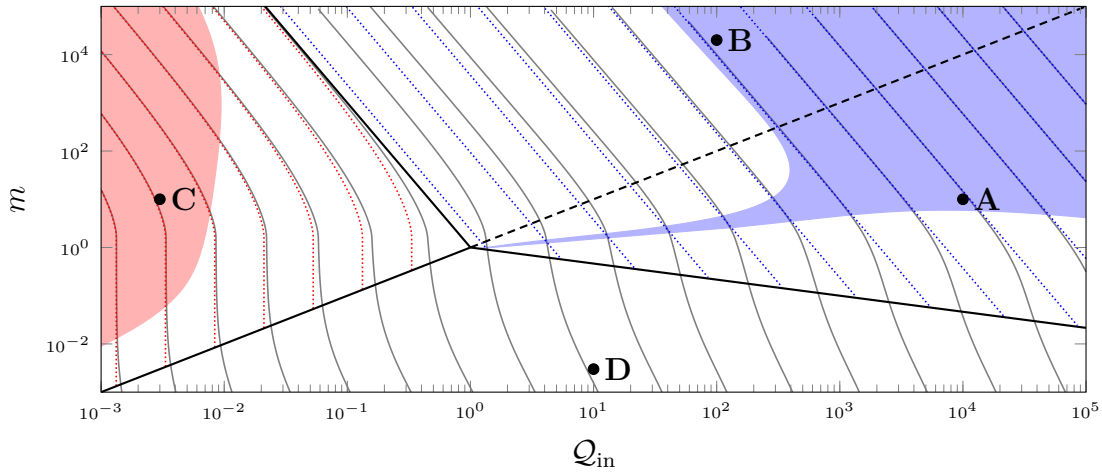

Fig. 5.12 Contours of constant values for the nose position ξ_* on a $(\mathcal{Q}_{\text{in}}, m)$-graph (solid grey) compared to the single-layer/Hele-Shaw asymptotics (dotted blue/red) together with the boundaries (5.89) and (5.102) between the regimes (solid black), including the viscosity/flux-dominated boundary $\mathcal{Q}_{\text{in}} \sim m$ for the single-layer limit (dashed black). Points **A** to **D** correspond to sample profiles shown in figure 5.13.

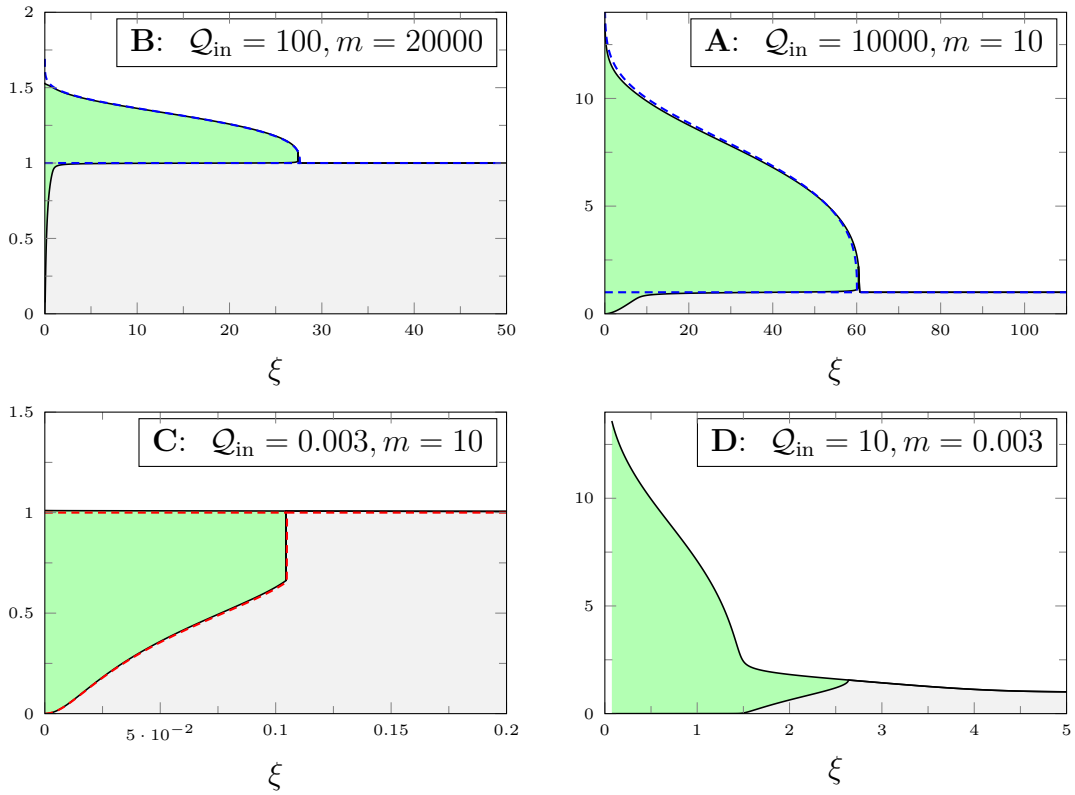

Fig. 5.13 Example solution profiles (solid lines) for the top surface and interface with influxes $\mathcal{Q}_{\text{in}}$ and viscosity ratios m as shown in figure 5.12. The appropriate asymptotic approximations compare excellently where applicable (dashed lines).

We apply the shift (5.103) to the similarity variable ξ defined in (5.10) resulting in

$$\xi \mapsto \xi\left(1 - \frac{\delta\widehat{t}}{t} + \cdots\right) = \xi\left(1 - \delta \mathrm{e}^{-\tau} + \cdots\right). \tag{5.104}$$

We then note from the definitions of the dimensionless variables that the height scales as a constant $h \sim 1$, and the flux scales as $q_\xi \sim t^{1/2}$ such that ξq_ξ also scales as a constant. Therefore, by using (5.104) we deduce that the axisymmetric late-time self-similar solutions $h = H_0(\xi)$ and $q_\xi = Q_0(\xi)$ are shifted to

$$H_0 \mapsto H_0 - \delta\xi H_0' \mathrm{e}^{-\tau} + \cdots, \qquad \xi Q_0 \mapsto \xi Q_0 - \delta\xi \left(\xi Q_0\right)' \mathrm{e}^{-\tau} + \cdots. \tag{5.105}$$

We recognise the result of this shift as a solution for the height and flux perturbations given by

$$H_1 = \delta\left(\frac{\xi Q_0}{\mathcal{M} H_0^3}\right), \qquad \xi Q_1 = \frac{\xi^2 H_1}{2} = \delta\left(\frac{\xi^3 Q_0}{2\mathcal{M} H_0^3}\right), \tag{5.106}$$

where we have used the steady axisymmetric version of (5.12) to eliminate the base-state derivatives H_0' and $(\xi Q_0)'$. The associated growth rate is given by $\sigma = -1$ from the factor $\mathrm{e}^{-\tau}$, showing that this mode indeed decays in time. Similar to §3.5.1, we can interpret the solution (5.106) as a perturbation current of height H_1 moving with velocity $\xi/2$, resulting from the time-dependence of the radial similarity variable ξ.

We then use (5.38) to find the scaling-invariant perturbation variables Θ_1 and Z_1 corresponding to these H_1 and ξQ_1 given in (5.106). This results in

$$\Theta_1 = \delta\left(\frac{\Theta_0}{2\mathcal{M} Z_0^3}\right) + \frac{\Theta_0'}{\Lambda_0'}\Lambda_1 = -\tfrac{8}{3}\Theta_0\Lambda_1 + (\delta - \Lambda_1)\left(\frac{\Theta_0}{2\mathcal{M} Z_0^3}\right), \tag{5.107a}$$

$$Z_1 = \delta\left(\frac{\Theta_0}{\mathcal{M} Z_0^3}\right) + \frac{Z_0'}{\Lambda_0'}\Lambda_1 = -\tfrac{2}{3}Z_0\Lambda_1 + (\delta - \Lambda_1)\left(\frac{\Theta_0}{\mathcal{M} Z_0^3}\right). \tag{5.107b}$$

Substituting these expressions into the scaling-invariant perturbation equations (5.29) gives three equations of the form $\Lambda_1' \propto (\delta - \Lambda_1)$, where the factors of proportionality are equal only if $m = 1$. Therefore, we deduce that a possible solution, valid for all viscosity ratios m, is given by a constant $\Lambda_1 = \delta$.

Extending to non-axisymmetric perturbations

So far, this analysis was concerned with axisymmetric perturbations where $k = 0$. We recall that in §3.5.1 we extended the axisymmetric solution, obtained from considering

a temporal shift, to a more general solution valid for all k by adding a azimuthal flux of the same magnitude as the radial flux resulting in a cobweb-like flow pattern. Motivated by the analysis in §3.5.1, we propose

$$H_1 = \delta \frac{\xi^{1+k} Q_0}{\mathcal{M} H_0^3}, \qquad \xi Q_1 = \left(\tfrac{2}{2}\xi^2 - k\mathcal{M}H_0^3\right) H_1. \tag{5.108}$$

From this, we deduce the scaling-invariant perturbations similarly to before:

$$\frac{\Theta_1}{\Theta_0} = -\left(\tfrac{8}{3} + k\right)\Lambda_1, \qquad \frac{Z_1}{Z_0} = -\left(\tfrac{2}{3}\right)\Lambda_1, \qquad \Lambda_1 = \delta \underbrace{\mathrm{e}^{k\Lambda_0}}_{\xi^k}, \tag{5.109}$$

where now the growth rate is given by

$$\sigma = -1 - \tfrac{1}{2}k. \tag{5.110}$$

Beyond the nose, we effectively have a single-layer gravity current already, and therefore, referring to Chapter 3, we recover the corresponding analytic solution

$$\widetilde{\Theta}_1 = \left(\tfrac{1}{3}\zeta - \tfrac{2}{3}k\zeta^4 - \left\{\tfrac{8}{3} + k\right\}\widetilde{\Theta}_0\right)\widetilde{\Lambda}_1, \qquad \widetilde{\Lambda}_1 = \delta\left(\frac{3\widetilde{\Theta}_0}{2\zeta^4 + 3\widetilde{\Theta}_0}\right)\underbrace{\mathrm{e}^{k\widetilde{\Lambda}_0}}_{\xi^k}. \tag{5.111}$$

It can be checked that the solutions (5.109) and (5.111) satisfy all boundary conditions, namely the far-field condition (5.40), the continuity conditions (5.41c,d), the no-flux condition (5.42b) and the origin condition (5.43).

5.C.2 Equal viscosities — perturbing a purely advective interface

A second analytic solution can be found by considering the case of equal viscosity fluids $m = 1$. In this case, the current is effectively a single-layer viscous gravity current: The evolution of the interface is completely decoupled from the evolution of the top surface as the mobility is $\mathcal{M} = 1$, and hence the interface is only passively advected by the current. Therefore, we can look for perturbations that leave the top surface and associated flux unperturbed, which, in terms of the physical perturbation variables, is expressed as $H_1 = 0$ and $Q_1 = 0$ with $\lambda_1 \neq 0$. Substituting these into (5.38) and (5.39), and relating the physical perturbation variables to the scaling-invariant perturbation

variables, and using (5.28), gives

$$\frac{\Theta_1}{\Theta_0} = \left(\frac{\Theta_0'}{\Theta_0\Lambda_0'}\right)\Lambda_1 = -\left(\tfrac{8}{3} + \frac{1}{2Z_0^3}\right)\Lambda_1, \tag{5.112a}$$

$$\frac{Z_1}{Z_0} = \left(\frac{Z_0'}{Z_0\Lambda_0'}\right)\Lambda_1 = -\left(\tfrac{2}{3} + \frac{\Theta_0}{Z_0^4}\right)\Lambda_1. \tag{5.112b}$$

By using these, we eliminate Θ_1 and Z_1 in (5.29), which results in a linear first-order differential equation for Λ_1. This equation can be solved analytically resulting in

$$\Lambda_1 = \delta Z_0^3 \exp\left(\int \frac{2\Theta_0 - Z_0 - 4(1+\sigma)Z_0^4}{2(\mathcal{F}-\lambda)\Theta_0}\,\mathrm{d}\lambda\right). \tag{5.113}$$

Beyond the nose we have $\widetilde{\Theta}_1 = \widetilde{\Lambda}_1 = 0$, as we are only perturbing the interface without affecting the top surface.

We can easily check that the boundary condition (5.50) for continuity at the nose and the boundary condition (5.67) at the origin are satisfied by (5.112) together with $\widetilde{\Theta}_1 = \widetilde{\Lambda}_1 = 0$. After some algebra, the no-flux boundary condition (5.53) at the nose results in

$$(\sigma - \sigma_{\mathrm{crit}})\,\Lambda_1 = 0, \tag{5.114}$$

where we have used the fact that for $m = 1$, we have $\lambda_{\mathrm{crit}} = 0$ and hence $\Theta_0/Z_0 = 1/3$ at the nose. We then expand (5.113) as $\lambda \to 0$, which results in

$$\Lambda_1 \sim \lambda^n \left(\zeta_*^3 + \frac{2(5+2n)\zeta_*^3 + 6(5+n)\zeta_*^6}{3 + 12\zeta_*^3}\lambda^2 + \cdots\right), \tag{5.115}$$

where we have introduced a rescaled growth rate n given by

$$\sigma = \sigma_{\mathrm{crit}} - \frac{n}{12\zeta_*^3} = -1 - \frac{n+1}{12\zeta_*^3}. \tag{5.116}$$

This expansion (5.115) shows that, to satisfy (5.114), we must have $n \geq 0$. Therefore, we have obtained a continuous spectrum of growth rates σ. We recall the discussion of the nose boundary condition in §5.A.2, where we discovered a similar issue with the upstream boundary condition, and we proposed mitigating this issue by assuming initial conditions such that the perturbations are analytic at the nose (also see Appendix Z). Here this corresponds to n being a non-negative integer $n \in \{0, 1, 2, \dots\}$, and hence, we recover a discreet spectrum of growth rates σ given by (5.116).

Finally, we can also expand (5.113) near the origin $\lambda \to 1$, which exactly recovers (5.63c) corresponding to g°_{Λ}. In §5.A.2, we suitably interpreted this type of expansion as associated with the hyperbolic advection of the interface, as opposed to the diffusive behaviour of a gravity current. The analytic solution (5.112) with (5.113) of perturbing the interface of a equal viscosity current is clearly a physically sensible solution, thereby confirming that we indeed have to admit the rapidly diverging eigenmodes (5.63) and that they are indeed linked to the hyperbolic nature of the interface advection equation.

Chapter 6

Conclusions and future work

6.1 Conclusions

In this thesis we have examined the stability of a viscous gravity current spreading radially from a constant-flux point source over a initially uniform ambient layer of fluid with equal density but different viscosity. This was motivated by experiments carried out by others, which revealed a fingering instability of such a current similar to the classical Saffman–Taylor instability in Hele-Shaw cells or porous media. Additionally, we also studied two related cases: first the linear stability of a classical single-layer viscous gravity current spreading over a rigid horizontal surface for a range of power-law influxes, and second the stability of a radial constant-flux intrusion into a Hele-Shaw cell with negligible diffusion and surface tension.

6.1.1 Shocks in two-layer viscous gravity currents

Before we embarked on any linear stability analysis, we considered the self-similar axisymmetric spreading of a viscous gravity current spreading over an initially uniform layer of ambient fluid in Chapter 2. We used lubrication theory to derive a set of ordinary differential equations for the self-similar shape of the interface and the top surface, dependent on three dimensionless parameters: the viscosity ratio m, the relative density difference ε, and a dimensionless influx parameter $\mathcal{Q}_{\text{in}}$.

We considered the case of equal densities ($\varepsilon = 0$), which we identified as a singular limit, in which the governing equation for the interface changes nature from a parabolic diffusion equation in the case of nonzero density differences to a hyperbolic advection equation in the case of equal densities.

A key result of the solutions in this singular limit, is that a vertical shock front forms at the nose of the intruding current, provided the ambient fluid is sufficiently more viscous than the intruding fluid. The critical viscosity ratio for the occurrence of these frontal shocks was derived as $m_{\text{crit}} = 3/2$, which is the same as for an intrusion of negligible diffusion and surface tension in a Hele-Shaw cell, as studied by Yang and Yortsos (1997). The similarity of these two flows was identified as a consequence of similar advection equations for the interfacial evolution in the two cases, in particular, them having the same flux function $\mathcal{F}$ defined by the ratio of intruding to total flux.

In the context of the Hele-Shaw flows studied by Yang and Yortsos (1997), it was not possible to physically regularise the problem and thus also not possible to uniquely determine the height of the frontal shock. In contrast to a Hele-Shaw flow, the case of a two-layer viscous gravity current allowed us to find a natural regularisation by reintroduction of a small density difference ($0 < \varepsilon \ll 1$). As a result of the steep interfacial gradient near the nose, even a small density difference between the intruding and ambient fluids leads to a significant contribution to the pressure gradient. From this, we analytically derived local travelling-wave solutions at the nose. An analysis of these local solutions resulted in a constraint on the height of a frontal shock in the form of an Oleinik entropy condition, which yielded a unique frontal shock height for the self-similar axisymmetric base state.

Analysis via the method of characteristics of a simplified fully time-dependent system, where we assumed the top-surface evolution to be known, showed that the unique shock height is attained in finite time, after which the constraint of the Oleinik entropy condition inhibits any further evolution of the shock height. The pattern of the characteristics revealed a surprising result: once the final shock height is attained, characteristics start emerging from the nose. These carry the information of the Oleinik constraint upstream to the rest of the interface. This kind of shock is classed as a one-sided characteristic shock.

Experimental results obtained by others confirmed the self-similar nature of the current and compared very well to the top-surface profiles and nose positions predicted by the theory in all cases where the experiments remained stable and axisymmetric.

In an appendix, we outlined how equivalent results can be obtained for the case of a two-dimensional current spreading from a line source with a decreasing flux, such that the total volume of intruding fluid grows as the square-root of time. This particular influx was analysed as it corresponds to a constant height scale of the current (Lister and Kerr, 1989).

6.1.2 Stability of single-layer viscous gravity currents

In Chapter 3, we then turned to the stability of a single-layer viscous gravity current spreading from a point source with power-law flux , considering both the case of a standard gravity current as in Huppert (1982b) and also a gravity current in a porous medium with power-law variation of porosity and permeability with depth. We derived ordinary differential equations based on lubrication theory for the axisymmetric base state and for linear normal-mode perturbations with associated wavenumber k.

Motivated in part by the phase-plane formalism for self-similar gravity currents developed by Gratton and Minotti (1990), we introduced a new method to simplify the governing equations of a linear stability analysis of viscous gravity currents. This method was based on three steps: the introduction of scaling-invariant variables exploiting a symmetry of the equations, a change of independent variable to mitigate the singular nose, and finally rephrasing the perturbation variables in terms of their amplitude and a phase-plane angle, thereby decoupling the resulting equations. Altogether, these reduced the order of the equations by two, simplified the boundary conditions, and eliminated the undetermined small amplitude of the perturbations from the equations.

We obtained the eigenspectrum of the perturbations numerically, which revealed that a single-layer gravity current spreading from a point source on a horizontal rigid surface is stable for all parameters considered, including cases where the current spreads in a porous medium. As a subset of our analysis, the results compared excellently to the analytic solution for the case of a constant-volume current analysed by Mathunjwa and Hogg (2006).

By considering a small shift in temporal origin for a constant-flux current, we further derived an analytic solution for the axisymmetric case of the fundamental perturbation mode. Surprisingly, we were able to extend this to obtain an analytic solution for non-axisymmetric perturbations, and then derived a first integral and its associated growth rate, valid for all power-law influxes. From this we concluded that the fundamental mode is stable for all parameters, and from the numerical solutions we deduced that the fundamental mode is, in fact, the least stable eigenmode, thereby implying overall stability for all modes.

A further analytic result was obtained for the asymptotic case of large wavenumber $k \gg 1$. Physically, this was interpreted as equivalent to perturbations of a general moving front in lubrication theory. Again the results indicated stability for all parameters, with the least stable eigenmode having a growth rate scaling as $\sigma = O(k)$. Therefore,

any perturbation with a length scale as small as the pore size, decays extremely rapidly and reassuringly can be neglected.

6.1.3 Instability of radial intrusions in a Hele-Shaw cell

Moving away from gravity currents, Chapter 4 analysed the stability of an intrusion spreading radially from a constant-flux point source in a Hele-Shaw cell with negligible diffusion and surface tension. We rederived the self-similar solution of Yang and Yortsos (1997) based on lubrication theory for an axisymmetric intrusion, assuming the shocks occurring are constrained by an Oleinik entropy condition as in Chapter 2 which leads to the same relative shock height as in Chapter 2.

For the special cases of axisymmetric intrusions or equal-viscosity fluids, we derived fully nonlinear time-dependent solutions using the method of characteristics. These analytical results showed that the self-similar base state is stable in these cases, with perturbations decaying in time like $1/t$.

For the more general case, we derived equations for linear normal-mode perturbations and solved these numerically. This revealed that intrusions without a frontal shock, where the viscosity ratio is $m < 3/2$, are stable and no fingering can occur. This confirms many experimental observations that instability only occurs for sufficiently large viscosity ratios $m > 3/2$ (Bischofberger et al., 2014; Lajeunesse et al., 1997, 1999, 2001). For all cases with a frontal shock ($m > 3/2$), the model derived in Chapter 4 predicts an instability of the fundamental eigenmode provided that the wavenumber k is chosen sufficiently large. Lajeunesse et al. (1997, 1999, 2001) argued that the steep fronts provided by the shocks should mean that the analysis by Saffman and Taylor (1958), which also assumed box-shaped intrusions, can be applied. The model developed in Chapter 4 confirms this hypothesis theoretically.

Both numerical results, and a subsequent asymptotic analysis of the limit of large wavenumber $k \gg 1$ using the WKB method, predicted rapid growth of the fundamental perturbation mode for large wavenumber. The asymptotic result was confirmed by a second analytical method using local expansions instead of the WKB method. This singular behaviour at large wavenumber is a common feature observed in lubrication analyses of intrusions in Hele-Shaw cells which do not include any stabilising regularisation mechanism such as surface tension or horizontal shear. Unfortunately, as a consequence of this, the model developed in Chapter 4 cannot predict the most unstable wavenumber, though it is expected to scale with the cell height.

6.1.4 Instability of two-layer viscous gravity currents

Finally, in Chapter 5, we turned to the linear stability of a viscous gravity current spreading from a constant-flux point source over an initially uniform layer of ambient fluid. We derived the governing equations for linear perturbations to a self-similar axisymmetric base state in the form of a normal-mode analysis, using scaling-invariant variables, a change of independent variable, and phase-plane angles similar to Chapter 3.

We identified two unusual features of the perturbation modes associated with the hyperbolic nature of the advection equation for the interface: firstly, eigenmodes decaying sufficiently fast ($\sigma < -1$) diverge towards the downstream boundary at the fluid source and are valid only locally near the upstream boundary at the nose. And secondly, for cases without a shock ($m < 3/2$) and sufficiently fast decay rates $\sigma < \sigma_{\rm crit} < 1$ there exists a continuous spectrum of eigenmodes. Both features were illustrated in Appendix Z by investigating a toy equation of hyperbolic nature with singular boundaries.

Numerical solutions for the cases with a frontal shock ($m > 3/2$) revealed an instability similar to the one found in Chapter 4 for Hele-Shaw flows. Again, given any viscosity ratio m, the fundamental mode was found always to be unstable at sufficiently large wavenumber k, with rapid growth in the limit $k \to \infty$. Computing curves of marginal stability (growth rates $\sigma = 0$) in terms of a dimensionless influx $\mathcal{Q}_{\rm in}$, and as a function of the viscosity ratio m, revealed a C-shaped region of instability for each wavenumber. We concluded that intermediate influxes are the most unstable for fixed k, which matched qualitatively with experimental data obtained by others regarding an instability observed in two-layer viscous gravity currents. Both the theory and the experiments suggest a critical viscosity ratio below which the flow is stable for all influxes $\mathcal{Q}_{\rm in}$.

We further established two asymptotic limits of the model: firstly, for large influxes ($\mathcal{Q}_{\rm in} \gg 1$) or very viscous ambient fluids ($m \gg 1$), we showed that the intruding fluid slides on top of the ambient fluid effectively forming a single-layer viscous gravity current as in Chapter 3. Correspondingly, the numerical results showed that any given wavenumber perturbation becomes stable in that limit, and the experimental observations seem to suggest stability as well. Secondly, for low influxes ($\mathcal{Q}_{\rm in} \ll 1$), the model predicted a nearly flat top surface, thereby effectively leading to half the profile of an intrusion into a Hele-Shaw cell as in Chapter 4. Comparing the prediction of both theories in terms of the growth rates showed very good agreement. Experimentally however, low influxes seemed to give stable intrusions unlike the prediction of the theory. This, we argued, could be a result of the finite spatial and temporal extent

of the experiments, and, given the low flow rates, the potential stabilising effects of diffusion between the miscible fluids.

We concluded that there are very good qualitative points of agreement between the theory and the experiments, while to compare the two quantitatively would require significant extension of the theory to include a regularising mechanism that would stabilise large-wavenumber perturbations.

6.2 Future work

The work presented in this thesis opens up several avenues of potential future research, further exploring fingering instabilities and their applications to viscous gravity currents.

For example, we could consider a two-layer viscous gravity current spreading from a constant-flux point source, but where the intruding fluid is less dense than the ambient fluid. This would be particularly interesting to study, as such a current no longer exhibits the frontal shocks present in the singular case of equal densities, which were shown to be closely linked to the instability of the flow. In fact, we expect that for sufficiently large density differences the additional buoyancy forces stabilise the current, with the intruding fluid effectively floating on top of the ambient fluid as a single-layer gravity current. A further appealing reason to study such a current is that it would be a fairly simple and natural extension to the equal-density case, as many of the same theoretical methods such as lubrication theory and scaling-invariant variables would still be applicable. Additionally, such a current of less dense fluid could be easily modelled in the laboratory in order to investigate the potential instability experimentally. Finally, due to the purely diffusive nature of the equations in the case of nonzero density differences, one might expect a non-singular behaviour of any instability even for large azimuthal wavenumber, and hence it might be possible to predict a most unstable wavenumber (similar to Kowal and Worster, 2019b).

This directly leads on to a second possible extension of this thesis, by asking the question what physical mechanism, neglected in our model, regularises the rapidly unstable large-wavenumber perturbations of a two-layer equal-density viscous gravity current. We recall that one of the key simplifying assumptions made in this thesis is the use of lubrication theory, which neglects any horizontal shear forces. However, these forces are particularly significant near the vertical shock at the nose, where the current is no longer long and thin. Therefore, we could, for example, consider a fully three-dimensional Stokes flow near the singular nose. This could be solved separately from the full problem, and could also be applied to the nose of Hele-Shaw flows. In

particular, solving for this local Stokes flow could lead to a condition determining the shock height in a Hele-Shaw cell, which has previously been suggested to be governed by such a Stokes flow, though no theoretical analysis has yet been done to the best of our knowledge. This provides an additional motivation to attempt this analysis.

Another mechanism which could potentially regularise large-wavenumber perturbations, is to include surface tension between the fluids and the air above them. This would add a smoothing force to the top surface preventing growth of tightly rippled large-wavenumber perturbations to the top surface. However, it may not actually stabilise the large-wavenumber limit, but instead simply push the perturbations entirely onto the interface. Therefore, we may consider a slightly different problem, where the intruding and ambient fluids are immiscible, resulting in a small interfacial surface tension between the fluids. We compare this to the classical Saffman–Taylor instability of an immiscible intrusion into a Hele-Shaw cell, where interfacial surface tension plays a key role in regularising the problem and in selecting a most unstable wavenumber. Unfortunately, including any surface tension, either at the top surface or the interface, would no longer allow solutions which are self-similar. However, if we assume that there is only a small surface tension at the top surface, its only significant effect will be at the nose to balance the jump in pressure gradient at the nose, thereby preventing the discontinuity in the slope of the top surface at a nose with a shock present in the model discussed in this thesis. This may facilitate matching between a local solution at the nose including surface tension and a self-similar current away from the nose.

Instead of considering immiscible fluids with surface tension, we could consider another extension of our model by including diffusion between the miscible ambient and intruding fluid. The relative strengths of advection by the current and of molecular diffusion would introduce an additional parameter given by the Péclet number. This could be described as the gravity-current analogue of Goyal and Meiburg (2006), who analysed a diffusive miscible intrusion into a Hele-Shaw cell, and may reproduce intriguing results observed in Hele-Shaw flows, such as a critical case where diffusion can completely stabilise the flow (Videbæk and Nagel, 2019).

As a different avenue of future research, similar instabilities in more complex flows in a Hele-Shaw cell could be investigated. For example, Lajeunesse et al. (1997, 1999, 2001) describe the vertical displacement of an initially flat horizontal interface in a vertical Hele-Shaw cell with the lower fluid being more dense than the upper fluid. This density difference acts as a stabilising pressure gradient, which adds an additional parameter controlling the instability given by the relative strength of gravity and the influx rate. Again, a formal stability analysis has not been performed to the best of our knowledge,

and would hopefully be able to confirm the stability criterion suggested by Lajeunesse et al. (1997, 1999, 2001) based on the shock structure of the interface. A major difference between the vertical flow studied by Lajeunesse et al. (1997, 1999, 2001) and the radial intrusions studied in Chapter 4, is the geometric symmetry of the base state, which can be described as two-dimensional and axisymmetric, respectively. Linear stability analyses of self-similar radial currents are significantly easier, as the azimuthal angle θ is inherently self-similar, while any fixed length scale for a transverse spatial dependence of a self-similar two-dimensional current would become small compared to the ultimately long and thin extent of the current. Therefore, care needs to be taken when analysing the stability of such two-dimensional currents. However, a successful pursuit of this avenue would resolve the nature of the instability observed by Lajeunesse et al. (1997, 1999, 2001).

Finally, we could move beyond linear stability analyses and consider the fully nonlinear regimes. The experiments referred to in Chapters 2 and 5, for example, suggest a nonlinear regime with a fixed width of the fingers, without any further unstable splitting of these fingers. Unfortunately, the time-dependent equations derived in Chapters 3, 4, and 5 could only be applied to study nonlinear transient behaviour in the case of stable flows, due to the singular nature of the large-wavenumber limit in lubrication theory. However, a regularised model, for example, by including the effects of horizontal shear, or the effects of surface tension at the air–fluid interface, could be integrated starting from some initial condition. Potentially, it would even be possible to derive a model based on a balance of the regularising mechanism and the destabilising effects of the fingering instability from the interface, to capture the nonlinear behaviour of the fingers.

Any of these proposed avenues of further study would provide interesting insight into the interaction of fingering instabilities and viscous gravity currents, and generally advance our understanding of the exact nature of these instabilities, and their effects in the many relevant physical applications.

Appendix Z

An illustrative toy model for advection along the interface of Chapters 2 and 5

Z.1 Introduction

In Chapters 2 and 5, we analysed the flow of a two-layer equal-density viscous gravity current. We noted that the interface between the two layers evolves according to an advection equation and that the advective nature of the equation gives rise to several mathematical issues, especially concerning the boundary conditions for linear perturbations (see §5.A.2). Therefore, in this appendix, we consider an illustrative toy model to clarify these issues and give their resolutions.

A key idea discussed in Chapter 2 is that advective systems can lead to shock discontinuities, and can be regularised, for example, by introducing a diffusive term to the equation. Physically, in Chapter 2, this diffusive term was given by the additional pressure gradient resulting from a small but nonzero density difference between the two layers. A further feature present in Chapter 2 is that the horizontal advection velocity goes to zero both at the origin and at the stagnation point at the nose of the current. This is a key characteristic of the advection-velocity profile, which we want to include in the toy model of this appendix.

In Chapter 5, we noted two mathematical peculiarities arising from the advective nature of the interfacial evolution equation and the zero-velocity boundaries: firstly, in some cases the perturbation boundary condition imposing mass conservation at the nose was trivially satisfied for all possible solution branches. Secondly, we had to

allow solutions which diverge rapidly towards the origin, seemingly leading to infinite perturbations of the flux at the origin. In this appendix, we analyse how these features can arise in advective systems where the advection velocity vanishes at the boundaries.

Motivated by this, we consider a simple linear advection equation with zero-velocity boundaries, where we include a diffusive term to regularise the solutions, which we subsequently take to be vanishingly small. This will help us understand how the linear stability analysis of a purely advective system compares to the linear stability analysis of the corresponding diffusively regularised system.

The equation we consider is

$$\frac{\partial y}{\partial t} + 2\mathcal{U}\frac{\partial y}{\partial x} = \delta\frac{\partial^2 y}{\partial x^2}, \tag{Z.1}$$

which we might interpret as a vertical displacement $y(x,t)$, given as a function of the horizontal coordinate x and time t, and evolving via advection with horizontal characteristic velocity $2\mathcal{U}(x)$, and via diffusion with small constant diffusivity δ.

We consider a finite domain $x \in [0,1]$ and boundary conditions

$$y(0,t) = y(1,t) = 0. \tag{Z.2}$$

As (Z.1) is linear, we attempt a solution by separation of variables by writing $y(x,t) = Y(x)T(t)$. The temporal equation is $T' = \sigma T$ with solution $T \propto \mathrm{e}^{\sigma t}$, where σ is the growth rate. The spatial equation is then

$$\sigma Y + 2\mathcal{U}Y' = \delta Y''. \tag{Z.3}$$

This equation together with (Z.2) constitutes an eigenvalue problem, where we expect a discrete spectrum of eigenvalues σ with associated eigenmodes $Y(x)$. To find the time-dependent solution $y(x,t)$ from a given initial condition $y(x,0) = y_0(x)$, a linear combination of all the eigenmodes $Y(x)$ has to be considered.

The solutions and their structure depend crucially on the properties of the horizontal characteristic velocity $2\mathcal{U}(x)$. We look for a profile $\mathcal{U}(x)$ which goes to zero at both boundaries $x = 0$ and $x = 1$, making the boundaries singular points of the purely advective limit $\delta = 0$.

Z.2 Top-hat profile

A simple, non-trivial characteristic velocity with this property is given by a symmetric top-hat profile:

$$\mathcal{U}(x) = \begin{cases} 0, & \text{for } 0 < x < \alpha, \\ 1, & \text{for } \alpha < x < 1-\alpha, \\ 0, & \text{for } 1-\alpha < x < 1, \end{cases} \tag{Z.4}$$

for some constant $0 < \alpha < 1/2$. To simplify the subsequent analysis, we introduce a rescaled eigenvalue $\omega^2 = -\sigma/\delta$. The analytical solution to (Z.3) with boundary conditions (Z.2), the top-hat profile (Z.4), and satisfying continuity of Y at $x = \alpha$ and $x = 1-\alpha$ is given by

$$Y = c_0 \frac{\sin(\omega x)}{\sin(\omega\alpha)} \qquad \text{for} \qquad 0 < x < \alpha, \tag{Z.5a}$$

$$Y = c_1 \frac{\sinh(\Omega\{x-\alpha\})}{\sinh(\Omega\Delta)} \mathrm{e}^{\frac{x-1+\alpha}{\delta}} - c_0 \frac{\sinh(\Omega\{x-1+\alpha\})}{\sinh(\Omega\Delta)} \mathrm{e}^{\frac{x-\alpha}{\delta}} \qquad \text{for} \qquad \alpha < x < 1-\alpha, \tag{Z.5b}$$

$$Y = c_1 \frac{\sin(\omega\{1-x\})}{\sin(\omega\alpha)} \qquad \text{for} \qquad 1-\alpha < x < 1, \tag{Z.5c}$$

where $\Delta = 1 - 2\alpha$, the $c_{0,1}$ are constants of integration and Ω is a rescaled eigenvalue defined by

$$\Omega = \left(\delta^{-2} - \omega^2\right)^{1/2}. \tag{Z.6}$$

As we are interested in small diffusivity with $O(1)$ advection, i.e. $\delta \ll 1$, we will assume that all ω of interest are less than δ^{-1} and so $\Omega^2 > 0$. (If not, then the exponential solutions in (Z.5b) become oscillatory solutions with exponentially varying amplitudes.)

The solution (Z.5) has three unknowns: the two amplitudes $c_{0,1}$ and the eigenvalue ω. As the underlying equation (Z.3) is linear and homogeneous, we expect the overall amplitude to be arbitrary, and hence we need two conditions: one linking the amplitudes $c_{0,1}$ and one to determine the eigenvalue ω. These come from enforcing continuity of Y' at $x = \alpha$ and $x = 1-\alpha$, in order to ensure a sufficiently well-behaved Y'', and are

given by

$$c_0\omega\cot(\omega\alpha) = \frac{c_0}{\delta} - c_0\Omega\coth(\Omega\Delta) + \frac{c_1\Omega \mathrm{e}^{-\Delta/\delta}}{\sinh(\Omega\Delta)}, \tag{Z.7a}$$

$$-c_1\omega\cot(\omega\alpha) = \frac{c_1}{\delta} + c_1\Omega\coth(\Omega\Delta) - \frac{c_0\Omega \mathrm{e}^{\Delta/\delta}}{\sinh(\Omega\Delta)}, \tag{Z.7b}$$

respectively. After some algebra we obtain two separated equations, one linking the ratio of the amplitudes $c_{0,1}$ and another implicitly determining the eigenvalue ω:

$$\left(\frac{c_0}{c_1}\right)^2 = \left\{\frac{\delta\omega + \sin(2\omega\alpha)}{\delta\omega - \sin(2\omega\alpha)}\right\}\mathrm{e}^{-2\Delta/\delta}, \qquad \Omega\coth(\Omega\Delta) + \omega\cot(2\omega\alpha) = 0. \tag{Z.8}$$

Z.2.1 Relation to Schrödinger's equation for particles trapped in a potential well

The system described above, i.e. equations (Z.2)–(Z.4), is somewhat similar to the quantum-mechanics problem, governed by Schrödinger's equation, of a particle trapped in a potential well shaped like $\delta^{-1}\mathcal{U}$ and with infinite potential barriers at the boundaries $x = 0$ and $x = 1$. The solution (Z.5) reflects this, as there are oscillatory regions on either side of the top hat, and, as long as the 'energy' ω is smaller than the potential barrier of the top hat δ^{-1}, the solutions in the middle region $\alpha < x < 1 - \alpha$ are purely exponential. If the 'energy' ω is larger than δ^{-1}, the solutions become oscillatory in the middle region as well.

However, there is a big difference between (Z.3) and the corresponding quantum mechanics problem: $\mathcal{U}$ multiplies Y' instead of Y, giving an advective term with a preferred direction as opposed to a simple directionless potential barrier. This affects the structure of the exponential solutions in the middle region, where there is an additional exponentially growing factor $\mathrm{e}^{x/\delta}$. This is then also reflected in the amplitude c_1 of the region near $x = 1$, which according to (Z.8a) is exponentially larger than the amplitude c_0 of the region near $x = 0$. Figure Z.1 shows these differences very clearly by comparing an example of the solution (Z.5) with a solution to the corresponding quantum mechanics problem of a particle trapped in a potential well.

Physically, we can think of the solutions as standing-wave oscillations at either boundary, communicating to one another via the exponential region inbetween, which preferentially grows in the downstream direction of advection towards $x = 1$.

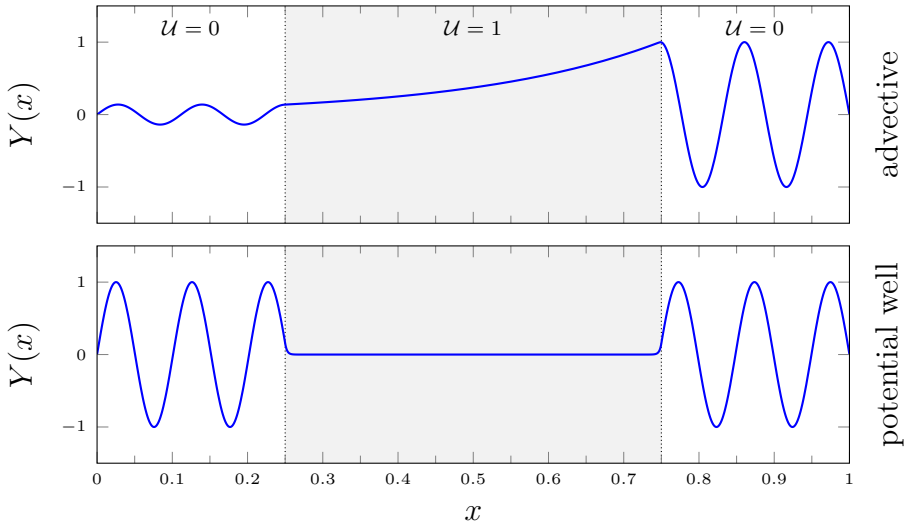

Fig. Z.1 (a) The solution (Z.5) for $\delta = 0.0025$, $\alpha = 1/4$ and eigenvalue $\omega \approx 56.27$ from (Z.8b), which clearly shows the directional nature of advection and the resulting exponential increase over the middle region $1/4 < x < 3/4$. (b) An example solution to the corresponding quantum mechanics problem of a particle trapped in a potential well, which clearly shows the directionless nature of a simple potential barrier and the resulting symmetry of the solution.

Z.2.2 The small-diffusivity limit ($\delta \to 0$) and the purely advective limit ($\delta = 0$)

To analyse the purely advective system, we first consider the limit of small diffusivity $\delta \to 0$. In this limit (Z.8b) becomes

$$\frac{\tan(2\omega\alpha)}{\omega} \sim -\delta + \cdots , \tag{Z.9}$$

which has solutions

$$\omega \sim n\pi \left(\frac{1}{2\alpha} - \frac{\delta}{4\alpha^2} + \cdots \right) , \tag{Z.10}$$

where $n \in \{1, 2, 3, \dots\}$ is an integer index of the eigenmodes. The amplitude relation (Z.8a) gives that the amplitude c_0 near $x = 0$ is exponentially small to leading order

and can be neglected, $c_0 = 0$. The solution $Y(x)$ in this limit is therefore given by

$$Y = 0 \qquad \text{for } 0 < x < \alpha, \tag{Z.11a}$$

$$Y = \sin\left(\frac{n\pi}{2}\right)\left(\frac{\mathrm{e}^{2\alpha/\delta} - \mathrm{e}^{2x/\delta}}{\mathrm{e}^{2\alpha/\delta} - \mathrm{e}^{2(1-\alpha)/\delta}}\right) \qquad \text{for } \alpha < x < 1-\alpha, \tag{Z.11b}$$

$$Y = \sin\left(\frac{n\pi(1-x)}{2\alpha}\right) \qquad \text{for } 1-\alpha < x < 1, \tag{Z.11c}$$

(where we have chosen a convenient value for c_1). This solution highlights that the even and odd eigenmodes separate into distinct cases: for even n we only get oscillations near $x = 1$ and no exponentially growing solution in the middle, while for odd n we get both the oscillatory and exponential regions.

Second, if we instead assume no diffusion at all, $\delta = 0$, then (Z.3) becomes

$$2\mathcal{U}Y' + \sigma Y = 0. \tag{Z.12}$$

As $\mathcal{U} = 0$ for both $0 < x < \alpha$ and $1 - \alpha < x < 1$, (Z.12) gives $Y = 0$ there also, and satisfies the boundary conditions (Z.2) at either end. The solution to (Z.12) for $\alpha < x < 1 - \alpha$ is

$$Y = c\mathrm{e}^{-\sigma x/2} \qquad \text{for} \qquad \alpha < x < 1-\alpha, \tag{Z.13}$$

where c is a constant. However, this solution cannot be matched continuously to $Y = 0$ on either side unless $c = 0$, which gives only the trivial solution $Y(x) = 0$. (It is not clear that continuity should be required, given the jump in $\mathcal{U}$ at α and $1 - \alpha$.)

In this simple example, while everything can be calculated in terms of elementary functions, it is not at all clear how to relate the small diffusion limit $\delta \to 0$ to the purely advective case $\delta = 0$. The difficulty is partially due to the discontinuous nature of $\mathcal{U}(x)$ in (Z.4). Hence, we now consider a continuous profile $\mathcal{U}(x)$.

Z.3 Triangular profile

We consider the piecewise linear triangular profile

$$\mathcal{U}(x) = \begin{cases} x, & \text{for } 0 < x < \frac{1}{2}, \\ 1 - x, & \text{for } \frac{1}{2} < x < 1, \end{cases} \tag{Z.14}$$

which again allows for an analytic solution to (Z.3) with boundary conditions (Z.2). This is given in terms of Kummer's confluent hypergeometric function M as

$$Y = x\,\mathrm{M}\left(\frac{2+\sigma}{4}; \frac{3}{2}; \frac{x^2}{\delta}\right) \quad \text{for} \quad 0 < x < \tfrac{1}{2}, \tag{Z.15a}$$

$$Y = \frac{\mathrm{M}\left(\frac{2+\sigma}{4}; \frac{3}{2}; \frac{1}{4\delta}\right)}{\mathrm{M}\left(\frac{4+\sigma}{4}; \frac{3}{2}; \frac{1}{4\delta}\right)}(1-x)\,\mathrm{M}\left(\frac{4+\sigma}{4}; \frac{3}{2}; \frac{(1-x)^2}{\delta}\right)\exp\left(\frac{(3-2x)(2x-1)}{4\delta}\right) \quad \text{for} \quad \tfrac{1}{2} < x < 1, \tag{Z.15b}$$

where the amplitudes of the two parts of this solution are chosen such that Y is continuous across $x = 1/2$ and, without loss of generality, we have chosen $Y'(0) = 1$. The growth rate σ needs to be such that Y' is continuous, which gives the condition

$$\frac{\mathrm{M}\left(\frac{4+\sigma}{4}; \frac{5}{2}; \frac{1}{4\delta}\right)}{\mathrm{M}\left(\frac{4+\sigma}{4}; \frac{3}{2}; \frac{1}{4\delta}\right)}(2-\sigma) - \frac{\mathrm{M}\left(\frac{6+\sigma}{4}; \frac{5}{2}; \frac{1}{4\delta}\right)}{\mathrm{M}\left(\frac{2+\sigma}{4}; \frac{3}{2}; \frac{1}{4\delta}\right)}(2+\sigma) = 24\delta. \tag{Z.16}$$

Though this is a complete analytical solution, it does not provide much insight into the structure of the eigenmodes and their limits as $\delta \to 0$. Hence, we consider asymptotic solutions instead and use the fully analytical solution for comparison and confirmation purposes only.

Z.3.1 The purely advective limit ($\delta = 0$)

We note first that we can solve the fully time-dependent system (Z.1) in the purely advective limit $\delta = 0$. Let us assume an initial condition $y(x,0) = y_0(x)$, with $y_0(0) = y_0(1) = 0$. We solve

$$\frac{\partial y}{\partial t} + 2\mathcal{U}\frac{\partial y}{\partial x} = 0, \qquad y(0,t) = y(1,t) = 0, \qquad y(x,0) = y_0(x). \tag{Z.17}$$

by using the method of characteristics, defining characteristic curves $x_c(t)$ by

$$\frac{\partial x_c}{\partial t} = 2\mathcal{U}(x_c)\,, \qquad\qquad x_c(0) = x_0, \tag{Z.18}$$

so that $y(x,t)$ is constant along characteristics $x = x_c(t)$. This gives us two possible forms of solution:

$$x_c = 1 + (x_0 - 1)\,\mathrm{e}^{-2t} \qquad \text{or} \qquad x_c = \begin{cases} x_0 \mathrm{e}^{2t}, & x_0 \mathrm{e}^{2t} < \frac{1}{2} \\ 1 - \frac{1}{4x_0}\mathrm{e}^{-2t}, & x_0 \mathrm{e}^{2t} > \frac{1}{2} \end{cases}, \tag{Z.19}$$

depending on whether $x_0 > 1/2$ or $x_0 < 1/2$, respectively.

As $y(x,t)$ is constant along $x = x_c(t)$, we have $y\left(x_c, t\right) = y_0\left(x_0\right)$, and we can invert (Z.19) to find the initial x_0 corresponding to a given $x_c = x$ at time t. This gives the full time-dependent advective solution as

$$y(x,t) = y_0\left(x\mathrm{e}^{-2t}\right) \qquad \text{for} \qquad 0 < x < \tfrac{1}{2}, \tag{Z.20a}$$

$$y(x,t) = y_0\left(\frac{\mathrm{e}^{-2t}}{4(1-x)}\right) \qquad \text{for} \qquad \tfrac{1}{2} < x < 1 - \tfrac{1}{2}\mathrm{e}^{-2t}, \tag{Z.20b}$$

$$y(x,t) = y_0\left(1 + (x-1)\mathrm{e}^{2t}\right) \qquad \text{for} \qquad 1 - \tfrac{1}{2}\mathrm{e}^{-2t} < x < 1. \tag{Z.20c}$$

It can easily be seen that this solution is continuous and satisfies the boundary and initial conditions (Z.17b,c). Figure Z.2 shows this full time-dependent advective solution and its characteristics for the initial condition $y_0(x) = x(1-x)$.

In the late-time limit as $t \to \infty$, we obtain

$$y(x,t) \sim x y_0' \mathrm{e}^{-2t} + \tfrac{1}{2}x^2 y_0'' \mathrm{e}^{-4t} + \cdots \qquad \text{for} \qquad 0 < x < \tfrac{1}{2}, \tag{Z.21a}$$

$$y(x,t) \sim \frac{y_0'}{4(1-x)}\mathrm{e}^{-2t} + \frac{y_0''}{32(1-x)^2}\mathrm{e}^{-4t} + \cdots \qquad \text{for} \qquad \tfrac{1}{2} < x < 1, \tag{Z.21b}$$

where all the derivatives of y_0 are evaluated at $x = 0$ and the third region from (Z.20c) is exponentially narrow. From the exponential decay of the various terms in (Z.21), we can identify a linear eigenspectrum with growth rates $\sigma = -2n$, where $n \in \{1, 2, 3, \dots\}$, and eigenmodes Y given by

$$Y = \frac{1}{n!}\left(\frac{\mathrm{d}^n y_0}{\mathrm{d}x^n}\right) x^n \qquad \text{for} \qquad 0 < x < \tfrac{1}{2}, \tag{Z.22a}$$

$$Y = \frac{1}{n!}\left(\frac{\mathrm{d}^n y_0}{\mathrm{d}x^n}\right)\left(\frac{1}{4(1-x)}\right)^n \qquad \text{for} \qquad \tfrac{1}{2} < x < 1, \tag{Z.22b}$$

again with the derivatives of y_0 evaluated at $x = 0$. We note that these eigenmodes still satisfy $Y(0,t) = 0$, but seem no longer to satisfy the other boundary condition $Y(1,t) = 0$, as we have neglected the exponentially narrow boundary layer near $x = 1$

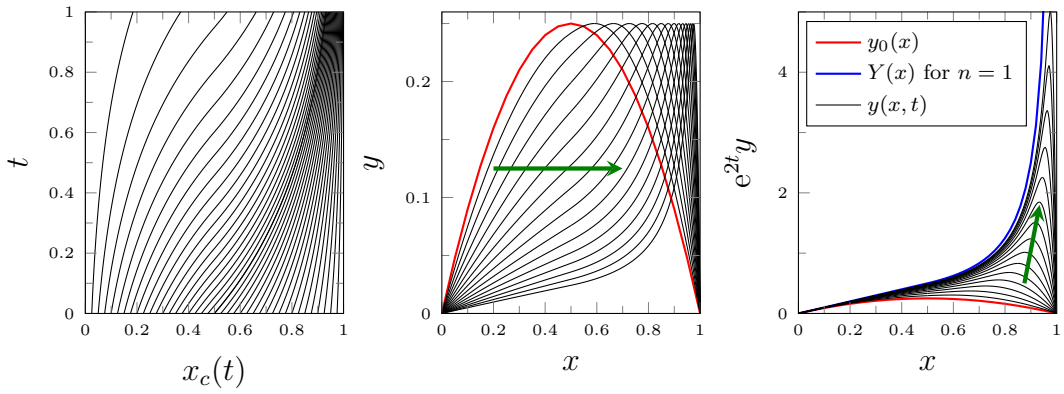

Fig. Z.2 The characteristic curves $x_c(t)$ as in (Z.19) and the time-dependent solutions $y(x,t)$ as in (Z.20) for the $\delta = 0$ limit with the triangular advection profile (Z.14). In red the initial condition $y_0(x) = x(1-x)$ and as a green arrow the direction of increasing time. Using a rescaled $e^{2t}y$ as a coordinate reveals the approach to the first eigenmode $Y(x)$ with $n = 1$ from (Z.22).

from (Z.20c). Figure Z.2 clearly shows the formation of this boundary layer and illustrates the dominant first eigenmode $Y(x)$ with $n = 1$. We can interpret this as a direct consequence of the purely advective nature of (Z.17): information is only carried downstream by the advection and hence any downstream boundary condition cannot affect the upstream solution in any way. In fact, equation (Z.21) shows that the late-time limit is determined entirely by the behaviour of y_0 near the upstream boundary $x = 0$.

Purely advective eigenmodes

Instead of identifying eigenmodes from the late-time expansion of the fully time-dependent solution (Z.20), we can directly consider $\delta = 0$ in equation (Z.3) for the eigenmodes $Y(x)$. This gives $2\mathcal{U}Y' + \sigma Y = 0$, similarly to (Z.12), which, for the triangular profile $\mathcal{U}$ given in (Z.14), can be solved resulting in

$$Y = c(2x)^{-\sigma/2} \qquad \text{for} \qquad 0 < x < \tfrac{1}{2}, \tag{Z.23a}$$

$$Y = c\,(2[1-x])^{\sigma/2} \qquad \text{for} \qquad \tfrac{1}{2} < x < 1, \tag{Z.23b}$$

where continuity at $x = 1/2$ has been imposed and c is an arbitrary constant amplitude. As long as $\sigma < 0$, $Y(x)$ satisfies the boundary condition $Y(0) = 0$. However, there is then no growth rate σ for which the solution (Z.23) would also satisfy the boundary condition $Y(1) = 0$.

We have to conclude that there are no purely advective eigenmodes, which satisfy both boundary conditions (Z.2). Motivated by the expansion of the time-dependent solution (Z.22), we abandon the boundary condition at $x = 1$. A discrete spectrum of growth rates σ is then obtained by demanding that the solution must be analytic at $x = 0$, i.e. that it has a Taylor series around $x = 0$. This gives that, as before, $-\sigma/2$ must be a positive integer and hence

$$\sigma = -2n, \tag{Z.24}$$

where $n \in \{1, 2, 3, \dots\}$. The assumption that Y is analytical at $x = 0$ is motivated by assuming that the initial condition is analytical at $x = 0$, implying that the solution remains analytical there for all times.

Z.3.2 The small-diffusivity limit ($\delta \to 0$)

Instead of considering the singular case $\delta = 0$, we now seek an asymptotic solution for the small-diffusivity limit $\delta \to 0$. This is done by means of a WKB analysis for which we write $Y(x) = \mathrm{e}^{S(x)}$ and expand $S(x) = \delta^{-1} S_0(x) + S_1(x) + O(\delta)$. Introducing a rescaled eigenvalue $\omega^2 = -\sigma\delta$ (different from the rescaling in §Z.2), we obtain the equations

$$\left(S_0'\right)^2 = 2\mathcal{U}S_0' - \omega^2, \qquad\qquad S_1' = \frac{S_0''}{2\mathcal{U} - 2S_0'}, \tag{Z.25}$$

with solutions

$$S_0 = \int \mathcal{U}\,\mathrm{d}x \pm \int \left(\mathcal{U}^2 - \omega^2\right)^{1/2} \mathrm{d}x, \qquad S_1 = -\tfrac{1}{2}\log S_0' - \tfrac{1}{4}\log\left(\mathcal{U} - \omega^2\right). \tag{Z.26}$$

The solution reveals that there are turning points where $\mathcal{U}(x) = \omega$, which, for (Z.14), are at $x_0 = \omega$ and $x_1 = 1 - \omega$. These turning points are crucial in determining whether we have exponential or oscillatory behaviour and split up the domain into four regions. With $\mathcal{U}(x)$ given by (Z.14), we can integrate (Z.26) analytically and write

down the asymptotic solution in these four regions:

$$Y \sim \frac{\exp\left(\frac{x^2}{2\delta} - \frac{1}{8\delta}\right)}{\left(\omega^2 - x^2\right)^{1/4}} c_0 \sin\left(\frac{x}{2\delta}\left\{\omega^2 - x^2\right\}^{1/2} + \frac{\omega^2+\delta}{2\delta}\sin^{-1}\left\{\frac{x}{\omega}\right\}\right)$$

$$\text{for } 0 < x < x_0, \quad \text{(Z.27a)}$$

$$Y \sim \frac{\exp\left(\frac{x^2}{2\delta} - \frac{1}{8\delta}\right)}{\left(x^2 - \omega^2\right)^{1/4}} \left[a_+ \frac{\exp\left(\frac{x}{2\delta}\left\{x^2 - \omega^2\right\}^{1/2}\right)}{\left(\frac{x}{\omega} + \left\{\frac{x^2}{\omega^2} - 1\right\}^{1/2}\right)^{\frac{\omega^2+\delta}{2\delta}}} + a_- \frac{\exp\left(-\frac{x}{2\delta}\left\{x^2 - \omega^2\right\}^{1/2}\right)}{\left(\frac{x}{\omega} - \left\{\frac{x^2}{\omega^2} - 1\right\}^{1/2}\right)^{\frac{\omega^2+\delta}{2\delta}}}\right]$$

$$\text{for } x_0 < x < \tfrac{1}{2}, \quad \text{(Z.27b)}$$

$$Y \sim \frac{\exp\left(\frac{1}{8\delta} - \frac{\tilde{x}^2}{2\delta}\right)}{\left(x^2 - \omega^2\right)^{1/4}} \left[b_+ \frac{\exp\left(\frac{\tilde{x}}{2\delta}\left\{\tilde{x}^2 - \omega^2\right\}^{1/2}\right)}{\left(\frac{\tilde{x}}{\omega} + \left\{\frac{\tilde{x}^2}{\omega^2} - 1\right\}^{1/2}\right)^{\frac{\omega^2-\delta}{2\delta}}} + b_- \frac{\exp\left(-\frac{\tilde{x}}{2\delta}\left\{\tilde{x}^2 - \omega^2\right\}^{1/2}\right)}{\left(\frac{\tilde{x}}{\omega} - \left\{\frac{\tilde{x}^2}{\omega^2} - 1\right\}^{1/2}\right)^{\frac{\omega^2-\delta}{2\delta}}}\right]$$

$$\text{for } \tfrac{1}{2} < x < x_1, \quad \text{(Z.27c)}$$

$$Y \sim \frac{\exp\left(\frac{1}{8\delta} - \frac{\tilde{x}^2}{2\delta}\right)}{\left(\omega^2 - \tilde{x}^2\right)^{1/4}} c_1 \sin\left(\frac{\tilde{x}}{2\delta}\left\{\omega^2 - \tilde{x}^2\right\}^{1/2} + \frac{\omega^2-\delta}{2\delta}\sin^{-1}\left\{\frac{\tilde{x}}{\omega}\right\}\right)$$

$$\text{for } x_1 < x < 1, \quad \text{(Z.27d)}$$

where $\tilde{x} = 1 - x$.

We recall that local analysis near a turning point in a WKB problem gives rise to Airy's equation at leading order, from which the far-field asymptotics of the Airy functions Ai and Bi can to be used to match across the turning point. Effectively, any phase shift of the oscillatory solution at the turning point is linked to a certain linear combination of Ai and Bi, which in turn is linked to a linear combination of decaying and growing exponentials on the other side of the turning point. The four matching conditions for (Z.27) across the turning points $x = x_{0,1}$ can shown to be

$$c_0 = \frac{2a_-}{\cos\theta_0}, \qquad c_0 = \frac{a_+}{\sin\theta_0}, \qquad \text{where} \qquad \theta_0 = -\tfrac{3}{2}\pi - \frac{\pi\omega^2}{4\delta}, \qquad \text{(Z.28a)}$$

$$c_1 = \frac{2b_-}{\cos\theta_1}, \qquad c_1 = \frac{b_+}{\sin\theta_1}, \qquad \text{where} \qquad \theta_1 = -\pi - \frac{\pi\omega^2}{4\delta}. \qquad \text{(Z.28b)}$$

Two further conditions come from continuity of Y and Y' at $x = 1/2$, which, after plenty of algebra, result in

$$\frac{2\omega a_+ - (1+\Omega)b_+}{2\omega a_- - (1-\Omega)b_-} + \left(\frac{1+\Omega}{1-\Omega}\right)^{\frac{\omega^2+\delta}{2\delta}} \mathrm{e}^{-\frac{\Omega}{4\delta}} = 0, \tag{Z.29a}$$

$$\frac{\left(\frac{2\omega}{1-\Omega}\right)a_+ - \left(\frac{\Omega^2+2\delta}{\Omega^2-2\delta}\right)b_+}{\left(\frac{2\omega}{1+\Omega}\right)a_- - \left(\frac{\Omega^2+2\delta}{\Omega^2-2\delta}\right)b_-} + \underbrace{\left(\frac{1+\Omega}{1-\Omega}\right)^{\frac{\omega^2+\delta}{2\delta}} \mathrm{e}^{-\frac{\Omega}{4\delta}}}_{\mu} = 0, \tag{Z.29b}$$

where $\Omega^2 = 1 - 4\omega^2$. The term labelled μ above is exponentially small.

Examining the matching conditions (Z.28), we note that

$$\frac{2a_-}{a_+} = \cot\theta_0 = \tan\left(\frac{\pi\omega^2}{4\delta}\right) = -\tan\theta_1 = -\frac{b_+}{2b_-}. \tag{Z.30}$$

Equations (Z.29) and (Z.30) provide four equations for the three independent ratios of $a_\pm$ and $b\pm$ in terms of $\tan\theta_0$ and μ. The solubility condition yields an equation for the phase shift θ_0:

$$\tan^2\theta_0 + \frac{1}{4\delta\mu}\left(4\left[\frac{\Omega^3-2\delta}{1-\Omega}\right] + \mu^2\left[\frac{\Omega^3+2\delta}{1+\Omega}\right]\right)\tan\theta_0 - 1 = 0. \tag{Z.31}$$

Z.3.3 Comparing the small-diffusivity limit to the purely advective limit

Since μ is exponentially small, the two solutions to (Z.31) are given to leading order by

$$\tan\theta_0 = \frac{(1-\Omega)\delta\mu}{\Omega^3-2\delta} + O\left(\mu^2\right) \qquad \text{and} \qquad \tan\theta_0 = -\frac{\Omega^3-2\delta}{(1-\Omega)\delta\mu} + O(1). \tag{Z.32}$$

If we assume that $\omega^2 = O(\delta)$ for $\delta \ll 1$ then $\Omega = 1 - 2\omega^2 + O\left(\delta^2\right)$ and (Z.32) becomes

$$\cot\left(\frac{\pi\omega^2}{4\delta}\right) \sim 2\delta\mu\omega^2 \ll 1 \qquad \text{or} \qquad \cot\left(\frac{\pi\omega^2}{4\delta}\right) \sim -\frac{1}{2\delta\mu\omega^2} \gg 1, \tag{Z.33}$$

where $\tan\theta_0$ was replaced using (Z.30).

We conclude from (Z.33) that, to leading order, $\omega^2 = 2n\delta$ and thus $\sigma = -2n$ where $n \in \{1, 2, 3, \cdots\}$. We note that the odd and the even values of n correspond respectively to the first and the second solution in (Z.33). These eigenvalues confirm that $\omega^2 = O(\delta)$ as anticipated, thereby showing our derivation is consistent.

To examine the form of the eigenfunctions, we choose c_0 such that $Y'(0) = 1$ and evaluate all other amplitudes in terms of c_0 by using (Z.28), (Z.29) and (Z.33). This gives

$$c_0 = \frac{2\omega^{3/2}\mathrm{e}^{1/8\delta}}{1+4n}, \qquad a_+ = c_0\cos\left(\frac{n\pi}{2}\right), \qquad a_- = \frac{c_0}{2}\sin\left(\frac{n\pi}{2}\right), \tag{Z.34a}$$

$$c_1 = \begin{cases} c_0\mu\omega/2, & n \text{ odd}, \\ 2c_0/\mu\omega, & n \text{ even}, \end{cases} \qquad b_+ = c_1\sin\left(\frac{n\pi}{2}\right), \qquad b_- = -\frac{c_1}{2}\cos\left(\frac{n\pi}{2}\right). \tag{Z.34b}$$

We then consider the limit of (Z.27) as $\delta \to 0$ by substituting $\omega^2 = 2n\delta$. The oscillatory regions near the boundaries become infinitesimally small boundary layers, and we are left with the exponential interior regions where

$$Y \sim \left[\left(\frac{\omega}{2}\right)^{n+\frac{1}{2}} a_+ x^{-n-1}\mathrm{e}^{x^2/\delta} + \left(\frac{2}{\omega}\right)^{n+\frac{1}{2}} a_- x^n\right]\mathrm{e}^{-1/8\delta} \qquad \text{for } x < \tfrac{1}{2}, \tag{Z.35a}$$

$$Y \sim \left[\left(\frac{\omega}{2}\right)^{n-\frac{1}{2}} b_+ \tilde{x}^{-n} + \left(\frac{2}{\omega}\right)^{n-\frac{1}{2}} b_- \tilde{x}^{n-1}\mathrm{e}^{-\tilde{x}^2/\delta}\right]\mathrm{e}^{1/8\delta} \qquad \text{for } x > \tfrac{1}{2}. \tag{Z.35b}$$

Substitution of the amplitudes from (Z.34) and using the fact that $\mu \sim \omega^{-2n-1}\mathrm{e}^{-1/(4\delta)}$ as $\delta \to 0$, then gives two cases:

- The odd eigenmodes: $n = 2j+1$

$$Y \sim \frac{(-1)^j c_0}{2}\left(\frac{2}{\omega}\right)^{n+\frac{1}{2}} x^n\mathrm{e}^{-1/8\delta} \qquad \sim c_*(2x)^n \qquad \text{for } x < \tfrac{1}{2}, \tag{Z.36a}$$

$$Y \sim \frac{(-1)^j\mu\omega c_0}{2}\left(\frac{\omega}{2}\right)^{n-\frac{1}{2}} \tilde{x}^{-n}\mathrm{e}^{1/8\delta} \qquad \sim c_*\left(2\tilde{x}\right)^{-n} \qquad \text{for } x > \tfrac{1}{2}, \tag{Z.36b}$$

  where c_* is a constant.

- The even eigenmodes: $n = 2j$

$$Y \sim (-1)^j c_0\left(\frac{\omega}{2}\right)^{n+\frac{1}{2}} x^{-n-1}\mathrm{e}^{\left(8x^2-1\right)/8\delta} \qquad \sim c_*(2x)^{-n-1}\mathrm{e}^{\left(8x^2-1\right)/8\delta} \qquad \text{for } x < \tfrac{1}{2}, \tag{Z.37a}$$

$$Y \sim \frac{(-1)^{j+1}c_0}{\mu\omega}\left(\frac{2}{\omega}\right)^{n-\frac{1}{2}} \tilde{x}^{n-1}\mathrm{e}^{\left(1-8\tilde{x}^2\right)/8\delta} \qquad \sim -c_*\left(2\tilde{x}\right)^{n-1}\mathrm{e}^{\left(1-8\tilde{x}^2\right)/8\delta} \qquad \text{for } x > \tfrac{1}{2}, \tag{Z.37b}$$

where c_* is a constant.

The odd eigenmodes correspond to the purely advective eigenmodes (Z.23) with growth rates (Z.24), which were obtained directly from solving $2\mathcal{U}Y' + \sigma Y = 0$ with the additional assumption of Y being analytic at $x = 0$. The even eigenmodes, on the other hand, contain an exponential factor that increases enormously by $\mathrm{e}^{1/2\delta}$ from $x = 0$ to $x = 1$. The dominant balance is between advection and diffusion. These modes are present for $\delta > 0$, but disappear completely for $\delta = 0$. Conversely, the analysis for $\delta = 0$ did produce modes for even values of n, but these had the same form as (Z.36) and not (Z.37). Therefore, the case $\delta = 0$ is a singular limit of $\delta \to 0$.

It may initially seem surprising that, while the odd advective eigenmodes are recovered as the limit of small diffusivity, the even advective eigenmodes are completely different from the small-diffusivity solutions (Z.37). A partial explanation concerns the effects of diffusion at the upstream boundary condition $x = 0$. The odd advective eigenmodes are also odd functions of x if extended into $x < 0$. Hence, even if diffusion is introduced as a small perturbation, these modes automatically continue to satisfy the boundary condition $y(0, t) = 0$. In contrast, if the even advective eigenmodes are extended into $-1 < x < 0$ as even functions (with $\mathcal{U}$ extended as an odd function) and then allowed to evolve on $-1 < x < 1$ under (Z.1), it is not the case that $y(0, t) = 0$ continues to be satisfied. This is most obvious for the case $n = 2$, where $Y''(0) \neq 0$, but is also true of the other even modes. Thus imposing the boundary condition at $x = 0$ has distinct effects with and without diffusion for the even eigenmodes but not for the odd eigenmodes. This can also be seen in full time-dependent simulations.

Figure Z.3 shows the profiles $Y(x)$ of the first four eigenmodes for small diffusivity $\delta = 0.01$, comparing the fully analytical solution (Z.15) with the asymptotic WKB solution (Z.27). This reveals excellent agreement between the two, except near the singular region of the turning points $x = \omega$ and $x = 1-\omega$, which is expected when using the WKB method. To avoid these turning-point singularities, we would need to include the local Airy-function behaviour. The solutions also highlight the exponentially larger nature of the even modes, giving us confidence in the analysis.

Z.4 Numerical results for the growth rates and comparisons

Both for the top-hat profile (Z.4) and for the triangular profile (Z.14), we have analytically derived implicit equations for the growth rate σ, given by (Z.8b) and

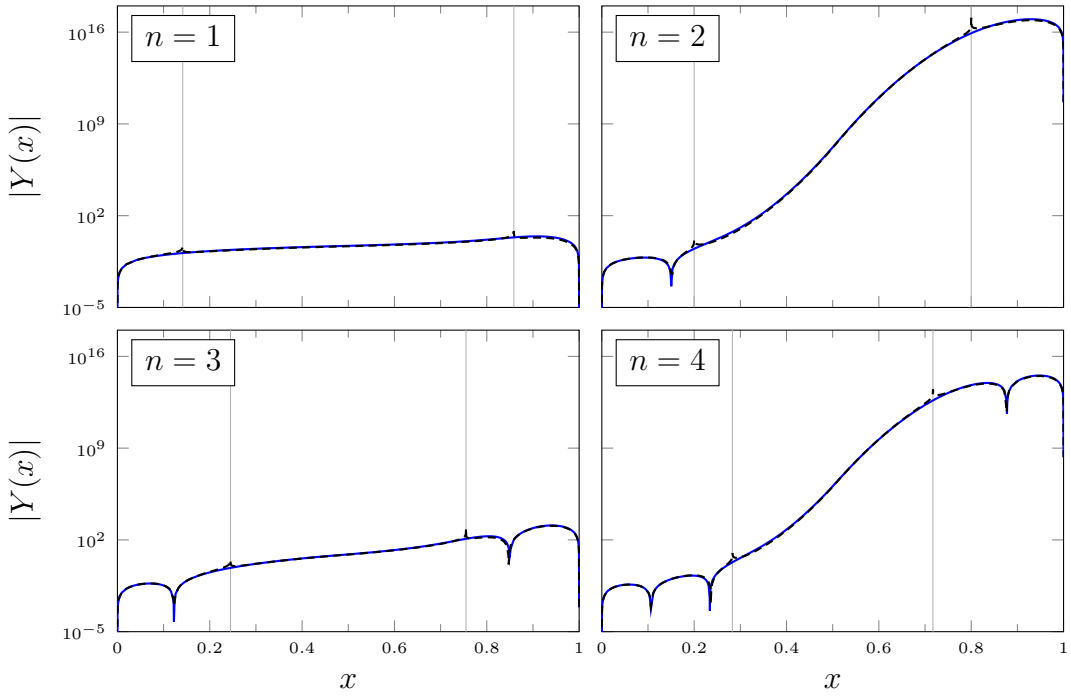

Fig. Z.3 The profiles $Y(x)$ of the first four eigenmodes for small diffusivity $\delta = 0.01$, comparing the fully analytical solution (Z.15) (solid blue lines) with the asymptotic WKB solution (Z.27) (dashed black lines). The turning points (vertical grey lines) are singular points of the WKB analysis.

(Z.16), respectively. As these are complex implicit relationships, they have to be solved numerically. The results of these numerically calculated growth rates for the two cases are plotted in figures Z.4 and Z.5, respectively.

Instead of plotting the growth rate σ directly, we have plotted rescalings, given by $\frac{2\alpha}{\pi}(-\sigma/\delta)^{1/2}$ and $-\sigma/2$ respectively, in order that the curves tend to the positive integers as $\delta \to 0$. In both cases we have also plotted the small-diffusivity asymptotic solutions given by (Z.10) and (Z.31) respectively, which compare very well to the full solutions. The different rescalings and different trends simply reflect the qualitative difference between the ways the two profiles $\mathcal{U}(x)$ approach 0 as $x \to 0, 1$.

We also recall that if the magnitude of the growth rate becomes sufficiently large, the behaviour of the solutions for $Y(x)$ change from exponential in the central region to purely oscillatory. For both cases we have found a parameter Ω governing the boundary between these regions, which we defined as $\Omega^2 = (\delta + \sigma)/\delta^2$ for the top-hat profile and as $\Omega^2 = 1 + 4\delta\sigma$ for the triangular profile. The corresponding numerical growth rates in figure Z.4 and figure Z.5 clearly show a change in behaviour as Ω^2 transitions from positive to negative.

Though not our main concern, we note that for large diffusivity δ, the advective term $2\mathcal{U}Y'$ in (Z.3) becomes negligible and $Y \to \sin(n\pi)$ with a positive integer n so that the growth rates are given by $\sigma = -\delta n^2\pi^2$. This corresponds to constants if we consider the rescaling $\frac{2\alpha}{\pi}(-\sigma/\delta)^{1/2}$ and linear behaviour if we consider the rescaling $-\sigma/2$, which is confirmed numerically in figures Z.4 and Z.5.

Z.5 Conclusions & Discussion

We summarise some key points about purely advective systems with zero-velocity boundaries:

- The downstream boundary conditions may be impossible to satisfy, with, for example, the advective eigenmodes diverging algebraically towards the downstream boundary.
- The upstream boundary conditions may be trivially satisfied for all advective eigenmodes, yielding a continuous spectrum of eigenmodes, for example $\sigma < 0$.
- We may need to impose the condition that the advective eigenmodes are analytic at the upstream boundary, which follows from considering analytic initial conditions. This additional boundary conditions recovers a discrete spectrum of eigenvalues.
- Some of the advective eigenmodes obtained with the analytic boundary condition, may not represent the limit of diffusive eigenmodes at all, although the eigenvalues seem to be predicted correctly by the purely advective system nonetheless. Conversely, some of the diffusive eigenmodes are not picked up by the purely advective analysis at all. These correspond to a balance of advection and diffusion.

These points might seem discouraging when attempting a normal-mode analysis to find a discrete set of eigenvalues to analyse the stability of purely advective systems with zero-velocity boundaries. However, we have shown that these features can be resolved by considering the limit $\delta \to 0$ of a regularised slightly diffusive system.

We now turn to the physical interpretation of purely advective systems not regularised by diffusion. In such a system, a disturbance near the upstream boundary gets transported downstream with its initial amplitude and does not decay or diffuse away in the Lagrangian frame of the disturbance. Therefore, any advective eigenmode decaying in time in an Eulerian frame must also grow spatially towards the downstream

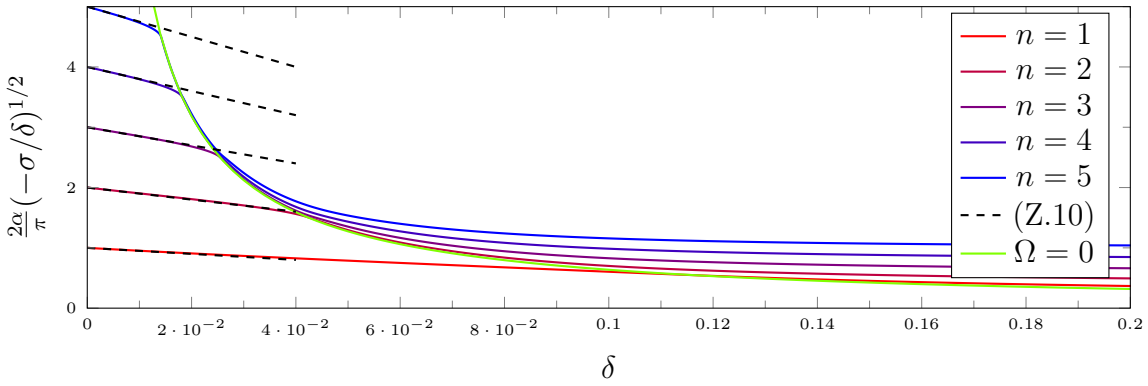

Fig. Z.4 The eigenvalues σ for normal modes of the advection–diffusion equation (Z.1) as a function of diffusivity δ for the top-hat velocity profile (Z.4) with $\alpha = 0.1$. The asymptotic result (Z.10) (dashed black) for $\delta \ll 1$ agrees well with the full numerical solution of (Z.8b) (solid red to blue). The boundary (solid green) between the regions of oscillatory solutions $\Omega^2 > 0$ and purely exponential solutions $\Omega^2 < 0$, with $\Omega^2 = (\delta + \sigma)/\delta^2$, marks a clear transition in the behaviour of the eigenvalues.

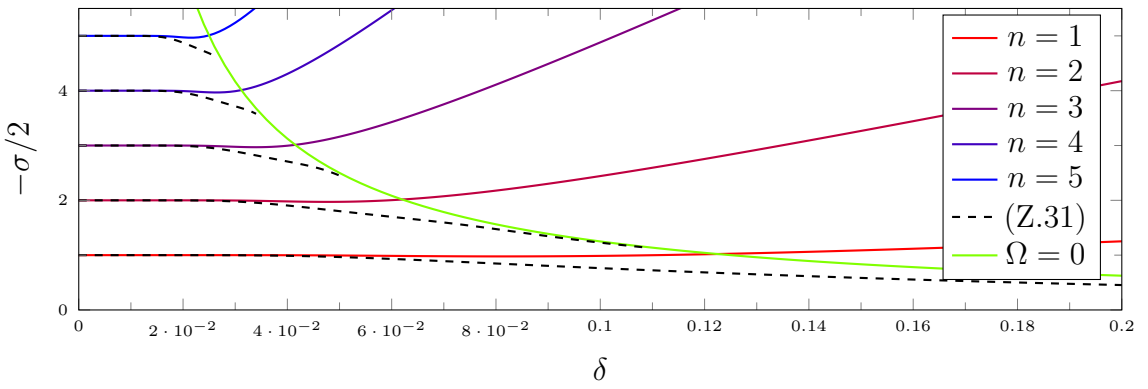

Fig. Z.5 The eigenvalues σ for normal modes of the advection–diffusion equation (Z.1) as a function of diffusivity δ for the triangular velocity profile (Z.14). The asymptotic result (Z.31) (dashed black) for $\delta \ll 1$ agrees well with the full numerical solution of (Z.16) (solid red to blue). The boundary (solid green) between the regions of oscillatory solutions $\Omega^2 > 0$ and purely exponential solutions $\Omega^2 < 0$, with $\Omega^2 = 1 + 4\delta\sigma$, marks a clear transition in the behaviour of the eigenvalues.

boundary, as the downstream part of the disturbance reflects the greater amplitudes that pertained some time ago when it originated upstream. For an alternative interpretation of the purely advective eigenmodes, we note that at late times the entire solution, except very near the downstream boundary, is governed by properties of the initial solution at the upstream boundary. Therefore, we can interpret these modes as local eigenmodes, which are valid only in a region near the upstream boundary whose size increases in time. The expansion (Z.21) shows a clear example, where the terms only form a well-ordered expansion in a region near $x = 0$ whose size grows exponentially like $O\left(\mathrm{e}^{2t}\right)$.

We conclude that as long as we are careful regarding the boundary conditions and interpret the results only locally, a stability analysis using normal modes can work even for purely advective systems with zero-velocity boundaries.

References

Abriola, L. M. (1987). Modelling contaminant transport in the subsurface: an interdisciplinary challenge. *Rev. Geophys.*, 25:125–134.

Acheson, D. J. (1990). *Elementary Fluid Dynamics*. Oxford University Press.

Acton, J. M., Huppert, H. E., and Worster, M. G. (2001). Two-dimensional viscous gravity currents flowing over a deep porous medium. *J. Fluid Mech.*, 440:359–380.

Balmforth, N. J., Craster, R. V., Perona, P., Rust, A. C., and Sassi, R. (2007). Viscoplastic dam breaks and the Bostwick consistometer. *J. Non-Newtonian Fluid Mech.*, 142:63–78.

Barenblatt, G. I. (1952). On some unsteady motions of fluids and gases in a porous medium. *J. Appl. Math. Mech.*, 16:67–78.

Benjamin, T. B. (1968). Gravity currents and related phenomena. *J. Fluid Mech.*, 31:209–248.

Billingham, J. and King, A. C. (2001). *Wave Motion*. Cambridge University Press.

Bischofberger, I., Ramachandran, R., and Nagel, S. R. (2014). Fingering versus stability in the limit of zero interfacial tension. *Nat. Commun.*, 5:5265.

Boyer, R. H. (1962). On some solutions of a nonlinear diffusion equation. *J. Maths. and Phys.*, 40:41–45.

Charba, J. (1974). Application of gravity current model to analysis of squall-line gust front. *Mon. Weather Rev.*, 102:140–.

Chen, C.-Y. and Meiburg, E. (1996). Miscible displacements in capillary tubes. Part 2. Numerical simulations. *J. Fluid Mech.*, 326:57–90.

Copley, A. and McKenzie, D. (2007). Models of crustal flow in the India-Asia collision zone. *Geophys. J. Int.*, 169:683–698.

Coumou, D., Driesner, T., Geiger, S., Heinrich, C. A., and Matthäi, S. (2006). The dynamics of mid-ocean ridge hydrothermal systems: splitting plumes and fluctuating vent temperatures. *Earth Planet. Sc. Lett.*, 245:218–231.

Courant, R. and Friedrichs, K. O. (1948). *Supersonic Flow and Shock Waves*. Intersience.

Dauck, T.-F., Box, F., Gell, L., Neufeld, J. A., and Lister, J. R. (2019). Shock formation in two-layer equal-density viscous gravity currents. *J. Fluid Mech.*, 863:730–756.

Dengler, Jr, A. T. and Wilde, P. (1987). Turbidity currents on steep slopes: application of an avalanche-type numeric model for ocean thermal energy conversion design. *Ocean Eng.*, 14:409–433.

Detournay, E. and Garagash, D. I. (2003). The near-tip region of a fluid-driven fracture propagating in a permeable elastic solid. *J. Fluid Mech.*, 494:1–32.

Di Federico, V., Archetti, R., and Longo, S. (2012). Similarity solutions for spreading of a two-dimensional non-Newtonian gravity current in a porous layer. *J. Non-Newton. Fluid*, 177–178:46–53.

Diez, J. A., Gratton, R., and Gratton, J. (1992). Self-similar solution of the second kind for a convergent viscous gravity current. *Phys. Fluids*, 4:1148–1155.

Doedel, E. et al. (2007). AUTO-07P: continuation and bifurcation software for ordinary differential equations. http://indy.cs.concordia.ca/auto/.

Drazin, P. (2002). *Introduction to Hydrodynamic Instability*. Camrbidge University Press.

Dullien, F. A. L. (1992). *Porous Media: Fluid Transport and Pore Structure*. Academic Press.

Fink, J. H. and Griffiths, R. W. (1990). Radial spreading of viscous-gravity currents with solidifying crust. *J. Fluid Mech.*, 221:485–509.

Fink, J. H. and Griffiths, R. W. (1998). Morphology, eruption rates, and rheology of lava domes: insights from laboritory models. *J. Geophys. Res.*, 103:527–545.

Fowler, A. C. (1997). *Mathematical Models in the Applied Sciences*. Cambridge University Press.

Goyal, N. and Meiburg, E. (2006). Miscible displacements in Hele-Shaw cells: two-dimensional base states and their linear stability. *J. Fluid Mech.*, 558:329–355.

Gratton, J. and Minotti, F. (1990). Self-similar viscous gravity currents: phase-plane formalism. *J. Fluid Mech.*, 210:155–182.

Gratton, J. and Minotti, F. (1999). Theory of creeping gravity currents of a non-Newtonian liquid. *Phys. Rev. E*, 60:6960–6967.

Griffiths, R. W. (2000). The dynamics of lava flows. *Annu. Rev. Fluid Mech.*, 32:477–518.

Griffiths, R. W. and Fink, J. (1993). Effects of surface cooling on the spreading of lava flows and domes. *J. Fluid Mech.*, 252:667–702.

Grundy, R. E. and McLaughlin, R. (1982). Eigenvalues of the Barenblatt–Pattle similarity solution in nonlinear diffusion. *Proc. Roy. Soc. A*, 383:89–100.

Gustafsson, B. and Vasil'ev, A. (2000). *Conformal and Potential Analysis in Hele-Shaw Cells*. Birkhäuser.

Hallworth, M. A., Huppert, H. E., Phillips, J. C., and Sparks, R. S. J. (1996). Entrainment into two-dimensional and axisymmetric turbulent gravity currents. *J. Fluid Mech.*, 308:289–311.

Hallworth, M. A., Phillips, J. C., Huppert, H. E., and Spark, R. S. J. (1993). Entrainment in turbulent gravity currents. *Nature*, 362:831–829.

Hele-Shaw, H. S. (1897). The flow of water. *Nature*, 58:34–36.

Hermann, F. and Hutter, K. (1991). Laboratory experiments on the dynamics of powder-snow avalanches in the run-out zone. *J. Glaciol.*, 37:281–295.

Hesse, M. A., Tchelepi, H. A., Cantwell, B. J., and Orr, Jr, F. M. (2007). Gravity currents in horizontal porous layers: transition from early to late self-similarity. *J. Fluid Mech.*, 577:363–383.

Hewitt, I. J., Balmforth, N. J., and De Bruyn, J. R. (2015). Elastic-plated gravity currents. *Eur. J. Appl. Math.*, 26:1–31.

Hogg, A. J. and Matson, G. P. (2009). Slumps of viscoplastic fluids on slopes. *J. Non-Newtonian Fluid Mech.*, 158:101–112.

Hoult, D. P. (1972). Oil Spreading on the sea. *Annu. Rev. Fluid Mech.*, 4:341–368.

Huppert, H. E. (1982a). Flow and instability of a viscous current down a slope. *Nature*, 300:427–429.

Huppert, H. E. (1982b). Propagation of two-dimensional and axisymmetric viscous gravity currents over a rigid horizontal surface. *J. Fluid Mech.*, 121:43–58.

Huppert, H. E. (2006). Gravity currents: a personal perspective. *J. Fluid Mech.*, 554:299–322.

Huppert, H. E. and Neufeld, J. A. (2014). The fluid mechanics of carbon dioxide sequestration. *Annu. Rev. Fluid Mech.*, 46:255–272.

Huppert, H. E. and Woods, A. W. (1995). Gravity-driven flows in porous layers. *J. Fluid Mech.*, 292:55–69.

Jacob, T., Wahr, J., Pfeffer, W. T., and Swenson, S. (2012). Recent contributions of glaciers and ice caps to sea level rise. *Nature*, 482:514–518.

Jacobs, D., McKinney, B., and Shearer, M. (1995). Traveling wave solutions of the modified Korteweg–deVries–Burgers equation. *J. Differential Equations*, 116:448–467.

Kerr, R. C. and Lister, J. R. (1987). The spread of subducted lithospheric material along the mid-mantle boundary. *Earth Planet. Sc. Lett.*, 85:241–247.

Koch, D. M. and Koch, D. L. (1995). Numerical and theoretical solutions for a drop spreading below a free fluid surface. *J. Fluid Mech.*, 287:251–278.

Kowal, K. N. and Worster, M. G. (2015). Lubricated viscous gravity currents. *J. Fluid Mech.*, 766:626–655.

Kowal, K. N. and Worster, M. G. (2019a). Stability of lubricated viscous gravity currents. Part 1. Internal and frontal analyses and stabilisation by horizontal shear. *J. Fluid Mech.*, 871:970–1006.

Kowal, K. N. and Worster, M. G. (2019b). Stability of lubricated viscous gravity currents. Part 2. Global analysis and stabilisation by buoyancy forces. *J. Fluid Mech.*, 871:1007–1027.

Lajeunesse, E., Martin, J., Rakotomalala, N., and Salin, D. (1997). 3D instability of miscible displacements in a Hele-Shaw cell. *Phys. Rev. Lett.*, 79:5254–5257.

Lajeunesse, E., Martin, J., Rakotomalala, N., Salin, D., and Yortsos, Y. C. (1999). Miscible displacement in a Hele-Shaw cell at high rates. *J. Fluid Mech.*, 398:299–319.

Lajeunesse, E., Martin, J., Rakotomalala, N., Salin, D., and Yortsos, Y. C. (2001). The threshold of the instability in miscible displacements in a Hele-Shaw cell at high rates. *Phys. Fluids*, 13:799–801.

Lake, L. W. (1989). *Enhanced Oil Recovery*. Prentice Hall.

LeFloch, P. G. (2002). *Hyperbolic Systems of Conservation Laws: The Theory of Classical and Nonclassical Shock Waves*. Birkhäuser.

Lister, J. R. (1990). Buoyancy-driven fluid fracture: similarity solutions for the horizontal and vertical propagations of fluid-filled cracks. *J. Fluid Mech.*, 217:213–239.

Lister, J. R. (1992). Viscous flows down an inclined plane from point and line sources. *J. Fluid Mech.*, 242:631–653.

Lister, J. R. and Kerr, R. C. (1989). The propagation of two-dimensional and axisymmetric viscous gravity currents at a fluid interface. *J. Fluid Mech.*, 203:215–249.

Lister, J. R., Peng, G. G., and Neufeld, J. A. (2013). Viscous control of peeling an elastic sheet by bending and pulling. *Phys. Rev. Lett.*, 111:154501.

Lister, J. R., Skinner, D. J., and Large, T. M. J. (2019). Viscous control of shallow elastic fracture: peeling without precursors. *J. Fluid Mech.*, 868:119–140.

Longo, S. and Di Federico, V. (2015). Stability analysis of gravity currents of a power-law fluid in a porous medium. *Math. Probl. Eng.*, 2015.

Longo, S., Di Federico, V., and Chiapponi, L. (2015). Propagation of viscous gravity currents inside confining boundaries: the effects of fluid rheology and channel geometry. *Proc. Roy. Soc. A*, 471.

Longo, S., Di Federico, V., Chiapponi, L., and Archetti, R. (2013). Experimental verification of power-law non-Newtonian axisymmetric porous gravity currents. *J. Fluid Mech.*, 731:R2.

Lyle, S., Huppert, H. E., Hallworth, M., Bickle, M., and Chadwick, A. (2005). Axisymmetric gravity currents in a porous medium. *J. Fluid Mech.*, 543:293–302.

Lyman, A. W. and Kerr, R. C. (2006). Effects of surface solidification on the emplacement of lava flows on a slope. *J. Geophys. Res.*, 111.

Mathunjwa, J. S. and Hogg, A. J. (2006). Self-similar gravity currents in porous media: linear stability of the Barenblatt–Pattle solution revisited. *Eur. J. Mech. B*, 25:360–378.

Mayfield, K. J., Shalliker, R. A., Catchpoole, H. J., Sweeney, A. P. ., Wong, V., and Guiochon, G. (2005). Viscous fingering induced flow instability in multidimensional liquid chromatography. *J. Chromatogr.*, 1080:124–131.

Mayor, S. D. (2010). Observations of seven atmospheric density current fronts in Dixon, California. *Mon. Weather Rev.*, 139:1338–1351.

McKenzie, D., Ford, P. G., Liu, F., and Pettengill, G. H. (1992). Pancakelike domes on Venus. *J. Geophys. Res.*, 97:15967–15976.

Naaim, M. and Gurger, I. (1998). Two-phase numerical model of powder avalanche theory and application. *Nat. Hazards*, 117:129–145.

Naranjo, J. L., Sigurdsson, H., Carey, S. N., and Fritz, W. (1986). Eruption of the Nevado del Ruiz Volcano, Colombia, on 13 November 1985: tephra fall and lahars. *Science*, 233:961–963.

Neufeld, J. A., Vella, D., Huppert, H. E., and Lister, J. R. (2011). Leakage from gravity currents in a porous medium. Part 1. A localized sink. *J. Fluid Mech.*, 666:391–413.

Nye, J. F. (1952). The mechanics of glacier flow. *J. Glaciol.*, 2:82–93.

Oron, A., Davis, S. H., and Bankoff, S. G. (1997). Long-scale evolution of thin liquid films. *Rev. Mod. Phys.*, 69:931–980.

Orr, Jr, F. M. (2009). Onshore geologic storage of CO_2. *Science*, 325:1656–1658.

Ottino, J. M. (1989). *The Kinematics of Mixing: Stretching, Chaos and Transport*. Cambridge University Press.

Paterson, L. (1985). Fingering with miscible fluids in a Hele Shaw cell. *Phys. Fluids*, 28:26–30.

Pattle, R. E. (1959). Diffusion from an instantaneous point source with a concentration dependent coefficient. *Quart. J. Mech. Appl. Math.*, 12:407–409.

Pegler, S. S., Huppert, H. E., and Neufeld, J. A. (2016). Stratified gravity currents in porous media. *J. Fluid Mech.*, 791:329–357.

Petitjeans, P. and Maxworthy, T. (1996). Miscible displacements in capillary tubes. Part 1. Experiments. *J. Fluid Mech.*, 326:37–56.

Pilkington, L. A. B. (1969). The float glass process. *Proc. Roy. Soc. Lond. A*, 314:1–25.

Pritchard, D. and Hogg, A. J. (2002). Draining viscous gravity currents in a vertical fracture. *J. Fluid Mech.*, 459:207–216.

Rakotomalala, N., Salin, D., and Watzky, P. (1996). Simulations of viscous flows of complex fluids with a Bhatnagar, Gross, and Krook lattice gas. *Phys. Fluids*, 8:3200–3202.

Reynolds, O. (1886). IV. On the theory of lubrication and its application to Mr. Beauchamp Tower's experiments, including an experimental determination of the viscosity of olive oil. *Philos. T. R. Soc. Lond.*, 177:157–234.

Richardson, S. M. (1989). *Fluid Mechanics*. Hemisphere Publishing Corporation.

Saffman, P. G. (1986). Viscous fingering in Hele-Shaw cells. *J. Fluid Mech.*, 173:73–94.

Saffman, P. G. and Taylor, G. I. (1958). The penetration of a fluid into a porous medium or Hele-Shaw cell containing a more viscous liquid. *Proc. Roy. Soc. A*, 245:312–329.

Saucedo, R., Maías, J. L., and Bursik, M. (2004). Pyroclastic flow deposits of the 1991 eruption of Volcán de Colima, Mexico. *B. Volcanol.*, 66:291–306.

Sayag, R. and Worster, M. G. (2013). Axisymmetric gravity currents of power-law fluids over a rigid horizontal surface. *J. Fluid Mech.*, 716:R5.

Sayag, R. and Worster, M. G. (2019a). Instability of radially spreading extensional flows. Part 1. Experimental analysis. *J. Fluid Mech.*, 881:722–738.

Sayag, R. and Worster, M. G. (2019b). Instability of radially spreading extensional flows. Part 2. Theoretical analysis. *J. Fluid Mech.*, 881:739–771.

Schoof, C. and Hewitt, I. (2013). Ice-Sheet Dynamics. *Annu. Rev. Fluid Mech.*, 45:217–239.

Sedov, L. I. (1959). *Similarity an Dimensional Methods in Mechanics*. Mir Publishers.

Simpson, J. E. (1997). *Gravity Currents: In the Environment and the Laboratory*. Cambridge University Press.

Smith, P. C. (1973). A similarity solution for slow viscous flow down an inclined plane. *J. Fluid Mech.*, 58:275–288.

Smith, S. H. (1969). On initial value problems for the flow in a thin sheet of viscous liquid. *Z. Angew. Math. Phys.*, 20:556–560.

Stix, J. (2001). Flow evolution of experimental gravity currents: implications for pyroclastic flows at volcanoes. *J. Geol.*, 109:381–398.

Stone, H. A., Stroock, A. D., and Ajdari, A. (2004). Engineering flows in small devices: microfluidics towards a lab-on-a-chip. *Annu. Rev. Fluid Mech.*, 36:381–411.

Takagi, D. and Huppert, H. E. (2007). The effect of confining boundaries on viscous gravity currents. *J. Fluid Mech.*, 577:495–505.

Thorey, C. and Michaut, C. (2016). Elastic-plated gravity currents with a temperature-dependent viscosity. *J. Fluid Mech.*, 805:88–117.

Turner, J. S. (1979). *Buoyancy Effects in Fluids*. Cambridge University Press.

Ungarish, M. (2009). *An Introduction to Gravity Currents and Intrusions*. Chapman and Hall/CRC.

Valentine, G. A. and Fisher, R. V. (1993). Glowing avalanches: new research on volcanic density currents. *Science*, 259:1130–1131.

Vázquez, J. L. (2007). *The Porous Medium Equation: Mathematical Theory*. Clarendon.

Vella, D. and Huppert, H. E. (2006). Gravity currents in a porous medium at an inclined plane. *J. Fluid Mech.*, 555:353–362.

Videbæk, T. E. and Nagel, S. R. (2019). Diffusion-driven transition between two regimes of viscous fingering. *Phys. Rev. Fluids*, 4.

von Kármán, T. (1940). The engineer grapples with nonlinear problems. *B. Am. Math. Soc*, 46:615–683.

Wilson, D. J. and Kiel, D. E. (1990). Gravity driven counterflow through an open door in a sealed room. *Build. Environ.*, 25:379–388.

Wooding, R. A. (1969). Growth of fingers at an unstable diffusive interface in a porous medium or Hele-Shaw cell. *J. Fluid Mech.*, 39:477–495.

Woods, A. W. and Mason, R. (2000). The dynamics of two-layer gravity-driven flows in permeable rock. *J. Fluid Mech.*, 421:83–114.

Worni, R., Huggel, C., Stoffel, M., and Pulgarin, B. (2012). Challenges of modeling current very large lahars at Nevado del Huila Volcano, Colombia. *B. Volcanol.*, 74:309–324.

Yang, Z. and Yortsos, Y. C. (1997). Asymptotic solutions of miscible displacements in geometries of large aspect ratio. *Phys. Fluids*, 9:286–298.

Zheng, Z., Christov, I. C., and Stone, H. A. (2014). Influence of heterogeneity on second-kind self-similar solutions for viscous gravity currents. *J. Fluid Mech.*, 747:218–246.